ERDC MP-23-3

Engineer Research and Development Center

US Army Corps of Engineers®
Engineer Research and Development Center

ERDC
ENGINEER RESEARCH & DEVELOPMENT CENTER

Development of Alternative Air Filtration Materials and Methods of Analysis

Ivan Philip Beckman

June 2023

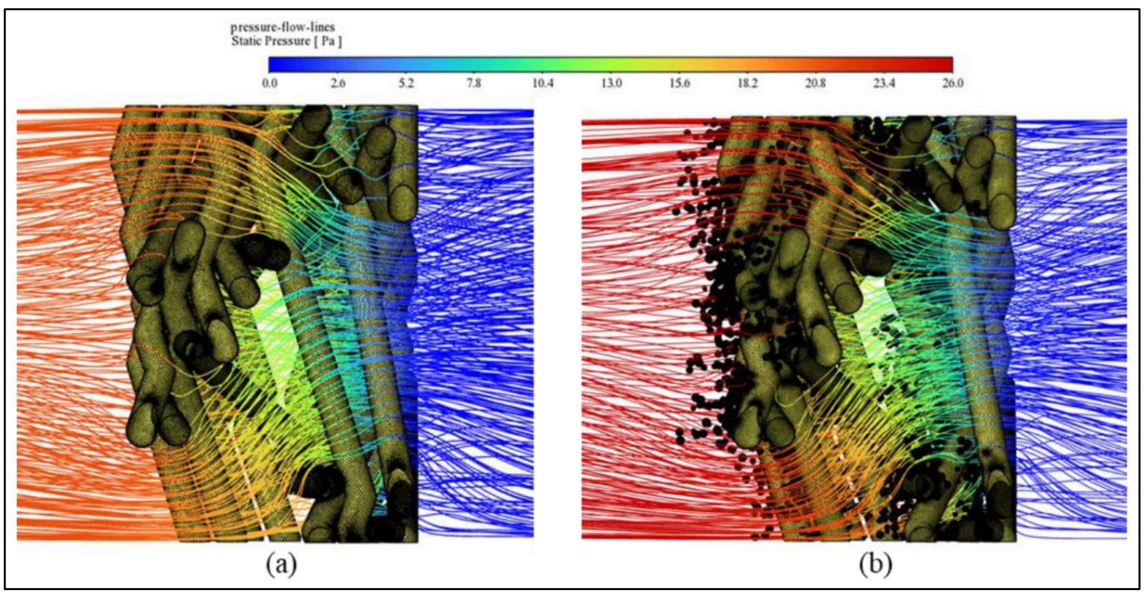

Distribution Statement A. Approved for public release: distribution is unlimited.

The US Army Engineer Research and Development Center (ERDC) solves the nation's toughest engineering and environmental challenges. ERDC develops innovative solutions in civil and military engineering, geospatial sciences, water resources, and environmental sciences for the Army, the Department of Defense, civilian agencies, and our nation's public good. Find out more at www.erdc.usace.army.mil.

To search for other technical reports published by ERDC, visit the ERDC online library at https://erdclibrary.on.worldcat.org/discovery.

ERDC MP-23-3
June 2023

Development of Alternative Air Filtration Materials and Methods of Analysis

Ivan Philip Beckman

US Army Engineer Research and Development Center (ERDC)
3909 Halls Ferry Road
Vicksburg, MS 39180-6199

Final Report

Distribution Statement A. Approved for public release: distribution is unlimited.

Prepared for Mississippi State University
Department of Mechanical Engineering
75 B. S. Hood Rd
Mississippi State, MS 39762

Preface

This study was conducted for the Mississippi State University (MSU), Department of Mechanical Engineering, “Development of Alternative Air Filtration Materials and Methods of Analysis.” The technical monitor was Heejin Cho, MSU.

This article was originally a dissertation submitted in December 2022 to the faculty of MSU in partial fulfillment of the requirements for the degree of Doctor of Philosophy in Engineering in the Department of Mechanical Engineering. This dissertation was approved by Heejin Cho (major professor), Shanti Bhushan, Like Li, Guillermo A. Riveros, Tonya W. Stone (graduate coordinator), and Jason M. Keith (dean, Bagley College of Engineering).

The work was performed by the US Army Engineer Research and Development Center (ERDC). COL Christian Patterson was commander of ERDC, and Dr. David W. Pittman was the director.

DISCLAIMER: The contents of this report are not to be used for advertising, publication, or promotional purposes. Citation of trade names does not constitute an official endorsement or approval of the use of such commercial products. All product names and trademarks cited are the property of their respective owners. The findings of this report are not to be construed as an official Department of the Army position unless so designated by other authorized documents.

DESTROY THIS REPORT WHEN NO LONGER NEEDED. DO NOT RETURN IT TO THE ORIGINATOR.

Development of alternative air filtration materials and methods of analysis

By

Ivan Philip Beckman

Approved by:

Heejin Cho (Major Professor)
Shanti Bhushan
Like Li
Guillermo A. Riveros
Tonya W. Stone (Graduate Coordinator)
Jason M. Keith (Dean, Bagley College of Engineering)

A Dissertation
Submitted to the Faculty of
Mississippi State University
in Partial Fulfillment of the Requirements
for the Degree of Doctor of Philosophy
in Engineering
in the Department of Mechanical Engineering

Mississippi State, Mississippi

December 2022

Name: Ivan Philip Beckman

Date of Degree: December 9, 2022

Institution: Mississippi State University

Major Field: Engineering

Major Professor: Heejin Cho

Title of Study: Development of alternative air filtration materials and methods of analysis

Pages in Study: 230

Candidate for Degree of Doctor of Philosophy

Clean air is a global health concern. Each year more than seven million people across the globe perish from breathing poor quality air. Development of high efficiency particulate air (HEPA) filters demonstrate an effort to mitigate dangerous aerosol hazards at the point of production. The nuclear power industry installs HEPA filters as a final line of containment of hazardous particles. Advancement air filtration technology is paramount to achieving global clean air. An exploration of analytical, experimental, computational, and machine learning models is presented in this dissertation to advance the science of air filtration technology. This dissertation studies, develops, and analyzes alternative air filtration materials and methods of analysis that optimize filtration efficiency and reduce resistance to air flow. Alternative nonwoven filter materials are considered for use in HEPA filtration. A detailed review of natural and synthetic fibers is presented to compare mechanical, thermal, and chemical properties of fibers to desirable characteristics for air filtration media. An experimental effort is undertaken to produce and evaluate new nanofibrous air filtration materials through electrospinning. Electrospun and stabilized nanofibrous media are visually analyzed through optical imaging and tested for filtration efficiency and air flow resistance. The single fiber efficiency (SFE) analytical model is applied to air filtration media for the prediction of filtration efficiency and air flow resistance. Digital twin replicas of nonwoven nanofibrous media are created using computer scripting and commercial digital geometry software. Digital twin filters are visually compared to melt-blown and electrospun filters. Scanning electron microscopy images are evaluated using a machine learning model. A convolutional neural network is presented as a method to analyze complex geometry. Digital replication of air filtration media enables coordination among experimental, analytical, machine learning, and computational air filtration models. The value of using synthetic data to train and evaluate computational and machine learning models is demonstrated through prediction of air filtration performance, and comparison to analytical results. This dissertation concludes with discussion on potential opportunities and future work needed in the continued effort to advance clean air technologies for the mitigation of a global health and safety challenge.

DEDICATION

I dedicate my dissertation to my mom and dad, Ann and Philip Beckman, who fully inspired, encouraged, and supported me in my journey from a dream to an ambition through ultimate fulfilment. Thank You mom and dad! This dissertation is dedicated to you.

ACKNOWLEDGEMENTS

With deepest gratitude I acknowledge my major professor, Dr. Heejin Cho, who inspired and guided me along this journey. Dr. Cho's confidence in me was the foundation of my success.

I also want to thank my committee members, Dr. Guillermo Riveros, Dr. Shanti Bhushan, and Dr. Like Li, who strengthened my work. I acknowledge the ever-optimistic energy of Dr. Riveros who kept me focused and on track. I also acknowledge the assistance and teamwork of Gentry Berry. I acknowledge the academic and professional inspiration I received from Mark Mitchell, Dr. Jeff Haslam, and Dr. James Kelly from Lawrence Livermore National Laboratory.

I acknowledge the leaders of the U.S. Army ERDC, who truly value People, and who made it possible for me to pursue advanced education. I want to thank Dr. Beth Fleming in particular who inspired me to just "go for it" and tracked my progress through completion. I would not have finished my degree without the encouragement and support of the leaders of ERDC.

Finally and most importantly I acknowledge the loving care of my wife Haerin who held our family together through the stressful days weeks and years of this academic pursuit.

TABLE OF CONTENTS

LIST OF TABLES

LIST OF FIGURES

LIST OF SYMBOLS

Symbol	Description	Unit of Measurement
A	filter media cross sectional area	m^2
B	mobility	s/kg
b	distance to boundary (Kuwabara model)	m
c	linear Density	Kg/m
C_c	Cunningham slip correction factor	dimensionless
c_{in}	count of particles approaching fiber	dimensionless
c_{out}	count of particles escaping by fiber	dimensionless
D	diffusion coefficient	m^2/s
d_c	characteristic dimension	m
d_f	fiber diameter	m
d_{fe}	effective fiber diameter	m
d_p	aerosol particle diameter	m
$\widehat{d_p}$	most penetrating particle size	m
E	tensile modulus	Pa
E_Σ	combined single fiber efficiency of components	dimensionless
$\widehat{E_\Sigma}$	minimum SFE (Lee and Liu)	dimensionless
E_D	SFE diffusion component	dimensionless
E_{DR}	SFE for interception of diffusing particles	dimensionless
E_E	SFE electrostatic component	dimensionless
E_F	total filter efficiency	dimensionless
E_G	SFE gravity component	dimensionless
E_I	SFE inertial impaction component	dimensionless
E_R	SFE interception component	dimensionless
E_S	specific Modulus (E/ρ)	dimensionless
EI	flexural Rigidity of a Beam	$N \cdot m^2$
F_d	force of drag on a particle	N
FOM	figure of merit, also quality factor	1/Pa
G	gravitational coefficient for SFE component	dimensionless
g	gravitational constant (9.81)	m/s^2
Kn	Knudsen number	dimensionless
Ku	Kuwabara hydrodynamic factor	dimensionless
k	Boltzmann constant, 1.38E-23 J/K	J/K
k_r	inverse of radius of curvature	1/m
m	mass of the particle	kg
M	moment of inertia	$kg \cdot m^2$
P_Σ	single fiber penetration	dimensionless

Symbol	Description	Unit of Measurement
P_{F}	total filter penetration	dimensionless
Pe	Peclet number	dimensionless
Q	volumetric flow rate of air	m^3/s
R	ratio of particle-to-fiber diameter	dimensionless
Re	Reynolds number	dimensionless
r_{f}	fiber radius	m
r_{p}	particle radius	m
s	fiber shape factor	dimensionless
S	particle stopping distance	m
Stk	Stokes number	dimensionless
T	absolute temperature	K
t	thickness of the air filter media	m
U_0	air velocity	m/s
u_{r}	radial velocity (Kuwabara model)	m/s
u_{θ}	tangential velocity (Kuwabara model)	m/s
α_{f}	solidity, solid volume fraction, packing density	dimensionless
ΔP	pressure differential, flow resistance	Pa
η	air viscosity	Pa·s
λ	mean free path of air, approximately 65 nm	m
ν	mean air velocity inside cell (Kuwabara model)	m/s
ν_0	initial velocity of a particle (mobility)	m/s
ν_{t}	terminal velocity of a particle (mobility)	m/s
ρ	volumetric density of the fiber material	kg/m^3
ρ_{g}	air density	kg/m^3
ρ_{p}	density of the particle	kg/m^3
τ	relaxation time	s
ψ	stream function (Kuwabara model)	dimensionless
ω	vorticity (Kuwabara model)	rotations/s
∇^2	vector Laplacian (Kuwabara model)	dimensionless

DERIVED UNITS OF MEASUREMENT

Unit	Description	SI Base Units
tex	measure of linear density	1.0E-6·kg/m
dtex	decitex, measure of linear density	1.0E-7·kg/m
de	denier, measure of linear density	9.0E-6·kg/m
gpd	grams per denier, measure of specific strength	8.826E4·$m^2 \cdot s^{-2}$
yuri	measure of specific strength	$m^2 \cdot s^{-2}$
MY	mega yuri, measure of specific strength	1.0E6·$m^2 \cdot s^{-2}$

This page intentionally left blank.

CHAPTER I

INTRODUCTION

Continual research, development, and advancement in air filtration technology is important to abate the ever-increasing health hazards of air pollution and global pandemics. Clean air is vital to sustaining life. In 2016, the World Health Organization (WHO) estimated between seven and eight million people globally die from poor air quality and air pollution [1]. Today more than 92% of the world's population lives in areas that exceed dangerous levels of particulate aerosol from both indoor and outdoor sources [1]. Surgical masks and N95 masks for personal protection were commonplace throughout three years of the global SARS-COVID19 pandemic. The United Nations Resolution 70/1, Transforming our world: the 2030 Agenda for Sustainable Development, set a goal for reducing the number of deaths worldwide caused by air pollution and contamination [2]. The 2019 UN Blue Skies Campaign clearly linked the negative effects of air pollution to human health, longevity, and climate change. General Assembly Resolution 74/212 of 2019 set September 7th as Clean Air Day and recognized, "Clean air is important for the health and day-to-day lives of people, while air pollution is the single greatest environmental risk to human health and one of the main avoidable causes of death and disease globally" [3].

Particulate matter aerosol pollution with an average particle diameter size of 10 µm or less (PM_{10}) is dangerous to our health. For size perspective, human hair is approximately 70 µm in diameter. Seven PM10 particles placed side by side would equal the diameter of one human hair. PM_{10} particles are dangerous because they are easily inhaled and trapped into the lungs where they cause asthma and lung cancer. Aerosol particles with average diameter size of 2.5 µm or less ($PM_{2.5}$) are exceptionally dangerous since they can also pass through the lungs into the bloodstream, where they can damage internal organs such as the heart and brain.

The development and advancement of high efficiency particulate air (HEPA) filters demonstrate efforts toward sustain clean breathable air. The U.S. Department of Energy (DOE) installs HEPA filters as a line of defense to contain hazardous particles in high level waste (HLW) storage tanks. For many years Lawrence Livermore National Laboratory (LLNL) has conducted extensive research on better materials and methods to filter and clean the ventilation air for HLW storage tanks [4]–[7]. HEPA filters are common today, however HEPA filter technology has seen only minor advancement over the past several decades. The most common filtration media in use today, glass fiber filter paper, is fragile and prone to fire and water damage, as demonstrated by the Rocky Flats fire of 1957 [8]. While better than the original cellulose-asbestos fibrous media, glass fibrous media performs poorly in high temperature applications and high humidity environments.

Global health and livelihood depend upon clean breathable air. A continuous effort to advance the science and technology of clean air is needed to mitigate health and safety risks associated with the global challenge of air pollution.

1.1 Research Goal

The research goal of this dissertation is to advance the science and technology of air filtration by 1) understanding the important mechanical and thermal characteristics of fibers and nonwoven fibrous materials, 2) improving experimental production of air filtration media, 3) developing digital twins of air filters that closely replicate their real counterparts, and 4) applying analytical models, machine learning models, and computational fluid dynamics models which transparently demonstrate the science of air filtration. Successful advancement of air filtration technology will improve global health and safety through mitigation of hazardous aerosols and reduction of particulate matter air pollution. The advancement of air filtration technology is, simply stated, the key to global clean air.

1.2 Detailed Research Objectives

1.2.1 Explore Characteristics of Fibers and Nonwoven Fibrous Media

The first research objective is to advance air filtration technology by studying mechanical, chemical, and thermal properties of fibers, and by informing filter designers of what fiber types should be explored for integration into air filter media.

1.2.2 Improve Air Filtration Media Production

The second research objective is to advance air filtration technology experimentally through improving electrospinning production techniques with polyacrylonitrile-graphene composite fiber air filter media. Electrospinning is an effective method of producing very small diameter fibers that work well in air filtration.

1.2.3 Analytical Modeling of Air Filtration

The third research objective is to advance air filtration technology through successful application of analytical single fiber efficiency models. Understanding the basic physics at the microscale and nanoscale levels of fiber-air-particle interaction results in successful analytical modeling of particle capture mechanisms.

1.2.4 Digital Twin Replication of Air Filtration Media

The fourth research objective is to develop digital twin duplication for air filter media that closely replicate the physical characteristics of real air filter media in a digital format.

1.2.5 Machine Learning Modeling of Air Filtration

The fifth research objective is to advance air filtration technology through development and application of machine learning models. Convolutional neural networks are effective models that advance the understanding of air filtration through computer vision.

1.2.6 Computational Fluid Dynamics Modeling of Air Filtration

The sixth research objective is to advance air filtration technology through application of computational fluid dynamics modeling of air filter media. Digital twin geometry of air filter media can be tested computationally for air filtration performance.

1.3 Dissertation Outline

This dissertation has nine chapters, including this introduction chapter, a conclusion chapter, and seven main body chapters to achieve the listed research objectives. Chapter II reviews the mechanical and thermal characteristics of the family of fibers and explores the fiber types and characteristics that would perform well in air filter media. Chapter III explores the single fiber efficiency analytical model of air filtration. Chapter IV details experimental effort undertaken for this dissertation to produce graphene-embedded nanofibers that may potentially adsorb volatile organic compounds while also filtering particulate matter from air. Chapters V and VI illustrate the production and refinement of a digital twin model for the creation of digital air filter media that closely replicates real world filter media. The application of Bertrand's paradox to the random fiber placement algorithm in Chapter VI improved the digital twin creation model by ensuring a uniform spatial distribution of fibers. A convolutional neural network was constructed in Chapter VII to analyze digital imagery produced from digital twin media and applied to an actual SEM image of electrospun media produced in Chapter IV. Finally, chapter VIII details efforts undertaken to model digital twin air filter media with computational fluid dynamics software, to include the digital twins used in the machine learning model, a comparison of clean media with particulate-laden media, and a digital twin designed to replicate H14 HEPA filter paper. A graphical representation of the dissertation outline is shown in Figure 1.1.

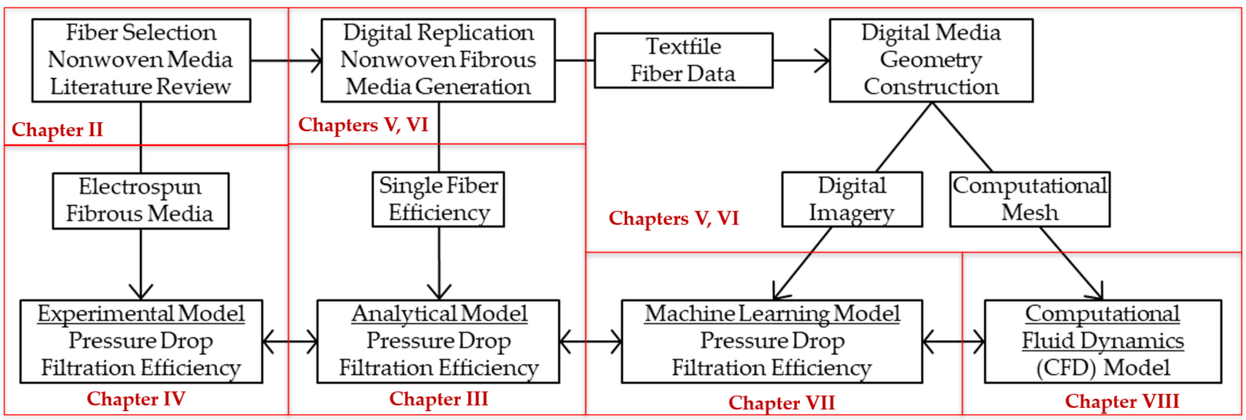

Figure 1.1 Dissertation outline.

1.4 Lines of Effort

The research effort of this dissertation flows along the outline shown in Figure 1.1, and results in four coordinated models represented by Chapters III, IV, VII, and VIII. The essence of this dissertation is the coordination of these four lines of effort, which include experimental modeling, analytical modeling, machine learning modeling, and computational fluid dynamics modeling of air filtration. Successful coordination of these four lines of effort into one integrated approach will advance the science of air filtration and improve our ability to produce and apply alternative air filtration materials and methods to improve global air quality.

CHAPTER II

LITERATURE REVIEW: ALTERNATIVE HIGH-PERFORMANCE FIBERS FOR NONWOVEN HEPA FILTER MEDIA[1]

The purpose of this chapter is to survey, categorize, and compare mechanical and thermal characteristics of fibers to assess their potential applicability in air filter media. The history of high efficiency particulate air (HEPA) filter development explains how we arrived at the current state of the art nonwoven fibrous borosilicate glass filter paper. This chapter explores the history and practical uses of fiber types and explains fiber production methods in general terms. The thermal and mechanical properties of fibers are examined using the codes and standards produced by the American Society of Mechanical Engineers (ASME) to generalize the applicability of fiber categories for HEPA air filter units within the nuclear air cleaning industry. This chapter discusses common measurements for specific strength and tenacity used by the textile and construction industries. Fibers are selectively compared for density, tensile strength, tensile stiffness, flexural rigidity, moisture regain, decomposition temperature, and thermal expansion. This chapter concludes with a subjective assessment of which types of fibers may be appropriate to study for HEPA air filtration.

[1] Content from this chapter is published in a journal article. Beckman, I.P., Berry, G., Cho, H. et al. Alternative High-Performance Fibers for Nonwoven HEPA Filter Media. Aerosol Sci Eng (2022). https://doi.org/10.1007/s41810-022-00161-6.

2.1 Introduction

Recent development of new materials and production techniques suggests better materials and designs may enable advancement of air filtration technology. Currently most personal protective masks are constructed with polypropylene fibers, while most industrial filter media are produced with pleated glass fiber paper. Alternative fiber types should be explored for inclusion in air filtration media, to continue the advancement of both safety and performance of HEPA filters. The U.S. Customs and Border Protection agency maintains a list of 1200 fiber trade names that represent 43 generic fiber categories, acknowledging that the list is neither exhaustive nor complete [9]. The purpose of this chapter is to survey fiber types and compare mechanical, thermal, and chemical characteristics of particular fibers in order to advance air filtration technology and assist developers in the selection of fibers for air filter media. Special attention in this chapter is toward HEPA filter media intended for use by the nuclear air and gas industry.

2.2 Background Information

2.2.1 A Brief History of HEPA Air Filtration

Lewis Haslett is credited with the first modern air filter respirator in 1849 with his “Lung Protector” invention and patent [10]. Haslett developed his respirator with woolen fabric filter media. Ninety years later, at the outbreak of the Second World War, gas masks intended for smoke and dust filtration were still built with wool and cotton. The threat of chemical warfare brought new advancement in air filtration. The masks protecting German soldiers were produced from fine asbestos fibers and coarse esparto grass fibers and noted for exceptionally high filtration efficiency and low airflow resistance to breathing [11], [12]. British gasmask woolen filters suffered from clogging with oil-based smoke aerosols and didn’t perform as well as the asbestos fibrous media [12]. The U.S. Army Chemical Warfare Services Command (CWS) in

Edgewood Maryland tested the German filter materials and noted the superior performance of the asbestos fibers within the cellulose filter paper [12]. From this experience, the CWS laboratory developed and produced “H-64” filtration paper which was later renamed “CWS type 6” paper and made from a combination of northern spruce sulfite, cotton, African esparto grass, and fine Bolivian Blue crocidolite asbestos fibers [11], [12]. The laboratory noted the superior filtration performance of asbestos fibers cleaved to under 0.25 µm diameter [11]. The U.S. Army went on to produce “collective protector” filtration units that required more airflow than personal gasmasks, by deep-pleating CWS6 paper into square-framed canisters [12].

The Army’s collective protector filter units were adopted by the U.S. Atomic Energy Commission (AEC) in the late 1940’s to contain airborne radioactive particles in nuclear research facilities and ventilation exhaust systems of experimental nuclear reactors. In order to reduce dependency on foreign materials, the AEC replaced Bolivian crocidolite with Canadian asbestos. From 1944 to 1951, collective protector filter units were entirely made from all natural materials. The AEC began considering alternatives to cellulose-asbestos filter media in 1949 to overcome the flammability hazard at moderate and high temperatures. This led to the development of combined glass-asbestos fibrous media and all-glass fibrous media in 1951. The Naval Research Laboratory (NRL) developed methods to reduce the diameter size of glass fibers to 250 µm suggesting glass could be a substitute for asbestos fibers. The AEC type 1 filters were also termed absolute, super-interception, super-efficiency, and nuclear filters [11], [12]. Humphrey Gilbert coined the acronym “HEPA” from a 1961 AEC report, “High-Efficiency Particulate Air Filter Units, Inspection, Handling, Installation” [12]. The term HEPA today describes filter materials that achieve a high efficiency of 99.97% of 300 nm particles while maintaining a low resistance to air flow, measured by pressure drop across the filter material.

The pleated borosilicate-glass nonwoven fibrous filter paper media produced in 1951 is essentially still in production and use as HEPA filter units today.

2.2.2 Fibers and Particulate Membranes

Air filters are commonly constructed with either fibrous media or porous particulate media [13]. Porous membrane media is generally denser than fibrous filter media, which creates complex flow streamlines with high efficiency but also high air flow resistance. Porous media can be produced by a variety of methods with ceramics or sintered powdered metals. Composite air filter materials could be designed with both fibrous media and porous media, combining the advantages of both, for example gaining mechanical strength from a porous substrate layer while gaining high efficiency from a fibrous layer. A topic for further development is optimization of composite filter media with porous membranes and fibrous layers, however the remainder of this chapter will focus on fibrous media.

2.2.3 Definition of a Fiber

While fiber cross sections have various shapes, fibers are generally distinguished from other materials as having a large aspect ratio of length to cross sectional diameter, typically in excess of 100:1. The characteristics of the wide range of raw materials used to make fibers determine what fiber types are useful, including long continuous fibers and short cut fibers. Short cut fibers are further classified as chopped strands, whiskers, or staple fibers depending on their method of production. Metal filaments with diameters greater than 100 µm are generally considered wires, while diameters less than 100 µm are considered metal fibers.

2.2.4 Fiber and Nonwoven Media Production Techniques

There many techniques to produce fibers, and many techniques to produce nonwoven media from fibers [14]. Basic methods of nonwoven fibrous media production include dry laying (including air-laid and carded), wet laying, spun-lanced, spun-bonded, melt-blown, thermal bonded, needle-punched, and electrospun [15], [16]. Fibers used in air filtration media can be classified as short (typically 1 mm to 20 mm) or long (greater than 20 mm). Dry-laid and wet-laid techniques use shorter fibers which are cut or produced at a target length, dispersed in air or water, and deposited into a mat to form nonwoven fibrous media [15]. Carding is a technique traditionally used in cotton production to mechanically disentangle, separate, and intermix fibers into a continuous mat. Needle punching or felting are techniques to bond short cut fibers into a nonwoven mat. Melt-blown, spun-bonded, and electrospun techniques have the ability to produce long fibers with small diameters. Electrospinning easily produces fibers with diameters in the 50 to 250 nm range. Melt-blowing produces fibers with diameters around 5 um, and spunbonded fibers range in the 20 µm range [15].

"Spinning" describes the method of fiber production, while "laying" describes the method to produce nonwoven media from fibers. Spinning represents the extrusion of a liquid material through a spinneret nozzle or needle to produce continuous fibers [17]. If the liquid material is prepared for spinning by melting, the process is known as melt spinning, which includes melt-blowing techniques. If the material is prepared for spinning by dissolution, the technique is known as solution spinning, which can be further categorized into dry-spinning, wet-spinning, dry-wet-spinning, sheared wet spinning, and gel-spinning. Electrospinning uses a high voltage electric field to eject fibers from the liquid and can be applied to both solution spinning and melt spinning. Other methods to produce fibers and whiskers for air filtration media include Chemical Vapor Deposition (CVD), bundle drawing, foil shaving, and machining.

Bundle drawing is a technique developed in the 1930's to produce malleable metallic fibers. Thousands of metal wires are bundled together and drawn through reducing dies to decrease the bundle diameter and the diameter of each individual fiber. The bundles are then grouped into larger numbers and redrawn, resulting in smaller hexagon-shaped fibers. Recent advances in bundle drawing have resulted in metallic fibers in the range of 200 nm and smaller [18]. To produce nonwoven media, bundle drawn wires must be chopped to size and assembled through dry-laid or wet-laid techniques.

2.2.5 Characteristics of Fiber Types

Fibers are organized and classified for comparison differently by the construction industry and textile industry. The textile institute publishes a fiber classification chart which first separates fibers into natural and man-made categories [19]. Natural fibers are those that occur in nature, to include fibers produced by plants, animals, and minerals. Another simple classification is whether the fibers are made from organic or inorganic materials. Organic fibers can be further categorized into synthetic polymer, natural cellulose, regenerated cellulose, keratin, and carbon fibers. Natural plant-based fibers are made with the protein cellulose, while animal-based fibers are made from the protein keratin. If the plant is harvested, dissolved, then synthesized into fibers, the term "regenerated" cellulose describes a dual synthetic-natural category. Inorganic fibers can be subdivided into ceramic, oxide, non-oxide, elemental, mineral, metal, and volcanic rock, as in basalt fibers.

2.2.5.1 Natural Plant-Based Cellulose Fibers

Wood pulp, derived from both hardwood (oak, gum, birch, beech, aspen, eucalyptus) and softwood (pine, spruce, fir, cedar, hemlock, redwood), is a common material in nonwoven fibrous filtration paper media [20]. Wood chips are typically cooked into pulp through the ‘kraft’ process, which uses sodium hydroxide, sodium sulfide, sulfurous acid, and bisulfite to break down the lignin at 170°C to create wood pulp. Wood fibers are then bleached, fibrillated, and wet-laid to form filter paper [20].

Natural plant-produced fibers other than those produced by trees are also called ‘vegetal’, ‘vegetable’, ‘plant’, ‘cellulosic’, and ‘lignocellulosic’ fibers to name a few names [21]. Cotton is a common cellulosic fiber made up of 99% pure cellulose. The cotton gin mechanically removes short fibers known as linters from harvested cotton. Cotton staple and first-cut linters can be made directly into air filtration material through a needle felting or needle punching process where nonwoven fibers are mechanically interlocked with special barbed needles that bonds fibers together. First-cut and second-cut linters can also be made into filtration media through a wet-laid process similar to wood pulp. Other common forms of cellulose fibers include abaca, hemp, esparto grass, sisal, jute, kenaf, and flax. Vegetal fibers are harvested from all parts of vegetable plants, and can be categorized into seed, stem, leaf, or husk as shown in Table 2.1.

Table 2.1 Vegetal Fiber Types and Examples

Seed	Stem (Bast)	Leaf	Husk/Fruit
Cotton, Kapok, Milkweed	Flax, Hemp, Jute, Ramie, Kenaf, Kudzu, Linden,	Esparto, Sisal, Abaca, Palm, Manila, Curaua	Coconut (coir), Banana, Agave

The relative global abundance and ease of harvesting natural cellulose fibers make them attractive candidates for air filtration. Cotton materials have significant use as filtration media for personal protective face masks, typically as outer layers for an inner layer of polypropylene fiber material. In addition to cotton, kapok fibers have seen increased interest and research in the filtration of oil based aerosols [22]. The bast fibers flax, jute, hemp, and ramie continuously undergo study for their usefulness in air filtration [23]–[28]. Esparto grass fibers were used in early HEPA filter development, while sisal and abaca fibers have similarly attracted attention and study for their potential in air filtration [29].

2.2.5.2 Regenerated Cellulose Fibers

Regenerated cellulose fibers are considered both natural and synthetic categories, since the basic cellulose is derived from harvested plant-based materials and synthesized into fibers. The first production of regenerated cellulose synthetic fibers is credited to Count Hilaire de Chardonnet in France in the early 1880s, receiving a patent on the process in 1885 [30]. The American Viscose Company produced regenerated cellulose fibers starting in 1910, while the Dupont Fibersilk Company started production in 1921 [30]. Today, viscose is a common term given to regenerated fibers that refers to the sodium hydroxide and carbon disulfide solution used to derive the cellulose. Rayon is a common term which replaced the initial description of synthetic silk in 1924 [30]. Viscose fibers were a common filtration media in the past, and still useful in automotive air filtration, however most home pleated air filters are now made from fully synthetic polypropylene.

2.2.5.3 Natural Animal-Based Keratin Fibers

Keratin is a natural protein with a fibrous structure produced by animals and found in hair, feathers, wool, horns, claws, and hooves. Wool was among the original filter materials of choice during the Second World War, and is still used as a common filter material for vacuum cleaner bags today [20]. Animal-based keratin protein fibers are categorized and grouped as wool, hair, and silk as shown in Table 2.2.

Table 2.2 Keratin Fiber Types and Examples

Wool	Hair	Silk
Sheep, Alpaca, Angora Rabbit, American Bison, Cashmere Goat	Horse, Camel	Spider Silk, Silkworm Silk

Sheep's wool in particular has attracted interest in indoor air pollution abatement, including separation of formaldehyde from breathable air [31]. Silk proteins can also be regenerated through an electrospinning process to produce environmentally friendly and efficient air filter materials to reduce indoor air pollution [32]. Additional research into the application of natural wood, vegetal, and animal-based fibers as air filter media might contribute to air filtration technology.

2.2.5.4 Synthetic Polymer Fibers

Nylon, the tradename for polyamide 6-6 fibers, was the first wholly synthetic polymer fiber credited to Carruthers and Hill in 1932 and produced in the United States by Du Pont since 1935 [30]. Paul Schlack of I. G. Farbenindustrie first polymerized caprolactam to polyamide-6 fibers in 1938, which were later produced commercially by the Allied Chemical Company in 1955 and known as Perlon fibers [30].

Polyester fibers were first produced shortly after polyamide fibers by the Calico Printers Association in England in 1940 under the name Terylene [30]. Du Pont Company in the United States began research into polyester fibers in 1945 and produced polyethylene terephthalate (PET) fibers from dimethyl terephthalate and ethylene glycol under the tradename Dacron [30]. Polyester fibers became popular textile blend fabrics worldwide.

Acrylic fibers by definition are composed of at least 85% of the polymer acrylonitrile, while modacrylic fibers contain between 35% and 85% acrylonitrile [30]. Acrylic and modacrylic fibers were produced by Du Pont, Monsanto, Union Carbide, and Eastman companies starting in the 1950s and carried brand names of Orlon, Acrilan, Vinon, Dynel, and Verel [30]. Polyacrylonitrile is easily produced in small nanometer scale diameter sizes through electrospinning and is a popular precursor fiber for conversion to carbon fibers.

Olefin fibers, specifically polypropylene fibers, were first produced through discoveries by Karl Ziegler in Germany and Julio Natta in Italy in 1954 [30]. Compared to all synthetic fibers, polypropylene is the least expensive to produce, while it is uniquely hydrophobic, resistant to chemicals, and stable in air and sunlight [30]. The low melting point of polypropylene in particular and olefin fibers in general is a major drawback for use in HEPA air filtration applications. However, polypropylene is the most popular fiber used in personal protective filter masks and air filters for home and industrial use where temperature range where low melting temperatures are acceptable. High density polyethylene (HDPE) and ultra-high molecular weight polyethylene (UHMWPE) are olefin fibers with the highest strength-per-weight ratio of all fibers discussed in this chapter and would perform well as HEPA air filter fibers if they had a higher melting point. Table 2.3 categorizes synthetic common synthetic polymer fiber types with trade name examples.

Table 2.3 Synthetic Polymer Fiber Types

Amide	Polyester	Liquid Crystalline	Olefin	Common Polymers
Nylon 6	PET	Para-aramid	Polypropylene	PVA, PTFE
Perlon	Dacron	Meta-aramid	Polyethylene	Polyurethane
Nylon 6.6	Terylene	Aromatic Heterocycle	(HDPE, LDPE,	Acrylic, Modacrylic
	Kodel	Copolyester	UHMWPE)	Polyacrylonitrile

2.2.5.5 Carbon Fibers

Carbon fibers are formed through heat treatment of precursor materials. Common precursors include polyacrylonitrile, various forms of natural and regenerated cellulose, and petroleum or pitch products. Laboratory tests have shown potential benefits of using carbon fibers in air filtration. Carbon nanotubes combined with activated carbon fibers show great potential for adsorbing ozone while also filtering particulate matter in indoor environments [33]. Activated and ionized carbon fibers were tested for indoor air filtration with good results. Carbon nanotubes were also noted for their high efficiency and low pressure drop during filtration in the free molecular flow region [34].

2.2.5.6 Ceramic Fibers

Initial attempts at ceramic fibers for air filtration date back to the Hurlburt Paper Company and Hollingsworth and Vose Company in the mid-1950s as they produced filter paper from Fiberfrax fibers made of silicon oxide-aluminum hydroxide [12]. Ceramic fibers show high potential for achieving HEPA level air filtration. Laboratory production and testing of aluminum oxide stabilized zirconium oxide fibers resulted in high filtration efficiency and low flow resistance [35]. In addition to high efficiency and low resistance, the lightweight ceramic air filtration paper produced through blow spinning showed excellent thermal and mechanical properties with high flexibility, foldability, temperature range, and burn resistance [35].

2.2.5.7 Glass and Quartz Fibers

Melt-blowing or melt-spinning are common methods to produce small diameter glass fibers. Glass fiber filter paper, initially produced and tested by NRL as a substitute for asbestos fiber paper in the 1950s, continues to be the media of choice for deep pleated HEPA filter units today. Glass fibers are produced from many varieties of glass, which is categorized based on the ingredients that accompany silicon dioxide (silica). Quartz fibers are fully crystalized silica. Two common quartz fibers are Quartzel and Astroquartz. Quartz fibers have attractive qualities for air filtration; however, they are expensive to produce.

2.2.5.8 Mineral Fibers

Asbestos is a naturally occurring long thin fibrous material formed on silicate minerals. Asbestos fibers are divided into two classifications: serpentine (curly fibers) and amphibole (needle-like fibers). Chrysotile is the only form of serpentine asbestos, while amphibole asbestos includes amosite, crocidolite, tremolite, anthophyllite, and actinolite, as shown in Table 2.4. Chrysotile is the most common form of asbestos found in buildings built before 1980.

Table 2.4 Asbestos Fiber Types

Serpentine Asbestos	Amphiboles Asbestos
Chrysotile	Amosite (asbestos grunerite), Crocidolite, Tremolite, Anthophyllite, Actinolite

Asbestos fibers have significant resistance to heat and make excellent thermal and electrical insulation. Asbestos fibers were used in air filtration since the Second World War and up until discovery of the health risks of asbestos particles. Asbestos was a primary source of early HEPA filtration [12]. In the 1970s, the health hazards caused by airborne asbestos fibers surfaced, and the use of asbestos fibers is now banned in many countries. Airborne asbestos fiber particles can become lodged deep into lungs and cause cancer. Asbestos fibers are no longer considered for HEPA filter media nor general construction because of the significant health risks.

2.3 Mechanical, Thermal, and Chemical Considerations for Fiber Selection

The mechanical and chemical properties of air filtration media play an important role in the overall performance of an air filter. Characteristics of the fiber surface determine the ability of the fiber to contact and retain particles. Fiber tensile and flexural strength are important to prevent tearing of the filter media under variable flow conditions. The chemical properties of the media determine whether it will oxidize or decompose over time, and whether the media will combust or degrade under high temperature conditions.

2.3.1 ASME AG-1 Specification

Since 1971 the American Society of Mechanical Engineers (ASME) has developed the code and standards to evaluate materials proposed for use in the nuclear air and gas industry. The initial ANSI N45.8 Committee was reorganized into the Committee on Nuclear Air and Gas Treatment in 1976 and produces the ASME AG-1 code for nuclear air and gas treatment. The AG-1 specifies requirements for materials testing and approval of nuclear grade HEPA filter media [36]. Section FC of the AG-1 serves as a useful guide to evaluate desirable physical and chemical properties important in air filtration media, to include tensile strength (under normal, heated, wet, and irradiated conditions), water repellency, combustion resistance, flexibility, and mildew resistance. Airflow resistance and particle filtration efficiency are two basic parameters to qualify as HEPA filter media. The maximum allowable pressure drop across the filter media is 320 Pa tested at ambient conditions with minimum face velocity of 2.5 cm/s. The filter media must have an efficiency of at least 99.97% when tested with 0.3 μm diameter particles and an efficiency of at least 99.9% when tested with the most penetrating particle size at 2.5 cm/s. The ASME AG-1 standards show a preference for noncombustible, water repellant, and mildew resistant fibers that have high strength, toughness, and flexibility shown in Table 2.5.

Table 2.5 Parameters and Specifications of HEPA Filter Media from ASME AG-1

Mechanical	Chemical	Thermal	Environmental Conditions
Tensile Strength, Flexural Strength, Flexibility	Water Repellant Mildew Resistant Non-Combustible Corrosion Resistant	Temperature Range Burn Resistance	Temperature Wet and Humid Irradiated

2.3.2 European and International Specifications

Since 1998, the European Committee for Standardization define H13 and H14 HEPA filter media as having an efficiency of 99.95% and 99.995% respectively with "High Efficiency Air Filters" standard EN 1822 [37]. The International Organization of Standards adopted the European EN 1822, and added categories to match other international standards in existence, with the publication of "High Efficiency Filters and Filter Media for Removing Particles from Air," ISO 29463 [38]. The ASME AG-1 specification for nuclear grade HEPA filters compares with the European and ISO standards as shown in Table 2.6. Notable differences include the air filtration nominal flow rate and particle size. The EN 1822 and ISO 29463 efficiency standards are based on the most penetrating particle size (MPPS), while the ASME AG-1 standard specifies both MPPS and 0.3 μm particle sizes.

Table 2.6 Comparison of HEPA Specifications for Nonwoven Fibrous Media

ISO 29463	EN 1822	ASME AG-1	Efficiency (%)	Flow Rate (cm/s)	Particle Size	Resistance (Pa)
35H	H13	-	99.95	5.3	MPPS	-
-	-	HEPA	99.97 / 99.9	2.5	0.3 μm / MPPS	320
40H	-	-	99.99	5.3	MPPS	-
45H	H14	-	99.995	5.3	MPPS	-

2.3.3 Fiber Diameter Sizes

Fiber diameter size is a critical parameter that affects filtration efficiency and flow resistance of an air filter. Smaller diameter fibers have a greater ratio of surface area to volume and generally result in higher filtration efficiency. The SFE model is useful in illustrating the effects of various fiber diameter sizes on filtration efficiency and flow resistance. Figure 2.1 illustrates three digital twin replica geometry of air filter media of varied diameter sizes, each with a consistent face coverage of 100%. Here face coverage is defined as the ratio of summed area of the fibers projected onto the plane perpendicular to airflow compared to total area, which can be thought of as the shadow the fibers on the plane normal to flow.

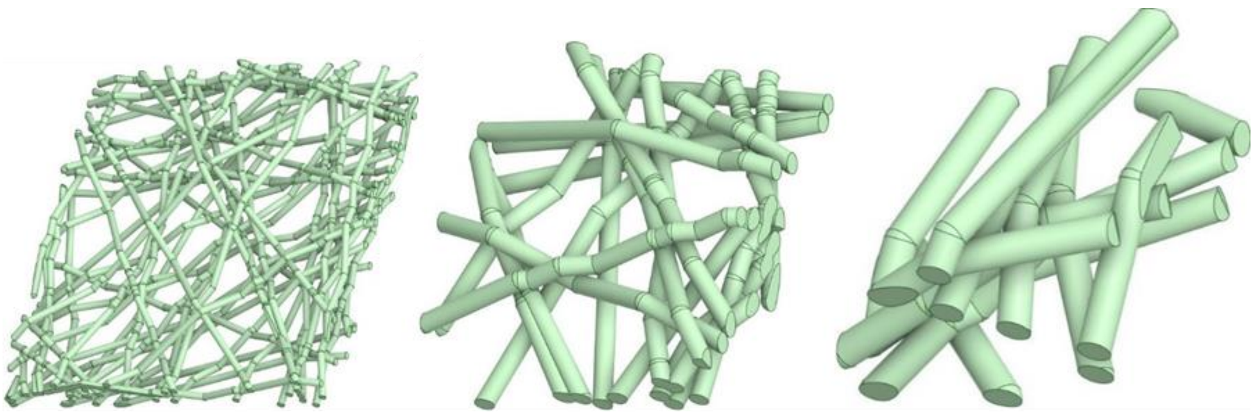

(a) (b) (c)

Figure 2.1 Comparison of filtration media produced from a range of diameter sizes. (a) 0.1 µm diameter fibers. (b) 1.0 µm diameter fibers. (c) 2.0 µm diameter fibers.

Figure 2.2 shows the resulting effects on air filtration efficiency and air flow resistance of varying fiber diameters from 1 to 20 µm, while maintaining consistent face coverage of 100%. For this analysis, a digital twin replica of filter media was produced using a computer program script and Ansys SpaceClaim using a procedure shown in Chapter V [39]. The thickness of the filter media varied from 1.32 µm to 11.28 µm, while the solidity varied from 6.24% to 15.35%.

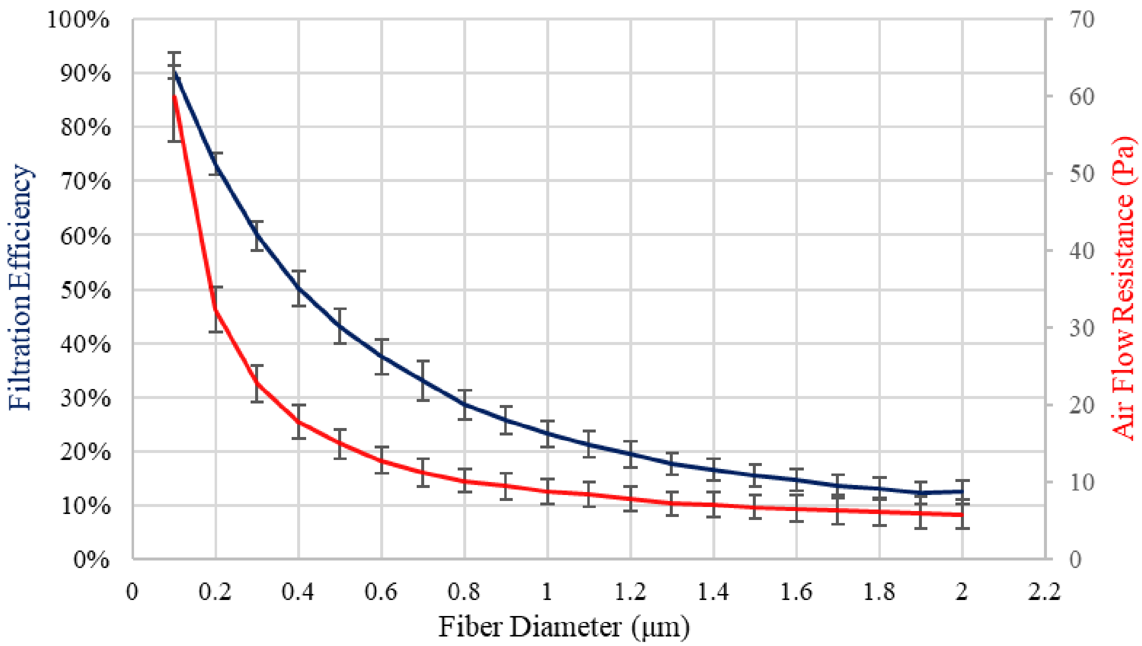

Figure 2.2 Resulting filtration efficiency and flow resistance. Error bars on filtration efficiency and air flow resistance represent 95% for 100 observations.

While many regenerated and synthetic fibers are available in various diameter sizes, most natural cellulose and keratin-based fibers are constrained by a range. The very small fiber diameters of carbon nanotubes, ranging from 1 to 5 nm, create a significant advantage in air filtration [40]. Electrospinning as well produces small diameter fibers in the range of 50 to 900 nm. Table 2.7 illustrates typical diameter ranges of select fibers. For comparison, the average size of a human hair is 50 to 70 µm.

Table 2.7 Comparison of Example Fiber Diameter Sizes

Fiber	Category	Typical Diameter (μm)
Carbon Nanotube	Carbon	0.001 to 0.005
Toyobo Zylon PBO	Synthetic Polymer	1.2
Honeywell Spectra 1000 UHMWPE	Synthetic Polymer	1.7 to 3.1
Alumina Saffil	Ceramic	3
E Glass (Alumina Borosilicate)	Glass	3 to 20
Toray T1100G Carbon Fiber (PAN)	Carbon	5
Fortisan Viscose Rayon	Regenerated Cellulose	9
Quartzel Fibers	Quartz	9 to 14
Basalt Fibers	Basalt	10 to 20
Solvay P25 Carbon Fiber (Pitch)	Carbon	11
American Uppers Cotton Fibers	Natural Cellulose	11 to 22
Dupont Kevlar 49	Synthetic Polymer	12
Oak Wood Fibers	Natural Cellulose	13
Nylon 6 Fibers	Synthetic Polymer	14
Polyacrylonitrile	Synthetic Polymer	16
Wool Fibers	Natural Keratin	18 to 44
Polypropylene	Synthetic Polymer	38
Human Hair for Comparison	Natural Keratin	50 to 70
SCS Ultra Silicon Carbide Fiber	Ceramic	75
Boron Fiber	Mineral	142

2.3.4 Fiber Density

Volumetric density and linear density are two measurements of fiber mass important for many extensive thermal and mechanical properties. Volumetric density, shown in Table 2.8, compares the mass of a fiber to its volume. Linear density similarly compares the mass to the fiber length. Over the past several hundred years, the textile industry developed the units of denier (de) and tex to compare and evaluate threads and yarns. One denier has a linear density of one gram of mass per 9000 meters of fiber. The tex is similarly a measurement of one gram mass per 1000 meters of fiber, and a decitex or dtex is one gram of mass per ten kilometers of fiber. Measurements of linear density become important when comparing the specific strength of fibers.

Table 2.8 Density of Fibers

Fiber Type	Density (g/cm^3)
Cellulose Fibers	0.14 to 1.54
Polymer Fibers	0.90 to 1.54
Keratin Fibers	1.30 to 1.34
Regenerated Cellulose	1.25 to 1.52
Carbon Fibers	1.74 to 2.20
Glass and Quartz Fibers	2.10 to 2.60
Ceramic Fibers	1.80 to 3.90
Mineral Fibers	2.64 to 2.70
Metallic Fibers	1.74 to 8.92

2.3.5 Fiber Strength and Stiffness

The ASME AG-1 specifies a tensile breaking strength of HEPA filtration media must be at least 430 N/m in the machine direction and 350 N/m in the cross direction, with a maximum allowable elongation of 0.5% at rupture [36]. This standard ensures HEPA filters are not easily ripped or torn by accident and do not rip and tear when subjected to sustained high pressure conditions. The filtration media must maintain high strength as well during heated, wet, and irradiating conditions. In the cross-machine-direction, the media must maintain a tensile strength of 110 N/m after high temperature airflow of 370 °C for five minutes, a tensile strength of 170 N/m after soaking in water at ambient temperature for 15 minutes, and tensile strength of 170 N/m after receiving gamma irradiation for an integrated dose of 6.0E7 to 6.5E7 rad at a dosage rate not to exceed 2.5E6 rad/hr [36]. While tensile strength of filtration media under heated, wet, and irradiated conditions depends greatly on the composition and characteristics of binders and other materials in the filtration media, the performance of individual fibers is critical to overall strength. Table 2.9 shows tensile strength in units of GPa, and tenacity in units of mega yuri (MY), which is described in detail below.

Table 2.9 Tensile Strength and Tenacity of Fibers

Fiber Family	Yield Strength (GPa)	Tenacity (MY)
Carbon Fibers	2.20 to 7.00	1.20 to 4.00
Glass and Quartz Fibers	2.00 to 6.00	0.78 to 2.72
Polymer Fibers	0.33 to 5.80	0.27 to 3.80
Ceramic Fibers	1.40 to 5.90	0.40 to 1.90
Mineral Fibers	2.50 to 4.80	1.00 to 1.80
Metallic Fibers	0.22 to 2.21	0.03 to 0.28
Keratin Fibers	0.19 to 1.40	0.14 to 1.07
Regenerated Cellulose	0.17 to 0.89	0.13 to 0.59
Cellulose Fibers	0.07 to 0.89	0.12 to 0.59

2.3.6 Fiber Tenacity (Specific Strength)

Typical measurements of material strength are given in units of force per cross sectional area, such as gigapascals. However, many fibers have irregular shaped cross sections and hollow cores making it difficult to accurately measure the cross-sectional area and volumetric density. Specific strength measures the breaking force of a fiber compared to its linear density, which determines the tensile force required to break a fiber compared to its denier or tex. The textile industry calls this measurement the tenacity of the fiber. Common measurements of tenacity include newtons per tex $\left(\frac{\mathrm{N}}{\mathrm{tex}}\right)$, grams per denier (gpd), and pascals per volumetric density $\left(\frac{\mathrm{GPa}}{\mathrm{g/cm^3}}\right)$. The international space elevator consortium advocated for a new unit “yuri” as a measure of specific strength for cable materials using SI base units. The equivalent cross-sectional areas of strength and density cancel leaving the breaking force divided by linear density as shown in Equation 2.1. Fiber tenacity has units of $\frac{\mathrm{m^2}}{\mathrm{s^2}}$.

$$\mathrm{yuri} = \frac{\mathrm{Pa}}{\frac{\mathrm{kg}}{\mathrm{m^3}}} = \frac{\frac{\mathrm{N}}{\mathrm{m^2}}}{\left(\frac{\mathrm{kg}}{\mathrm{m}}\right)\left(\frac{1}{\mathrm{m^2}}\right)} = \frac{\mathrm{N}}{\frac{\mathrm{kg}}{\mathrm{m}}} = \frac{\mathrm{N\ m}}{\mathrm{kg}} = \frac{\left(\frac{\mathrm{kg\ m}}{\mathrm{s^2}}\right)\mathrm{m}}{\mathrm{kg}} = \frac{\mathrm{m^2}}{\mathrm{s^2}} \tag{2.1}$$

Breaking force is implicit in the textile industry measurement of grams per denier (gpd). Grams of mass multiplied by the acceleration of gravity reveals breaking force as gram-force newtons as shown in Equation 2.2 which also shows the conversion between gpd and yuri. Equation 2.3 relates the measurement of newtons per tex to gpd and yuri, showing one mega yuri equivalent to one newton per tex and 11.33 gpd. The construction industry measures specific strength of fibers as the breaking strength of the fiber per volumetric density. The units resolve such that one $\frac{\mathrm{MPa}}{\mathrm{g/cm^3}}$ is equivalent to 1000 yuri, and one $\frac{\mathrm{GPa}}{\mathrm{g/cm^3}}$ is equivalent to one $\frac{\mathrm{N}}{\mathrm{tex}}$ and one MY as shown in Equation 2.4.

$$\mathrm{gpd} = \frac{\mathrm{g}}{\mathrm{den}} \approx \frac{\mathrm{g}\left(9.80665\,\frac{\mathrm{m}}{\mathrm{s^2}}\right)}{\frac{\mathrm{g}}{9{,}000\ \mathrm{m}}} \approx\ 88{,}260\,\frac{\mathrm{m^2}}{\mathrm{s^2}} \approx 88{,}260\ \mathrm{yuri} \tag{2.2}$$

$$\frac{\mathrm{N}}{\mathrm{tex}} = \frac{\frac{\mathrm{kg\ m}}{\mathrm{s^2}}}{\frac{\mathrm{g}}{1{,}000\ \mathrm{m}}} = 1{,}000{,}000\,\frac{\mathrm{m^2}}{\mathrm{s^2}} = \mathrm{MY} \approx 11.33\ \mathrm{gpd} \tag{2.3}$$

$$\frac{\mathrm{GPa}}{\mathrm{g/cm^3}} = \frac{1{,}000{,}000{,}000\,\frac{\mathrm{N}}{\mathrm{m^2}}}{\left(\frac{\mathrm{kg}}{1{,}000}\right)\left(\frac{1{,}000{,}000}{\mathrm{m^3}}\right)} =\ 1{,}000{,}000\,\frac{\mathrm{m^2}}{\mathrm{s^2}} = \frac{\mathrm{N}}{\mathrm{tex}} = \mathrm{MY} \tag{2.4}$$

The comparison of tensile strength and specific strength of fibers is shown by Figure 2.3, with the stronger fibers on the left side of the chart. While polyacrylonitrile-based carbon fibers are the strongest overall fibers, the synthetic UHMWPE fibers have slightly higher tenacity because of the lower density of UHMWPE materials. Conversely, ceramic, glass, and metallic fibers have lower values of tenacity because they are composed of very dense material.

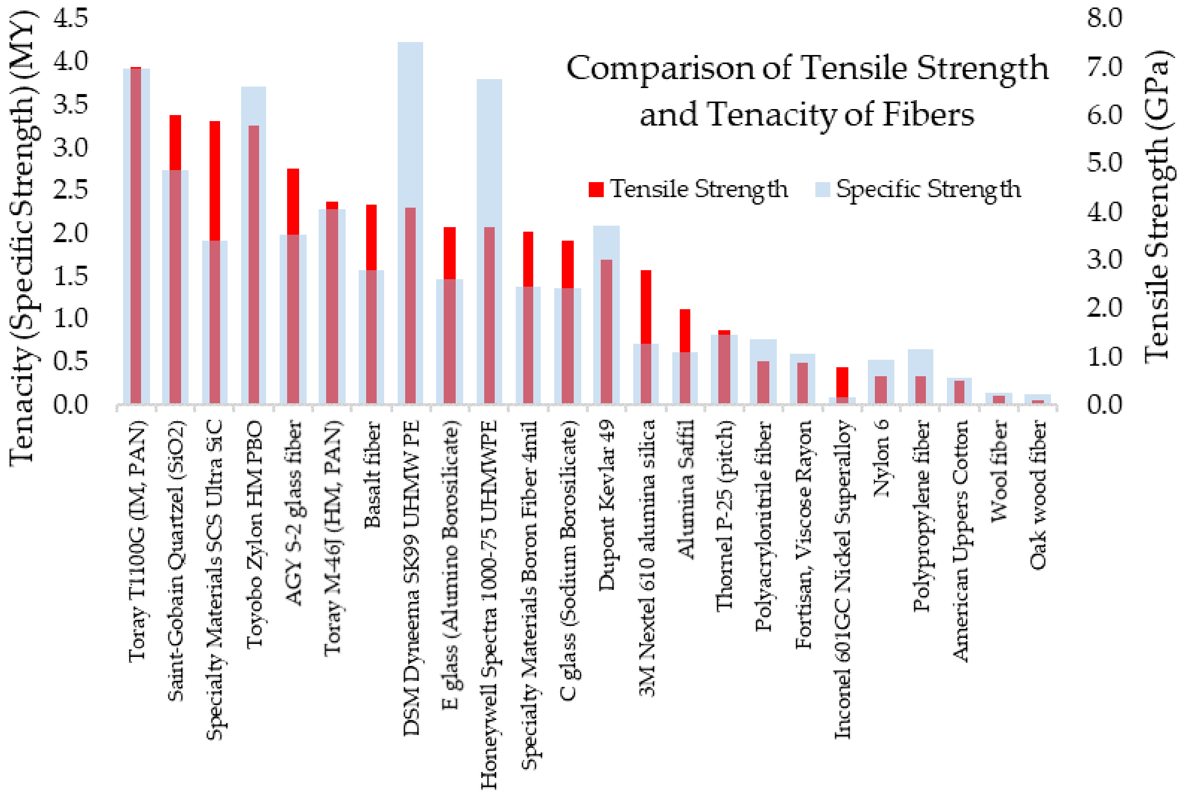

Figure 2.3 Comparison of tensile strength and tenacity of select fibers.

2.3.7 Fiber Stiffness

Fiber stiffness is a parameter that accompanies fiber strength in importance. Air filter materials must resist excessive strain when exposed to high pressure. Carbon, ceramic, and mineral fibers are the stiffest, while natural cellulose and keratin fibers have the least stiffness. Natural wood fibers, synthetic polymer fibers, and regenerated cellulose fibers are the most elastic. An overall comparison of fiber strength and stiffness is shown in Figure 2.4.

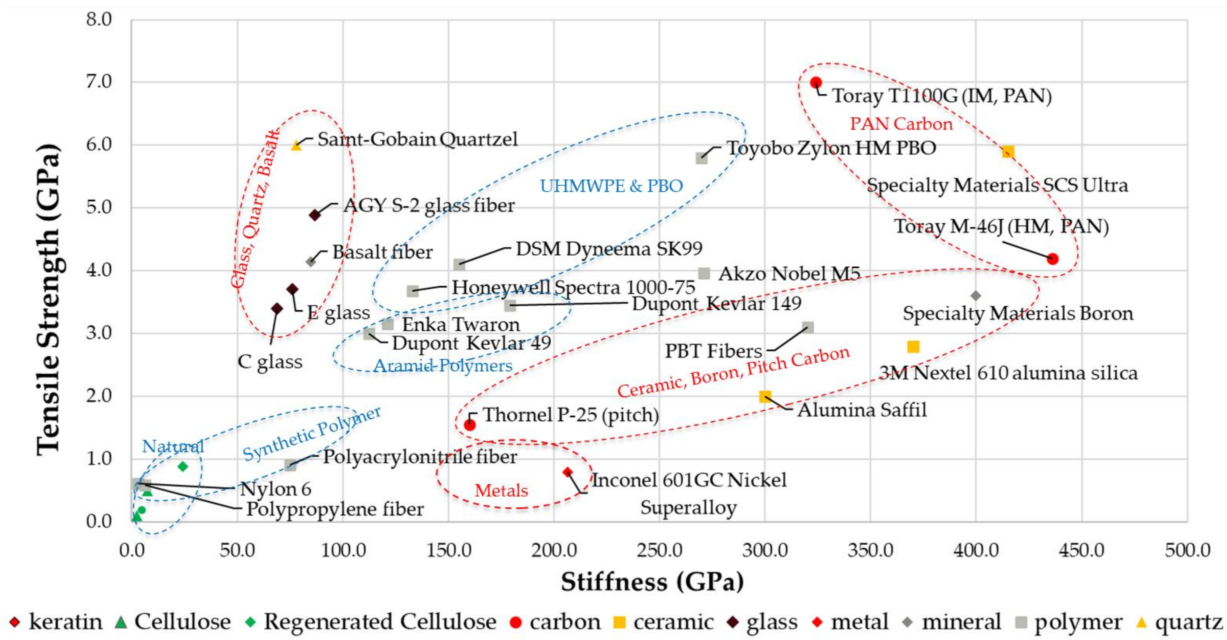

Figure 2.4 Comparison of tensile strength and stiffness of fibers.

2.3.8 Fiber Flexibility and Flexural Rigidity

Fiber flexibility and flexural rigidity can be thought of as the respective ease or resistance to bending motion of the fiber. Fiber flexibility is important in air filter design. The ASME AG-1 specifies a standard for media flexibility, requiring the media to show no tears, breaks, cracks, or fiber separation after being drawn back and forth five times over a 4.8 mm mandrel to an arc of 180 degrees [36]. The filtration media must maintain the same filtration performance, with no more than 0.03% penetration by a monodisperse 300 nm particle and no more than 0.1% penetration by the most penetrating particle size. This standard favors the selection of fibers that are tough yet flexible enough to bend repeatedly without breaking.

Fiber flexibility can be shown by the ratio k_r/M where k_r represents the inverse of the fiber radius of curvature, and M is the moment of inertia. Equation 2.5 shows the inverse relationship between fiber flexibility, tensile modulus E, and fiber diameter d. In classical beam theory, flexural rigidity of a beam is given as EI, with E in units of Pa and I as the second moment of area in units of m^4, resulting in units of N·m^2. The textile industry measures flexural rigidity of fibers using classical beam theory as shown in Equation 2.6 with s as the fiber "shape factor," ρ the volumetric density, c the linear density, and E_s the specific modulus (E/ρ) of the fiber.

$$\frac{k_r}{M} = \frac{64}{\pi E d^4} \tag{2.5}$$

$$EI = \frac{s E_s c^2}{4\pi\rho} \tag{2.6}$$

Taking into account realistic diameter sizes of each fiber type as shown in Table 2.7 above, Equation 2.6 can provide a comparison of expected flexural rigidity, as shown in Figure 2.5. Clearly fibers with larger diameters are rigid, and fibers with smaller diameters are flexible.

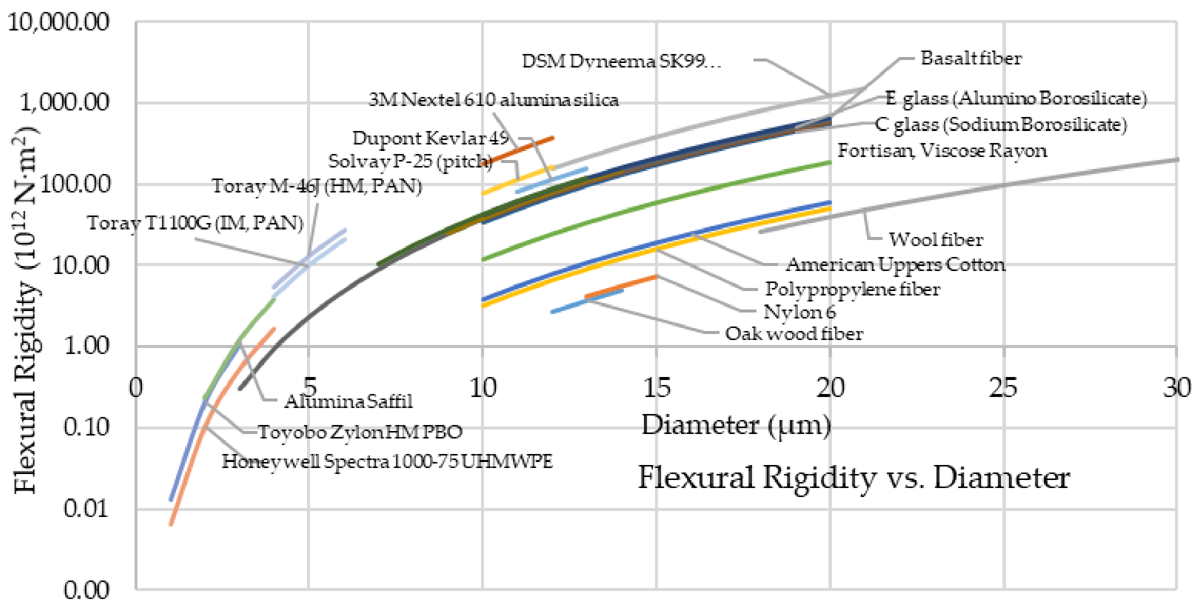

Figure 2.5 Flexural rigidity at actual fiber diameter sizes.

2.3.9 Fiber Water Repellency and Mildew Resistance

Filter media must repel water in order to avoid problems in high humidity and wet conditions. The ASME AG-1 specifies the media must be prepared in accordance with the Technical Association of the Pulp and Paper Industry (TAPPI) standard T402, and tested for water repellency with procedure 125-8-1 Q101 [36]. To achieve the specification, the material must have an average water repellency of at least 5000 Pa. The degree of hydrophobicity of individual fibers is an important characteristic when selecting fibrous materials for filter media. The ASME AG-1 also specifies the filter media must be tested for mildew growth in accordance with MIL-STD 810 method 508 if required by the user.

Moisture regain indicates a fiber’s ability to absorb moisture, expressed as a percentage of water weight absorbed by the fiber compared to the dry weight of the fiber. Many organic fibers are hydrophilic and hygroscopic, meaning they have a strong affinity toward water and tend to absorb moisture from the air. Natural keratin and cellulose fibers absorb the most moisture. Wool fibers absorb nearly 17% of their dry fiber weight while silk fibers absorb approximately 11% moisture [41]. Wood fibers absorb nearly 15% of their weight as moisture. Cotton, jute, flax, and hemp absorb a significant amount of moisture from the air, as well do most regenerated cellulose fibers, which are also considered hygroscopic. Some but not all synthetic polymer fibers absorb moisture, depending on the properties of the synthetic material. Inorganic fibers, including ceramic, metallic, basalt, and glass, are nonhygroscopic and do not absorb moisture from the air. Figure 2.6 compares the moisture regain of selected fibers, showing mainly the fibers that will have significant moisture problems.

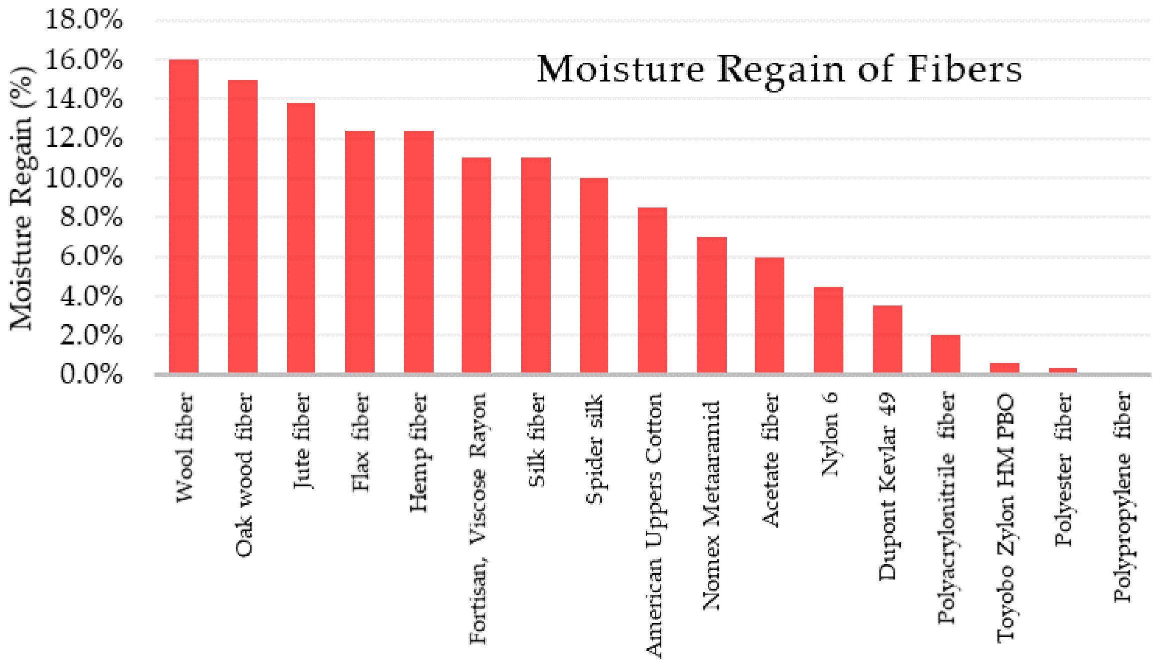

Figure 2.6 Moisture regain of selected fibers.

2.3.10 Fiber Temperature Threshold and Fire Resistance

To pass ASME AG-1 specifications, the filter media must be non-combustible and must withstand high temperatures. The ASME AG-1 specifies that the combustible material in the filter media shall not exceed 7% by weight. This standard is tested by IEST-RP-CC021.1 by measuring the weight loss after subjecting the filtration media to elevated temperatures. The AG-1 also specifies the filter material must withstand a sustained pressure of 2400 Pa while subjected to continuous heated air flow of 370 °C. These standards ensure the filter is capable of sustained high efficiency filtration even when exposed to fire. The fibers shown in Figure 2.7 have decomposing or melting temperatures lower than or near 370 °C. Cellulose fibers, keratin fibers, regenerated cellulose fibers, and synthetic polymer fibers are mostly unsuitable for HEPA filter units because of low temperature threshold. Ceramic, metallic, mineral, carbon, basalt, and glass fibers have temperature thresholds well above the 370 °C threshold. Zylon PBO is a synthetic polymer fiber with a reported degradation temperature of 650 °C which is above the threshold.

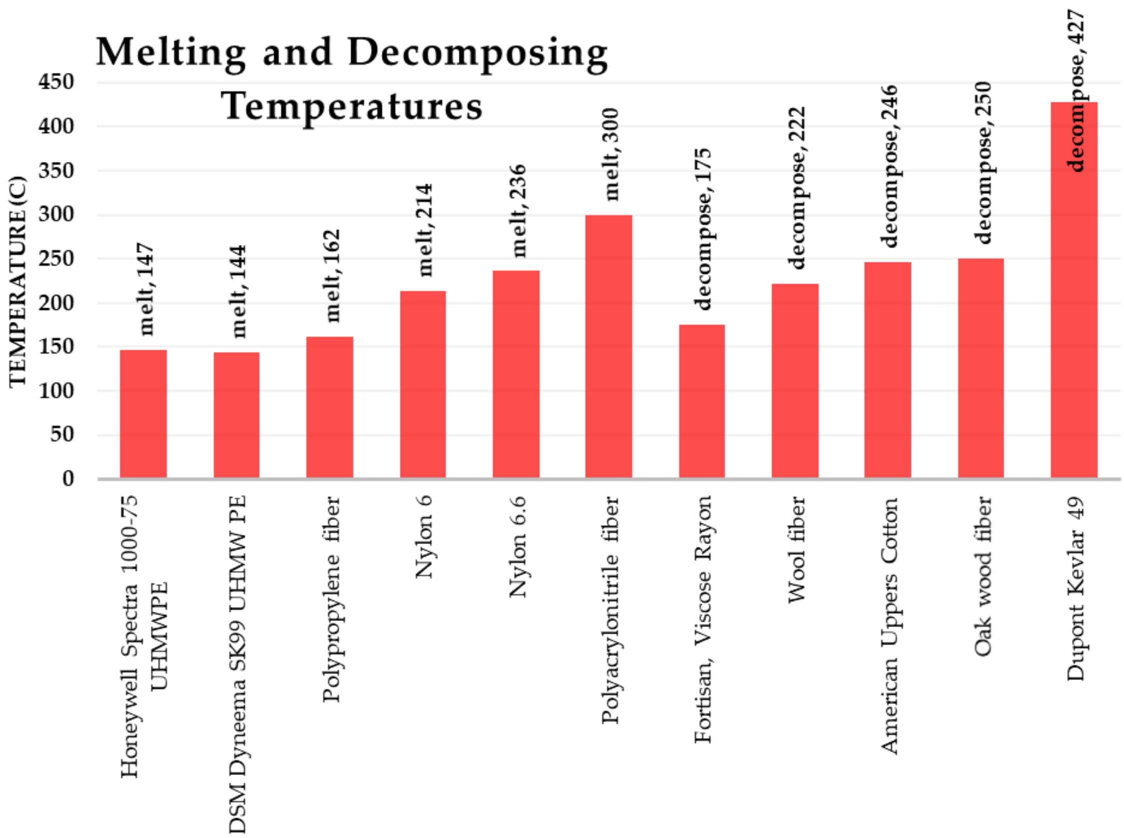

Figure 2.7 Comparison of melting and decomposing temperatures of select fibers.

2.3.11 Thermal Expansion and Contraction

The coefficient of linear thermal expansion (CTE) is a material property that indicates the extent to which a material expands or contracts when the material changes temperature. Most fibrous materials have a slightly positive CTE which indicates they expand when heated and contract when cooled. Some fibrous materials, for example Kevlar and Zylon, have a negative CTE indicating contraction when heated and expansion when cooled. The disadvantage of using fibers in air filter media with a highly positive or highly negative CTE is the expansion or contraction changes the dimensions of the fibers, in turn affecting the air filtration and air flow resistance performance of the media. The advantage of carbon fibers, quartz fibers, and glass fibers is they have a very small CTE and are thus resistant to expansion or contraction when the filter media heats up or cools down. A comparison of thermal expansion coefficients for selected fibers is shown in Figure 2.8.

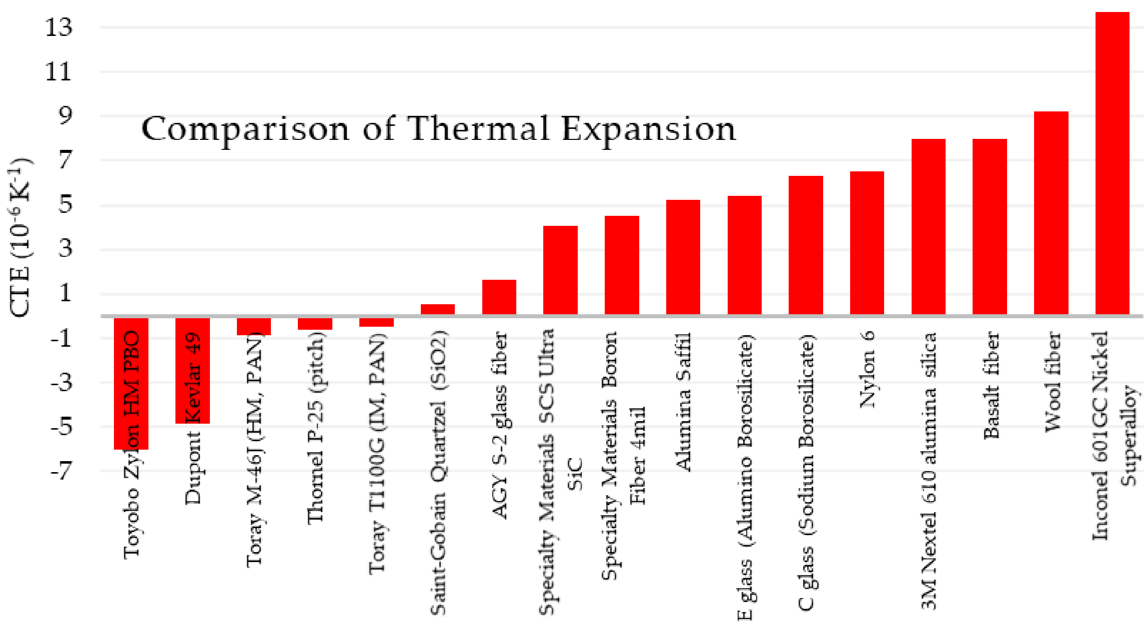

Figure 2.8 Comparison of thermal expansion.

2.3.12 Overall Fiber Comparison

An overall subjective comparison of twenty-four fibers is presented in Table 2.10 to guide the selection of fibers for research and development of potential alternative HEPA filtration media. The particular fibers listed in the table are meant to represent their general category of fibers, for example American Uppers Cotton fiber is intended to represent natural cellulose fibers, while Torray T1100 is intended to represent polyacrylonitrile-based carbon fibers. Melt-blown glass fibers are currently the dominant choice for HEPA filters based on ease of production, availability, and overall performance. Cellulose, regenerated, keratin, and most synthetic polymer fibers are unsuitable for HEPA consideration because of moisture or temperature requirements discussed above. In addition to other types of glass fibers, the fiber categories carbon, ceramic, mineral, basalt, and metallic are worthy of consideration for HEPA filtration.

Table 2.10 Overall Fiber Subjective Comparison

Fiber	Category	Tensile Strength	Tensile Modulus	Bending	Moisture Regain	Thermal Expansion	Temp 370 °C
Cotton [42]	Cellulose	Fair	Elastic	Flexible	Very High	Low	Decompose
Wood [43]	Cellulose	Fair	Elastic	Flexible	Very High	Low	Decompose
Rayon [44]	Regenerated	Fair	Elastic	Flexible	Very High	Low	Decompose
Wool [41]	Keratin	Fair	Elastic	Flexible	Very High	Low	Decompose
Spectra, Dyneema [45] [46]	UHMWPE	High	Stiff	Moderate	None	Negative	Melt
Nylon 6/6.6 [47]	Polymer	Fair	Elastic	Flexible	High	Low	Melt
Dupont Kevlar 49 [48]	Aramid	Moderate	Stiff	Moderate	Moderate	Negative	Decompose
Toyobo Zylon PBO [49]	Polymer	Very High	Stiff	Rigid	Moderate	Negative	Near Max
Polyacrylonitrile [50]	Polymer	Fair	Stiff	Moderate	Moderate	Low	Melt
Polypropylene [44]	Polymer	Fair	Elastic	Flexible	None	Low	Melt
Toray M-46J (PAN) [51]	Carbon	High	Most Stiff	Most Rigid	None	Negative	Safe
Toray T1100G (PAN) [51]	Carbon	Very High	Stiff	Rigid	None	Very Low	Safe
Solvay P-25 (pitch) [52]	Carbon	Fair	Stiff	Moderate	None	Very Low	Safe
Saffil [53]	Ceramic	Moderate	Stiff	Rigid	None	Low	Safe
3M Nextel 610 Al Si [54]	Ceramic	Moderate	Very Stiff	Rigid	None	Low	Safe
SCS Silicon Carbide [55]	Ceramic	Very High	Very Stiff	Highly Rigid	None	Low	Safe
Quartzel, Astroquartz [56]	Quartz	Very High	Stiff	Moderate	None	Very Low	Safe
S2 glass fiber [57]	Glass	High	Stiff	Moderate	None	Very Low	Safe
E glass [58]	Glass	High	Stiff	Moderate	None	Low	Safe
C glass [58]	Glass	Moderate	Stiff	Moderate	None	Low	Safe
D glass [58]	Glass	Moderate	Stiff	Moderate	None	Low	Safe
Boron 4mil [59]	Mineral	Moderate	Very Stiff	Highly Rigid	None	Low	Safe
Basalt [60]	Volcanic	High	Stiff	Moderate	None	Low	Safe
Inconel 601GC Nickel [61]	Metal	Fair	Stiff	Rigid	None	Moderate	Safe

2.4 Nonwoven Air Filtration Media

Many of the fibers listed in Table 2.10 are already in production as nonwoven media, primarily intended for structural reinforcing in composites but also potentially capable of air filtration. Table 2.11 shows examples of nonwoven fabric, paper, and matting [62].

Table 2.11 Trade Names of Non-Woven Fabric, Paper, and Matting

Fiber Family	Nonwoven Fabric, Paper, and Matting
Glass	Verlock, Textoglass, JPS, Nittobo, Orcoweb, SFT, Vetrotex
Carbon	Carbotex, Carboflex, Carrfibre, Graflok, Uniloc, Unilay,Layrite, Fibral, Technoglas, Fortafil, Panex, Torayca, Fibertec, Technimat, Kureha, Filacron
Metals	Bekinox, Bekipor, Brunsmet, Lantorine, Fensor, Fibrex
Oxidized PAN	Fortafil, Oxipan, Panox, Sigrafil, Avox, Pyromex, Panotex, Pyron
Aramid	Carrfibre, Nomex, Aralok, Fibertek
UHMWPE	Spectra, Dyneema, PBI, Tekmilon, Texxes, Kermel, Tenfor

2.4.1 Glass Fiber Nonwoven Media

Most industrial HEPA filter units today are made with melt-blown borosilicate glass fiber pleated paper. Example producers of H14 filtration paper found online are shown in Table 2.12, with stated filtration efficiency, flow resistance, basis weight, thickness, and media tensile strength.

Table 2.12 Example Producers of H14 HEPA Filter Media

	Guangzhou Clean Link [63]	Hebei Amusen [64]	Shandong Renfeng [65]	Hebei Fangyu [66]	CHMLAB [67]
Efficiency (%) at 5.3 cm/s	99.993	99.995	99.998	99.995	99.995
Resistance (Pa) at 5.3 cm/s	380	390	372	420	450
Basis Weight (g/m^2)	75	75	76	74	75
Thickness (mm)	0.50	0.35	0.40	0.33	0.35
Tensile Strength MD (N/m)	980	1000	1000	1250	800
Tensile Strength CD (N/m)	500	400	-	-	700

MD: Machine Direction, CD: Cross Direction

Figure 2.9 shows a comparison of melt-blown glass fiber HEPA filter media with electrospun and stabilized polyacrylonitrile filter media. The glass filter media in Figure 2.9(a) qualifies for nuclear grade HEPA filter media under ASME AG-1 specifications. At the same magnification, the electrospun and stabilized polyacrylonitrile filter media has smaller diameter nanofibers packed more densely. As discussed in section 3.3 and illustrated in Figure 2.2 above, the fiber diameter size has a significant impact on the air filtration efficiency and air flow resistance. Media with smaller fiber diameter sizes, such as the polyacrylonitrile fiber media in Figure 2.9(b), has a higher total filter efficiency than comparable media with larger diameter sizes such as the glass media shown in Figure 2.9(a). However, the polyacrylonitrile fiber media in Figure 2.9(b) would also exhibit a higher resistance to air flow than the glass media of Figure 2.9(a), which also must be considered. Additional considerations besides the air filtration efficiency and air flow resistance of comparable filter media shown in Figure 2.9 include the media overall strength, resistance to tearing, and flexibility

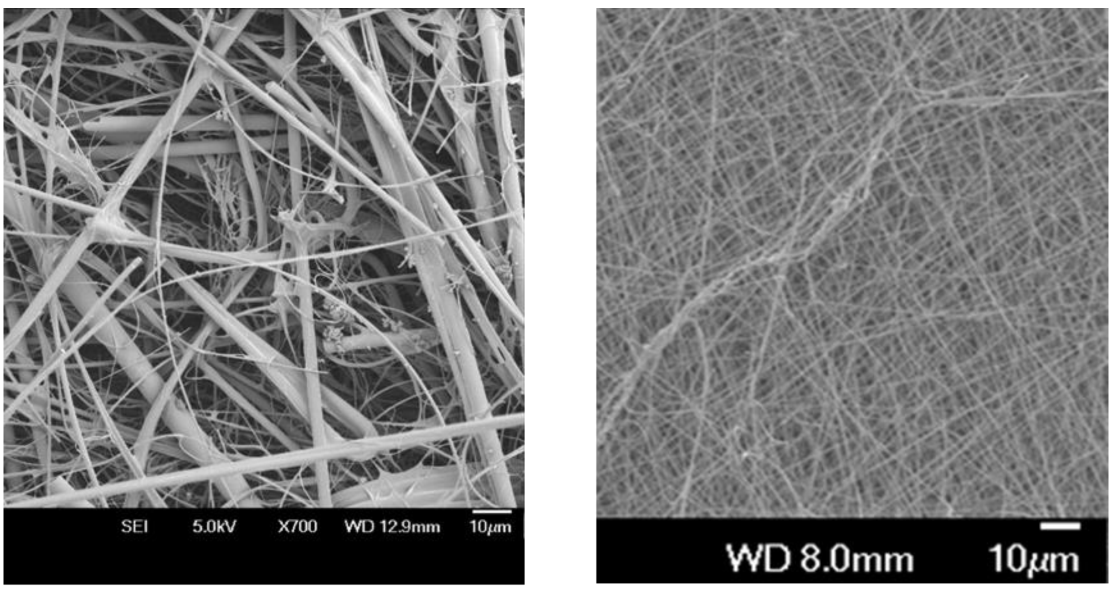

(a) (b)

Figure 2.9 SEM images of filter media. (a) Melt-blown borosilicate glass HEPA filter media. (b) Electrospun and stabilized polyacrylonitrile fiber media at the same level of resolution.

Continual advancements in glass technologies have created many potential alternatives for HEPA filtration media. Dry-laying and wet-laying glass staple fibers, chopped strands, and yarns are alternative methods to produce filter media. The limitation for advancement of glass media for HEPA filtration is the range of possible diameter sizes.

2.4.2 Basalt Fiber Nonwoven Media

Basalt fibers can be produced through the same methods as glass fiber production, however without any additives to the basalt. The abundance of basalt, ease of production, and physical characteristics of basalt fibers make them well suited for high temperature HEPA filtration. Long-term burst testing of filter bags at the Nebraska Power Sheldon Station showed a distinct advantage of the basalt media over other media types [68]. The basalt composite filter bags maintained the same strength over several years of exposure to high temperature exhaust air flow above 200 °C while the other media types lost 20% or greater strength capacity in the same conditions [68]. Basalt composite filter media is capable of capturing exceedingly hot particles, as in the production of nickel film or molybdenum powder production, where the captured particles often exceed 800 °C [68]. Long-term permeability testing of filter bags at the St. Lawrence cement plant in Ontario Canada showed basalt-P84 composite filter bags superior to glass-PTFE composite media for pulse cleaning and re-use [68]. These examples illustrate significant viability of basalt filter media for high temperature HEPA filtration.

2.4.3 Carbon Fiber Nonwoven Media

Many companies commercially produce carbon fiber nonwoven media primarily intended for structural composite reinforcement. Activated carbon media is also available for home and industrial air filtration, however most activated carbon filters use polymer fibers for filtration and activated carbon only for gas adsorption. Electrospun, stabilized, and carbonized polyacrylonitrile filter media has significant potential for HEPA filtration. Electrospinning has an advantage over melt-blowing in the production of smaller fiber diameter sizes. Electrospun nanometer fibers are well suited for high filtration efficiency and low flow resistance.

2.4.4 Ceramic Fiber Nonwoven Media

Continual advancement of polymer science and ceramics is widening the potential application of nonwoven ceramics in air filtration. Oxide and non-oxide ceramics can be dissolved into solution and electrospun into nanometer size diameter fibers through the sol-gel process, resulting in nonwoven filter media. Ceramic fibers also do not absorb moisture and easily withstand high temperatures.

Over the past several years Lawrence Livermore National Laboratory developed and tested high strength oxide ceramic air filters intended for nuclear air ventilation [69]–[71]. Oxide ceramic nanofibers, created with electrospinning and thermal heat treatment, can be assembled into nonwoven filter media with mean fiber diameters between 50 nm and 150 nm [69]. Ceramic filter media elements survived exposure to high temperature air flows of 500 °C [69].

Laboratory experiments of filtration efficiency using aluminum oxide-stabilized zirconium dioxide (ASZ) ceramic filter media illustrate the significant potential of ceramic HEPA media [35]. The ASZ filter paper media, created with a simple solution blow spinning and calcination method, demonstrated flexibility, foldability, and temperature usage capacity up to 1100 °C [35]. Foldable ceramic fiber nonwoven media such as ASZ might easily form pleated filter paper for use in HEPA units. Another novel design for using ceramic fiber nonwoven media in HEPA applications developed at Lawrence Livermore is the “mini-tubular” construction method [71]. The mini-tubular design reduces the problems associated with ceramic filter element shrinkage during production. The mini-tubular ceramic filter concept shows potential for HEPA air filtration.

2.4.5 Metal Fiber Nonwoven Media

Bekaert designs and produces sintered metallic nonwoven fibrous media intended for use as HEPA filtration [18]. Metal fibers and metallic filtration media easily withstand the strength, durability, flexibility, and high temperature requirements of the ASME AG-1 specifications listed above. The ductility of metallic nonwoven media is noted as a distinct advantage over brittle media, as the metallic media can be shaped and compressed to modify the solidity with less danger of fibers breaking [72]. For this reason metallic media is appropriate for intake and exhaust filtration of combustion engines and other machinery that experiences vibration [72].

Metal fibers do not absorb moisture and resist bacteria growth which is a distinct advantage over moisture-absorbing fiber types. While not absorbing moisture, metal fiber media has characteristically high wettability, making it advantageous for coalescence air filtration [72]–[74] A direct comparison of Sullube 32 oil droplet aerosol filtration efficiency and air flow resistance between 6.0 µm glass fiber media and 6.5 µm stainless-steel fiber media revealed significant performance advantage of the stainless-steel media [72].

The noted challenge in advancing metal fibers for HEPA filtration is the limitation on available metal fiber diameter sizes. Metallic filter media has good potential as a component of composite HEPA filter media, by combining the mechanical advantages of metal media with the smaller diameter size advantage of other media types.

2.4.6 Polymer Fiber Nonwoven Media

Air filters for personal protective gear and home filter units are made with nonwoven polymers. Polypropylene does not absorb moisture like many other synthetic and natural fibers and has become the dominant fiber for personal face masks and pleated filter cartridges. Studies indicate melt blown polypropylene fibers may have a higher quality factor than glass H13 filter paper through dust loading [75]. Shanghai Mingguan Purification Materials produces melt blown polypropylene filter paper for personal protective masks and filter units that achieve H13 and H14 standards [76]. However polypropylene fibers cannot withstand the high temperature requirements specified by ASME AG-1 to qualify as a nuclear grade HEPA filter media. Spectra and Dyneema are UHMWPE polymer fibers which don't absorb moisture, and although not capable of meeting ASME AG-1 specifications because of temperature limitations, may potentially serve as suitable alternatives to polypropylene fibers for use in moderate temperature environments. Polyimide P84 fibers and Nomex aramid fibers are used extensively in industrial air and gas separation bag filter units for cement factories and power plants. These polymer filter materials are also limited to temperatures below the AG-1 specification.

Besides melt blowing, many polymers are well suited for electrospinning into filter media with nanometer scale fiber diameters and uniform fiber shape, resulting in high filtration efficiency [77]–[79]. Figure 2.9(b) shows the smaller fiber diameter sizes and uniformity of fiber shapes compared to the melt-blown borosilicate glass media shown in Figure 2.9(a). Electrospinning polyacrylonitrile nanofibers into air filter media results in high filtration efficiency with low flow resistance [80]. The advantage of electrospun polyacrylonitrile fibers is they can be stabilized carbonized into HEPA filter media that achieves ASME AG-1 standards for high temperature.

2.5 Chapter Summary

Air filtration began in earnest on the battlefields of the First World War eighty years ago, relying entirely on natural materials to include cotton, esparto, wool, and asbestos. Significant advancement in air filtration technology over the decades included the replacement of natural materials for safer and more efficient synthetic materials. Melt-blown borosilicate glass has become the fiber of choice for nonwoven HEPA filter units today, while melt-blown polypropylene fibers are the choice for personal protective equipment. However more materials research may advance air filtration technology to increase the efficiency and reduce the flow resistance of HEPA filter units. The research topics shown in Table 2.13 are recommended for further HEPA air filtration development of alternative filter media.

Table 2.13 Recommended Materials Research in Filter Materials

Fiber Type	Further Research Recommendation
Glass	Testing additional glass fiber types (A, C, E, ECR, S2, R, etc) Production methods to reduce fiber diameter size
Basalt	Production of nonwoven continuous basalt fibers in filter media
Carbon	Electrospinning carbon precursors for air filtration media Carbon nanotube filtration in free molecular flow regime
Ceramics	Electrospinning of sol-gel nonwoven ceramic filter media
Metals	Advancing sintered metal filter media

Any newly developed HEPA filter media must be tested and classified according to, ISO 29463, EN 1822, or ASME AG-1 depending on the particular intended application. In order to qualify a newly developed filter media for use in nuclear grade HEPA filter units, additional testing is required beyond filtration efficiency and flow resistance to ensure the media integrates into the filtration infrastructure and system. For example, the support infrastructure must withstand the weight and vibration requirements of new filter media as it is tested as part of the overarching air filtration system.

CHAPTER III

ANALYTICAL MODELING OF AIR FILTRATION[2]

Classical modeling of fibrous air filter media consists of two-dimensional analytical representations of aerosol flow around fibers. The single fiber efficiency model is a well-known analytical tool present in literature and relatively simple to implement that predicts the total filtration efficiency of filter media based on the particle capture efficiency of a single, isolated fiber positioned perpendicular to the direction of flow [13], [81], [82]. As illustrated by Figure 3.1, SFE models consider the number of particles approaching the fiber geometrically incident to the fiber's cross section. Classical SFE models estimate the percentage of approaching particles that are captured by the fiber. The purpose of this chapter is to provide an overview of analytical modeling for air filter media. The works of Davies, Happel, and Brown in particular are recommended further reading in this topic [13], [83].

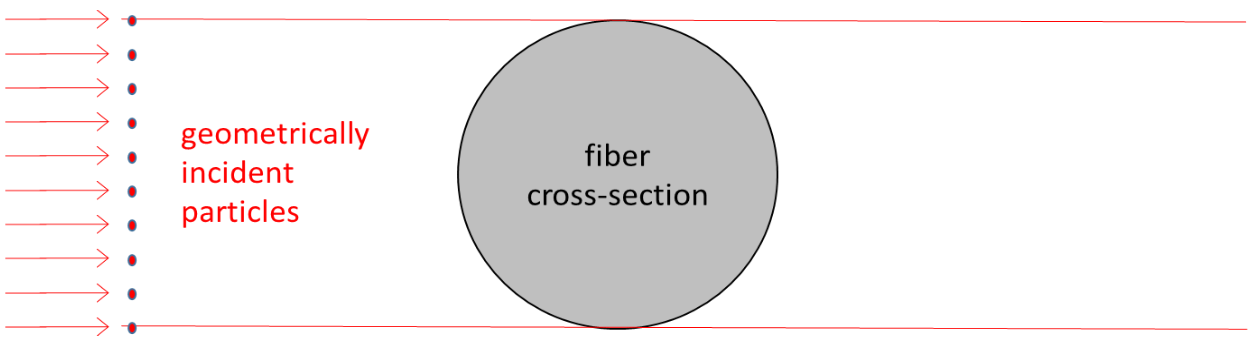

Figure 3.1 Geometrically incident particles approaching a fiber cross section.

[2] Content from this chapter is published as an appendix in a journal article. Beckman, I.P.; Berry, G.; Cho, H.; Riveros, G. Digital Twin Geometry for Fibrous Air Filtration Media. Fibers 2021, 9, 84. https://doi.org/10.3390/fib9120084

3.1 Air Filtration Theory

Up until the search for better protective filter materials during the Second World War, air filtration was thought to be similar to water filtration [12]. Nobel Laureate Irving Langmuir is credited with initial development of modern air filtration theory based on particulate retention on fibers [12]. Aerosol particles flowing through a filter media which come into contact with fibers stick to the fibers by electrostatic forces including Van der Waals forces. Langmuir's air filtration theory was based on particle contact and retention from interception and diffusion mechanisms [12]. Additions to his theory by Ramskill, Anderson, and many other researchers included the effects of inertial impact, gravitational settling, and electrostatic attraction [12]. The individual particle capture mechanisms were consolidated into a single fiber efficiency (SFE) model by Davies in 1951 to integrate the combined effects of the many capture mechanisms [13], [83], [84]. The SFE model is covered well throughout literature. Very small particles less than 0.3 μm in diameter are predominantly collected by Brownian diffusion, while particles larger than 0.3 μm are predominantly collected by interception and inertial impaction. The consolidated effects of multiple collection mechanics of a single fiber, including interception, diffusion, interception of diffusing particles, inertial impaction, gravitational settling, and electrostatic forces, represent that single fiber's efficiency.

Of utmost importance is fiber diameter. Smaller diameter fibers have greater surface area to volume ratio. For example, by reducing the diameter by half, four smaller fibers now have equal volume of the larger fiber and four times the surface area. The increase in surface area for the same solid volume fraction is beneficial to filtration efficiency while detrimental to air flow drag. Fiber diameter d_{f}, fiber packing density α_{f}, and filter thickness t are three important parameters that combine with the single fiber efficiency E_Σ in the calculation of total filter efficiency E_F.

3.2 Kuwabara Cell Model

Prior to 1959 the single fiber model assumed each fiber acted independently within an infinitely sized flow field. Two authors in 1959, Kuwabara and Happel, separately improved the single fiber model to account for the effects of neighboring fibers [85], [86]. Kuwabara developed a cell model to represent cylinders and their surrounding space as cells as shown in Figure 3.2.

Airstreams flow around nanometer diameter fibers differently than expected by the no-slip boundary condition and cannot rely on the assumption of a continuum. As the radius of the fiber approaches the mean free path of air molecules, the no-slip boundary condition no longer accurately portrays air-fiber dynamics. The fiber surface allows a slipping condition for air molecules, which must be taken into account during computational fluid dynamics modeling attempts. The solidity α_f of a filtration media is the fraction of the volume of fiber and deposited particles to the total volume of the filter media. This is also known as packing density or solid volume fraction and is the complement of the media's porosity. The dynamics of aerosol particles must be understood to apply a filtration model. It is worth noting that filters are primarily designed for laminar airflow which is indicated by a relatively low Reynolds number of less than 2000 [87].

The Kuwabara cell model uses the stream function as a biharmonic equation in polar coordinates. Particles are assumed to travel precisely along the flow streamlines, and any particle following a streamline that is within one particle radius to the filter fiber will touch the fiber and become intercepted and deposited onto the fiber. Kuwabara's model calculated filtration efficiency by relating the solid volume fraction and ratio of the radii for the particle and fiber. The model assumes the flow velocity is slow enough to neglect the inertial terms of the Navier-Stokes equation when the representative Reynolds number (Re) is 0.05 or less. The representative Reynolds number is shown in Equation 3.1, where η, ρ_g, and U_0 are air viscosity, density, and velocity respectively.

$$\mathrm{Re} = \frac{\rho_g d_f U_0}{\eta} \tag{3.1}$$

The Kuwabara cell model assumes that the radial and tangential velocities vanish at the fiber surface, the vorticity at the cell boundary cancels with the vorticity of the adjacent fiber cell, and the radial velocity along the cell boundary is a function of $\cos(\theta)$ [88]. The Kuwabara cell model is depicted in Figure 3.2 and Table 3.1.

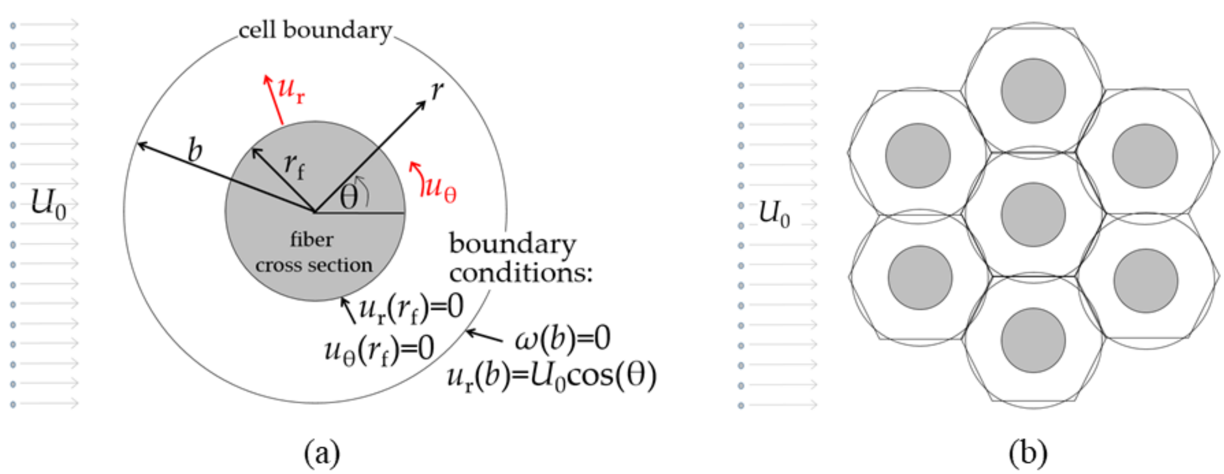

Figure 3.2 Kuwabara cell model for single fiber efficiency. (a) Kuwabara single fiber with boundary conditions. (b) Kuwabara flow field arrangement of fiber cross sections.

Table 3.1 Kuwabara Cell Model

Symbol	Description	Calculations and Boundary Conditions
ψ	Stream function	$\nabla^4\psi = 0$
∇^2	Vector Laplacian	$\nabla^2 = \frac{\delta^2}{\delta r^2} + \frac{1}{r}\frac{\delta}{\delta\theta} + \frac{1}{r^2}\frac{\delta^2}{\delta\theta^2}$
α_f	Solid Volume Fraction	$\alpha_\mathrm{f} = \frac{fiber\ volume}{total\ volume}$
b	Distance to boundary	$b = \frac{r_\mathrm{f}}{\sqrt{\alpha_\mathrm{f}}}$
ν	Mean velocity inside cell	$\nu = \frac{U_0}{(1-\alpha_\mathrm{f})}$
u_r	Radial velocity	$u_\mathrm{r}(b) = u_0\cos\theta$ $u_\mathrm{r}(r_\mathrm{f}) = 0$
u_θ	Tangential velocity	$u_\theta(r_\mathrm{f}) = 0$
ω	Vorticity	$\omega = -\nabla^2\psi$ $\omega(\mathrm{b}) = 0$

The Kuwabara hydrodynamic factor shown in Equation 3.2 is a dimensionless number derived entirely from the filter solidity and is significant for the prediction of the interception component of the SFE model.

$$\mathrm{Ku} = -\frac{1}{2}\ln\alpha_\mathrm{f} - \frac{3}{4} + \alpha_\mathrm{f} - \frac{{\alpha_\mathrm{f}}^2}{4} \tag{3.2}$$

The solution to the Kuwabara model in cylindrical polar coordinates is shown as Equation 3.3 [88].

$$\psi = \frac{\nu r}{2\mathrm{Ku}}\left(2\ln\frac{r}{r_\mathrm{f}} - 1 + \alpha_\mathrm{f} + r_\mathrm{f}^2\left(1 - \frac{\alpha_\mathrm{f}}{2}\right) - \frac{\alpha_\mathrm{f}}{2}\frac{r^2}{r_\mathrm{f}^2}\right)\sin\theta \tag{3.3}$$

On the cell boundary where r = b in Figure 3.2, the stream function has the solution shown in Equation 3.4 where y is the distance from the center of the approaching stream normal to flow.

$$\psi = \nu b\sin\theta = \nu y \tag{3.4}$$

The Kuwabara cell model enables the calculation of streamflow around a single fiber, while accounting for the effects of its neighboring fibers, with geometrically incident particles that are assumed to follow the streamflow paths. This is the basic foundation of the SFE model, which analyzes particle motion in relation to flow streamlines around a fiber cross section and predicts the percentage of particles captured by the fiber compared to all particles approaching the fiber on geometrically incident streamlines as shown in Figure 3.3.

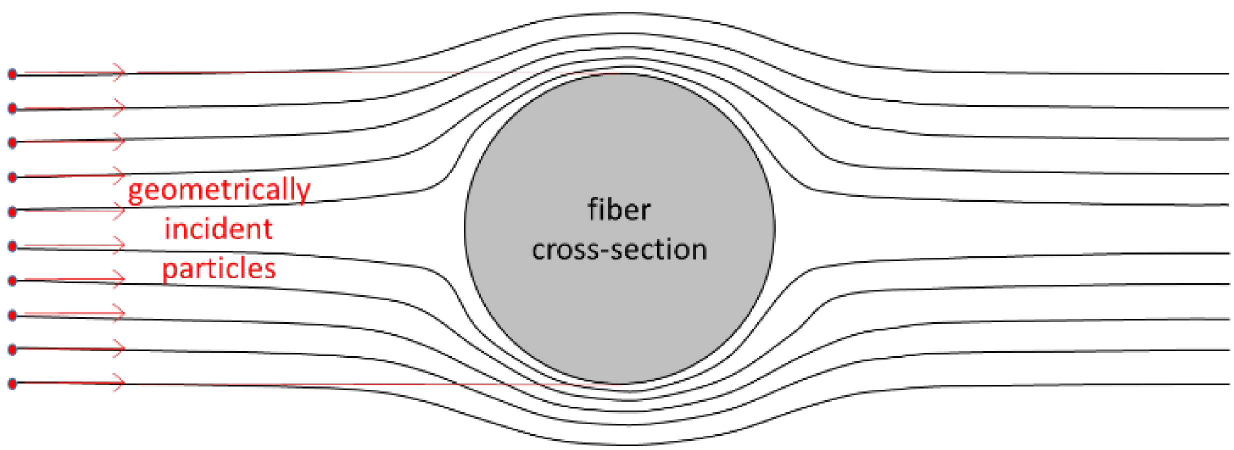

Figure 3.3 Single fiber flow field streamlines.

3.3 Particle Deposition Mechanics

To understand and apply the SFE model and other filtration models, the dynamics of aerosol particles must be understood. Lee and Liu, along with other authors, refined and expanded the SFE model to account for multiple particle deposition mechanics to include interception, inertial impaction, Brownian diffusion, gravitational settling, and electrostatic forces [81], [89], [90]. Particles that contact a fiber by these deposition mechanics are usually assumed to attach and remain affixed to the fiber through Van der Waals force. Figure 3.4 shows as an example three particles captured by interception, diffusion, and inertial impaction, as well as two particles that escaped capture by the fiber. The particles that escaped capture are known as penetrants.

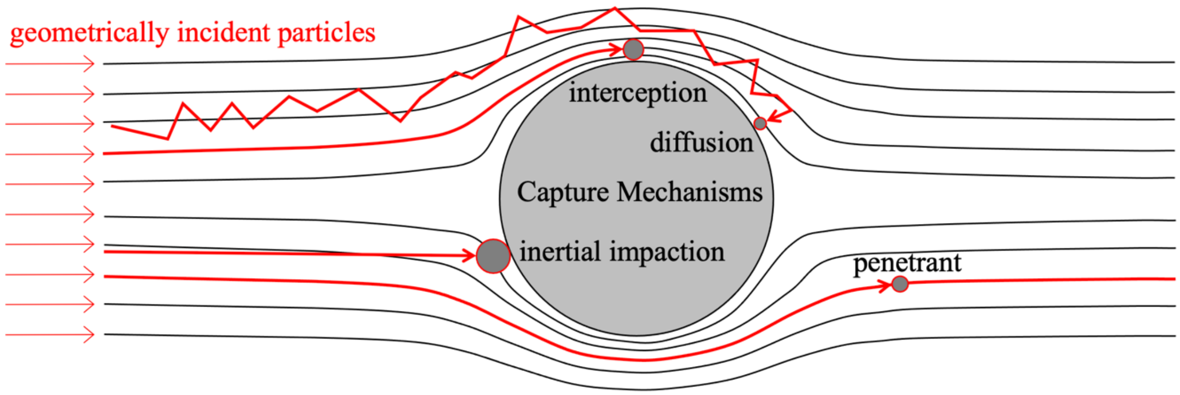

Figure 3.4 Particle deposition mechanics.

3.4 Single Fiber Penetration and Filtration Efficiency

Single fiber penetration, designated as the variable P_{Σ}, is the percentage of geometrically incident particles that approached the fiber incident to the fiber cross section but escaped past the fiber and avoided collection. The single fiber efficiency E_{Σ} is the complement of P_{Σ} and is defined as the percentage of incident particles approaching the fiber that become captured, given in Equation 3.5 with c_{in} and c_{out} given as number count of particles approaching incident to the fiber and escaping the fiber respectively.

$$E_{\Sigma} = 1 - P_{\Sigma} = (c_{\text{in}} - c_{\text{out}})/c_{\text{in}} \tag{3.5}$$

As suggested by the symbol, E_{Σ} is a combination of the component efficiencies for each deposition mechanic: Interception Efficiency (E_{R}), Diffusion Efficiency (E_{D}), Interception of Diffusing Particles Efficiency (E_{DR}), Inertial Impaction Efficiency (E_{I}), Gravitational Efficiency (E_{G}), and Electrostatic Efficiency (E_{E}). For typical air filter conditions with laminar air flow over a fiber and typical dust particle density while neglecting electrostatic effects, the size of the aerosol particle indicates the predominant capture mechanism as shown in Table 3.2 [13]. It is worth noting that many alternative analytical model versions for the deposition mechanics and flow resistance exist. The SFE model presented in this chapter is based primarily on the SFE model presented by Hinds [13].

Table 3.2 Particle Capture Mechanisms Based on Particle Size

Mechanism	Particle Size	Particle Diameter (nm)	Explanation
E_{D} Diffusion	Very Small	$0 < d_{\mathrm{p}} < 100$	Particles stray from flowlines by Brownian diffusion and collide with fibers
E_{R} Interception	Medium	$100 < d_{\mathrm{p}} < 200$	Particles follow flowlines and collide with fibers within one radius of flowline
E_{I} Inertial Impaction	Large	$d_{\mathrm{p}} > 300$	Particles stray from flowlines by inertia and collide with fibers
E_{G} Gravitational	Very Large	$d_{\mathrm{p}} > 500$	Particles stray from flowlines by force of gravity

3.5 Interception Efficiency E_{R}

Interception is a key mechanism for the collection of particles smaller than 0.2 μm which generally follow along laminar airflow streamlines through the filter media. As illustrated in Figure 3.5, particles following streamlines that come within one particle radius from the fiber surface contact the fiber and are assumed to stick to it.

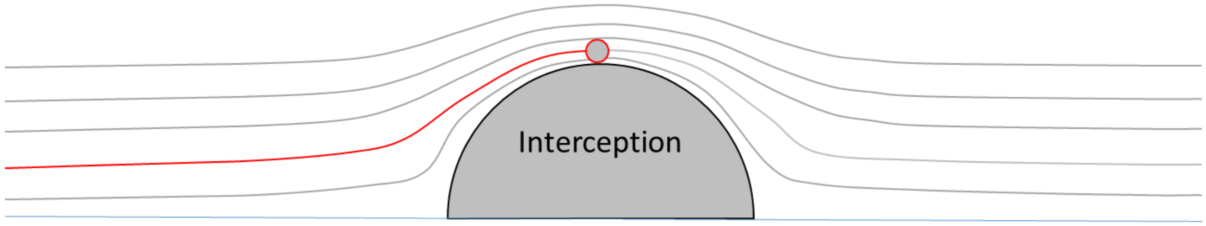

Figure 3.5 Interception deposition mechanism.

In polar coordinates, the stream flow lines come nearest the fiber surface at $\theta = \frac{\pi}{2}$ in Figure 3.2 where the flow streamlines are parallel to the overall direction of flow. For a given fiber with radius r_{f} and a given particle size with radius r_{p}, the particle will collide with the fiber if the sum of the particle and fiber radii is greater than the distance from the center of the fiber to the stream flow line at $\theta = \frac{\pi}{2}$. The interception efficiency for a single fiber when considering only the particles geometrically incident to the fiber is therefore shown by Equation 3.6.

$$E_{\mathrm{R}} = \frac{2y}{2r_{\mathrm{f}}} = \frac{\psi}{\nu r_{\mathrm{f}}} \tag{3.6}$$

Defining R as the ratio of particle diameter to fiber diameter as shown in Equation 3.7, the Interception Efficiency (E_{R}) can be written from the stream flow model as shown in Equation 3.8 [15].

$$R = \frac{d_{\mathrm{p}}}{d_{\mathrm{f}}} \tag{3.7}$$

$$E_{\mathrm{R}} = \frac{1+R}{2\mathrm{Ku}}\left(2\ln(1+R) - 1 + \alpha_{\mathrm{f}} + \left(\frac{1}{1+R}\right)^2\left(1 - \frac{\alpha_{\mathrm{f}}}{2}\right) - \frac{\alpha_{\mathrm{f}}}{2}(1+R)^2\right) \tag{3.8}$$

However, there have been several efforts to simplify Equation 3.8 for E_{R}. One of the most widely used approximations is shown in Equation 3.9 [15].

$$E_{\mathrm{R}} = \frac{(1-\alpha_{\mathrm{f}})R^2}{(\mathrm{Ku})(1+R)} \tag{3.9}$$

Up to this point, this model does not account for slip boundary conditions for very small fibers, which are generally smaller than 2 μm in diameter. A useful non-dimensional number commonly used to address slip is the Knudsen number, defined as the ratio of molecular mean free path length of a gas to a characteristic length, such as the diameter or radius of a particle or fiber. The Knudsen number for a fiber is the mean free path of air, λ, divided by the fiber radius as shown in Equation 3.10 (although this form is based upon the fiber diameter). The mean free path of air is approximately 65 nm at standard conditions.

$$\mathrm{Kn} = \frac{2\lambda}{d_\mathrm{f}} \tag{3.10}$$

The smaller the fiber diameter, the larger the Knudsen number, which is an indicator of the boundary slip condition of an airstream along a fiber surface. Air flow around a fiber falls into one of four categories depending on the Knudsen number as shown in Table 3.3.

Table 3.3 Knudsen Number Significance

Kn	Category	Fiber Diameter (d_f)	
$\mathrm{Kn} < 0.01$	Continuum (Non-Slip)	$d_\mathrm{f} > 200(\lambda)$	$d_\mathrm{f} > 13$ µm
$0.01 < \mathrm{Kn} < 0.25$	Slip Flow	$8(\lambda) < d_\mathrm{f} < 200(\lambda)$	520 nm $< d_\mathrm{f} < 13$ µm
$0.25 < \mathrm{Kn} < 10$	Transient	$0.2(\lambda) < d_\mathrm{f} < 8(\lambda)$	13 nm $< d_\mathrm{f} < 520$ nm
$10.0 < \mathrm{Kn}$	Free Molecule Range	$d_\mathrm{f} < 0.2(\lambda)$	$d_\mathrm{f} < 13$ nm

Most nanofiber filters are in the range of slip flow and transient flow categories, with fiber diameters ranging from 13 nm to 13 µm and Knudsen numbers ranging from 0.01 and 10.00. HEPA filters are mostly in the transient flow category with fiber diameters less than 500 nm. Larger values of Kn indicate that small particles traveling along air flow streamlines are less likely to be influenced and collected by the fibers, resulting in higher penetration and lower pressure drop. Brownian diffusion becomes the primary SFE component for small particles at large Knudsen numbers, especially aerosol particles with diameter sizes in the range of the mean free path of air molecules.

A simple modification of the Kuwabara hydrodynamic factor to account for slip conditions on the fiber boundary is applied by adding the Knudsen number to the hydrodynamic factor in Equation 3.9. The resulting SFE component for interception efficiency is shown in Equation 3.11.

$$E_{\mathrm{R}} = \frac{(1-\alpha_{\mathrm{f}})R^2}{\left(\mathrm{Ku}+\frac{2\lambda}{d_{\mathrm{f}}}\right)(1+R)} \tag{3.11}$$

3.6 Inertial Impaction Efficiency E_{I}

Inertial impaction plays the primary role in the collection of particles generally larger than 0.3 µm and can be neglected for very small particles with low momentum. Momentum and particle stopping distance are key parameters of inertial impaction. A visual representation of inertial impaction is depicted in Figure 3.6.

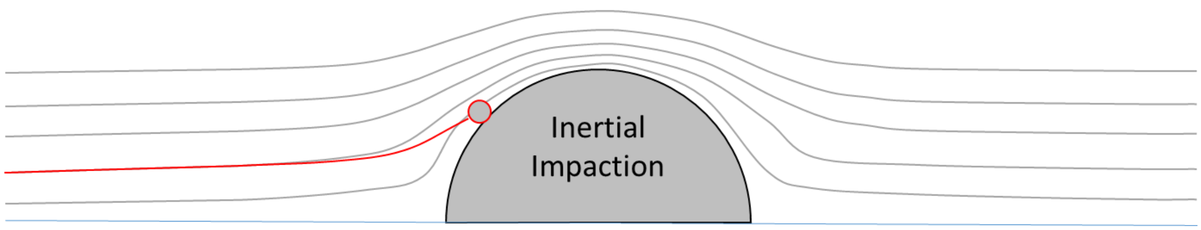

Figure 3.6 Inertial impaction deposition mechanism.

The Reynolds number earlier described in relation to the fiber and air flow is now considered in relation to the aerosol particle. The Reynolds number is the ratio of inertial force to frictional viscous force as the particle flows through air, which is important for impaction deposition mechanics. The motion of a particle with a low Reynolds number is governed by frictional force, which will cause it to generally follow air flow streamlines. Conversely the motion of a particle with high Reynolds number is governed by inertial force which will tend veer outside of a streamline when the streamline changes direction. For high Reynolds number between 1000 and 200,000, Newton’s resistance law enables the calculation of the drag force using an empirical coefficient of drag, density, diameter, and velocity of an object. The transition range is for Reynolds number between 1 and 1000. Most aerosols flow with low Reynolds number, less than unity, where viscous forces are greater than inertial forces. Stokes Law becomes important for inertial impaction in the region of Stokes flow, where a significant amount of air filtration takes place. By dismissing inertial forces as negligible and assuming incompressible flow, the Navier-Stokes equations simplify, eliminating higher order terms and yielding solvable linear equations. In this case, the force of drag experienced by a particle is shown in Equation 3.12.

$$F_{\mathrm{d}} = 3\pi\eta\nu_{\mathrm{t}}d_{\mathrm{p}} \tag{3.12}$$

The terminal velocity ν_{t} can be calculated by equating the drag force of a particle to the force exerted on the same particle, such as the force from gravity. Thus, the particle mobility B, illustrated in Equation 3.13, is the ratio of the terminal velocity of a particle to the steady force producing that velocity. It is convenient to consider this variable as a relative guide for the particle attaining a steady motion. For example, a large particle mobility indicates that a particle achieves terminal velocity with a smaller amount of force, while a small particle mobility indicates a larger force is required for a particle to achieve terminal velocity.

$$B = \frac{\nu_{\mathrm{t}}}{F} \tag{3.13}$$

Relaxation time τ may be defined as the time required for a particle to adjust to a new velocity for a newly applied force. This is illustrated in Equation 3.14 and may be calculated by utilizing the terminal velocity divided by acceleration, or the mass of the particle multiplied by the particle mobility. A particle reaches 63% of its terminal velocity after its relaxation time, and 95% of its terminal velocity after three times its relaxation time.

$$\tau = mB = \frac{\rho_{\mathrm{p}} d_{\mathrm{p}}^2 C_{\mathrm{c}}}{18\eta} \tag{3.14}$$

Building upon the relaxation time, the concept of a stopping distance may be introduced as the distance a particle will travel with a given initial velocity ν_0 until it stops. The particle stopping distance S may be calculated if the particle is within the Stokes region using Equation 3.15.

$$S = \tau v_0 \tag{3.15}$$

Finally, curvilinear motion is characterized by the Stokes number, which may be defined as the stopping distance divided by a characteristic dimension. The fiber diameter is typically used in the analysis of fibrous filters as the characteristic dimension, shown in Equation 3.16.

$$\mathrm{Stk} = \frac{S}{d_{\mathrm{c}}} = \frac{\tau U_0}{d_{\mathrm{f}}} \tag{3.16}$$

The Stokes number is an indication of a particle's ability to change direction and follow along air flow streamlines around a fiber, in the case of Equation 3.16. For large Stokes numbers much greater than unity, a particle has adequate inertia to continue in a relatively straight line when the air molecules surrounding it turn, creating a high probability of the particle veering outside the flow line and colliding with a nearby fiber, thus being collected by the inertial impaction mechanism. For low Stokes numbers much less than unity, a particle has insufficient inertia to veer outside flow lines while it moves along with the air flow. In this manner the Stokes number is the measurement of a particle's persistence to stay along a flow streamline in comparison to the size of a fiber. The SFE for Impaction (E_{I}) is calculated using Stk, α_{f}, and Ku as shown in Equation 3.17.

$$E_{\mathrm{I}} = \frac{(\mathrm{Stk})J}{2(\mathrm{Ku})^2} \text{ where } J = \left(29.6 - 28\alpha_{\mathrm{f}}^{\;0.62}\right)R^2 - 27.5R^{2.8} \tag{3.17}$$

3.7 Diffusion Efficiency E_D

Diffusion generally plays the role of the primary deposition mechanism for the filtration of particles smaller than 0.3 µm. Brownian diffusion is the seemingly random motion of particles interacting with the collision energy of the transporting medium. In this, particles tend to veer outside of flow streamlines with seemingly random and erratic movement, thus colliding with and adhering to fibers. This is illustrated in Figure 3.7 below.

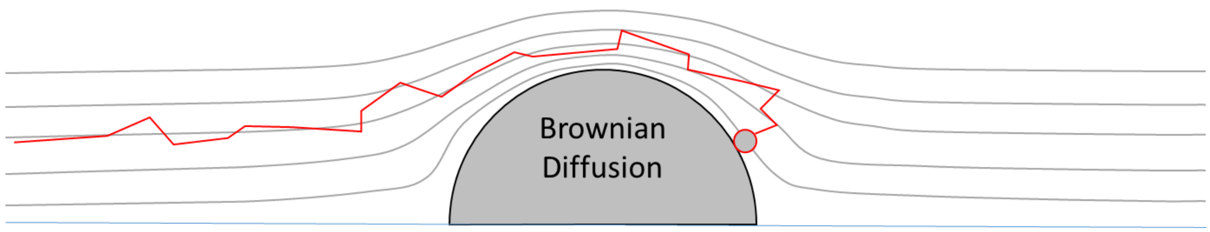

Figure 3.7 Brownian diffusion deposition mechanism.

However, since Brownian diffusion is known to be the result of many molecular collisions with a particle, it cannot be applied directly to very small particles generally less than 1 µm diameter, without being corrected. This is because as described above, Stokes Law cannot account for the dynamics of very small particles capable of slipping between the air molecules due to the particle's very small size. To address this issue, Cunningham developed a slip correction factor for Stokes Law based on the particle diameter and the mean free path of air as shown in Equation 3.18.

$$C_{\mathrm{c}} = 1 + \frac{2.52\lambda}{d_{\mathrm{p}}} \tag{3.18}$$

For particles below 100 nm diameter, an alternative version of the slip correction factor is necessary, and the resulting correction factor is shown in Equation 3.19.

$$C_{\mathrm{c}} = 1 + \frac{\lambda}{d_{\mathrm{p}}}\left(2.34 + 1.05\mathrm{e}^{-0.39 d_{\mathrm{p}}/\lambda}\right) \tag{3.19}$$

The viscosity of air is an important factor in air filtration, which can be calculated as shown in Equation 3.20 using the absolute temperature T and yielding units of $Pa \cdot s$.

$$\eta = \frac{1.458\mathrm{E} - 6 \cdot T^{1.5}}{T + 110.4} \tag{3.20}$$

The diffusivity or coefficient of diffusion reflects the tendency of gas particles to spread out over time. The diffusivity D may be calculated from the absolute temperature in Kelvin, the Boltzmann constant k of 1.38E-23 J/K, air viscosity η, particle diameter d_{p} and slip correction factor C_{c} as shown in Equation 3.21 with units of m^2/s.

$$D = \frac{kTC_{\mathrm{c}}}{3\pi\eta d_{\mathrm{p}}} \tag{3.21}$$

Finally, the Peclet number may be defined as a dimensionless ratio of the rate of advection of a quantity to the rate of diffusion of the same quantity. This may be calculated, as shown in Equation 3.22, as the product of the velocity v and fiber diameter d_{f} divided by the particle diffusion coefficient.

$$\mathrm{Pe} = \frac{(v)(d_{\mathrm{f}})}{D} \tag{3.22}$$

The single fiber efficiency based on the diffusion of particles may now be calculated from using the Peclet number, as shown below in Equation 3.23.

$$E_{\mathrm{D}} = 2\mathrm{Pe}^{-2/3} \tag{3.23}$$

A low value for Peclet number indicates the prominence of the diffusion mechanism E_D.

3.8 Diffusion-Interception Efficiency E_{DR}

A common assumption when using the SFE model is that each of the different deposition mechanisms work independently of the others. Although a valid assumption in many cases, it is not always realistic or applicable and thus sometimes an additional efficiency term is added to account for the interaction between the different prevailing deposition mechanisms. Equation 3.24 illustrates the efficiency term accounting for the enhanced collection of diffusing particles through the interception mechanism.

$$E_{\mathrm{DR}} = \frac{1.24R^{2/3}}{(\mathrm{Ku} \cdot \mathrm{Pe})^{1/2}} \tag{3.24}$$

3.9 Gravitational Settling Efficiency E_G

Gravity plays a role in air filtration, forcing particles to either enter the airstream or depart from the airstream. The dimensionless constant that governs gravitational settling efficiency is shown in Equation 3.25.

$$G = \frac{V_{\mathrm{TS}}}{U_0} = \frac{\rho_{\mathrm{g}} d_{\mathrm{p}}^2 C_{\mathrm{c}} g}{18\eta U_0} \tag{3.25}$$

The efficiency gained or lost by gravitational settling depends on the direction of airflow compared to the direction of gravitational force, given in Equation 3.26. If the airflow is in the same direction as gravity, $E_{\mathrm{G}} = G(1 + R)$ which has a positive effect on single fiber efficiency. However, if the airflow is in the opposite direction, gravity has a negative effect on single fiber efficiency, as $E_{\mathrm{G}} = -G(1 + R)$.

$$E_{\mathrm{G}} = \pm G(1 + R) \tag{3.26}$$

3.10 Total Filter Efficiency

The single fiber efficiencies based on individual deposition mechanisms described above can be combined into the single fiber efficiency as shown in Equation 3.27. As stated previously, this method makes the assumption that each deposition mechanism acts independently of the other deposition mechanisms, although additional terms are sometimes added to address the interaction between them.

$$E_{\Sigma} = 1 - (1 - E_{\mathrm{R}})(1 - E_{\mathrm{D}})(1 - E_{\mathrm{DR}})(1 - E_{\mathrm{I}})(1 - E_{\mathrm{G}})(1 - E_{\mathrm{E}}) \tag{3.27}$$

The total filter penetration P_{F} may now be calculated for the filter media as a whole using an exponential function with the single fiber efficiency, filter solidity, filter media thickness, and fiber diameter variables as shown in Equation 3.28. The total filtration efficiency is then the complement of total filter penetration as shown in Equation 3.29 [13]. It is worth specifically stating that these equations for total filter penetration and efficiency are based on a singular particle size, which is factored into the single fiber efficiency E_{Σ}.

$$P_{\mathrm{F}} = \exp\left(\frac{-4\alpha E_{\Sigma} t}{\pi d_{\mathrm{f}}}\right) \tag{3.28}$$

$$E_{\mathrm{F}} = 1 - P_{\mathrm{F}} = 1 - \exp\left(\frac{-4\alpha E_{\Sigma} t}{\pi d_{\mathrm{f}}}\right) \tag{3.29}$$

A representation of component single fiber efficiencies and total filter efficiency is over a range of particle diameters is shown in Figure 3.8.

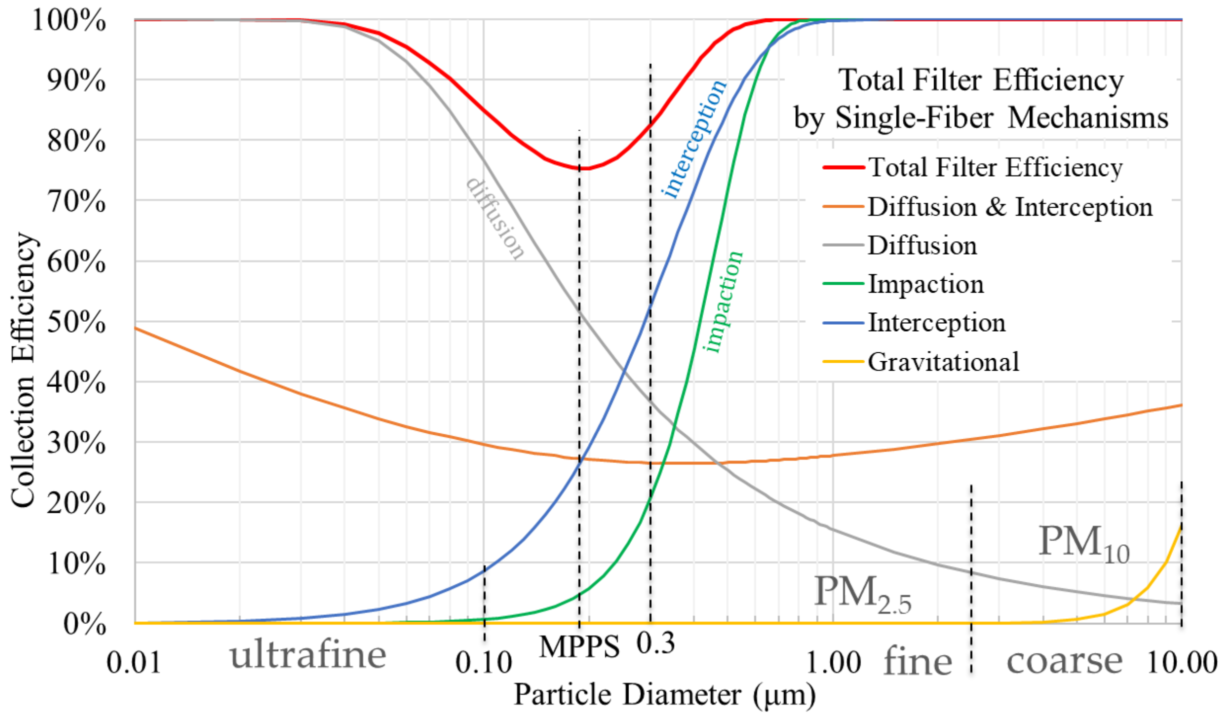

Figure 3.8 Total filter efficiency by single fiber deposition mechanisms.

The single fiber efficiency model shown here is dependent on known particle sizes to calculate the MPPS and the total filter efficiency. However, Lee and Liu developed a set of equations in 1980 to predict minimum single fiber efficiency and the most-penetrating particle size based solely on the interception and diffusion deposition mechanisms, shown in Equations 30 and 31 [90]. The minimum single fiber efficiency from Equation 3.30 may be substituted into Equation 3.29 above to calculate the total filter efficiency if the analysis is conducted regarding the MPPS.

$$\widehat{E_\Sigma} = 1.44\left[\left(\frac{1-\alpha}{\mathrm{Ku}}\right)^5\left(\frac{\sqrt{\lambda}kT}{\eta}\right)^4\left(\frac{1}{U_0^4 d_\mathrm{f}^{10}}\right)\right]^{1/9} \tag{3.30}$$

$$\widehat{d_\mathrm{p}} = 0.885\left[\left(\frac{\mathrm{Ku}}{1-\alpha}\right)\left(\frac{\sqrt{\lambda}kT}{\eta}\right)\left(\frac{d_\mathrm{f}^2}{U_0}\right)\right]^{2/9} \tag{3.31}$$

3.11 Air Flow Resistance

The filter's resistance to air flow, measured by pressure drop across the media, is equally as important as the filtration efficiency when evaluating the filter's overall performance. The goal of filter design is to achieve low flow resistance with high filtration efficiency. The pressure drop across the filter ΔP can also be related to the filter thickness, fiber diameter, a function of the solidity $f(\alpha_{\mathrm{f}})$, along with the air velocity U_0 and air viscosity η.

The basis of this relation is Darcy's Law, named for Henri Darcy who experimentally calculated the head loss due to friction of water transport through sand filters. This established a proportional relationship between the pressure head loss across the sand filter ΔP, the filter length and cross-sectional area L, A, the dynamic viscosity and volumetric flow rate of the fluid μ, Q, as represented by Equation 3.32 where k is the experimentally determined permeability of the porous medium.

$$\frac{\Delta PA}{\mu QL} = \frac{1}{k} \tag{3.32}$$

Using Darcy's work with flow through porous medium as a guide, Davies developed a similar relationship for air filtration through nonwoven fibrous media, which includes the pressure drop across the media ΔP, the mean fiber radius r, the cross sectional area A, the air viscosity η, and the volumetric air flow rate Q shown in Equation 3.33 [91].

$$\frac{\Delta PAr^2}{\eta Qt} = f(\alpha) \tag{3.33}$$

Davies developed an empirical correlation for the filter media pressure drop using a function of solidity $f(\alpha_{\mathrm{f}})$ as shown in Equation 3.34, where $\Delta P, t, U_0, \eta, and\ d_{\mathrm{f}}$ are the pressure drop, filter thickness air velocity, air viscosity, and mean fiber diameter.

$$\Delta P = \frac{\eta t U_0}{d_f^2} f(\alpha_f) \quad with \; f(\alpha_f) = 64{\alpha_f}^{1.5}(1 + 56{\alpha_f}^3) \tag{3.34}$$

The pressure drop across a filter is directly proportional to the air viscosity, air face velocity, filter thickness, and the filter's solid volume fraction. Many subsequent authors created air flow resistance models through analytical, numerical, and empirical means [84]–[86], [92], [93]. The Kuwabara and Happel models use ordered arrays of cylinders that are perpendicular to the flow, while the Spielman-Goren model presents four cases for fibers aligned in different orientations to the flow, allowing for different fiber geometries [93]. Conveniently, many of these may be incorporated into Equation 3.34 through a dimensionless function of the solidity $f(\alpha_f)$. The work of a few authors is included in Table 3.4.

Table 3.4 Flow Resistance Coefficients Based on Solidity for Various Authors

Author	$f(\alpha)$
Happel [94]	$\dfrac{-\,32\alpha}{\left[ln(\alpha) + \dfrac{(1-\alpha^2)}{(1+\alpha^2)}\right]}$
Kuwabara [94]	$\dfrac{-64\alpha}{2ln(\alpha) + 3 - 4\,\alpha + \alpha^2}$
Davies [13]	$64\alpha^{1.5}(1 + 56\alpha^3)$
Henry and Ariman [88]	$2.446\alpha + 38.16\alpha^2 + 138.9\alpha^3$
Rao and Faghri [82]	$2.653\alpha + 39.34\alpha^2 + 144.5\alpha^3$

3.12 Effective Fiber Diameter

It is worth noting here that the equations for calculating the pressure drop may be manipulated in order to estimate the effective fiber diameter of the filtration media, if the other variables in the equation are known. The effective fiber diameter may then be calculated as shown in Equation 3.35.

$$d_{\mathrm{fe}} = \sqrt{\frac{\eta t U_0 f(\alpha_{\mathrm{f}})}{\Delta P}} \tag{3.35}$$

3.13 Filter Figure of Merit FOM

Ultimately, the objective of air filtration is to maximize the filtration efficiency while minimizing air flow resistance. The ability of a filter to maximize efficiency while minimizing flow resistance is described as the filter "quality" and is measured by a parameter known as filter figure of merit (FOM). The quality of a filter may be thought of as a comparison of the particle collection efficiency to flow resistance. The FOM is calculated as a ratio of filtration efficiency per unit thickness divided by pressure drop per unit thickness, and is calculated as shown in Equation 3.36 with units of inverse Pascal [13]. A higher FOM represents a higher ratio of filtration efficiency to flow resistance.

$$\mathrm{FOM} = \frac{-\ln(P_{\mathrm{F}})}{\Delta P} = \frac{-\ln(1 - E_{\mathrm{F}})}{\Delta P} \tag{3.36}$$

3.14 Sensitivity Analysis

The analytical model for air flow under low Reynolds Number conditions (Re < 0.05) with slip or transient flow conditions (Kn > 0.01) can be summarized as listed in Table 3.5 with eight input parameters.

Table 3.5 Analytical Model Summary

Model Inputs	Intermediate Calculations	Model Outputs
Fiber Diameter	Filter Solidity	SFE
Fiber Length	Kuwabara Factor	TFE
Filter Thickness	Reynolds Number	ΔP
Air Velocity	Air Viscosity	FOM
Air Temperature	Slip Correction	
Mean Free Path	Knudsen Number	
Particle Diameter	Diffusivity	
Particle Density	Peclet Number	
	Particle Mobility	
	Stokes Number	

Sensitivity analysis shows the resulting changes in the total filtration efficiency and air flow resistance based on isolated changes in each of the eight input parameters, while keeping the remaining seven parameters constant. Figure 3.9 shows the sensitivity analysis for total filter efficiency, while Figure 3.10 shows sensitivity analysis for air flow resistance.

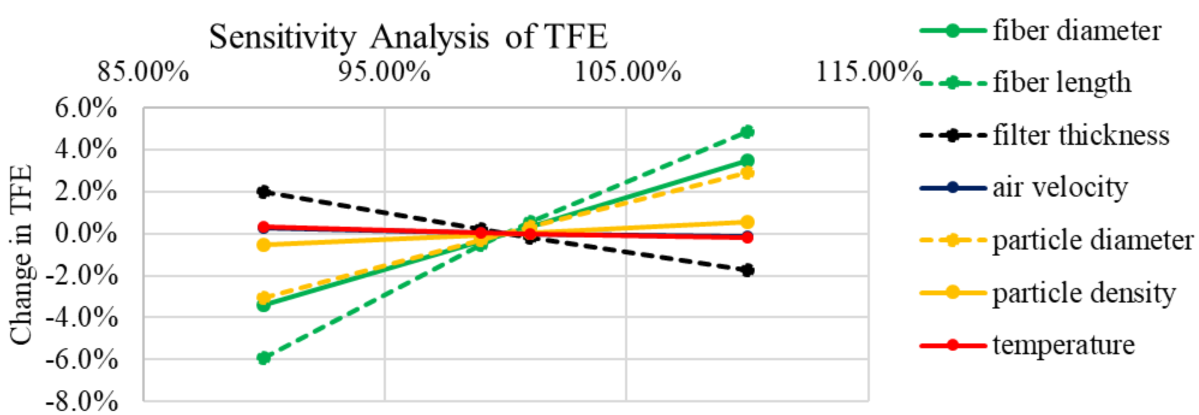

Figure 3.9 Sensitivity analysis for total filtration efficiency.

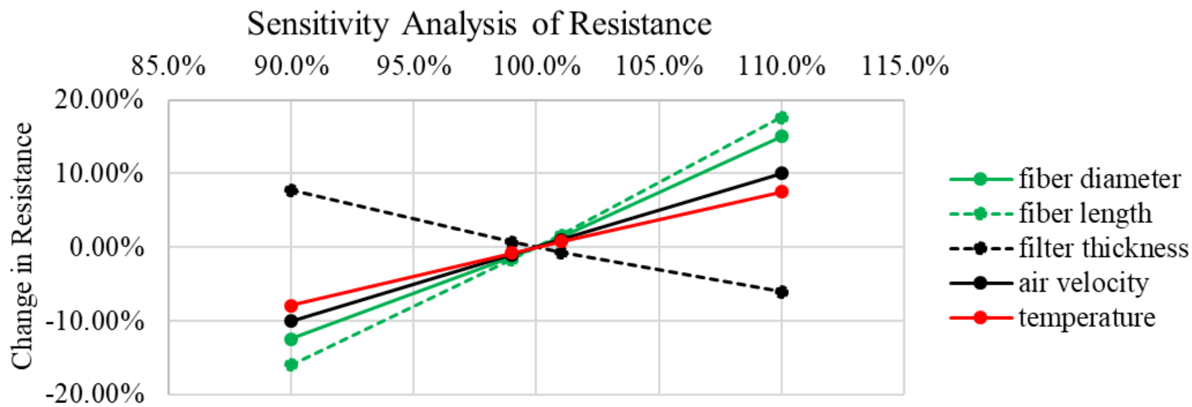

Figure 3.10 Sensitivity analysis for air flow resistance.

3.15 Chapter Summary

Analytical modeling of the capture mechanisms and air flow resistance of air filtration media greatly advances our understanding of the science of air filtration. At typical air filtration conditions with low Reynolds numbers, the nine parameters of fiber diameter and length, filter thickness and solidity, particle diameter and density, and air velocity, viscosity, and temperature will estimate the air filter media's filtration efficiency and air flow resistance.

CHAPTER IV

EXPERIMENTAL DEVELOPMENT OF ALTERNATIVE AIR FILTER MEDIA THROUGH ELECTROSPINNING POLYACRYLONITRILE

Particulate matter air pollution and volatile organic compounds released into the air from incomplete combustion of fossil fuels and wildfires creates significant damage to human health and to our environment. Nonwoven nanofibrous air filtration media in use today is unchanged from materials and technology developed decades ago. This chapter details an effort to explore new materials and methods for production of nonwoven air filtration media through electrospinning graphene-based composite polyacrylonitrile fibers. This chapter explores the potential benefits of electrospinning, stabilizing, and carbonizing polyacrylonitrile nanofibers into nonwoven filtration media. The methods involved included electrospinning fibrous matting onto stainless-steel wire mesh, stabilizing the nanofibrous media in a chamber furnace, testing for air filtration penetration and flow resistance, and observations of fiber uniformity using optical microscopy. Results of this effort indicate electrospun, stabilized, and carbonized nonwoven nanofibrous media could potentially benefit modern air filtration technology and reduce hazards associated with particulate matter and volatile organic compounds.

4.1 Introduction

Recent studies indicate the magnitude of global health problems associated with particulate matter (PM) air pollution [95]. Volatile organic compounds (VOCs) released into the air from natural and accidental fires and incomplete combustion of fossil fuels damages our environment and contributes to global warming. Fossil fuel combustion is the largest source of contribution to greenhouse gases for the U.S. Army [96]. Airborne VOCs combine with nitrogen oxide to create ground-level ozone, smog, health problems, and climate damage [97]. Airborne VOCs also released from wildfires threaten and damage the climate and environment.

Electrospun polyacrylonitrile nanofibers, both with and without graphene oxide (GO) additives, have proven to be effective in air filtration for removal of $PM_{2.5}$ aerosol pollution [98]–[103]. Experiments with activated polyacrylonitrile-based carbon nanofibers have shown noteworthy adsorption of formaldehyde [102]. Activated carbon has long been used as an adsorbent for air purification and separation, while the increased surface area ratio is an attractive benefit of activated carbon nanofibers [104]. Graphene-based materials have significant potential for adsorption of hazardous VOCs while filtering $PM_{2.5}$ aerosol [105]. Kumar et. al. illustrated the potential for graphene-based composite materials to evolve into next generation air filter materials for VOC adsorption and mitigate airborne hazards causing harm to the environment and climate [105]. Recent efforts of electrospinning polyacrylonitrile with graphene oxide and polyimide demonstrated promising results of filtration efficiency and air flow resistance [106]. Studies have shown enhanced mechanical properties gained by electrospun polyacrylonitrile fibers infused with graphene oxide [106], [107]. Successful development of graphene-based nanomaterials with high VOC adsorption could significantly improve air separation and purification technology and improve air quality.

Advances in electrospinning technology enable further research into composite carbon nanofibers for air filtration. The term “spinning” represents the extrusion of a liquid material through a spinneret nozzle or needle to produce continuous fibers [108]. Electrospinning has seen an increase in popularity over the past several decades due to the increase in exploration of nanomaterial technology [109]. Electrospinning, first patented for commercial use in 1934 by Anton Formhals, uses a high voltage electric field to eject fibers from a liquid solution onto a grounded collector in the form of nonwoven media [110]. While more than 50 types of polymers today are suitable for electrospinning into nanofibers, the electrospinning of polyacrylonitrile enables the production of carbon nanofibers through a subsequent carbonization process.

The intent of this effort is to advance innovative materials technology into air purification capabilities that enable mitigation of VOC airborne hazards caused by combustion exhaust systems, wildfires, and other VOC-producers. Better VOC adsorbing air filtration applied to exhaust flow of combustion systems will reduce VOCs at the point of production. Development of VOC-adsorbing air filters is achievable through synthesis and characterization of novel electrospun nanomaterials.

4.2 Methods and Materials

Polyacrylonitrile was selected as the base electrospinning material because it is a common precursor to carbon fibers. Electrospinning produces nanometer sized fibers. Successful stabilizing and carbonizing of electrospun polyacrylonitrile fibers would result in nonwoven carbon nanofibrous air filtration media with potentially substantial air filtration efficiency and low air flow resistance

Polyacrylonitrile was obtained from Sigma Aldrich with average molecular weight of 150,000 (Product Number 181315) and used as received. The solvent, DMF, was obtained from Sigma Aldrich with assay of 99.8% (Product Number 319937). Graphene Nano Platelets were obtained from XG Sciences, Lansing MI, of type xGnP C-750.

4.2.1 Stabilized Polyacrylonitrile

Polyacrylonitrile is a polymer with nitrile functional groups (CN) attached to a polyethylene backbone with a linear formula $(C_3H_3N)_n$. Polyacrylonitrile fibers are noncombustible, flame resistant, corrosion resistant, and mildew and mold resistant. Additionally, polyacrylonitrile fibers do not degrade from UV light, do not easily dissolve, and have a thermal decomposition temperature of 327 °C. Acrylic fibers can be dry-spun, wet-spun, or electrospun from polyacrylonitrile. The advantage of electrospinning is the ease of attaining sub-micron fiber diameters, while the other methods result in larger size fiber diameters. Electrospinning polyacrylonitrile fibers typically results in fiber diameters in the range of 5 nm to 500 nm [111]. The stretching and drawing of polyacrylonitrile fibers during the electrospinning process serves to reduce the fiber diameter while also aligning the polymer molecules, which increases the resulting tensile strength [112]. Polyacrylonitrile was first spun into fibers in 1938, while DuPont began producing commercially available polyacrylonitrile fibers under the name Orlon in 1944 [111].

Polyacrylonitrile nanofibers can be carbonized into carbon nanofibers through a multi-phase process including oxidative stabilization and inert carbonization. Oxidative stabilization typically occurs at 270 °C, while carbonization occurs between 1000 °C and 1500 °C. Carbonization yields a turbostratic carbon fiber structure of folded basal planes [112]. The thermal and mechanical properties of carbon nanofibers are desirable properties for air filtration media.

4.2.2 Solution Preparation

Solution concentrations and molecular weight selection were informed by previous works which obtained good results for polyacrylonitrile fibers with 8% to 16% concentration for 73,400 g/mol and 121,000 g/mol molecular weights [113]. Initially three ten-gram solutions of polyacrylonitrile dissolved in DMF were prepared at 6%, 9%, and 12% mass ratio. The solutions were mixed overnight at room temperature in 20 ml glass bottles with small spinning magnets at 600 rpm on a Corning PC-620D magnetic stirring plate. All three solutions were tested for electrospinning suitability. The viscosity of the 12% solution prevented its further use. The 6% and 9% solutions were capable of electrospinning through 21 gauge and 23-gauge needles. Based on the success of the 9% mass ratio polyacrylonitrile, additional solutions were prepared for electrospinning. All three solutions were tested for electrospinning suitability. The viscosity of the 12% solution prevented its further use. The 6% and 9% solutions were capable of electrospinning through 21 gauge and 23-gauge needles. Based on the success of the 9% mass ratio polyacrylonitrile, additional solutions were prepared for electrospinning. Figure 4.1 shows the electrospinner and a graphene-embedded solution prepared for use.

(a) (b)

Figure 4.1 Solution preparation for electrospinning. (a) NanoNC electrospinner. (b) Solution prepared with graphene additive.

4.2.3 Graphene Additive

The advantage of polyacrylonitrile nanofibers is the potential to carbonize the media into carbon nanofibers. Activated carbon is well established in air filtration. However activated carbon alone lacks effectiveness to adsorb formaldehyde and other low molecular weight VOCs [105]. Composite materials with graphene, GO, and reduced GO are well suited for VOC adsorption [105]. Recent efforts of electrospinning polyacrylonitrile with GO and polyimide nanofibers have showed promising results with high filtration efficiency, low air flow resistance, and excellent mechanical properties [106]. The graphene platelets were added to the solutions to produce composite polyacrylonitrile-graphene nanofibers that can be later carbonized into carbon-graphene nanofibers.

4.2.4 Stainless-Steel Woven Wire Mesh

Type 304 stainless-steel woven wire meshes were obtained from local sources with dimensions shown in Table 4.1. A 20-gauge mesh was used for a flat plate collector, while an 8-gauge mesh was used for a 939 mm diameter cylindrical roller collector. The stainless-steel meshes were configured for flat plate and roller collection as shown in Figure 4.2.

Table 4.1 Stainless-Steel Wire Mesh Dimensions

	Use	Aperture (μm)	Wire Diameter (μm)	Open Area (%)	Mass Density (kg/m^2)
20-Gauge SS mesh	Flat Plate	900	400	52	1.25
8-Gauge SS mesh	Roller	2500	800	60	2

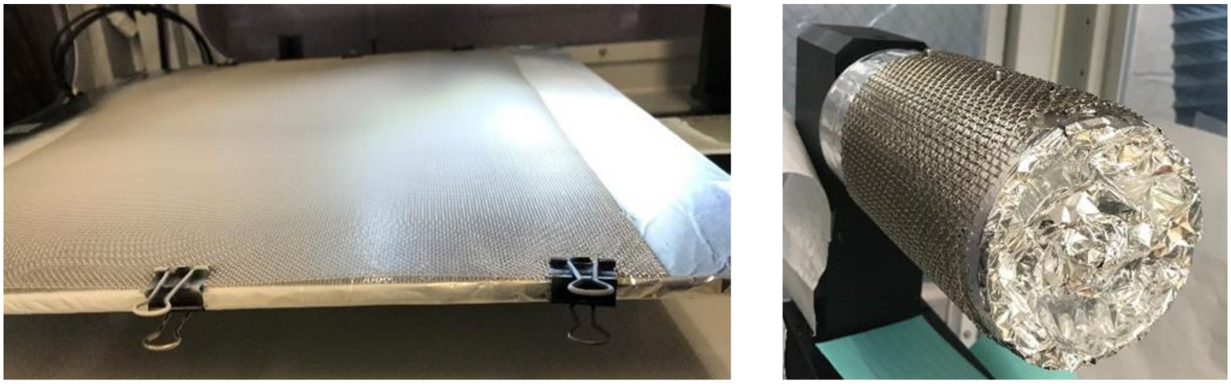

(a) (b)

Figure 4.2 Stainless-steel woven wire mesh configurations for (a) flat plate and (b) roller.

4.2.5 Electrospinning

The solutions were electrospun into polyacrylonitrile fibers on a NanoNC model ESR200R2D electrospinner. The electrospinner was first configured for vertical alignment onto the horizontal stainless-steel flat plate, then later configured for horizontal alignment onto the roller collector. For the flat plate setup, the 20-gauge stainless-steel mesh was cut to 300 mm x 405 mm and fastened onto the collector plate using steel binder clips as shown in Figure 4.2(a). For the roller setup, the 8-gauge stainless-steel mesh was cut to dimensions 295 mm x 152 mm and fastened into a cylinder with 93.9 mm diameter as shown in Figure 4.2(b).

The polyacrylonitrile-DMF solutions were placed into 20 ml plastic syringe bottles with 25 mm long 23-gauge stainless-steel needle having 0.34 mm inside diameter. The tip-to-collector distance (TCD) and electrical potential were selected based on previous works that showed good results with 16 cm distance and 20 kV [113]. The TCD was set at 15 cm from the collector. For the first two iterations, the needle was electrified to a potential of 20 kV, and the collectors were grounded. The electrical potential was increased to 25 kV for the third and fourth iterations. The fifth through ninth iterations included a positive potential of 25 kV on the needle and negative 5 kV on the collector, for total electrical potential of 30 kV. Previous experimental studies in the literature have shown smaller diameter polyacrylonitrile fibers result from lower concentration solution mixtures at higher voltage and greater TCD, while larger diameter polyacrylonitrile fibers result from higher concentration solution at lower voltage and smaller TCD [114].

The solutions were pumped through the syringe needle initially at a rate of 0.8 ml/hr for the flat plate collector, and 1.1 ml/hr for the cylindrical roller collector. The solution flow rate was increased for subsequent iterations to up to a maximum of 1.5 ml/hr. The electrospinning configurations are shown in Figure 4.3.

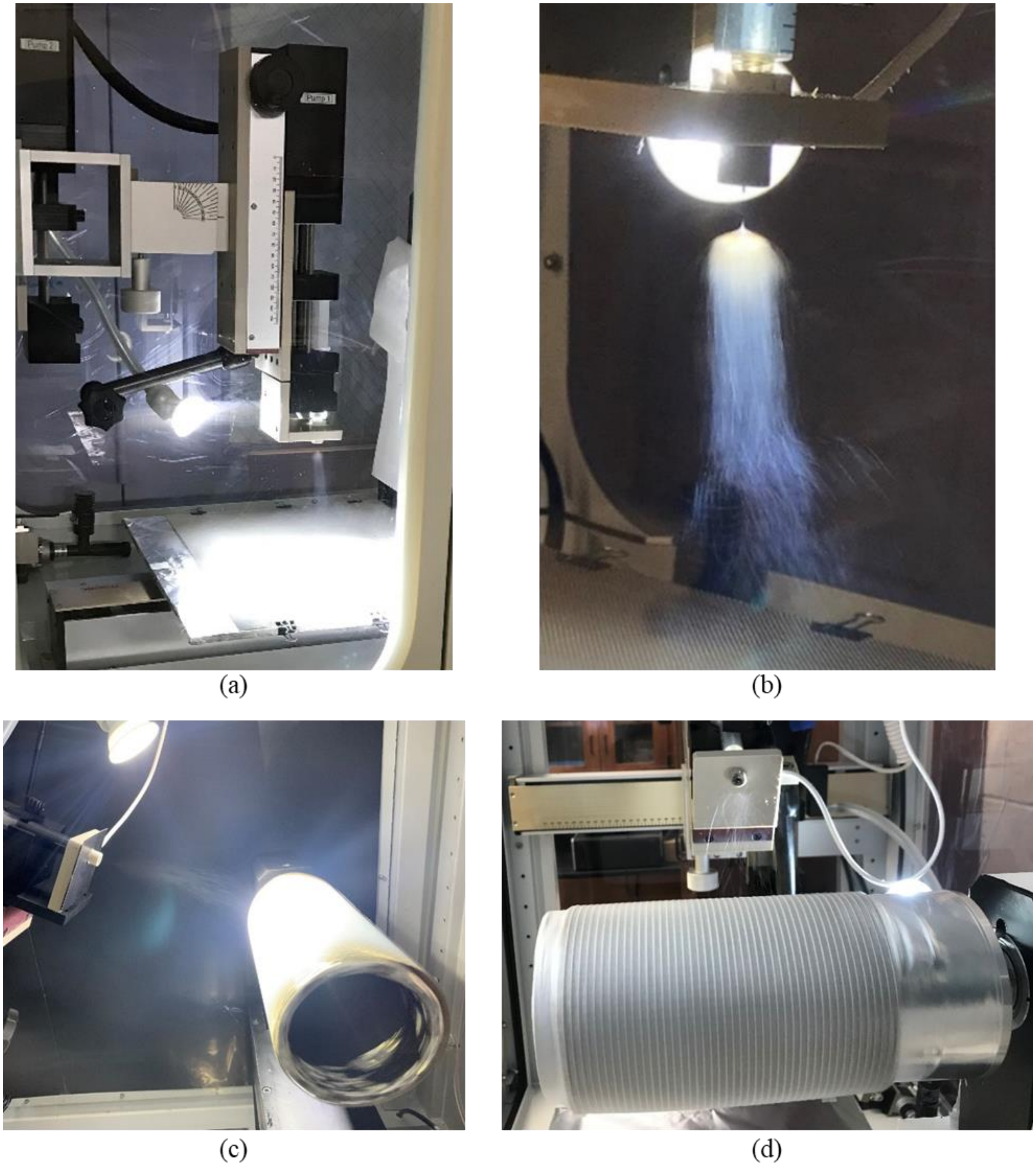

Figure 4.3 Electrospinning configurations. (a) Vertical alignment onto flat plate. (b) Spray pattern for vertical alignment. (c) Side view of horizontal alignment onto cylindrical roller. (d) Rear view of roller alignment.

4.2.6 The Science of Electrospinning

The science of electrospinning involves six forces acting on particles of a dissolved polymer jet as it travels from syringe needle to collector: body, external electrostatic, internal electrostatic, viscoelastic, surface tension, and drag [115]–[118]. Gravity is the primary body force acting on the jet molecules, attracting them toward the earth. Electrostatic force of attraction between charged jet particles and the grounded collector is the primary force that propels the jet toward the collector. Surface tension between the molecules within the jet attempts to keep the jet particles together. Electrostatic force of repulsion between similarly charged jet particles causes them to repel one another, serving to lengthen and whip the jet. Viscoelastic force between the charged jet particles resists particle separation. The drag force on the jet particles caused by interaction with air molecules resists the jet's movement toward the collector.

Electrospinning involves a "dial in" technique to obtain desired results of fiber size and shape by changing solution parameters and process parameters. Changeable solution parameters include molecular weight, percent hydrolysis, and concentration of the dissolved polymer. Solution parameters that can be measured include surface tension, apparent viscosity, longitudinal viscosity, and electrical conductivity. Changeable process parameters include electric field potential, shape of the electric field, distance between the needle and collector, direction from needle to collector, needle diameter, and pump flow rate. Environmental parameters that can be controlled include temperature, humidity, and barometric pressure.

Dialing in electrospinning parameters shown in Table 4.2 resulted in stable polyacrylonitrile jets as shown in Figure 4.4. The electrostatically charged jet is ejected from the stainless-steel nozzle in a straight line. After approximately two centimeters, the jet destabilizes and whips. The whipping motion of the jet evaporates the solvent. The residual polyacrylonitrile fiber continues to the collector and forms a nonwoven fibrous mesh.

Figure 4.4 Electrospinning jet formation.

4.2.7 Polyacrylonitrile Stabilization

Polyacrylonitrile fiber stabilization takes place between 200 °C and 300 °C in air. At a temperature over 180 °C, homopolymer polyacrylonitrile molecular chains unfold and slide around. Five chemical reactions during this phase include: oxidation, dehydrogenation, cyclization, aromatization, and crosslinking, as listed below and depicted in Figure 4.5 [119].

(1) Oxidation. In the oxidation reaction, oxygen atoms attach to the carbon chain, ejecting two hydrogen atoms in the form of N2 gas. The fibers incorporate approximately 8% oxygen during this exothermic process. Oxidation is the gain of oxygen atoms and loss of hydrogen atoms.
(2) Hydrogenation. In the dehydrogenation reaction, double bonds are formed be-tween carbon atoms to stabilize the carbon chain and eject oxygen and hydrogen atoms in the form of water vapor and N_2 gas.
(3) Cyclization. In the cyano group cyclization reaction, the C≡N triple bonds are broken, and formation of single and double bonds in a continuous ladder structure be-tween alternating carbon and nitrogen atoms.

(4) Aromatization. The aromatization reaction is the formation of a heterocyclic system created by cyclization of the nitrogen atoms.
(5) Crosslinking. The crosslinking reaction is the bonding of one polymer chain to another. The structure results in aromatic pyridine groups as the carbon atoms lose hydrogen atoms and give off hydrogen gas. The crosslinking reaction sets the carbon structure.

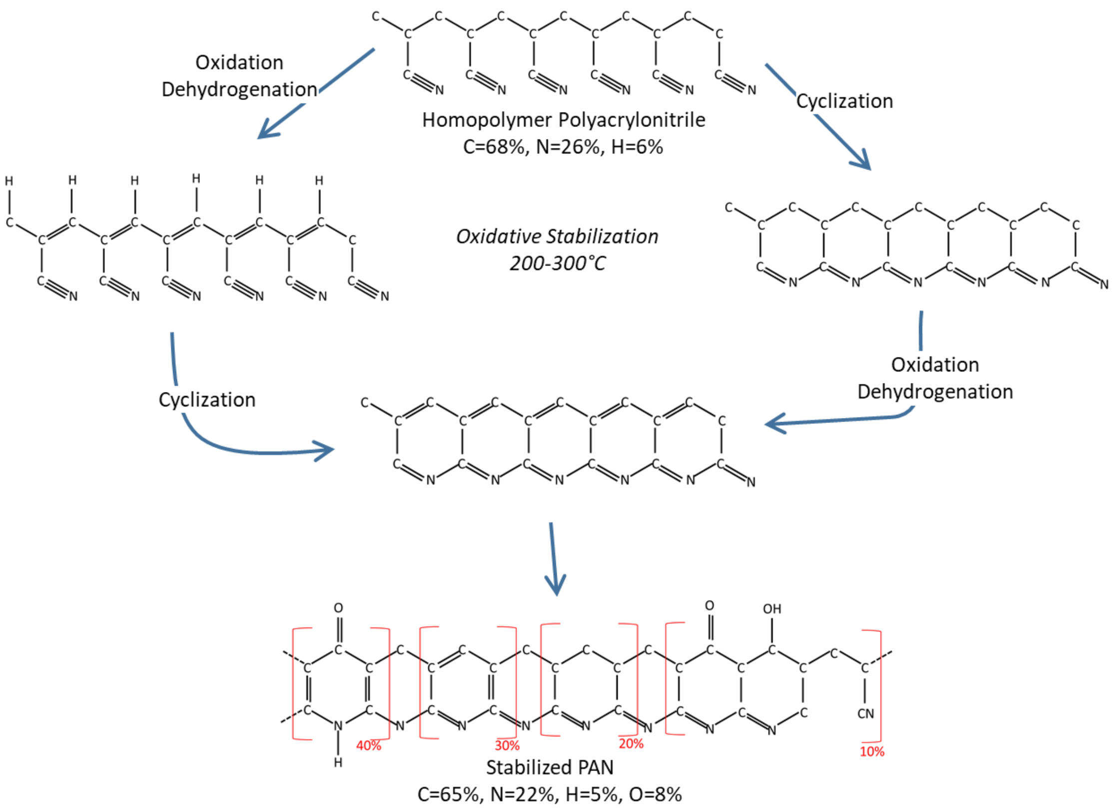

Figure 4.5 Polyacrylonitrile fiber stabilization chemical process.

Important considerations for polyacrylonitrile fiber stabilization include the temperature, temperature ramp rate, and duration. Previous studies for polyacrylonitrile fiber stabilization informed the experimental setup [120]–[122]. A Carbolite model ELF 11/23 chamber furnace was used to stabilize the as-spun polyacrylonitrile fibers into stabilized polyacrylonitrile fibers. Stainless-steel mesh with as-spun polyacrylonitrile fibers removed from the electrospinner were allowed to dry for 24 hours prior to placement into the furnace. The furnace was programmed for heating to 270 °C, which was anticipated as the optimal stabilization temperature [121]. Initially a heating ramp rate of 5 °C/min was programmed, however initial tests at that rate showed shrinking and tearing of the nonwoven media. The heating rate was reduced for subsequent iterations to 1 °C/min for a more even heating rate to shrinkage problems. Other authors have reported optimal heating rates between 2 °C/min and 5 °C/min [120]. The stabilization configuration is shown in Figure 4.6.

(a) (b)

Figure 4.6 Stabilization of flat media. (a) Chamber furnace. (b) Stabilized flat plate.

4.2.8 Polyacrylonitrile Nonwoven Media Characterization

Stabilized polyacrylonitrile nonwoven media detached easily from the stainless-steel wire mesh. The media was measured and weighed on a Sartorius digital scale as shown in Figure 4.7. A summary of solution, electrospinning and stabilization parameters is provided in Table 4.2.

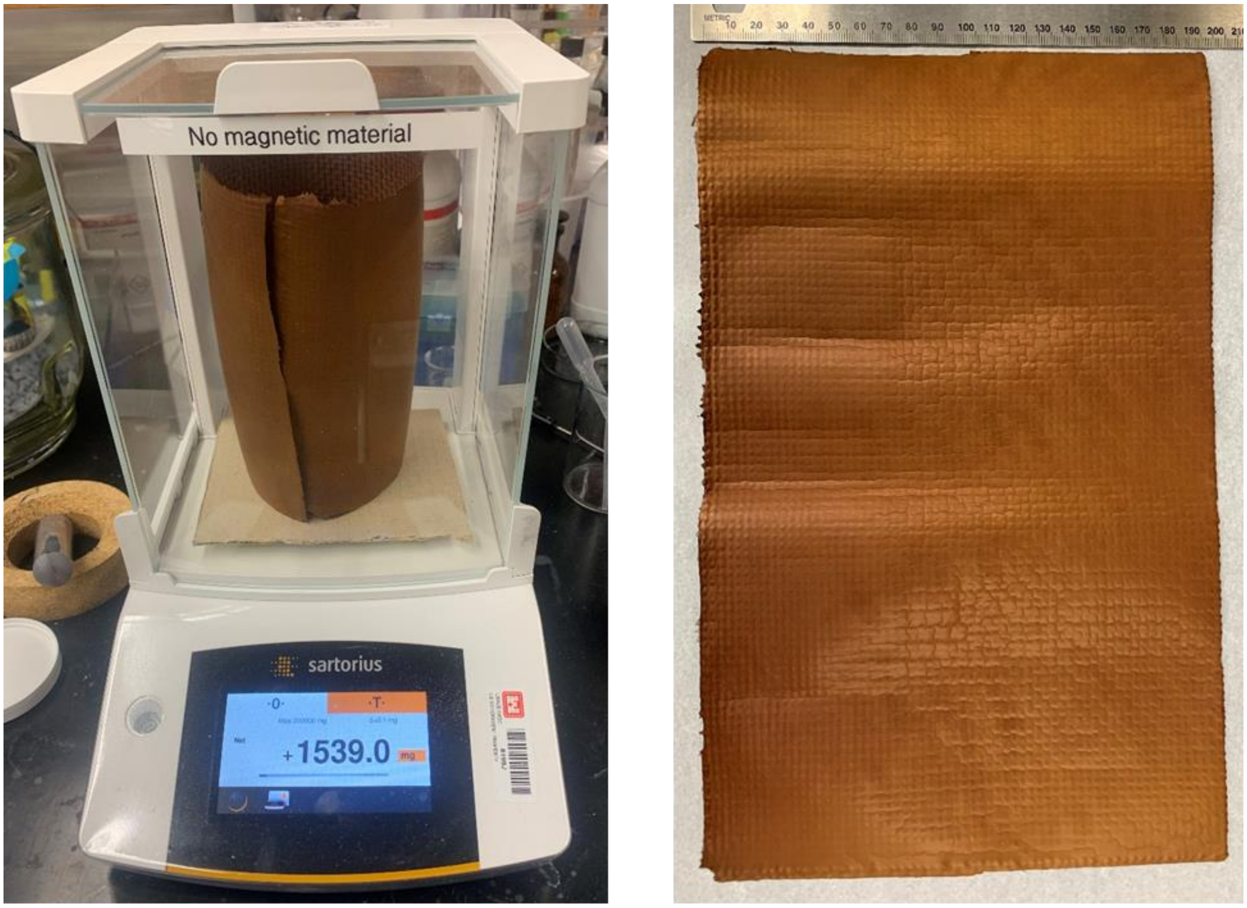

(a) (b)

Figure 4.7 Size and weight measurements of stabilized polyacrylonitrile media. (a) Detached media weight measurement on digital scale. (b) Size measurement.

Table 4.2 Summary of Solution, Electrospinning, and Stabilization Parameters

	1	2	3	4	5	6	7	8	9
Solution Details									
PAN (by weight %)	6.0	9.0	9.0	9.0	9.0	9.0	9.0	9.0	9.0
Graphene (solid %)	-	-	-	-	-	0.1	0.5	1.0	-
Graphene (solution %)	-	-	-	-	-	0.01	0.05	0.1	-
Electrospinning									
Orientation	Flat	Flat	Roller	Roller	Roller	Roller	Roller	Roller	Roller
Needle Gauge	23	23	23	23	23	21	21	21	21
Tip-to-collector (cm)	15	15	15	15	15	15	15	15	15
Electric Potential (kV)	20	20	25	25	30	30	30	30	30
Pump Rate (ml/hr)	0.8	0.9	1.1	1.1	1.1	1.5	1.5	1.5	1.5
Pump Time (min)	213	233	545	545	1091	800	800	800	1600
Roller Speed (rpm)	-	-	180	180	180	90	90	90	90
Total Deposition (ml)	2.84	3.49	10.0	10.0	20.0	20.0	20.0	20.0	40.0
Stabilization Details									
Stabilization Temp (°C)	270	270	270	270	270	270	270	270	270
Temp Ramp (°C/min)	5.0	5.0	1.0	1.0	1.0	1.0	1.0	1.0	1.0
Stabilization Time (min)	40	80	240	240	240	240	240	240	240
Resultant Mass									
Stabilized Mass (mg)	-	-	764.1	825.0	1257.3	1481.8	1554.9	1539.4	3433.0
Areal density (mg/cm^2)	-	-	1.194	1.289	1.965	2.315	2.430	2.405	5.364

4.2.9 Material Analysis

The as-received polyacrylonitrile was analyzed using thermogravimetric analysis (TGA) in a TGA 5500 (TA Instruments) to observe the degradation at a heating rate of 10 °C/min to 1000 °C. The change in weight indicates the elimination of moisture and volatile components from the substance at various temperatures. The as-received polyacrylonitrile began losing mass at approximately 270 °C and lost nearly 20% of its mass within the range of 200°C to 500°C. Figure 4.8 shows the TGA analysis with the derivative line in green. This graph confirms the target stabilization temperature of 270°C.

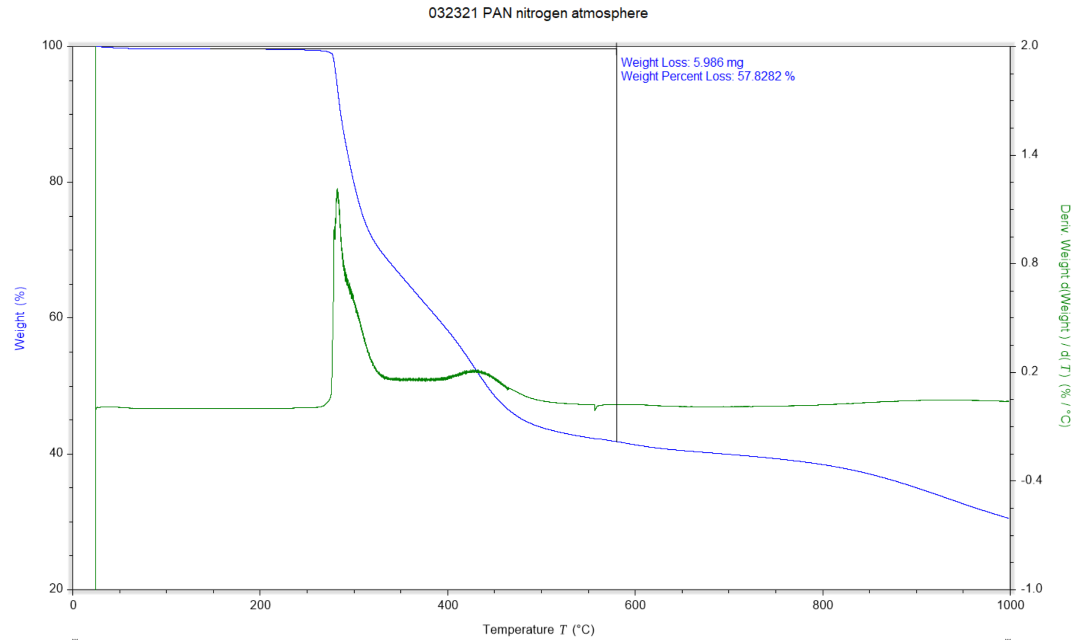

Figure 4.8 Thermogravimetric analysis of polyacrylonitrile.

4.2.10 Air Filtration Testing

Air filtration testing was performed at the Institute for Clean Energy Technology (ICET), Mississippi State University, using a TSI model 8130A automated filter tester. Polyalphaolefin (PAO) was used as the challenge aerosol for testing, with estimated particle size distribution set to mean diameter of 0.2 um with geometric standard deviation of 1.6. The flat media filtration test area was circular cross section with a diameter of 114.3 mm and area of 102.6 cm^2. The nominal volumetric flow rate was set to 32.0 L/min with standard room temperature, air pressure, and relative humidity, resulting in a projected face velocity of 5.198 cm/s through the filter media.

4.3 Results

4.3.1 As-Spun Nonwoven Fibrous Media

The 6% and 9% solutions of polyacrylonitrile electrospun easily and uniformly onto the stainless-steel wire mesh grounded collector. Prior to electrospinning the solutions were tested by hand with both 21-gauge and 23-gauge needle sizes, both of which flowed easily. However, efforts to electrospin the 12% polyacrylonitrile solution were terminated because the solution was too viscous to push through an 18-gauge needle.

An aluminum fiber span gauge with various hole sizes was used to observe the uniformity of electrospun media as shown in Figure 4.9(a) below. Both the six percent and nine percent solutions covered all hole sizes of the span gauge indicating there would be no trouble spanning the 20-gauge and 8-gauge stainless-steel woven wire meshes. The fiber uniformity over the span gauge indicated the solution will spin effectively on smaller gauge wire meshes with even larger gaps.

(a) (b) (c)

Figure 4.9 Resulting nonwoven fiber medium. (a) Fiber span gauge. (b) As-spun polyacrylonitrile fibers. (c) Intact stabilized polyacrylonitrile fiber media.

The as-spun polyacrylonitrile fibrous media was white in color and covered the flat mesh and cylindrical mesh. The roller collector resulted in a more uniform distribution of fibers than the flat mesh connector, which was attributed to differences in the electromagnetic field of the flat mesh. Stabilizing the polyacrylonitrile media resulted in a dark brown shade. Figure 4.10 compares resulting polyacrylonitrile nonwoven media as spun and as stabilized.

(a) (b)

Figure 4.10 Stabilization of cylindrical media. (a) As-spun polyacrylonitrile fiber media. (b) Stabilized polyacrylonitrile media.

4.3.2 Effects of Stabilization

Prior to stabilization, the white polyacrylonitrile fibrous media exhibited the physical characteristics of spider web and it was not possible to detach the media from the stainless-steel mesh without tearing and damaging the media. After stabilization, the media exhibited the physical characteristics of a thin sheet of paper and was easily detached from the stainless-steel mesh. Figure 4.11 illustrates the physical characteristics of as spun and stabilized polyacrylonitrile fibrous media.

(a)

(b)

Figure 4.11 Comparison of as-spun media with stabilized media. (a) Side-by-side comparison. (b) Close up view of as-spun polyacrylonitrile fibers.

Experimentation determined the delicacy of the stabilization process. The stabilizing temperature was set at 270 °C for all iterations. However, the temperature ramp rate and stabilization duration were parameter which were adjusted. If the nonwoven polyacrylonitrile media was not exposed to the stabilization temperature for a long enough duration, the color was lighter. If the temperature ramp rate was set too high, the media tore from the effects of shrinkage. Figure 4.12 shows the effects of a shortened stabilization duration and excessive temperature ramp rate. The optimal temperature ramp rate was experimentally determined as 1 °C/min, while the stabilization duration was experimentally determined as 240 minutes after reaching the 270 °C temperature.

(a) (b) (c) (d)

Figure 4.12 Effects of stabilization. (a) A shortened 120-minute duration resulted in partial stabilization. (b) An excessive 720-minute stabilization resulted in tearing. (c, d) An excessive temperature ramp rate of 5 °C/min resulted in tearing.

4.3.3 SEM and Optical Imaging of Fiber Media

The resultant fibers were photographed using a Keyence VHX-7000 optical microscope at 2000 zoom. The resulting imagery indicates the stabilized polyacrylonitrile fibers were uniform and continuous. For comparison, an SEM image of typical glass fiber filter paper is shown as Figure 4.13. Compared to the glass HEPA filter fibers, the stabilized polyacrylonitrile fibers are significantly more uniform and continuous.

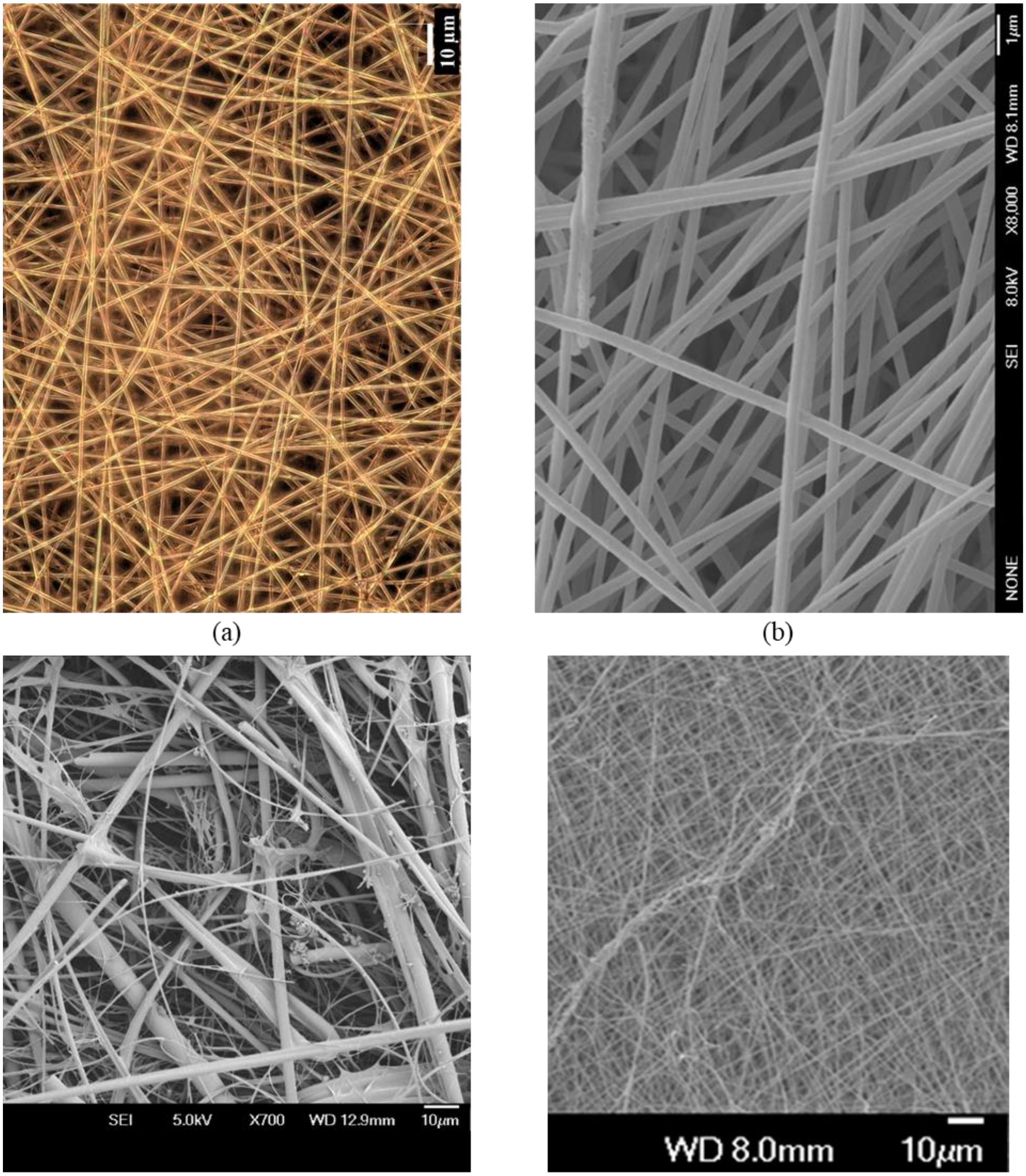

Figure 4.13 Optical and SEM imagery. (a) Optical image stabilized polyacrylonitrile at 2000 zoom. (b) SEM image of stabilized polyacrylonitrile at 8000 zoom. (c) Nonwoven glass HEPA media at 700 zoom. (d) Comparative stabilized SEM media.

4.3.4 Air Filtration Testing

Stabilized polyacrylonitrile nonwoven filter media samples were tested at MSU ICET using a TSI8130 air filtration test stand. Each sample was subjected to five consecutive tests without removal from the testing machine, which required the test holder to open and close five times on each media sample. Due to the delicacy of the samples, the opening and closing of the test machine resulted in visible damage to the media which may have affected the filtration performance. Figure 4.14 shows the air filtration testing in progress.

(a) (b)

Figure 4.14 Air filtration testing at MSU ICET. (a) TSI8130 test machine setup and preparation. (b) Air filtration test in progress.

The American Society of Mechanical Engineers (ASME) Code on Nuclear Air and Gas Treatment (AG-1) provides standards for which to evaluate air filtration efficiency and air pressure drop across the filter for nuclear grade HEPA filters [36]. Typical air filtration testing is performed at a flow velocity of 2.5 cm/s. Data obtained from filtration testing for two samples is compared to ASME AG-1 standards in Table 4.3. While neither sample achieved AG-1 HEPA filter standards for minimum air filtration efficiency and maximum air flow resistance, the results indicate potential for achieving HEPA standards by improving the production parameters of the electrospun stabilized polyacrylonitrile. The tested samples were thin and delicate, which led to problems with testing. The performance of the stabilized polyacrylonitrile filter media can be improved with additional thickness and by combining layers. The filter viability can also be improved by producing composite filter media with combined larger diameter fibers for structural strength and smaller diameter nanofibers for air filtration.

Table 4.3 Comparison of Filtration Results to ASME AG-1 Standards

	Face Velocity (cm/s)	Penetration (%)	Efficiency (%)	Flow Resistance (Pa)
HEPA Standard	2.50	0.03	99.97	320.0
Solution 1	5.15	2.17	97.83	512.9
Solution 3	5.17	2.38	97.62	157.9

The filtration testing showed a general increasing trend of penetration while the flow rates remained constant. The first sample showed an initial filtration efficiency of 99.8% which decreased to an efficiency of around 98% after the fifth test. The second sample was untestable due to the delicate condition of the media. The third sample showed an initial filter efficiency of 97.8% which decreased only slightly to 97.6% after five tests. The pressure drop measurements across each media sample indicated an increasing trend of air flow resistance through five tests. The increasing flow resistance and increasing penetration are anticipated, as the filter materials become loaded with collected aerosol during filtration testing. Pressure and penetration data are depicted in Figure 4.15.

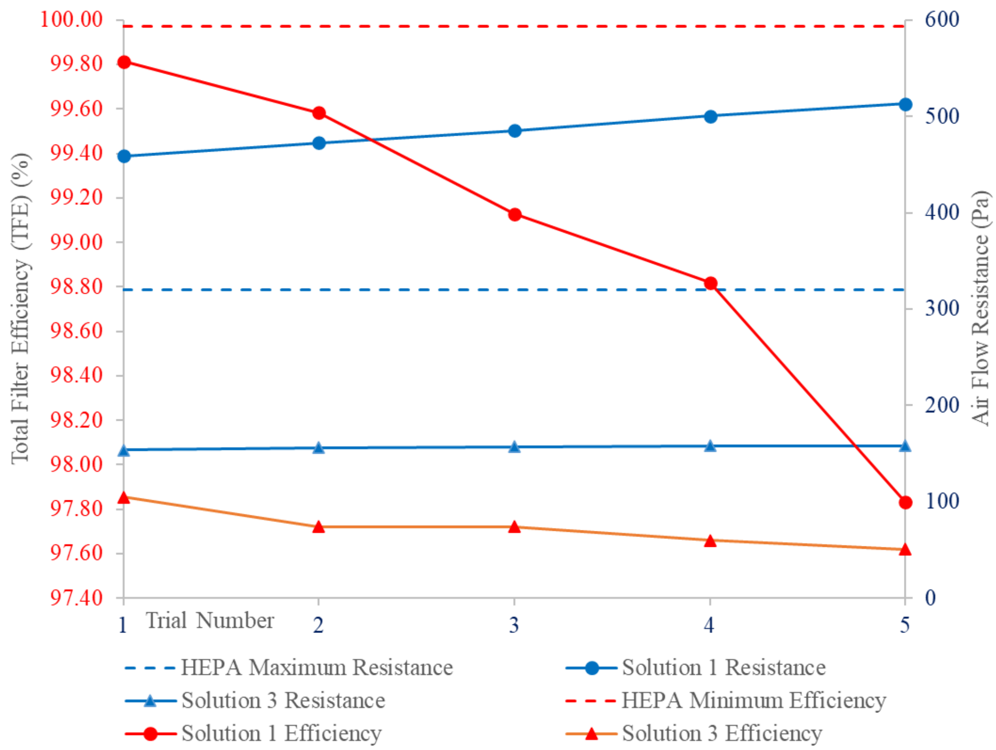

Figure 4.15 Air filtration test results.

4.4 Chapter Summary

The results of this effort indicate potential to create nonwoven nanofibrous air filtration media by electrospinning and stabilizing polyacrylonitrile. The solutions of polyacrylonitrile dissolved in DMF were consistent, stable, and easy to electrospin. The mixed solutions, sealed in air-tight containers, maintained consistent properties with no precipitation or hardening over an extended duration. The six and nine percent solutions flowed evenly through the electrospinning syringe. Graphene supplements were easily added to the solutions and easily electrospun with polyacrylonitrile and DMF. The nozzle spray patterns were consistent throughout electrospinning, from the first minute to the last. The nonwoven nanofibrous coverage on stainless-steel wire mesh was uniform and consistent, especially with the roller configuration.

The imagery comparison of the electrospun polyacrylonitrile fibers to the HEPA filter glass fibers indicates the electrospun fibers are much more uniform and continuous than the glass fibers. As seen in Figure 4.13(c), the glass HEPA filter media ranges from fiber diameters of approximately 500 nm to 7 µm while the electrospun polyacrylonitrile fibers are uniform and consistent at approximately 1 µm. The glass fiber media also requires binder agents that affect the uniformity of the fibers, the filtration efficiency, and the pressure drop. Electrospun and stabilized polyacrylonitrile filter media has no requirement for similar binder agents.

The result of this effort indicates excellent viability for electrospun and stabilized polyacrylonitrile-graphene nonwoven air filter media. The authors recommend further research, experimentation, and testing of electrospun and stabilized polyacrylonitrile-graphene nonwoven nanofibrous media. Carbonization of polyacrylonitrile-graphene media may potentially create air filter materials that effectively adsorb dangerous airborne VOCs while also removing $PM_{2.5}$ particulate matter from the air.

Graphene-embedded stabilized and carbonized polyacrylonitrile nanofibers have additional potential applications beyond air filtration and VOC adsorption based on superior mechanical, chemical, and electrical properties. The increased surface area ratio and electrical conductivity gained from graphene-embedded carbon fibers are desirable characteristics for superconducting materials needed for energy storage and transmission applications [104]. Graphene-embedded carbon fibers have excellent potential for a growing list of applications to include air filtration, VOC adsorption, water purification, supercapacitors, energy conversion, and energy storage.

CHAPTER V

DEVELOPMENT OF DIGITAL TWIN GEOMETRY FOR AIR FILTER MEDIA[3]

Computational modeling of air filtration is possible by replicating nonwoven nanofibrous meltblown or electrospun filter media with digital representative geometry. This chapter presents a methodology to create and modify randomly generated fiber geometry intended as a digital twin replica of fibrous filtration media. Digital twin replicas of meltblown and electrospun filter media are created using computer program scripting and Ansys SpaceClaim. The effect of fiber stiffness, represented by a fiber relaxation slope, is analyzed in relation to resulting filter solid volume fraction and thickness. Contemporary air filtration media may also be effectively modeled analytically and tested experimentally in order to yield valuable information on critical characteristics, such as overall resistance to airflow and particle capture efficiency. An application of the single fiber efficiency model is incorporated in this chapter to illustrate the estimation of performance for the generated media with an analytical model. The resulting digital twin fibrous geometry compares well with SEM imagery of fibrous filter materials. This chapter concludes by suggesting adaptation of the methodology to replicate digital twins of other nonwoven fiber mesh applications for computational modeling, such as fiber reinforced additive manufacturing and composite materials.

[3] Content from this chapter is published in a journal article. Beckman, I.P.; Berry, G.; Cho, H.; Riveros, G. Digital Twin Geometry for Fibrous Air Filtration Media. Fibers 2021, 9, 84. https://doi.org/10.3390/fib9120084

5.1 Introduction

Contemporary HEPA filters are manufactured with melt-blown polypropylene or glass fibers into a mesh of non-woven, randomly aligned, small-diameter fibers [75]. Overall filtration efficiency and flow resistance are key aspects of a filter. Successful analytical models correlate filtration efficiency E_{F} and air flow resistance ΔP to filter thickness t, solidity α_{f}, fiber radius and diameter $r_{\mathrm{f}}\ and\ d_{\mathrm{f}}$, volumetric air flow rate Q, filter face area A, and air viscosity η. The diameter of fibers not only impacts the collection efficiency of airborne particles, but also the resistance to airflow of the filtration media as well. These concepts are illustrated in Chapter III. For the same number and length of fibers within a given volume, an increasing fiber diameter will have the effect of increasing the solidity of the media. However, the fiber diameter and solidity are not expressly dependent on each other and thus are typically considered as independent characteristics and variables of the filtration medium. From the analytical equations, flow resistance will increase with increasing solidity and decrease with increasing fiber diameter. Furthermore, a decrease in the fiber diameter results in an increase in overall collection efficiency.

Analytical and empirical models of air filtration media are important tools in predicting filtration efficiency, flow resistance, and filter service life [123]–[126]. However analytical models are not a perfect representation of reality and often struggle in their ability to describe the stochastic nature of filtration [127]. Analytical models use structured geometry to represent fibrous media, such as an ordered array of fibers oriented parallel to each other and perpendicular to the airflow. An example of this is the Kuwabara cell model [85], described in the Chapter III. The creation of air filter media through a melt blowing or electrospinning process, however, results in random deviations from an ideal homogenous structure which yields non-uniform and tortuous airflow channels. Analytical models typically use ordered fiber geometry as a foundation, and then often account for the inhomogeneity of the fibrous materials through empirical correlation factors and variables such as an effective fiber diameter, inhomogeneity factor, or effective fiber length [81], [128]. It is important to note the differences that accounting for the inhomogeneity in the filtration media has regarding the performance of the filtration media.

Computational modeling of air filtration media is important to complement experimental and analytical efforts. Computational modeling presents an ideal toolset to address the difficult nature of describing the performance of fibrous filtration media and the dynamic nature of the filtration process. The stochastic nature of filtration may be easily incorporated into computational simulations, as well as other difficult concepts such as particle shadowing, where they may be accounted for automatically [127]. Advances in high performance computing have made computational fluid dynamics (CFD) a viable tool for air filtration research. A prerequisite of CFD modeling is the generation of digital "twin" geometry that closely replicates actual filtration media. Without a realistic model of the fibrous geometry, the results from a CFD simulation should be questioned regarding their validity and accuracy. The purpose of this chapter is to present a methodology for constructing digital twin geometry for nonwoven fibrous air filtration media, intended for use with computational modeling tools such as CFD and finite element method (FEM) software.

5.2 Virtual Three-Dimensional Geometric Models

Efforts to build realistic digital twin geometry has progressed significantly over the past two decades. A summary list is provided in Table 5.1 for convenience. In 2005, Faessel et al. presented a method of generating a three-dimensional model of curved fibers to represent the random layout of cellulosic fibrous networks in low density wood-based fiberboards [129]. The authors generated director lines and curvature points as objects in Visual Toolkit (VTK) software and extruded a radius along the curve to form fibers, where the objects were converted into mesh for FEM analysis. Wang et al. in 2006 and 2007 developed a three-dimensional virtual model for depositing straight fibers horizontally onto one another without allowing penetration [94], [130]. Maze et al. in 2007 developed a three-dimensional model of compressed fiber webs with bending fibers that prevented inter-fiber penetrations throughout the media, using square cross-sections to represent spun bonded media [131]. Subsequent work by the same authors enabled bending by splitting the straight fibers at intersections and angling downward on both sides of the intersection [132]. Hosseini and Tafreshi developed a C++ computer program in 2009 to generate and stack fiber mesh layers to form a three dimensional filter media model [133]. Their model allowed interpenetration of fibers with an assertion that the flow resistance and filtration efficiency are not affected by the interpenetrations as long as the exact porosity is accurately calculated. Fotovati et al. in 2009 developed a method using a FORTRAN code to construct a three dimensional model of fibers with specific in-plane orientation [134]. Fotovati's paper arranged straight unbroken fibers of identical diameter with in-plane alignments of 15°, 30°, and 45° with through-plane alignment of 0°, for the purpose of studying the effect of fiber alignment on filtration efficiency. In 2013, Saleh et al. developed a method of producing three-dimensional geometry of disordered fibrous structures to study the effects of dendrite formation within nonwoven air filtration media [124]. Saleh's model generated random two-dimensional in-plane fiber orientations and subsequently stacked the planes to form the three-dimensional geometry similar to the previously cited work of Hosseini and Tafreshi. In 2016, Karakoc et al. modeled composite structure fiber networks as planar projections and intersections of rectangular cross-section shaped fibers [135]. Finally, in 2019 Yousefi and Tafreshi made use of computer program scripting and C++ programming to replicate electrospun fiber materials using Kelvin-Voight method of representing fibers as a series of springs and dampers [136], [137]. The current effort presented in this work is intended to complement these accomplishments by offering a simple methodology to produce digital fibrous geometry.

Table 5.1 Significant Efforts Constructing 3D Digital Twin Air Filter Geometry

Author	Year	Description
Faessel et al [129]	2005	3-D model generated with Aphelion software and Visual ToolKit
Wang et al [130]	2007	3-D model with straight cylinders
Maze et al [131]	2007	3-D model using stacked layers of square cross-sectional fibers
Tafreshi et al [138]	2009	3-D model generated as Boolean voxel-based geometry using GeoDict software
Fotovati et al [134]	2010	3-D model generated with FORTRAN code
Hoseinni and Tafreshi [133]	2010	3-D model generated with C++ code using randomness algorithm
Gervais et al [139]	2012	Bi-modal fibrous media generated as voxel-based geometry using GeoDict
Saleh et al [124]	2013	3-D model generated with C++ code using randomness algorithm
Mead-Hunter et al [140]	2013	3-D model generated using a custom Blender script
Grothaus et al [141]	2014	3-D surrogate air-lay process with stochastic differential equations
Karakoc et al [135]	2017	Stochastic straight fibers trimmed to fit the domain, coded in Mathematica
Abishek et al [142]	2017	Generation of straight and curved fibers from line segments in Blender
Yousefi and Tafreshi [136]	2020	Physics-based modeling technique to simulate electrospun fibrous media with embedded spacer particles

5.3 Digital Twin Model Development

Computational modeling of filter media begins with geometry. SpaceClaim, a fundamental module of Ansys Workbench, was used to generate the solid model. Cylindrical fibers can be created in SpaceClaim by specifying coordinates for the fiber start point, end point, and a point on the fiber surface perpendicular to the end point. While the graphical user interface is convenient to visualize geometry, SpaceClaim also has the ability to utilize a scripting feature capable of importing a text file list of coordinates for the construction of fibers. As illustrated by

Figure 5.1, the data describing a mat of randomized fibers can be generated with a simple computer program script and subsequently output as text file for use in SpaceClaim.

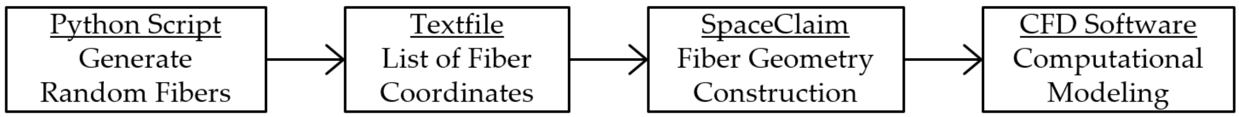

Figure 5.1 Methodology for random fiber generation and filter geometry construction.

A simple method for constructing three-dimensional filter geometry starts with a two-dimensional model to represent a square cut from the filter paper. Fiber endpoints are designated within the square with x and y coordinates. To achieve a random orientation for fibers originating and terminating at the edge of the square, a random number is drawn between 0 and 4 and traced clockwise around the perimeter of the square as shown in Figure 5.2b. The fiber starting point is designated at the x and y coordinates at that particular point on the perimeter. The fiber end point is designated in a similar method however to avoid fibers that start and end on the same edge of the square, a random number is drawn between 0 and 3 and added to the next vertex clockwise along the perimeter. The two-dimensional square is developed into three-dimensional media by randomizing the z coordinates of the fiber starting and ending points within a designated media thickness. The diameter of each individual fiber is a random number driven by a user-defined distribution, such as a normal or log-normal distribution. Individual fiber volumes are calculated by the length and diameter of the fiber within the defined volume representing the total volume of the geometry model. Comparing the fiber volume to the total volume formed by the square and designated model thickness provides fiber solidity. This process is looped to add fibers until the desired solidity is achieved.

Figure 5.2a shows a Scanning Electron Microscope (SEM) image of a generic melt-blown glass HEPA filter media sample. The goal for generating a realistic fiber geometry model of filter media is to replicate this SEM image as closely as possible with a digital twin. From an inspection of Figure 5.2a, it may be seen that the glass fibers have broken ends and a bimodal distribution of fiber diameter sizes, consisting of a few very large fibers and many smaller fibers. By adjusting the input parameters of the computer program script, digital geometry can be generated that closely resembles the SEM image. The digital geometry in Figure 5.2c was produced with similar dimensions as the SEM image, with side length 100 µm, thickness of 20 µm, 50% of the fibers are terminating inside the volume, 75% of the fibers have diameters between 200 and 600 nm while 25% of the fibers have diameters between 2.0 and 3.5 µm.

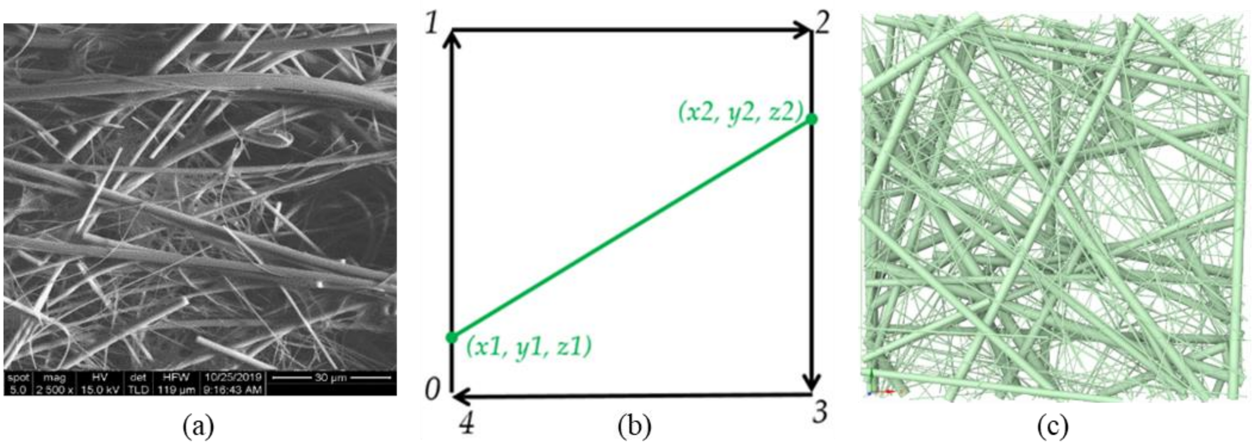

Figure 5.2 Fiber nonwoven mesh generation. (a) SEM image of melt-blown glass fiber HEPA filter. (b) Random selection of fiber endpoints along perimeter. (c) Resulting digital twin replica.

One noted flaw of the result shown in Figure 5.2c is that the fibers are allowed to interpenetrate since there is no control of the fiber orientation in comparison with previously inserted fibers inside the volume. This creates complexities for meshing software and may not result in a realistic portrayal of real filter material. A solution to this problem is to account for previous fibers already placed within the volume by evaluating intersection points with a newly generated fiber and breaking the new fiber into segments. These new fiber segments are adjusted to new coordinates to lay on top of previous fiber geometry. This method is depicted in Figure 5.3 below. A new random fiber is designated with *x* and *y* coordinates for the endpoints as shown in Figure 5.3a. The fiber can be thought of as dropping into the page. The algorithm evaluates the list of previous fiber segments and determines coordinates of potential intersecting points as shown in Figure 5.3b. In the illustrated example there are eight potential intersecting points represented by letters *a* through *h*. Now rotating the box to view the same new fiber dropping into the box from top to bottom of the page (by rotating the z axis in Figure 5.3c to where the y axis was in Figure 5.3b), potential intersecting points are evaluated based upon their height and distance along the fiber. A maximum fiber slope, designated as the relaxation slope, is specified to enable fiber flexibility to conform to the necessary shape indicative of realistic materials. This is illustrated below in Figures 5.3c and 5.3d. Starting from the highest potential intersecting point (point *c* in the example shown), the maximum relaxation slope is traced in both directions along the fiber. Potential intersecting points occurring below the maximum slope line are eliminated. In this illustration, points *a*, *f*, *g*, and *h* are retained while points *b*, *d*, and *e* are eliminated. The algorithm then evaluates the next highest potential intersecting point (point *g* in this illustration) and repeats the process. As depicted in Figure 5.3d, point *f* which was earlier retained is now eliminated as it falls below the maximum slope line from point *g*. The algorithm continues for all intersecting points and results in a final list (points *a*, *c*, *g*, and *h* in this illustration). The finalized lines form the profile of the new fiber broken into segments. Segment break points are calculated at the intersections as shown in Figure 5.3e. In this illustration, the fiber is broken into eight segments with segment endpoints specified at the points where the segments touch.

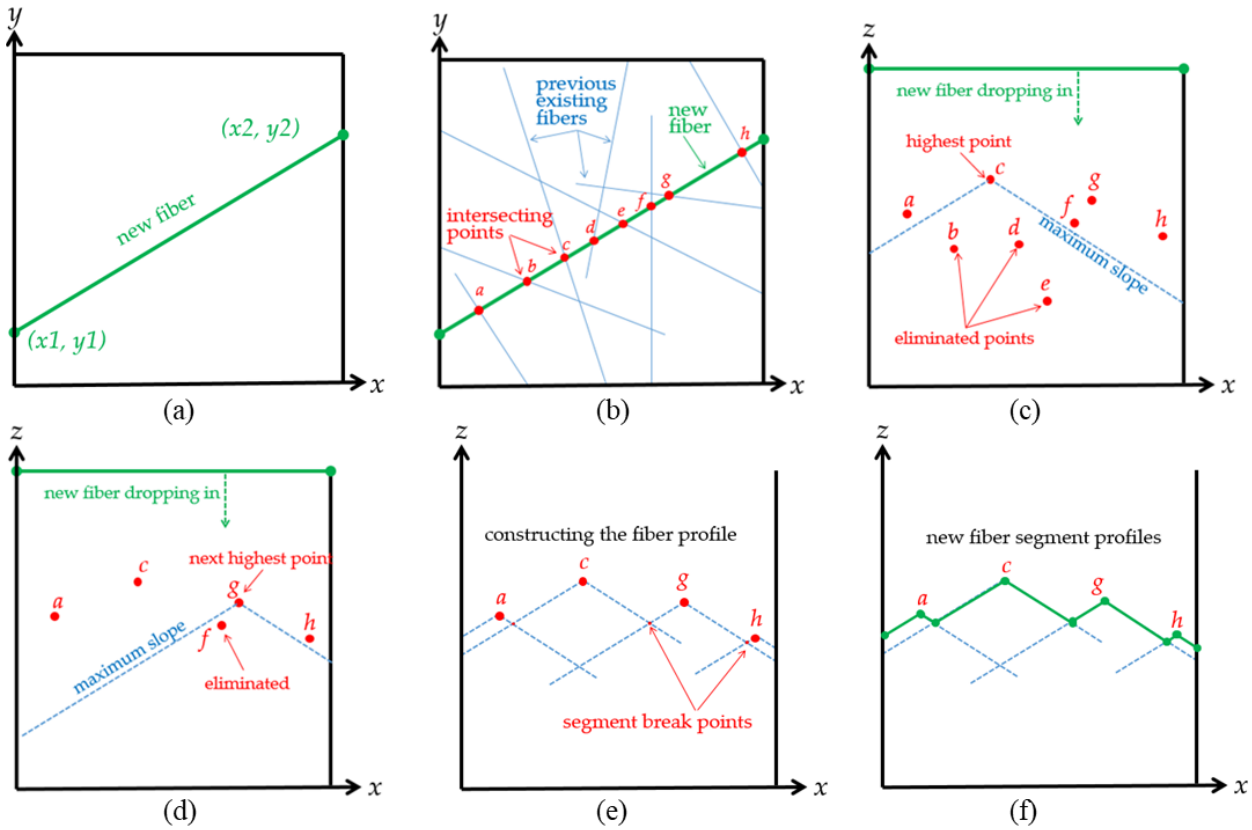

Figure 5.3 Process for breaking a new fiber into segments to conform to previous geometry. (a) New random fiber specified starting and ending points. (b) Potential intersection points are evaluated below the fiber. (c) Height of potential intersecting points are evaluated against maximum slope. (d) Potential intersecting points eliminated that fall below the maximum slope line. (e) Fiber segment profile is constructed from the remaining maximum slope lines. (f) New fiber segment starting and ending points are finalized.

The height (*z* coordinate) is determined for each segment end point by adding the radii of the new fiber segment and the previous fiber segment responsible for the spatial adjustment. Additional spacing between fibers can be added by increasing the *z* coordinates for the new fiber segment end points. Figure 5.4 illustrates the process of closing the newly segmented fiber sections with a spherical joint between each new segment, resulting in a continuous, solid fiber.

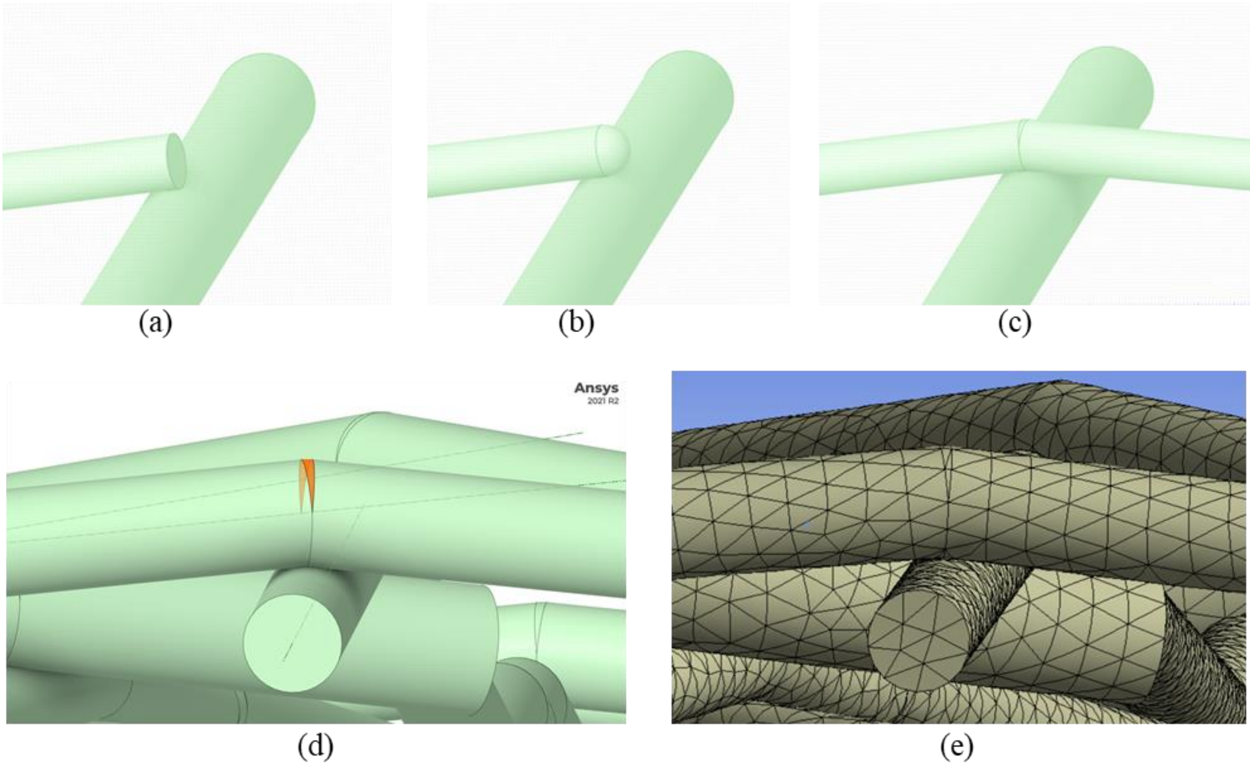

Figure 5.4 Spherical joints at the fiber segment connections. (a) New fiber segment resting on previous fiber. (b) Spherical joint at segment endpoint. (c) Continuation from joint. (d) Completed fiber with highlighted joint. (e) Completion of meshing.

By eliminating fiber interpenetrations, the digital twin nonwoven fibrous geometry is much easier to mesh since the meshing software can take advantage of straight fiber segments with cylindrical joints as shown in Figure 5.5 below.

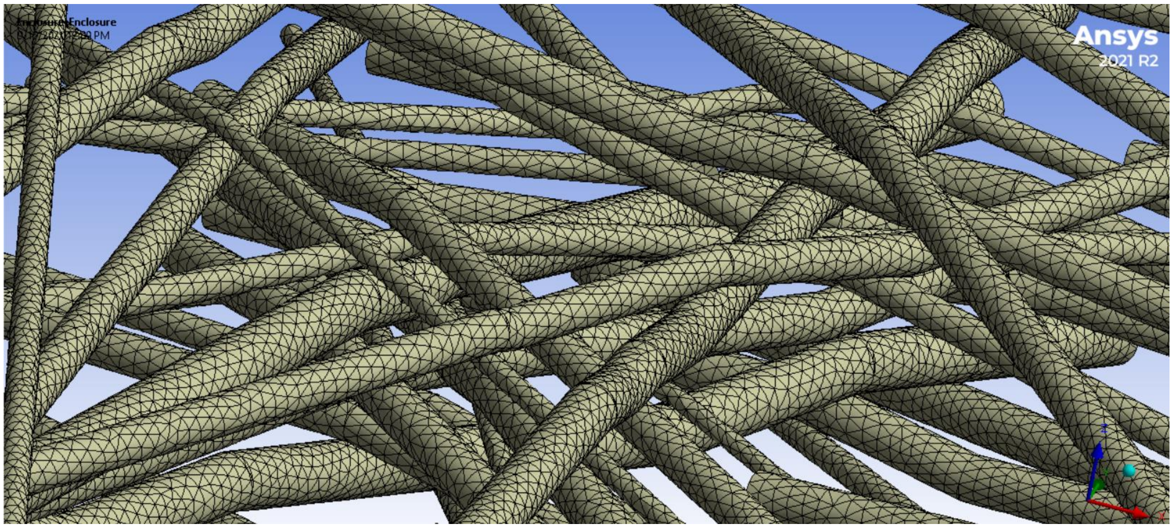

Figure 5.5 Non-intersecting fibers meshed with Ansys Mechanical.

5.4 Results: Filter Solidity, Face Coverage, Thickness, and Flow Resistance

The solidity, thickness, and face coverage are parameters that indicate a quantity of fibers in a filter medium. Thickness is a one-dimensional measurement. Face coverage is a two-dimensional measurement of the fiber profile normal to the direction of air flow, comparing the cross-sectional coverage of the fibers with the cross-sectional area of the box. The solidity is a three-dimensional concept, defined as the ratio of the total volume occupied by fibers to the total volume of the media. Figure 5.6 shows an example of nonwoven fibrous air filter media created with the digital twin geometry script, constructed into solid geometry with SpaceClaim, and meshed with Ansys Mechanical. The available input parameters used to adjust the digital twin geometry to match SEM images include face coverage, relaxation slope, distribution of fiber radius, and percentage of fibers that are broken inside the box. The resulting digital twin geometry can be meshed and then input into CFD software for analysis.

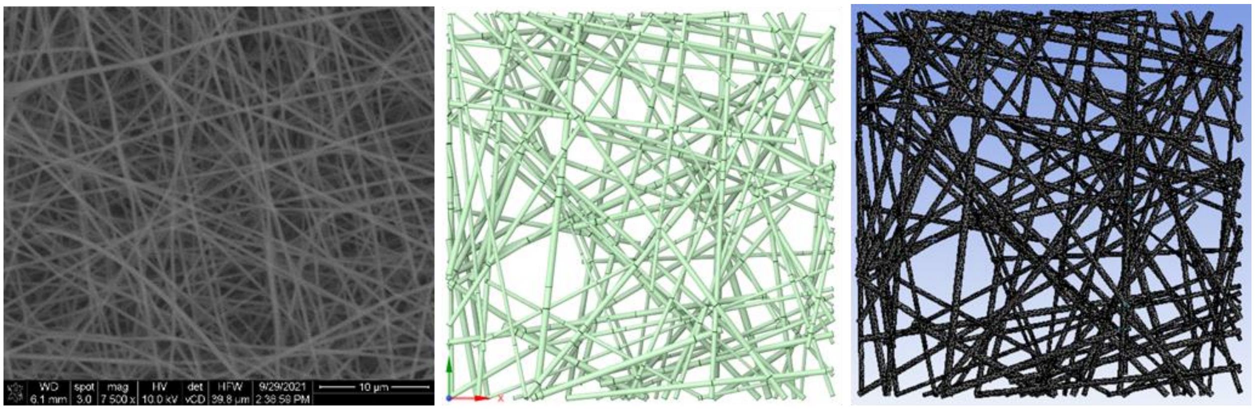

(a) (b) (c)

Figure 5.6 Non-intersecting air filter media geometry. (a) SEM image of electrospun filter media. (b) Top view as created with SpaceClaim. (c) Filter media meshed by Ansys Mechanical.

The algorithm illustrated in Figure 5.3 eliminates the problem of fiber interpenetrations illustrated in Figure 5.2. It is worth noting that the face coverage, media thickness, or flow resistance can be used as design criterion while solidity becomes a dependent parameter. The algorithm can continually add fibers on top of the filter until the desired face coverage is achieved, while filter thickness and solidity become dependent on the face coverage. Fiber flexibility is a significant factor in this method to determine the thickness and solidity, which can be adjusted with the maximum relaxation slope specified in the model. Figure 5.7 shows a profile view of a model built to a specified face coverage of 1.0, given various relaxation slope allowance from straight fibers with 0% slope to bent fibers with 25% slope. The solidity of these models varies from about 1.80% to 12.0% while the thickness varies from about 132 nm to 17 nm. This illustrates the effect of relaxation slope on the overall filter thickness and solidity.

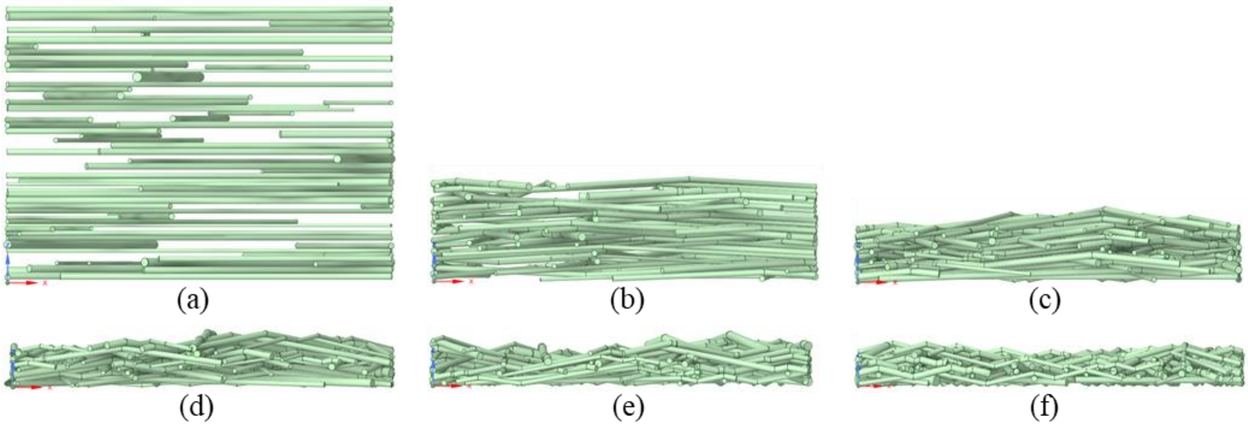

Figure 5.7 Profile view of fiber geometry with varied maximum slope. (a) Straight fibers (0% slope). (b) 5% Slope. (c) 10% Slope. (d) 15% Slope. (e) 20% Slope. (f) 25% Slope.

Figure 5.8 shows the relationship between the specified fiber relaxation slope and resulting filter thickness and solidity for a given face coverage area. This analysis was performed on a 100 µm x 100 µm area with mean fiber diameter of 700 nm and a face coverage of 2.0. It is worth noting here that since the generation of geometry is completely random, the characteristics of the generated media, such as solidity, will be unique for every generated sample, even with identical inputs. If the filter solidity, filter thickness, and fiber diameters of a specific piece of fibrous medium are known, the digital twin geometry can be iteratively tuned to match its parameters by adjusting the relaxation slope or adding fiber spacing between fibers.

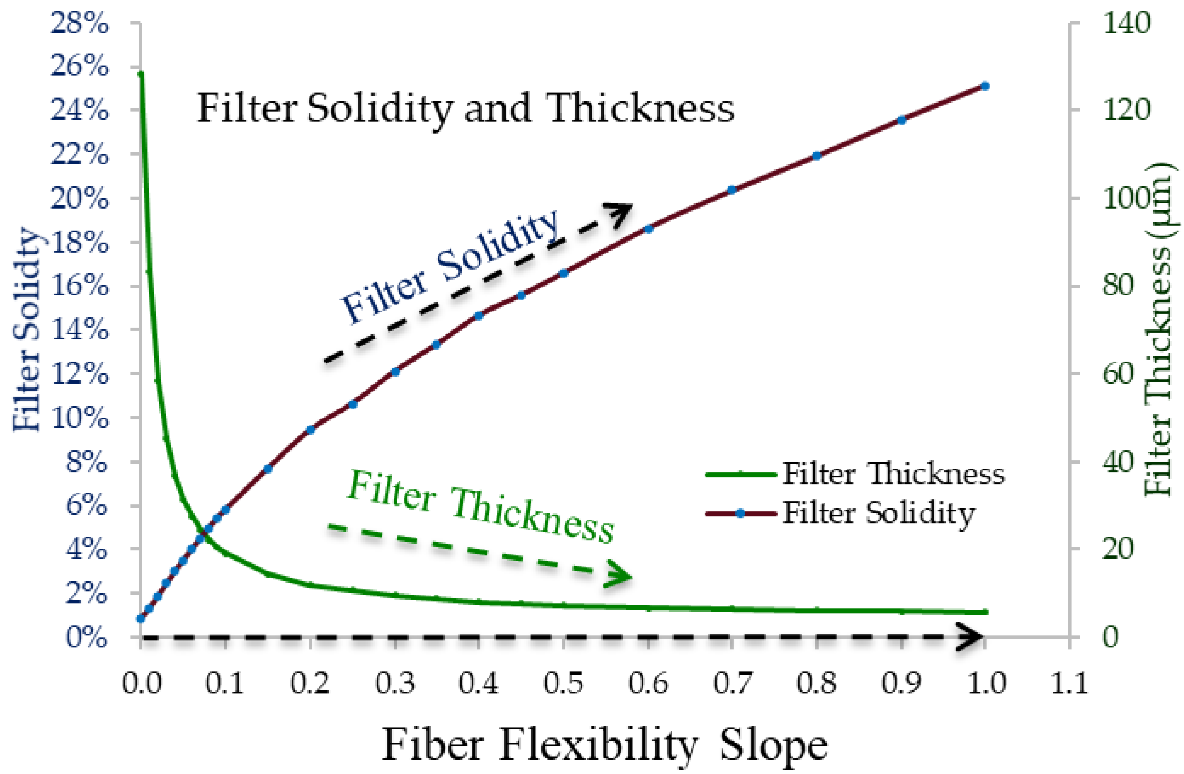

Figure 5.8 Filter solidity and thickness vs. maximum slope of segments. Data represents mean values of samples drawn at each fiber relaxation slope.

In addition to face coverage area, the overall filter thickness can be used as design criteria by utilizing a while loop to continually add fibers on top of the previous layers until the desired thickness is achieved. A simple method is to measure filter thickness by the height of the tallest fiber endpoint. As expected, changes to filter solidity and filter thickness by adjusting the fiber flexibility slope lead to corresponding changes to total filter efficiency and air flow resistance as shown in Figure 5.9.

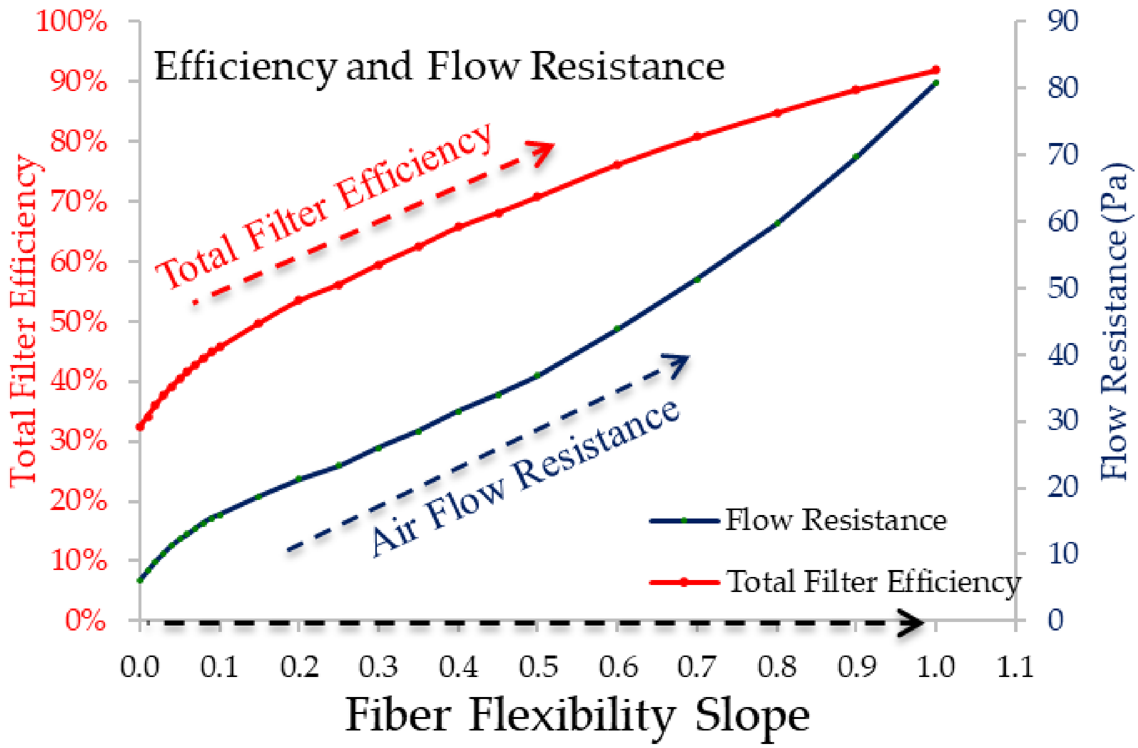

Figure 5.9 Total filter efficiency and air flow resistance vs. maximum slope of segments.

5.5 Discussion: Analytical Modeling of Digital Twin Filter Geometry Performance

The SFE model is a well-known analytical tool that has been traditionally prevalent in literature which may be used to estimate the total filtration efficiency of filter media based on a calculated particle capture efficiency of a single, isolated fiber positioned perpendicular to the direction of flow [8,27,28]. Yousefi and Tafreshi in 2020 demonstrated the use of the SFE model to predict the filtration efficiency, flow resistance, and FOM of digital twin electrospun filter media embedded with spacer particles [136]. Using their method as a guide, the SFE model can be applied to predict the filtration efficiency, flow resistance, and FOM for our digital twin filter. The SFE model may be easily incorporated into the script to automatically generate geometry that yields desired analytical results, such as total filter efficiency and air flow resistance. Key filter material input factors include solidity, thickness, and fiber diameter. Key aerosol factors include particle diameter and particle density, while key airflow factors include air velocity, density, temperature, and viscosity. The SFE model is useful for describing the collection efficiency based on a uniform fiber diameter and for a single particle size. However, the SFE model introduces inherent error since both aerosols and fibers typically follow a statistical distribution. This limitation can be addressed by describing the situation with representative variables, such as a mean fiber diameter or mean particle diameter. Conversely it is also possible to select a representative fiber diameter and analyze the filtration media over a range of particle sizes. This is a particularly useful analysis and allows for the evaluation of the most penetrating particle size (MPPS). The MPPS is simply the particle size that the filter is least efficient at collecting under a specified set of circumstances. It is worth noting that this value is dynamic and will change with changing values such as the air flow velocity and mean fiber diameter. The flow resistance is measured as the air pressure differential between the upstream and downstream air flows relative to the filter media, which depends on the drag induced by the fibers in the media as well as any particles collected onto those fibers. The efficiency and flow resistance then determine the filter's FOM.

5.5.1 Example Digital Media Generation

Figure 5.10 shows an example nonwoven air filter media digital twin with dimensions of 100 µm x 100 perpendicular to the direction of flow. All fibers span the box with four-sided symmetry. The relaxation slope was set to 15% with a constant fiber radius of 1.4 µm, for a face coverage area of 4.0 with no additional spacing between fibers. This design resulted in the production of 337 fibers with 3204 segments, a solidity of 9.48%, and a thickness of 47.0 µm. With a specified airflow face velocity of 2.5 cm/s, the analytical model predicted flow resistance of 21.2 Pa. The total filter efficiency graphs show a minimum efficiency of 41.9% for aerosol particles with diameter of 215.4 nm, resulting in a FOM rating of 0.01972 Pa^{-1}. However, for 300 nm diameter particles, the filter media achieves an efficiency of 45.0% with a FOM rating of 0.0212 Pa^{-1}.

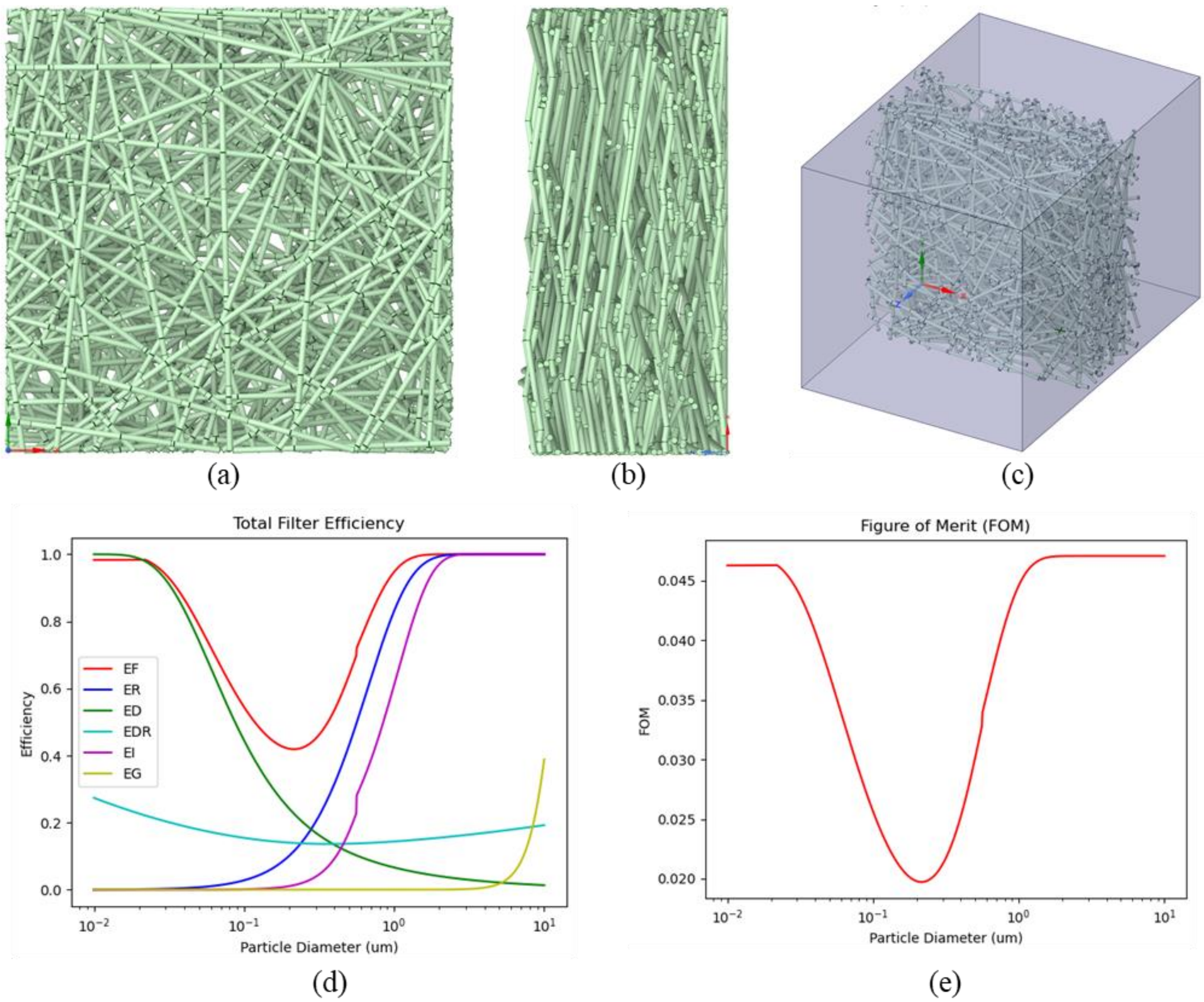

Figure 5.10 Analytical modeling of digital twin. (a) Top view of face area perpendicular to flow. (b) Side view showing filter thickness. (c) Geometry loaded into enclosure for CFD modeling. (d) Total filter efficiency shown by SFE model components. (e) Resulting figure of merit.

For clean filtration media, the flow resistance is dependent on the airflow parameters and independent of the aerosol characteristics, although it is worth noting that the characteristics of the aerosol will determine how the flow resistance changes as the particles are captured. Therefore, the flow resistance for clean filter media, measured as the pressure differential between the upstream and downstream airflows relative to the filter media, can be analytically predicted without yet knowing filter efficiency or aerosol characteristics. Similar to fiber face coverage and filter thickness, the flow resistance can be used as a design parameter for generation of digital filter geometry by setting a while loop to continue adding fibers on top of the filter until the specified maximum pressure drop is achieved.

5.5.2 HEPA Maximum Air Flow Resistance

By definition, HEPA filters are required to maintain 99.97% filtration efficiency for 300 nm diameter particles with a maximum flow resistance of 320 Pa at ambient conditions with air velocity of 2.5 cm/s [36]. For illustrative purposes, using the HEPA specified maximum flow resistance as the driving criteria, a digital twin geometry sample was created. Figure 5.11 shows the digital twin sample, which has square side dimensions of 20 µm, fiber diameters of 500 nm, a fiber relaxation slope of 15%, and an airflow velocity of 2.5 cm/s at standard conditions. The digital twin geometry algorithm to generate an original geometry, calculate the resulting predicted flow resistance, and iterate the process until the predicted flow resistance reached 320 Pa. The resulting filter slice had 884 fibers with 5494 segments, thickness of 68.5 µm, a face coverage of 19.3, and a solidity of 11.17%. The minimum filtration efficiency was 99.97% for the most penetrating particle size of 153.5 nm with a FOM rating of 0.00312 Pa^{-1}. Thus, according to the SFE model and Davies' pressure drop model, a piece of filtration media with the same characteristics and structure as the digital twin geometry would meet HEPA standards with a filtration efficiency of 99.999% occurring at particle size of 300 nm.

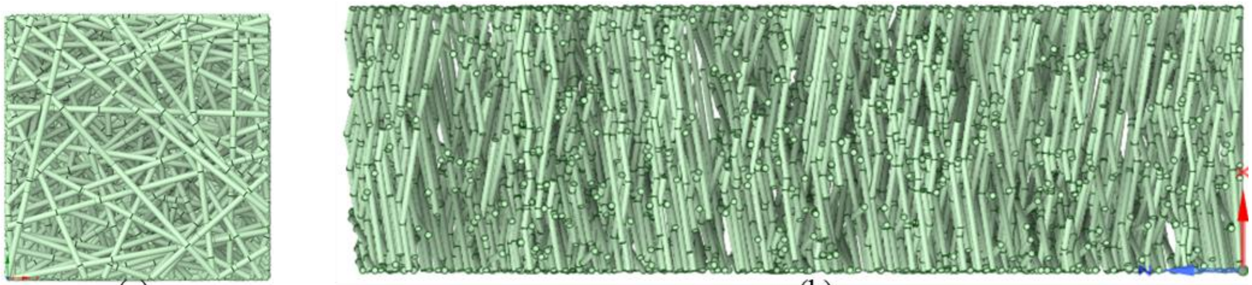

Figure 5.11 Digital twin HEPA filter built to 320 Pa flow resistance. (a) Top view of face area perpendicular to flow. (b) Side view showing filter thickness.

5.5.3 HEPA Minimum Filtration Efficiency

A second iteration was performed with a while loop to iterate the process until the total filter efficiency achieved 99.97% in accordance with HEPA standards. The resulting filter slice, again with fiber diameters of 500 nm, had 575 fibers with 3791 segments, thickness of 42.3 µm, a face coverage of 12.76, and a solidity of 11.98%. This achieved a 99.97% efficiency at particle size of 300 nm with a flow resistance of 223 Pa and resulting FOM of 0.00448 Pa^{-1}. Filtration media with the same characteristics and structure would meet HEPA standards. The resultant digital replica for this iteration with its corresponding total filtration efficiency graph is shown in Figure 5.12.

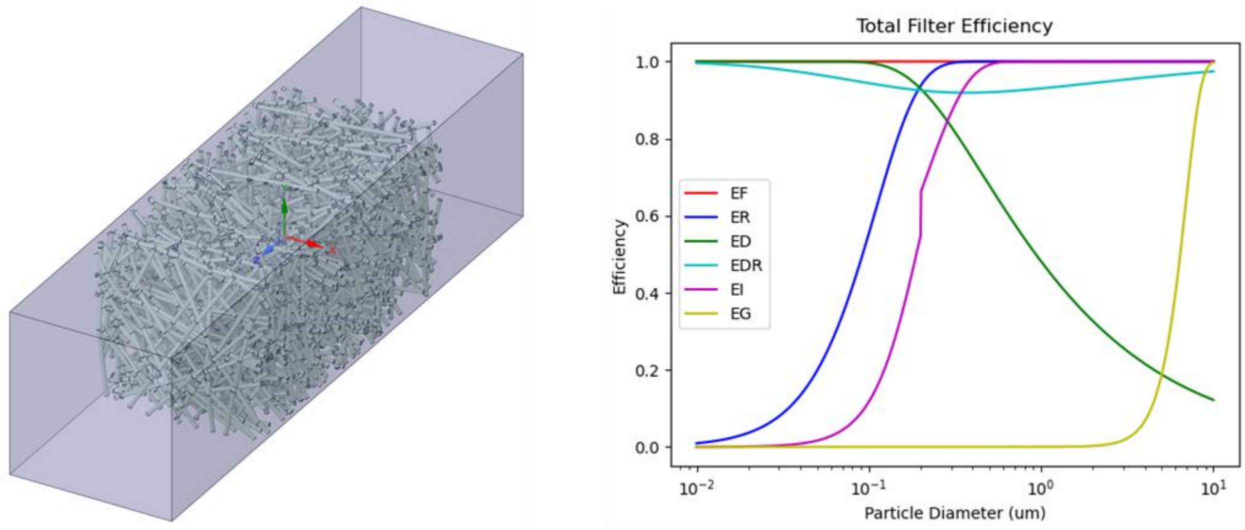

(a) (b)

Figure 5.12 Digital twin HEPA filter built to 99.97% efficiency. (a) Geometry loaded into enclosure for CFD modeling. (b) Total filter efficiency shown by SFE model components.

5.5.4 Fiber Diameter Sensitivity Analysis

A sensitivity analysis was performed by varying the fiber diameter of the digital twin geometry, ranging from 200 nm to 1.6 µm while using a relaxation slope of 15% until achieving a face coverage of 4.0. The error bars were calculated using a confidence level of 95%. It is interesting to note that for a particle size of 300 nm, the total filtration efficiency increased from 40.0% to 99.4% by reducing the fiber diameter from 1.6 µm to 200 nm. The solidity changed from 9.81% to 7.20% and the filter thickness changed from 52.0 µm to 8.84 µm over this same reduction of diameter sizes. This illustrates that filtration media with different characteristics, such as fiber diameter or solidity, will perform differently regarding differently sized particles. The sensitivity analysis for total filter efficiency and air flow resistance based on fiber diameter size is depicted in Figure 5.13.

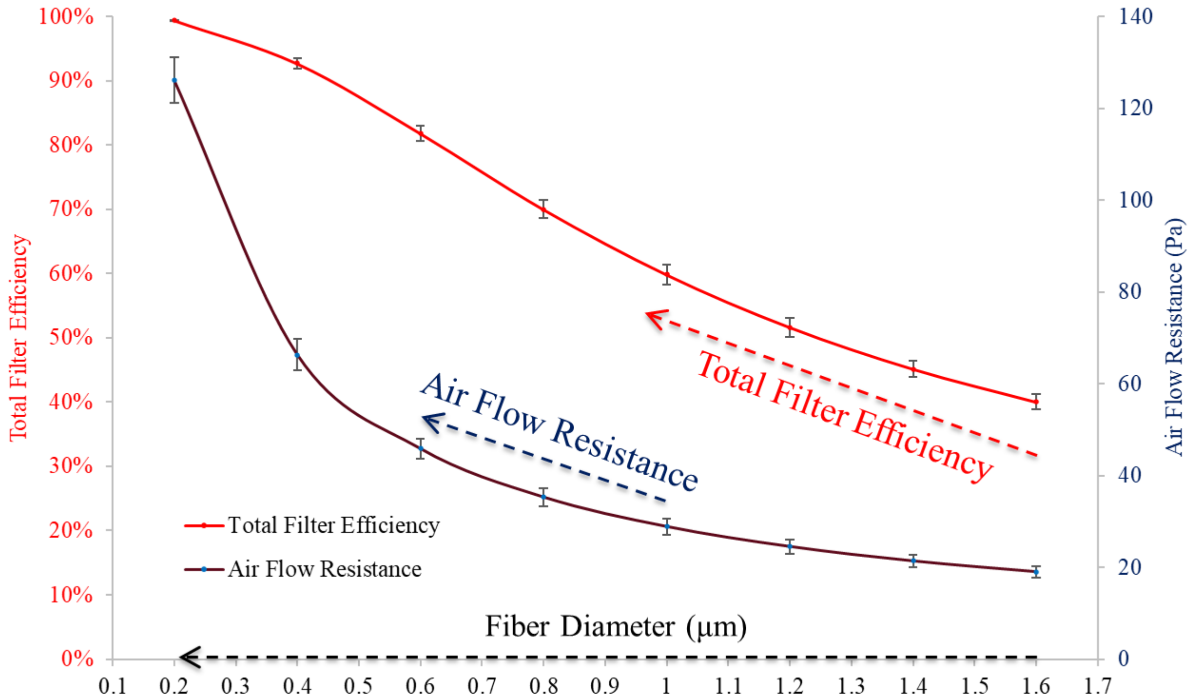

Figure 5.13 Sensitivity analysis for total filter efficiency and air flow resistance. Data represents mean values of samples drawn at each diameter size. Error bars represent 95% confidence level.

5.6 Chapter Summary

This chapter presents a simple method for constructing digital twins for nonwoven fibrous air filtration media using a computer program script and geometry software package. The primary advantage of this geometry generation method may be stated to be the simplicity and ease of adjusting parameters to achieve realistic random, semi-random, and aligned fiber orientations. Input parameters are easily adjusted to tune the resulting digital twin geometry into realistic replicas of electrospun or melt-blown nonwoven fibrous filter media. This chapter also demonstrates the usefulness of the SFE analytical model along with a pressure drop model to predict the filtration efficiency and flow resistance of a digital twin filter, and how it may be applied with the presented algorithm to generate a geometry to yield desired predicted characteristics. To illustrate this concept, a HEPA quality digital twin filter slice was created and analyzed. A visual comparison between an SEM image of electrospun media and a generated digital twin shows good agreement regarding a similarity in their fiber geometries. Furthermore, the ability to use the SFE model along with the script used to generate the digital twins was shown to be useful in estimating the performance of the generated geometry, or useful in generating geometry with a specific estimated performance in mind. Recommended future efforts include the refinement of this digital twin geometry creation algorithm and CFD analysis of air filtration media with the goal of matching experimental, analytical, and computational models of air filtration. This method of nonwoven fiber mesh digital twin creation may also be extended to other computational models requiring semi-random fiber placement, to include mechanical and thermal evaluation of fiber reinforced composite materials produced by additive manufacturing [119].

CHAPTER VI

ACHIEVING UNIFORM RANDOM DISTRIBUTION OF FIBERS FOR COMPUTATIONAL ANALYSIS OF NONWOVEN FILTRATION MEDIA[4]

This chapter considers the random placement of fibers on a square to achieve a desired homogeneous uniform distribution, as required in production of digital twin geometry for computational analysis of composite materials. Six methods of random fiber placement were demonstrated. Bertrand's paradox for placement of random chords on a circle provided the framework to compare, contrast, and evaluate similar methods for placing fibers on a square. Simulations were performed with chord placement on a circle and fiber placement on a square. Results were evaluated using uniformity of areal line density and fragment size distributions. A combined approach for placement of fibers on a square was developed that achieved homogeneous uniform distribution. A proposed exact solution to achieve the desired uniform distribution was demonstrated. A statistical analysis and data regression demonstrated the homogeneous results achieved by the combined approach and the proposed exact solution. The objectives of this chapter were achieved through demonstration of both a combined approach and a proposed exact solution to random fiber placement on a square to achieve homogeneous, uniform distribution of fibers for use in digital twin geometry for computational testing of composite materials.

---

[4] Content from this chapter is published in a journal article. Beckman, I. P.; Beckman, P, Cho, H.; Riveros, G. Modeling Uniform Random Distributions of Nonwoven Fibers for Computational Analysis of Composite Materials. Composite Structures 302, 2022, https://doi.org/10.1016/j.compstruct.2022.116242.

6.1 Introduction

In a recent effort to construct digital twin geometry of nonwoven nanofibrous media, Beckman et al implemented a method of choosing a random fiber layout over a square by selecting random fiber endpoints along the perimeter of a square [1]. One point was randomly selected on each of two distinct randomly chosen sides of the square as shown in Figure 6.1(b). The line segment connecting the two points represents a fiber within the volume of a box. This method created digital twin replica of electrospun fibers. At first glance this method appears to provide a uniform distribution of fibers as shown in Figure 6.1 (c).

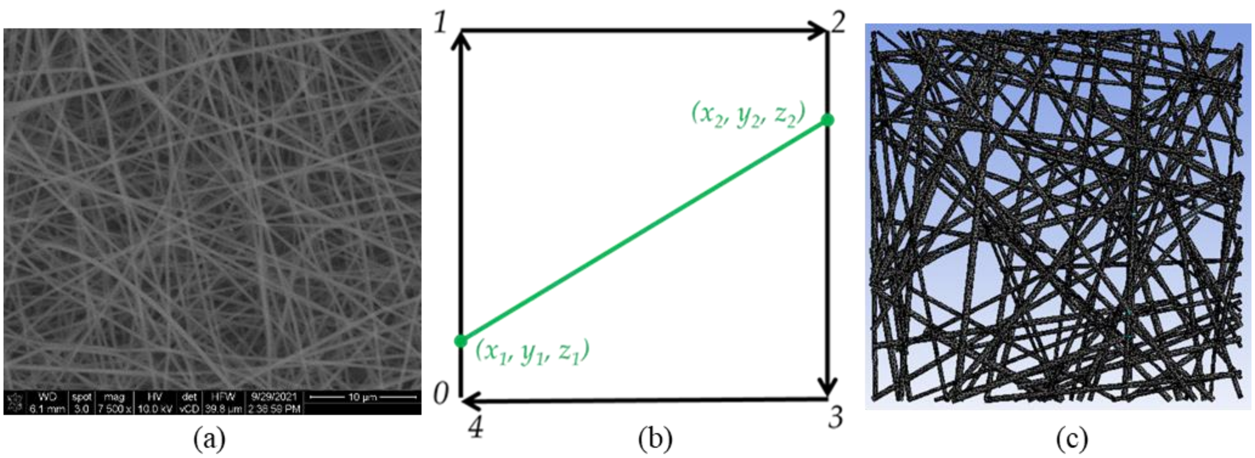

Figure 6.1 One method for selecting uniform random distribution of fibers on a square. (a) SEM image of nonwoven fibrous media. (b) Two points randomly selected along the perimeter of a square for fiber endpoints. (c) Digital twin media constructed from random fibers.

However, the question posed by Joseph Bertrand in 1888 regarding random chords on a circle calls into question whether there are multiple methods for selecting random fibers across a square, and if so, whether the method shown in Figure 6.1(b) is the best method [2]. In what became known as “Bertrand’s paradox,” the seemingly simple question was considered, “what is the probability that a random chord drawn on a circle is longer than the side length of the inscribed equilateral triangle [3]–[9]?" More than one plausible answer has been proposed and can be logically defended.

By extension from circle to square, the question Bertrand posed in 1888 suggests careful consideration of methods for selecting random fibers on a square to achieve a uniform random distribution. Bertrand's paradox, showing multiple methods of chord selection on a circle result in dissimilar random uniform chord distributions, suggests that multiple methods of fiber selection on a square may result in dissimilar random uniform fiber distributions. The purpose of this chapter is to evaluate, compare, and contrast various methods for selecting uniform random fibers on a square frame for applications such as the creation of digital twin geometry for computational analysis of composite materials [1].

6.2 Bertrand Paradox Explained

Although there may be debate about whether or not the question of Bertrand is actually a paradox, this term first given by Poincare is used for this study to illustrate that more than one method may be used and justified for random placement of fibers and among the methods to select the procedure that produces the best result [10]. An equilateral triangle is inscribed onto a unit circle as shown in Figure 6.2. One method for drawing a random chord on the circle is by selecting random points along the perimeter for chord endpoints. Since the question is on chord length while orientation is irrelevant, the chords can be rotated around the circle until one endpoint is at a vertex of the inscribed equilateral triangle as shown in Figure 6.2(a). As endpoints are randomly selected over the domain of the circle perimeter, clearly one third of the chords would be longer than the triangle side length (shown in red), while two thirds would be shorter.

The second method posed by Bertrand and illustrated in Figure 6.2(b) considers placement of the chord midpoints. Each chord drawn on the circle must have a midpoint at a given distance from the center of the circle. Again, ignoring orientation, if all chords are rotated until they are parallel to one of the triangle sides shown in red in Figure 6.2(b), the midpoints can be selected from a uniformly random distribution of distance from the circle center along the radius. Since the centroid for a triangle divides the median in the ratio of $2/3$ to $1/3$, the red chord in Figure 6.2(b) must divide the radius of the circle in the ratio of $1/2$ to $1/2$ thus supporting the plausible answer that one half of the chords would be longer than the side of the inscribed equilateral triangle, while also one half of the chords would be shorter.

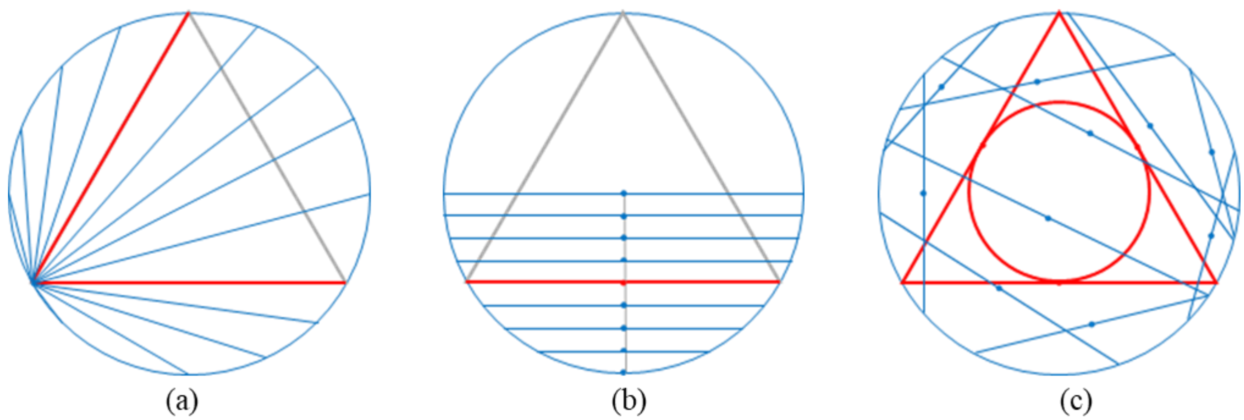

Figure 6.2 Bertrand paradox for random chord selection on a circle. (a) Chords drawn between random points along the circle perimeter. (b) Chords constructed from random midpoints along the circle radius. (c) Chords drawn from random midpoints selected by area.

The third method posed by Bertrand and illustrated in Figure 6.2(c) again considers random selection of midpoints within circle, however the circle area is the domain for random selection instead of distance from the circle center. If the chord midpoint is contained within the inscribed circle of the equilateral triangle, shown in red in Figure 6.2(c), the resulting chord will be longer than the side of the equilateral triangle. Since the radius of the inscribed circle is $1/2$

the radius of the circumscribed circle for the equilateral triangle, the area of inscribed circle is $1/4$ of the area of the circumscribed circle thus supporting the plausible answer that $1/4$ of the randomly drawn chords would be longer than the side of the equilateral triangle, and $3/4$ shorter.

Thus, Bertrand's paradox ponders whether a randomly drawn chord on the circle has a one-quarter, one-third, or one-half probability for being longer than the length of the side of the inscribed equilateral triangle since each of the plausible responses can be logically justified. Bertrand stated none of the three answers are false, none are correct, thus the question is ill posed [2]. Some authors contend there are multiple problems involved, and each problem has separately correct answers [10]–[17]. Some authors regard the question as well posed and solvable as stated [5], [6], [18], [19]. While Bertrand's question sparked a lively debate among scholars, it illustrates the importance of evaluating, comparing, and contrasting best practices in randomization of fiber placement whether upon a circle, square, or perhaps another shape.

In addition to the three methods considered by Bertrand shown in Figure 6.2, another six variations are shown in Table 6.1. Method 4 is an obvious method of selection of random chord lengths uniformly from zero to the circle diameter [3]. Method 5 is the selection of one random point along the circumference and a chord constructed with a random angle of elevation from that point, which is noted as essentially the same as Bertrand's first method and included for later analysis on a square. Method 6 considers a point within the circle interior at random distance from the circle center, with a chord constructed from a random angle of elevation. Method 7 considers a point selected at random within the domain of circle area and a chord constructed from a random angle of elevation. Method 8 selects two random points within the circle area and extends the line between them into a chord. Method 9 constructs a chord by extending a line from a randomly selected point within the circle area and a randomly selected point along the perimeter of the circle. While additional methods of random chord selection may be available, the nine methods chosen are sufficient to achieve the objective of this chapter. Five entities for random choice, including perimeter points, interior points, angle of elevation, chord midpoint location, and distance from the circle center, are presented in Table 6.1.

Table 6.1 Entities for Random Chord Selection on a Circle

Method	Perimeter Points	Interior Points	Angle of Elevation	Chord Midpoint	Distance From Center
1	$(x_1, y_1), (x_2, y_2)$				
2		(x_3, y_3)		(x_5, y_5)	R
3		(x_3, y_3)		(x_5, y_5)	
4	$(x_1, y_1), (x_2, y_2)$				
5	(x_1, y_1)		Θ		
6		(x_3, y_3)	Θ		R
7		(x_3, y_3)	Θ		
8		$(x_3, y_3), (x_4, y_4)$			
9	(x_1, y_1)	(x_3, y_3)			

Results from sampling 500 random chords are illustrated in Figure 6.3 for the original three methods of Bertrand’s paradox. The distribution of chord midpoints from a sample of 10,000 chords is shown in Figure 6.4. The visual observation of chords and midpoints from different methods of random selection clearly illustrate a wide range of uniform distributions.

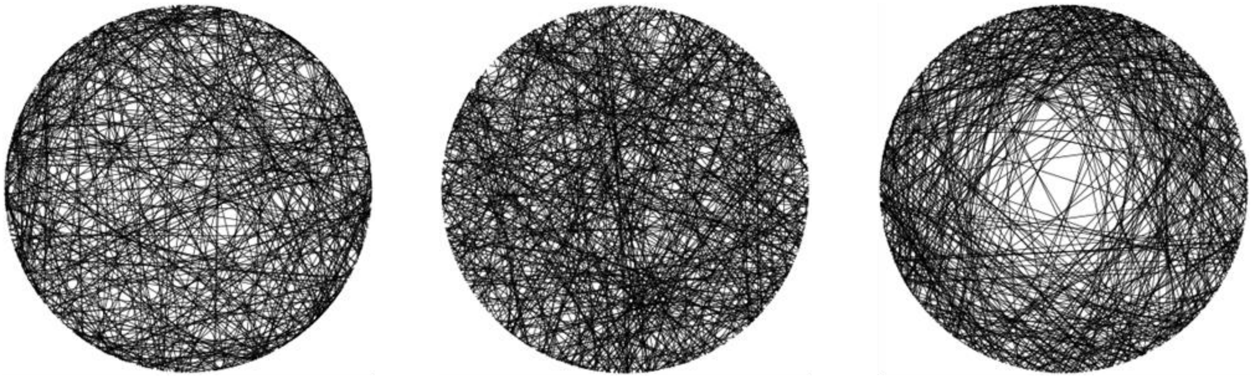

(a) (b) (c)

Figure 6.3 Chord and midpoint distribution on a circle, sampling 500 chords. (a) Random chord endpoints on the circle perimeter. (b) Random distance from chord midpoints and circle center. (c) Random chord midpoints selected within the circle area.

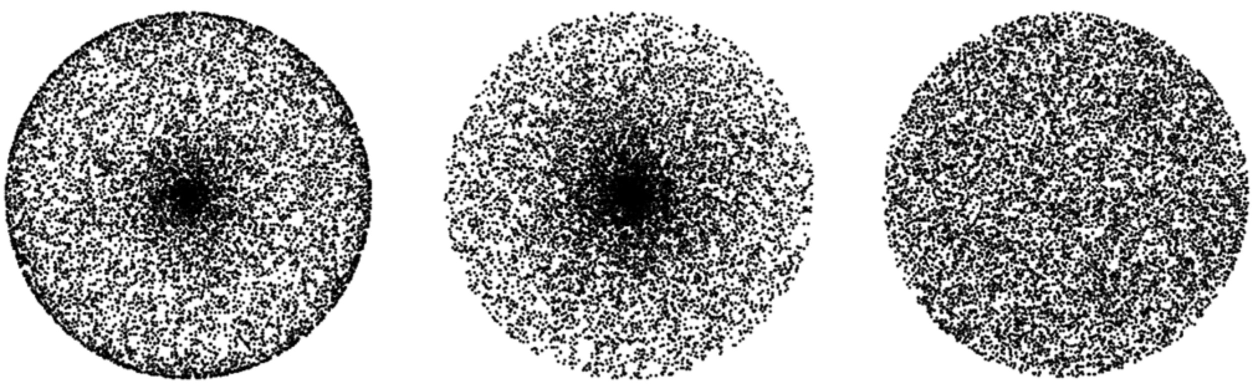

(a) (b) (c)

Figure 6.4 Chord midpoint distribution on a circle, sampling 10,000 chords. (a) Random chord endpoints on the circle perimeter. (b) Random chord midpoints along the circle radius. (c) Random chord midpoints within the circle area.

6.2.1 Simulation of Random Placement of Chords on a Circle

A computer program was created for random placement of chords on the circle by each of the nine methods. Results from sampling ten million chords are shown in Table 6.2, illustrating the percentage of chords that are longer than the side length of an inscribed equilateral triangle, noted as $\sqrt{3}$ for a unit circle, as Bertrand originally questioned. As expected, methods 1, 2, and 3 show ratios of one third, one half, and one fourth. It is obvious to the reader as well that method 4 results in 13.4% chords longer than the inscribed equilateral triangle side length.

Table 6.2 Comparison of Random Chords Longer than Triangle Side Length

	Entities of Random Chord Placement	Chord Longer than Equilateral Triangle Side Length (%)
1	Two random endpoints on circle perimeter	33.3
2	Random distance chord midpoint to circle center	50.0
3	Random chord midpoint within circle area	25.0
4	Random length of chord	13.4
5	One random perimeter point and random angle	33.3
6	Random point from circle center, random angle	75.2
7	Random point within circle and random angle	60.9
8	Chord extended from two random interior points	74.7
9	Random perimeter endpoint and interior point	60.9

Aerts and de Bianchi suggested that since there are many methods to choose random chords, the principle of indifference must first be applied to the more general problem of selecting from the multiple methods of choosing random chords [19]. In this case, with equal preference for each of the nine methods, a universal average would result in an answer of 47.4% of chords longer than the side length of an inscribed equilateral triangle.

Edwin Jaynes showed Bertrand’s question is in fact logically well posed and has a correct solution if the result must be invariant to the group of Euclidean transformations to include rotational invariance, scale invariance, and translational invariance [6]. Jaynes suggested the lack of clarity in Bertrand’s question implies the solution must be invariant to transformation, and since only method 2 (selection of chord midpoints a random distance from the circle center) is invariant to translation, the correct answer is in fact 50%.

The debate regarding whether Bertrand's paradox is a paradox, whether the question is well posed or ill posed, and whether there is a correct solution is beyond the scope of this chapter. Regardless, Bertrand's paradox provides a useful framework for analyzing methods of fiber placement on a square.

6.2.2 Line Density

Definition: as used within this chapter, the term "**line density**" is the sum of lengths of line segments within a particular area divided by the sum of lengths of line segments for the total area. For example, the chords on the circle in Figure 6.3(c) show heavier line density near the circle perimeter and lighter line density near the center of the circle.

Although fibers in composite materials have length, cross sectional area, surface area, and mass, for purposes of this study fibers are simplistically represented by lines which can be thought of as the fiber centerlines, while line density as defined above is similarly representative of fiber mass density. A homogeneous fibrous filter mass density is represented in this study as having uniform line density throughout the total area of the medium. For example, Bertrand's third method for choosing chord midpoints at random within the area of the circle shown in Figure 6.3(c) illustrates heavy line density nearer the perimeter of the circle and light line density nearer the center.

6.2.3 Euclidean Transformations as a Test for Homogeneity

The method Jaynes used to demonstrate a resolution to Bertrand's paradox through invariance throughout Euclidean transformations is precisely required for a homogeneous solution [6]. Any solution invariant to rotation, scale, and translation will show consistent and uniform line density throughout the result.

6.2.4 Central Divisions of a Square and Circle

To evaluate the uniform distribution of fibers on a square in the next section, the sides of a square were divided into three equal segments providing nine cells of equal area as shown in Figure 6.5(a). A homogeneous solution would result in 1/9 or 11.11% of observations for the central ninth. In a similar manner not related to the incircle of the equilateral triangle shown above in Figure 6.2(c), concentric circles were defined wherein the radius of the inner circle was chosen as 1/3 of the radius of the outer circle shown in Figure 6.5(b) also expecting 1/9 or 11.11% of line density to occur within the inner circle. Similar to a quadrant on a square, a "ninth" is a term used throughout this chapter to indicate a one ninth subdivision of area for a square and a circle.

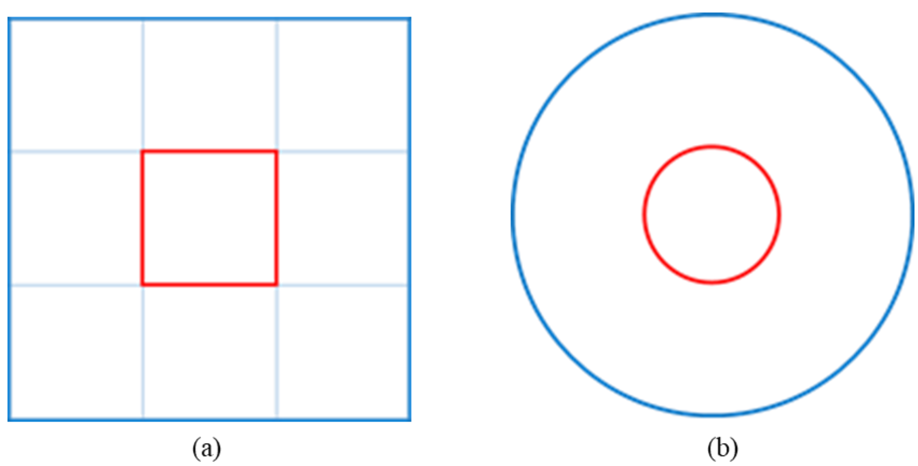

Figure 6.5 Ninth central divisions of a square and circle used in evaluating translational invariance for homogeneity of results. (a) Square divided into nine equal parts with a central ninth shown in red. (b) The central ninth of a circle shown in red.

If the particular method of random chord selection achieves translational invariance, the line density will be the same in all local regions. A line density of one ninth (11.11%) would indicate translational invariance and the uniform homogeneous solution sought. For the purposes of this chapter, methods that result in greater than one ninth line density in the inner circle are described as having a “central tendency,” while methods with less than one ninth are described as having “outward tendency.”

Using a computer script and placing ten thousand random chords on the circle from each of the nine methods, it is clear from Figure 6.6 and Table 6.3 that Bertrand’s second method, selecting chord midpoints a random distance from the circle center, is the only method of the nine evaluated that precisely results in homogeneous line density of chords within the circle. Each of the other eight methods show either inward or outward tendency. This confirms Jaynes’ analysis showing Bertrand’s second method as the only one that achieves translational invariance [6].

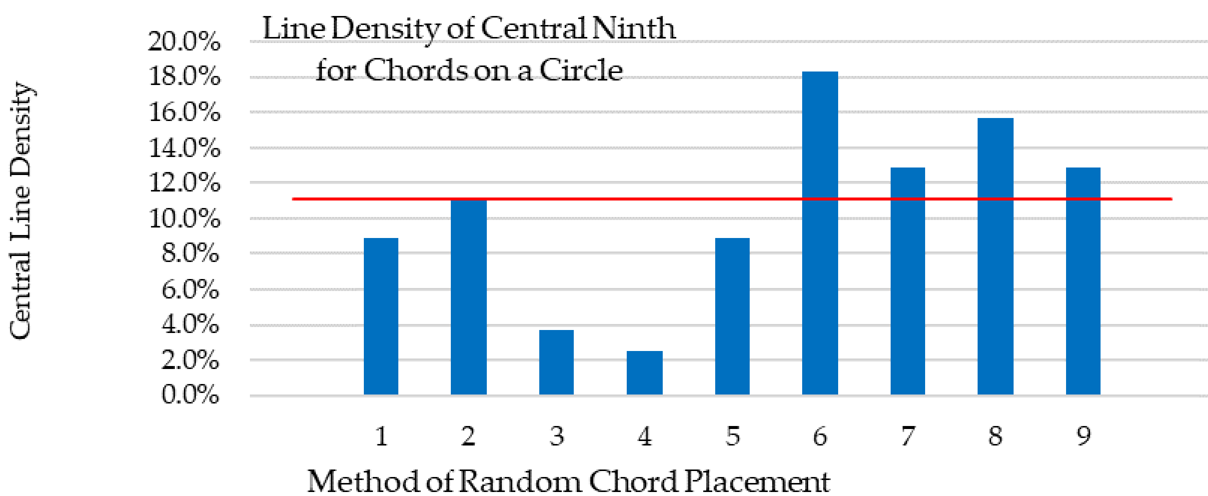

Figure 6.6 Line density comparison for the central subdivision for each of nine methods. The red line on the graph represents the target 11.11% line density for the inner red circle.

Table 6.3 Line Density Comparison of the Central Circle, Sampling Ten Million Chords

	Entities of Random Chord Placement	Central Ninth Density (%)	Tendency	Outer Ninth Density (% per ninth)
1	Two perimeter points	8.86	Slight Outward	11.39
2	Chord midpoint distance from center	11.11	Balanced	11.11
3	Chord midpoint in circle area	3.70	Heavy Outward	12.04
4	Chords of uniform length	2.53	Heavy Outward	12.18
5	One perimeter point and angle	8.85	Slight Outward	11.39
6	Point along radius and angle	18.36	Heavy Central	10.21
7	Point interior and angle	12.91	Slightly Central	10.89
8	Two interior points	15.69	Heavy Central	10.54
9	Perimeter point, interior point	12.90	Slightly Central	10.89

6.3 Beyond Bertrand's Circle: the Square

The framework established to evaluate random chords on a circle can be applied to a square. The objective is to compare and contrast distributions for observations resulting from different methods of random fiber selection. Figure 6.7, for example, illustrates the difference between two distinct methods of random fiber selection. The method used in Figure 6.7(a) is similar to Bertrand's first method for random chords on a circle, while the method used in Figure 6.7(b) is similar to Bertrand's third method for random chords on a circle. In order to achieve a homogeneous result, the line density must conform to invariance of scale, rotation, and translation. It appears method (b) has more central tendency than method (a).

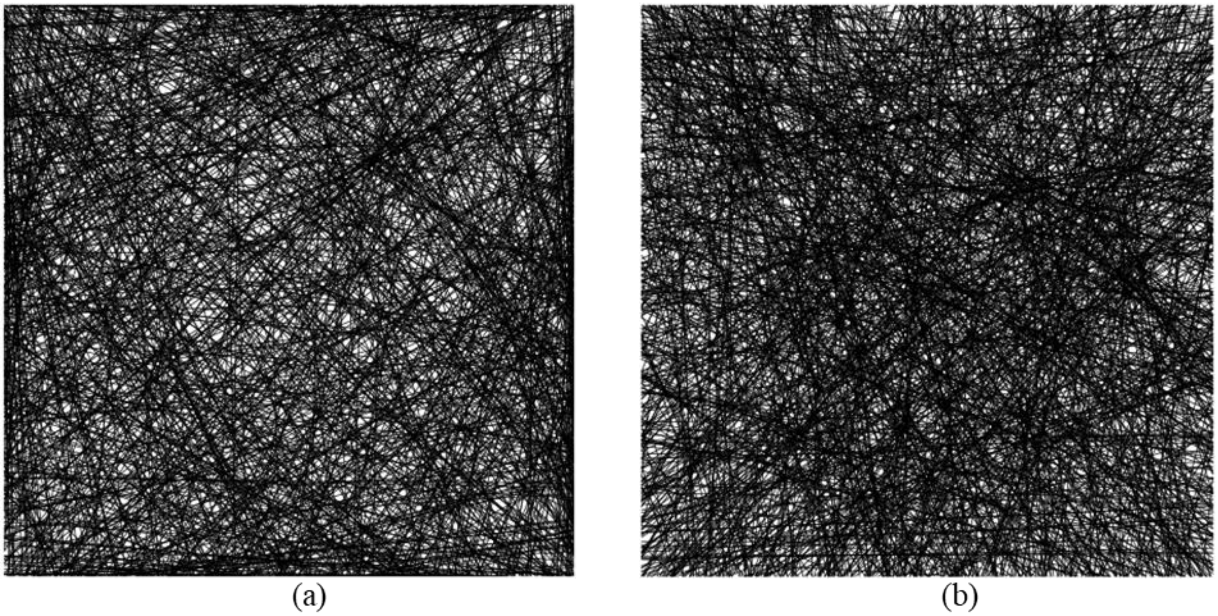

Figure 6.7 Random fiber distribution on a square from two unique methods. (a) Selection of 1000 fibers constructed from two random points along the perimeter. (b) Selection of 1000 fibers constructed from a random point inside the square with a random angle intersecting the perimeter.

6.3.1 Methods for Selecting Fibers on a Square

Including the two methods of random fiber selection illustrated by Figure 6.7, five initial methods were considered to achieve uniform fiber distribution on a square. Each method is a combination of three entities: perimeter points, interior points, and angles of elevation. The five methods evaluated are: a) selecting two random points on the square perimeter (x_1, y_1) and (x_2, y_2) and connecting the two points with a line, b) selecting a random interior point (x_3, y_3) and extending a line through a random angle of elevation θ to the square perimeter, c) selecting one random point on the square perimeter (x_1, y_1) and extending a line through a random angle of elevation θ to the square perimeter, d) selecting of two random interior points (x_3, y_3) and (x_4, y_4) and extending the line containing both points to two endpoints on the square perimeter, and e) selecting a random point on the square perimeter (x_1, y_1) and a random interior point (x_3, y_3) and extending the line containing both points to the square perimeter. These five methods of random selection each require two entities as shown in Table 6.4 and are illustrated graphically in Figure 6.8.

Table 6.4 Entities for Random Fiber Selection on a Square

Method	Perimeter Points	Interior Points	Angle of Elevation
(a)	(x_1, y_1) (x_2, y_2)	-	-
(b)	-	(x_3, y_3)	θ
(c)	(x_1, y_1)	-	θ
(d)	-	(x_3, y_3) (x_4, y_4)	-
(e)	(x_1, y_1)	(x_3, y_3)	-

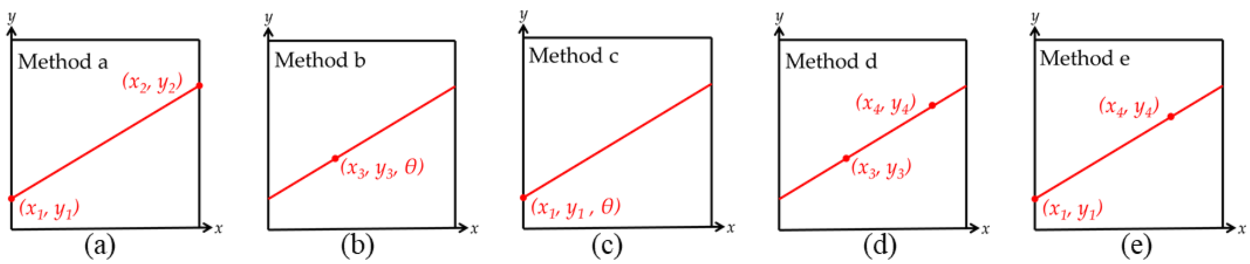

Figure 6.8 Five methods for selecting random fibers across a square.

6.3.2 Simulation of Random Placement of Fibers on a Square

A computer program was created to randomly place 1000 fibers across a square using each of the five methods. A subjective appreciation for the uniformity of fiber line density is observable in Figure 6.9, which clearly shows a central tendency for methods (b), (d), and (e), while showing an outward tendency for method (c). Method (c) appears sparse in the central region while method (d) appears more dense in the central region.

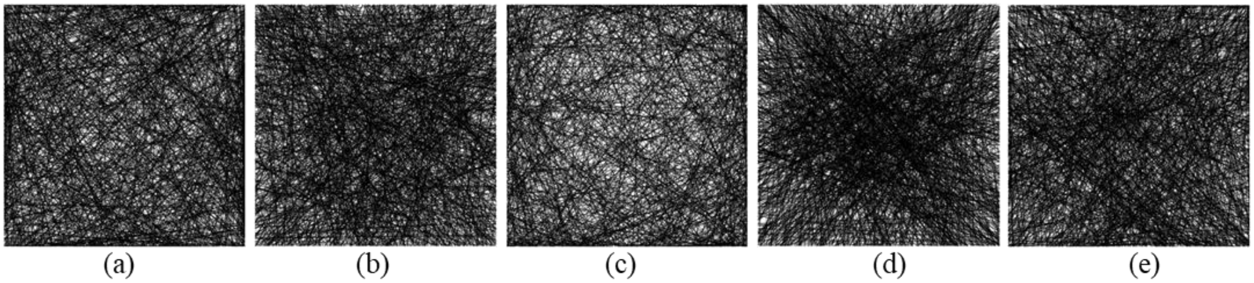

Figure 6.9 Results of 1000 randomly placed fibers using methods (a) through (e).

Similar to the earlier evaluation of line density in the central ninth of a circle, the line density of the central ninth of the square can be compared to the density of the outer ninths. Unlike the circle, the outer ninths of the square are unique as corner ninths and side ninths as shown in Figure 6.10. To achieve a homogeneous uniform distribution of fibers, each of the ninths (central, side, and corner) should contain 11.11% of the total fiber line density.

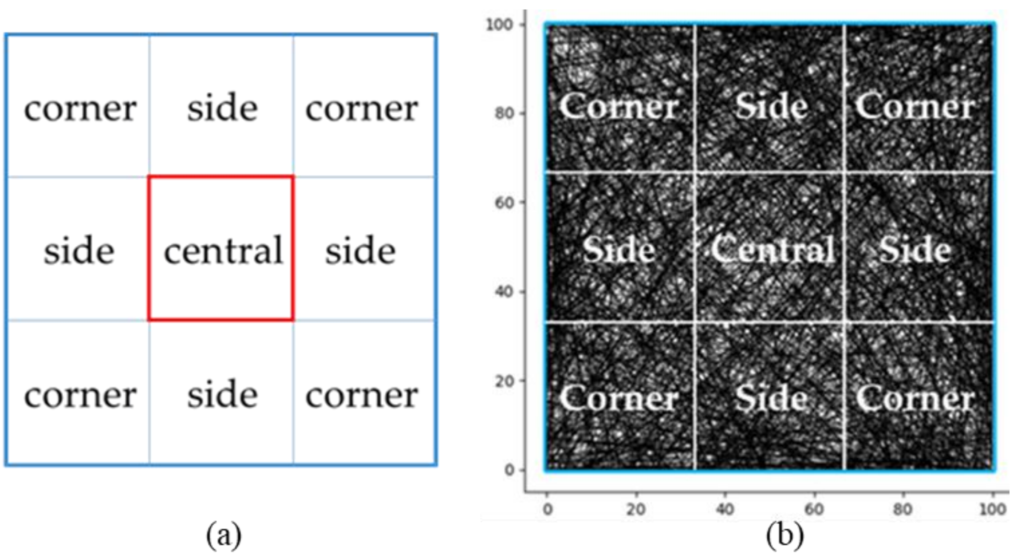

Figure 6.10 Evaluation of uniform distribution of fiber placement methods. (a) The central ninth red square is one third of the length and width of the outer square. (b) Grid placement on a square.

Running each of the five methods of random fiber placement for one million fibers resulted in the line densities per ninth shown in Figure 6.11. None of the five methods resulted in an exact one ninth line density in the central ninth. Methods (a) and (c) resulted in sparse line density in the central ninth, indicating an outward tendency, while methods (b), (d), and (e) indicated central tendency. Additionally, comparison of the line densities in the four side ninths and four corner ninths of each method reveals the tendency of each method to favor either the side or corner ninths.

11.20%	11.35%	11.16%
11.34%	9.93%	11.32%
11.20%	11.33%	11.16%

(a)

10.25%	11.49%	10.25%
11.52%	12.96%	11.49%
10.27%	11.50%	10.27%

(b)

12.00%	10.78%	12.01%
10.74%	8.92%	10.80%
11.99%	10.75%	12.01%

(c)

9.91%	11.22%	9.91%
11.23%	15.44%	11.20%
9.94%	11.24%	9.92%

(d)

10.41%	11.40%	10.42%
11.39%	12.76%	11.42%
10.42%	11.41%	10.38%

(e)

Figure 6.11 Density of lines comparison on a 3x3 grid of ninths, using one million randomly placed fibers in methods (a) through (e).

6.3.3 Square Tiling

The homogeneity of line density can also be visually observed by tiling individual squares into a matrix of tiles. Figure 6.12 shows 100 x 100 squares outlined in blue, similar to that of Figure 6.10(b), tiled into a 3 x 5 matrix. The observation of lighter or darker patterns within the 3 x 5 tiling in the center or along the edges of individual tiles indicates lighter or heavier line density. Although the pattern of squares should be visible because none of the fibers cross from one square tile into another, a homogeneous medium created by uniformly dense fiber placement should result in a uniform shade throughout the tiling.

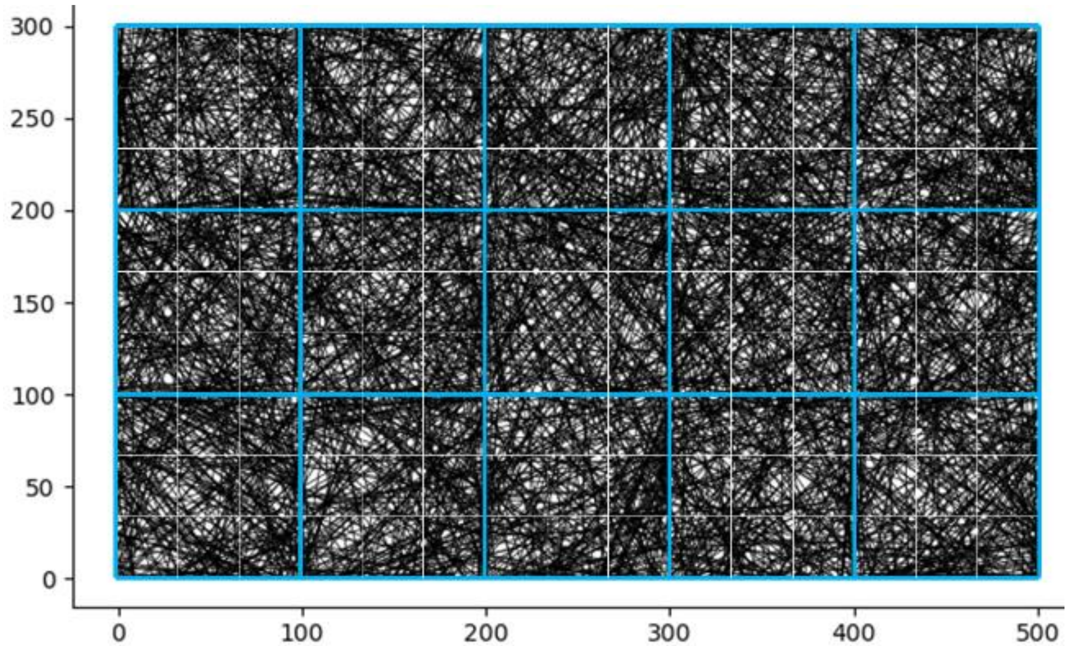

Figure 6.12 Arrangement of fiber squares as 3 x 5 tiles to observe patterns.

Results from tiling the five methods of random fiber placement are shown in Figure 6.13. The central tendency of method (d) and the outward tendency of method (c) are clearly visible using this tiling method. Method (e) appears sparse in the corners.

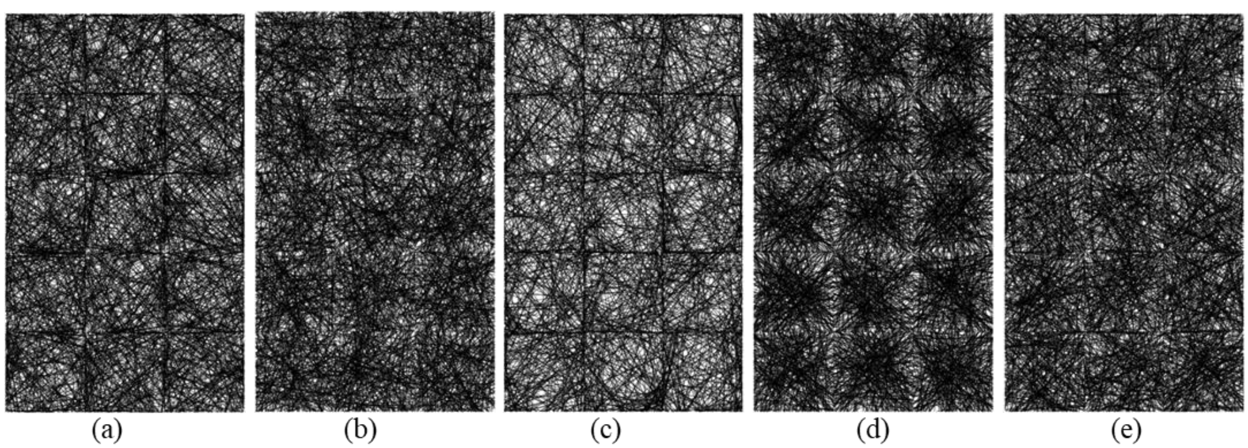

Figure 6.13 Arrangement of fiber squares as 5 x 3 tiles to observe patterns with 250 fibers in each square, using methods (a) through (e).

6.3.4 A Combined Approach

Since none of the five methods resulted in homogeneous uniform line density, combining multiple methods of random fiber placement can achieve the desired result. For example, method (a) favors the side ninths, method (c) favors the corner ninths, and method (e) favors the central ninth. Combining these three methods can result in a balanced line density throughout the square. A computer program was developed to modulate between methods (a), (c), and (e) in a self-correcting process targeting 11.11% line density of all ninths. After each fiber placement, the algorithm recalculates the line density of central, corner, and side ninths to determine which method to select for placement of the next random fiber, as shown in Figure 6.14.

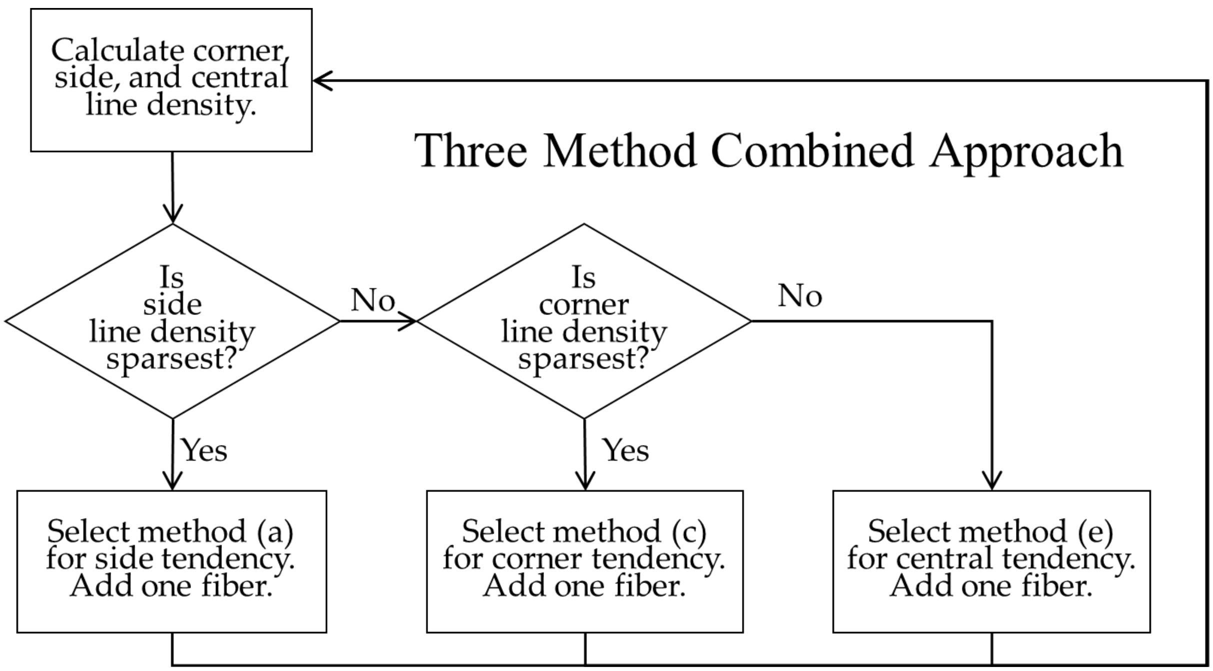

Figure 6.14 Flowchart for a three-method combined approach with methods (a), (c), and (e).

The algorithm selects the method that favors whichever ninth is most sparse. Running the program for the random placement of 1000 fibers is illustrated in Figure 6.15(a), with red fibers placed by method (c) for corner tendency, blue fibers placed by method (e) for central tendency, and black fibers placed by method (a) for side tendency. Modulating among the three methods resulted in a balanced line density throughout the square. Figure 6.15(b) shows the resulting line density for each of the ninths.

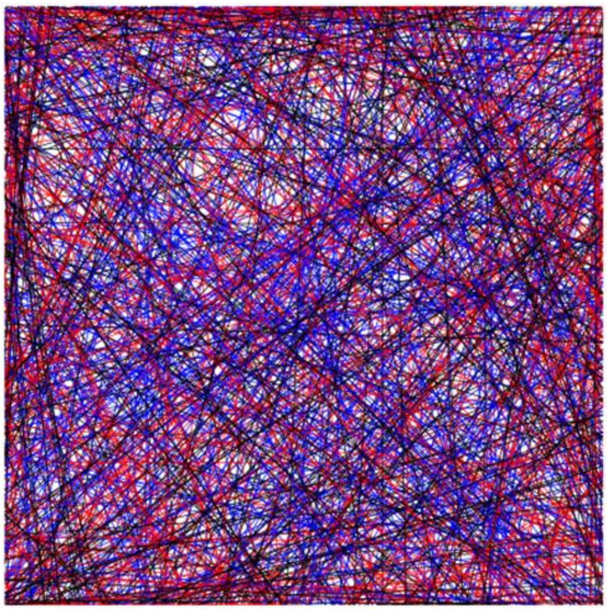

(a)

11.10%	11.13%	11.09%
11.13%	11.10%	11.13%
11.10%	11.13%	11.10%

(b)

Figure 6.15 Combined methods (a), (c), and (e) to produce a uniform distribution of fibers. (a) Single tile with 1000 fibers. Fibers from method (a) are shown in black, from method (c) in red, and from method (e) in blue. (b) Line density comparison of combined approach with methods (a), (c), and (e), showing all ninths fairly balanced.

The three-method combined approach is tiled into a 3 x 5 grid to visually observe uniform line density in Figure 6.16. The grid pattern is visible since none of the fibers cross boundaries from one grid square to another, however the line density is fairly balanced.

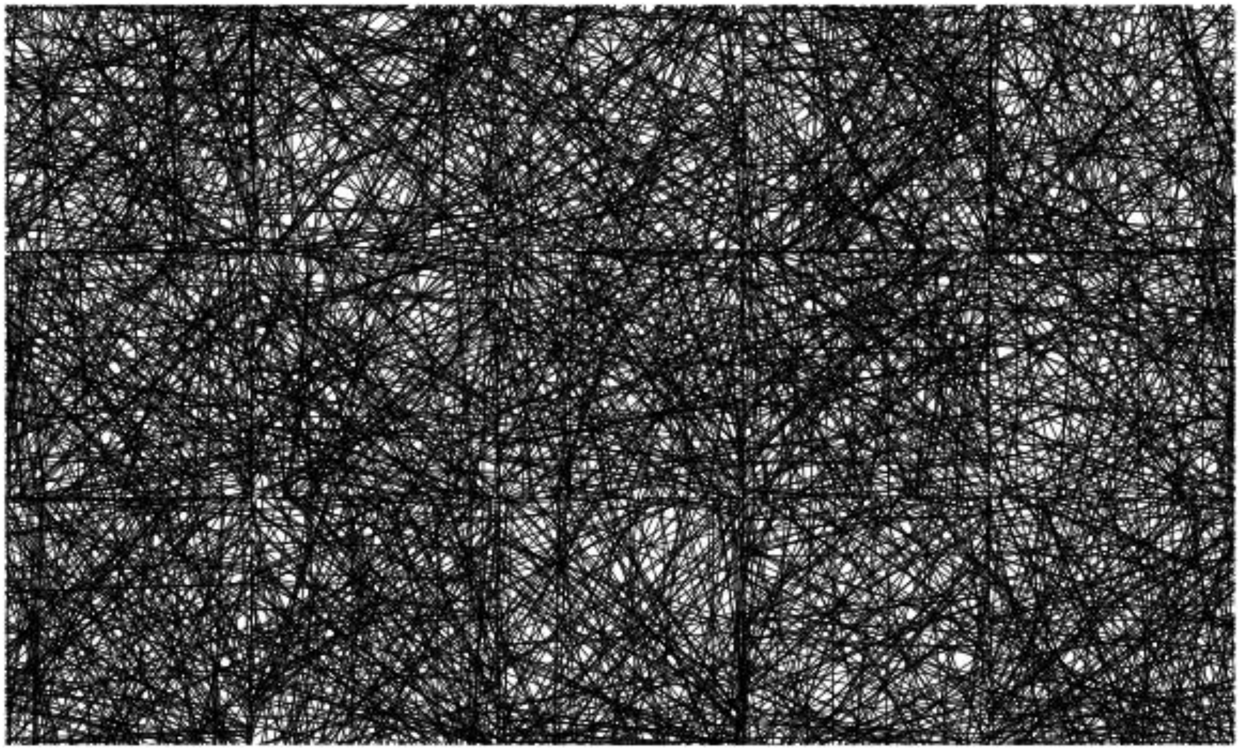

Figure 6.16 Tiled 3 x 5 pattern of the three-method combined approach, each tile with 250 fibers shown in black.

6.3.5 A Proposed Exact Solution: Normal to Uniformly Distributed Radial Distance from Center

For a homogeneous uniform distribution of chords on a circle, Bertrand's second method of choosing chord midpoints at random distance from the circle center proved invariant to Euclidean transformations. This method can be replicated with a square. The entities of randomness for this method include a random angle for a centerline segment at the center of the square and a random distance along the centerline segment for a point. A fiber is constructed from the segment of a line drawn through that point normal to the centerline as it crosses the square. Figure 6.17 illustrates the process to construct random fibers across the square using this proposed exact solution. Figure 6.17(a) shows a square with centerline limits drawn in blue, while Figure 6.17(b) shows five randomly placed centerlines in red. Figure 6.17(c) shows fifty random fibers constructed normal to one particular red centerline. By randomly selecting the centerline angle and distance from center, the distribution of fibers is uniform and homogeneous throughout the entire square.

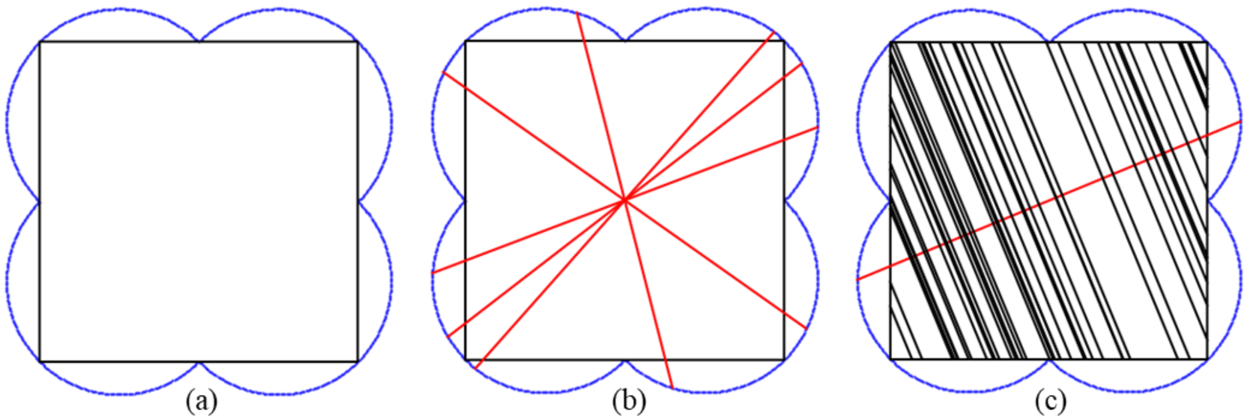

Figure 6.17 Proposed exact solution for homogeneous fiber distribution on a square. (a) The limits of radii are drawn in blue. (b) Five random diameter lines drawn through the center of the square drawn in red. (c) Fifty fibers drawn in black across the square normal to one particular diameter line in red.

Holbrook and Kim illustrated a similar concept for considering of Bertrand's paradox on a circle using a proposed physical experiment with parallel cosmic rays entering a Wilson cloud chamber [5]. Considering all parallel rays of light entering the chamber from all angles produces a uniform distribution of chords on the circular plane. Similarly considering a uniform distribution of parallel fibers across a square at a uniform distribution of central angles produces an exact heterogeneous distribution of randomly placed fibers across the square. A computer program was used to randomly place 1000 fibers onto a square in the method described above. The result shown in Figure 6.18 confirms the homogeneity of the fiber placement.

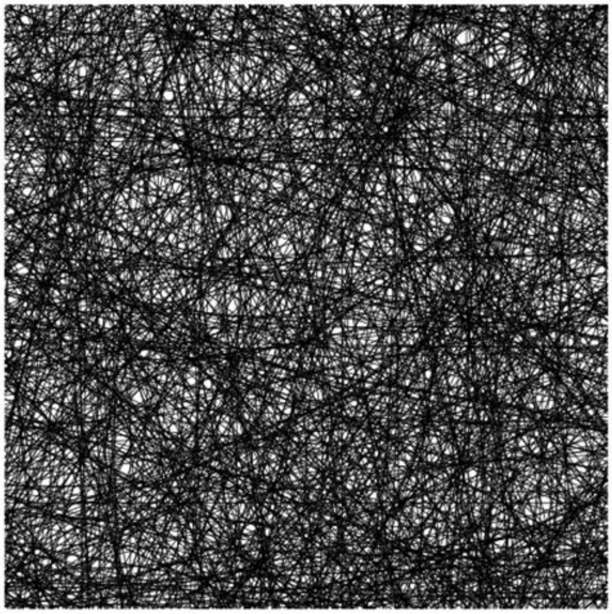

(a)

11.10%	11.11%	11.12%
11.11%	11.11%	11.11%
11.13%	11.10%	11.12%

(b)

Figure 6.18 Placement of random fibers onto a square with the proposed exact solution. (a) Placement of 1000 fibers. (b) Fiber line density percentages by ninth. This result confirms uniform line density.

Running the same computer program as before using the proposed exact solution for fiber placement into a 3x5 grid of squares is shown in Figure 6.19. The boundary lines between the fifteen grid squares is nearly indistinguishable even as none of the fibers cross from one grid square to another. This result clearly illustrates the homogeneous nature of the solution.

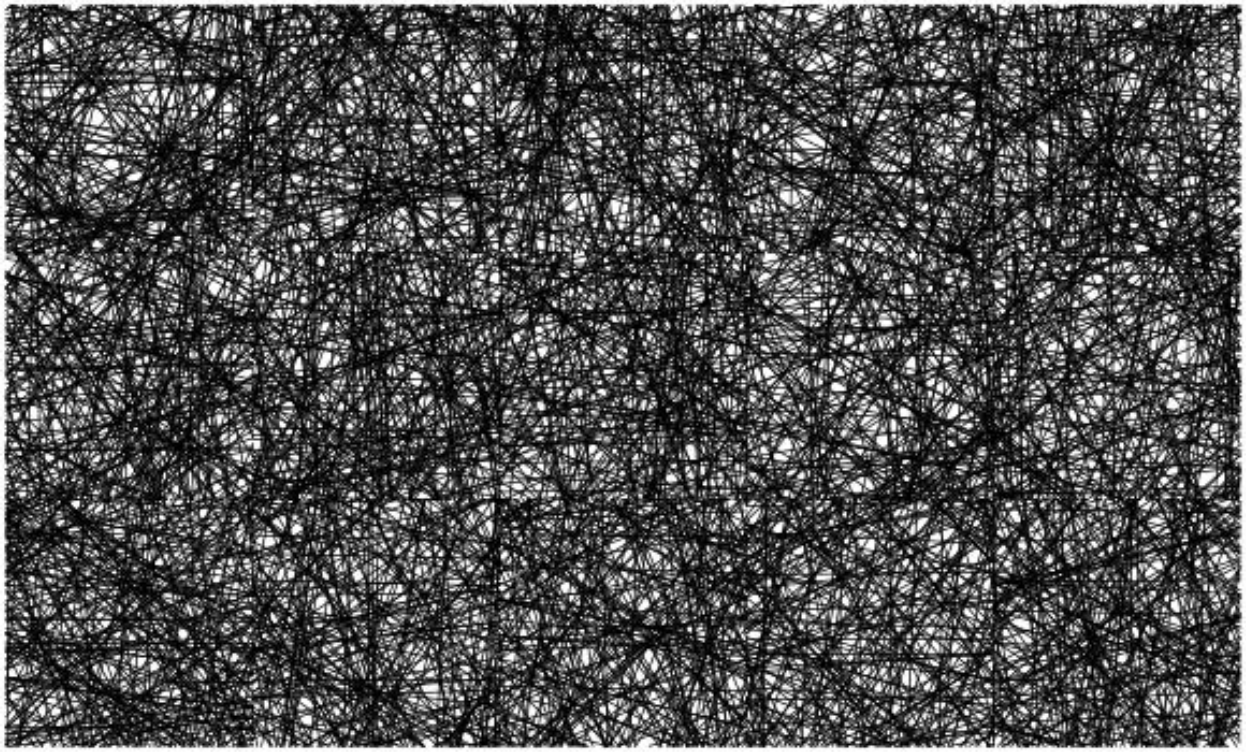

Figure 6.19 Tiled 3 x 5 pattern of the proposed exact solution, each tile with 250 fibers, all shown in black.

6.3.6 Summary Comparison of Line Density

Figure 6.20 and Table 6.5 compare the line densities for the central, corner, and side ninths.

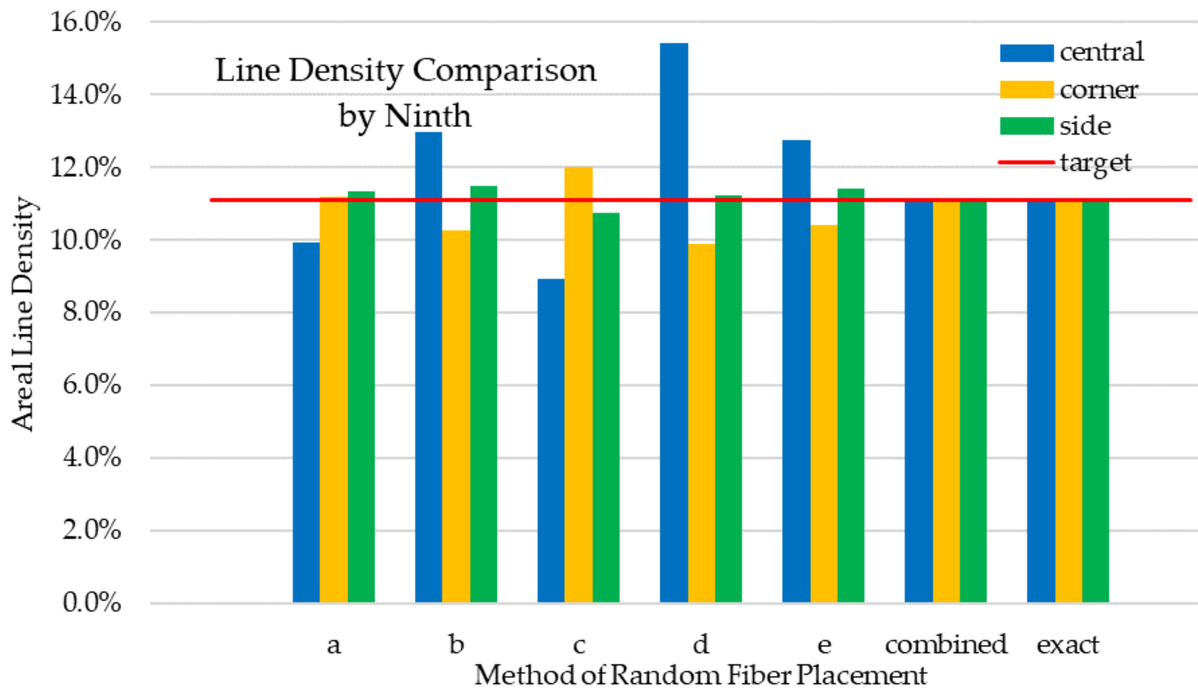

Figure 6.20 Line density comparison by ninths for one million randomly placed fibers using methods (a) through (e). The combined three-method approach is shown as (f) and the exact method approach is shown as (g).

Table 6.5 Line Density Comparison of the Central, Side, and Corner Ninths

	Entities of Random Selection	Central Ninth (%)	Side Ninth (%)	Corner Ninth (%)	Tendency
(a)	Two perimeter points	9.93	11.34	11.18	Side, Corner, Central
(b)	Interior point & angle	12.96	11.50	10.26	Central, Side, Corner
(c)	Perimeter point & angle	8.92	10.77	12.00	Corner, Side, Central
(d)	Two interior points	15.44	11.22	9.92	Central, Side, Corner
(e)	Interior & perimeter point	12.76	11.41	10.40	Central, Side, Corner
(f)	Combined methods (a, c, & e)	11.10	11.13	11.10	Balanced
(g)	Proposed exact solution	11.11	11.11	11.12	Balanced

6.3.7 Fragment Analysis for Homogeneity

Definition: throughout this chapter, the term “**fragment**” is used to indicate the area of the polygonal shaped gaps or regions bounded by intersecting fibers.

In addition to the uniformity of areal line density, a complementary indicator of homogeneity is to consider the whitespace or gaps among the fibers. Of the five methods of random fiber placement on the square, it was expected that methods with outward tendency would show larger gap sizes near the center of the square, while methods that create central tendency would show the opposite.

6.3.8 Fragment Size

Figure 6.21 shows the concept of using fragment analysis to evaluate the homogeneity of fibers on a square. A square was drawn with side length of 100 units for an area of 10,000 square units. A computer program was used to calculate the area of each polygon-shaped fragment and determine the distance of each fragment centroid from the center of the square. The program identified and listed each polygon by calculating vertex coordinates of intersecting lines. Polygons were split and reformed with each additional line added to the square. The area of each polygon was summed from the areas of component triangles, calculated with Heron's formula. The centroid of each fragment was then calculated by averaging the x and y coordinates of vertices. As an illustration, the twenty fibers depicted in Figure 6.21(a) resulted in 107 polygon shaped fragments of various sizes ranging from 1.15E-3 to 609.1 square units, with an average area of 93.46 square units per fragment. Similarly, Figure 6.21(b) illustrates 500 fibers, resulting in 60,755 fragments ranging in size from 1.03E-11 to 7.94 square units, for an average area of 0.1646 square units per fragment.

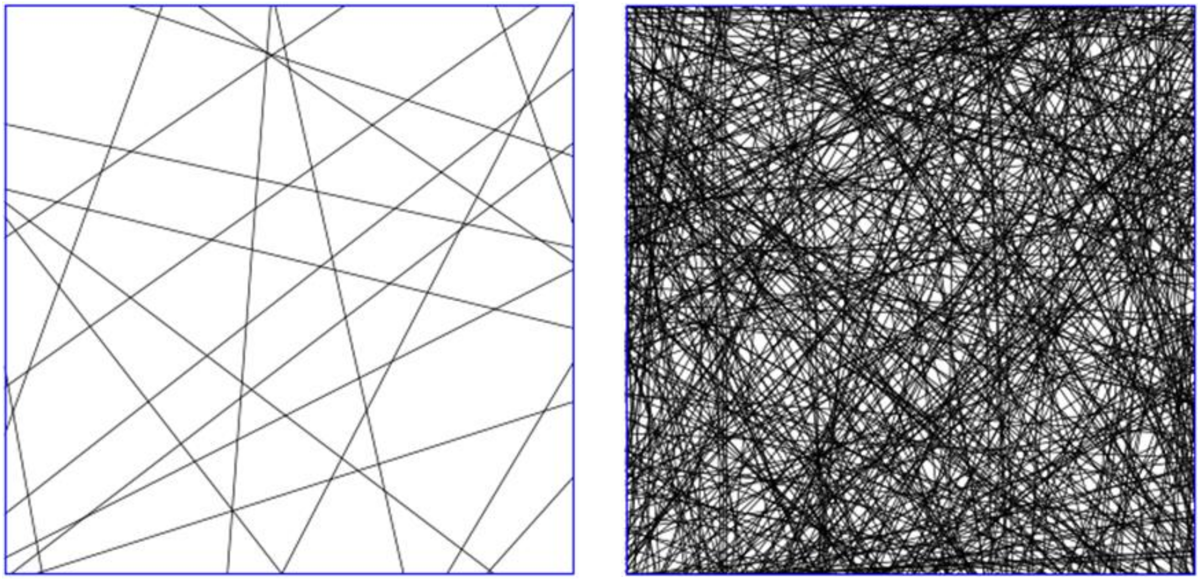

Figure 6.21 Analysis of gap spaces between fibers. (a) Fragment analysis of twenty fibers on a square having 107 fragments. (b) Fragment analysis of 500 fibers having 60,755 fragments.

Running the computer program to subdivide the square into polygon-shaped fragments for 1500 fibers for each of the five methods (a) through (e) and the combined approach resulted in the count, mean, variance, standard deviation, and maximum fragment size shown in Table 6.6. Significant differences were noted among means and variances of distributions. Results were contrasted by considering the value within each distribution for percentiles 5, 25, 50, 75, and 95. The distributions of fragment size shown in Figure 6.22 indicate nearly identical distributions for areas smaller than the median, while the distribution of size rapidly diverged at larger percentiles. The divergence, while noticeable at the 95th percentile, was especially significant at the maximal value for each distribution.

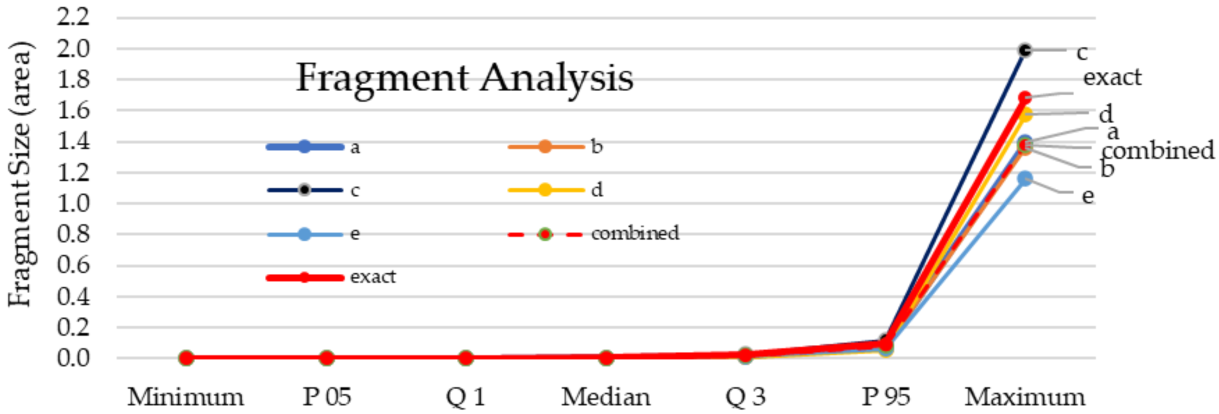

Figure 6.22 Distribution of fragment sizes for each method (note the axis scale is not uniform).

Table 6.6 Analysis of Areas of Fragments for Each Method of Selection with 1500 Fibers

Entities of Random Selection	Fragment Count	Mean Size	Variance	Standard Deviation	Max Size
(a) Two perimeter points	532,854	0.01877	1.47E-03	3.83E-02	1.3935
(b) Interior point and angle	646,535	0.01547	1.05E-03	3.24E-02	1.3634
(c) Perimeter point and angle	366,585	0.02731	3.36E-03	5.79E-02	1.9942
(d) Two interior points	776,998	0.01287	8.79E-04	2.97E-02	1.4634
(e) Interior and perimeter	666,350	0.01501	9.38E-04	3.06E-02	1.1621
(f) Combined (a, c, e)	532,260	0.01881	1.41E-03	3.76E-02	1.3833
(g) Proposed exact solution	450,245	0.02222	1.94E-03	4.41E-02	1.6812

Figure 6.23 and Table 6.7 show the relative sizes of fragments in the central, corner, and side ninths for each of the five methods (a) through (e) and combined approach. Since each method produced a different number of fragments, the sizes are normalized for each method into a relative fragment size. The larger fragment sizes in the central ninth for methods (a) and (c) confirm the observed outward tendency with sparse center. The corner tendency is greater than the side tendency for each method except method (c), which favors the corners over the sides. The combined approach shows a balanced central, corner, and side ninth fragment size, similar to the balanced line density in each of the ninths shown earlier in Figure 6.20. As expected, the proposed exact solution resulted in the most uniform fragment sizes of all methods, for each of the ninths.

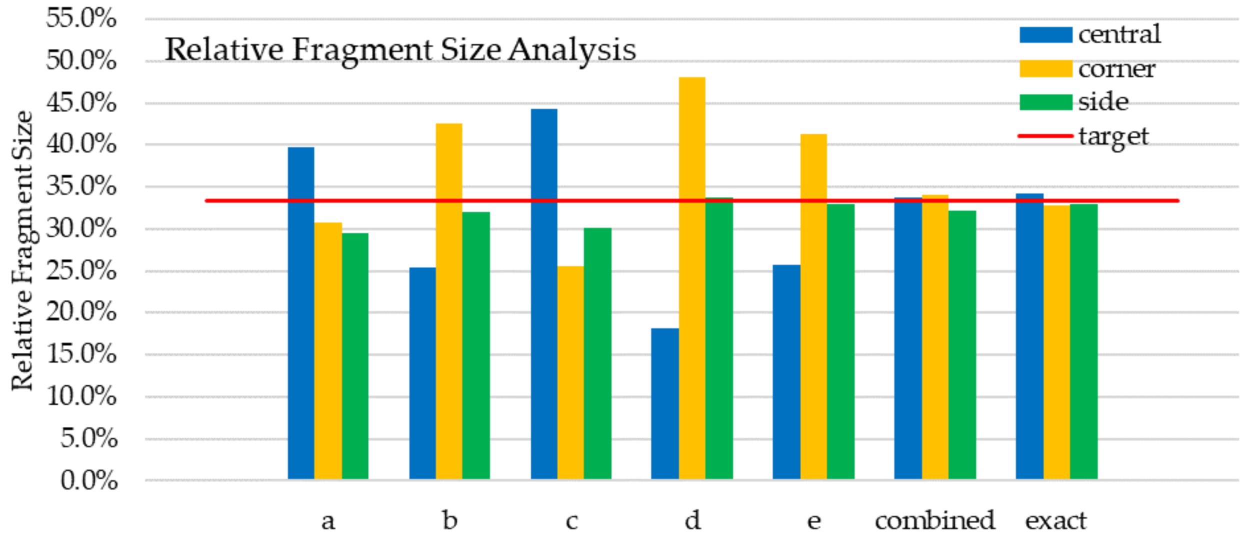

Figure 6.23 Analysis of central, corner, and side tendencies of each method of random fiber placement, based on relative fragment size.

Table 6.7 Analysis of Areas of Fragments for Each Method of Random Fiber Selection

Entities of Random Selection	Central Ninth		Corner Ninths		Side Ninths	
	Count	Mean	Count	Mean	Count	Mean
(a) Two perimeter points	46,057	0.02416	238,241	0.01867	248,556	0.01791
(b) Interior point and angle	98,232	0.01131	235,299	0.01889	313,003	0.01421
(c) Perimeter point and angle	26,686	0.04198	183,748	0.02421	156,151	0.02851
(d) Two interior points	170,064	0.00654	255,948	0.01736	350,986	0.01267
(e) Interior and perimeter	101,027	0.01102	251,007	0.01771	314,316	0.01415
(f) Combination (a, c, e)	58,200	0.01912	230,495	0.01930	243,564	0.01827
(g) Proposed exact solution	48,767	0.02291	162,992	0.02198	201,003	0.02215

6.3.9 Fragment Size Relative to Distance from the Center

The homogeneity of fibrous media can also be evaluated by the relationship, if it exists, between the distance to the fragment centroid from the center of the square and the size of the fragment. Methods of random fiber placement that result in a sparse central ninth, for example, would show larger fragment sizes closer to the center of the square, while methods resulting in dense central ninth would show smaller fragments in the center and larger fragments in the outer ninths. This can be observed in Figure 6.24 and Table 6.8 by plotting the size of each fragment against the distance of the fragment centroid from the center of the square. Plots for each of the methods, including the combined approach and the proposed exact solution, are shown in the appendix.

The magnitude of slope in Figure 6.24 is an indicator of the tendency. A positive slope shows central tendency, while a negative slope shows outward tendency. As expected, methods (a) and (c) show a negative relationship between fragment size and distance from the center, indicating larger fragment sizes in the sparse central ninth, and heavier density of lines with many smaller fragments in the outer ninths. As expected, the slope of the proposed exact solution is nearly flat. Multiple evaluations of the model revealed both slightly positive and slightly negative slope, indicating homogeneous distribution of fragment sizes throughout the square.

The coefficient of determination R^2 indicates how well the fragment sizes follow the given trend. Higher values of R^2 indicate more prevalence of central or outward trend, while lower values of R^2 indicate a lack of trend as expected for a homogeneous distribution. The combined approach shows a low value for R^2, however the lowest R^2 was achieved by the proposed exact solution. The flat slope and low R^2 value for the proposed exact solution confirm the homogeneous nature of the fragment sizes throughout the square.

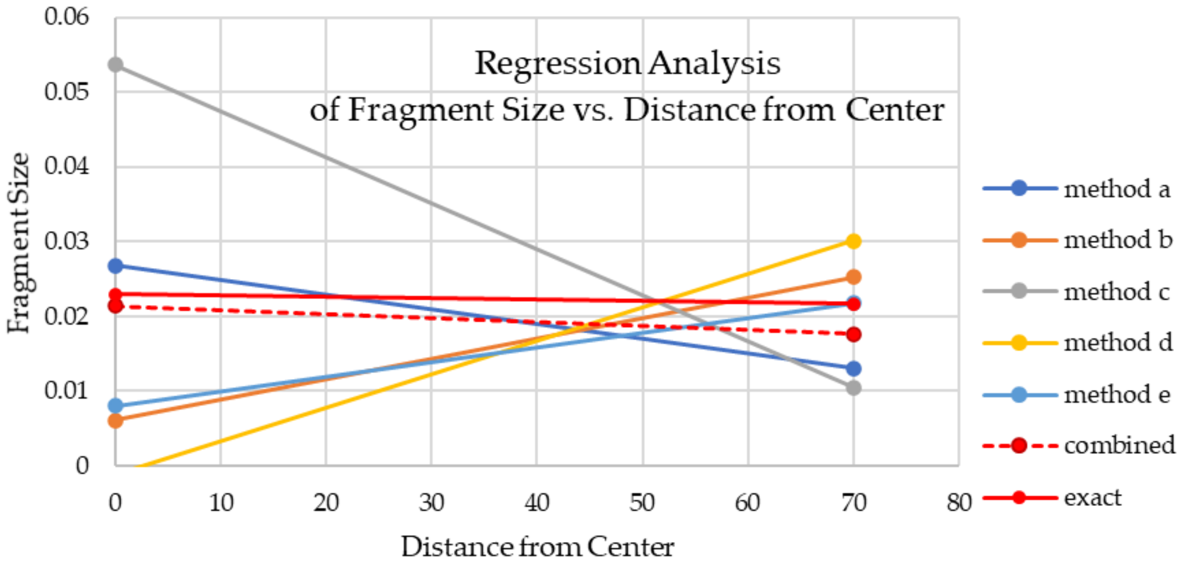

Figure 6.24 Comparison of fragment sizes to distance of fragment centroids from the center of the square.

Table 6.8 Linear Regression Analysis of Fragment Size and Distance from Center

	Entities of Random Selection	Slope	Intercept	Trend	R^2
(a)	Two perimeter points	-1.968E-04	2.683E-02	outward	4.94E-03
(b)	Interior point and angle	2.744E-04	6.042E-03	central	1.39E-02
(c)	Perimeter point and angle	-6.166E-04	5.364E-02	outward	2.18E-02
(d)	Two interior points	4.468E-04	-1.162E-03	central	4.44E-02
(e)	Interior and perimeter	1.969E-04	8.007E-03	central	8.59E-03
(f)	Combination (a, c, e)	-5.373E-05	2.135E-02	balanced	3.84E-04
(g)	Proposed exact solution	-1.907E-05	2.297E-02	balanced	3.43E-05

6.4 Discussion

None of the original five methods presented for random fiber placement on a square produced a homogenous result of line density nor fragment size across the area of the square. This was observed by dividing the square into ninths and evaluating areal line densities, distribution of fragment sizes, and the relationships between fragment size and distance from the center of the square. A combined approach of modulating among random fiber placement methods can produce a homogeneous result. The combination of selecting two perimeter points (method a), selecting a perimeter point and angle of elevation (method c), and selecting a random interior point with random perimeter point (method e) resulted in uniform line density and fragment sizes throughout the media.

The proposed exact solution that considers fibers on the square as parallel rays of light from all possible directions produced a heterogeneous uniform layout. This was confirmed by line density analysis and fragment size analysis in each of the square ninths. The uniform distribution of fragment sizes throughout the square was demonstrated as well by the low slope of the regression analysis, and the very low correlation coefficient that showed a lack of trend. The combined approach of modulating among three different methods is a workable solution. The proposed exact solution should be used for fiber placement on a square if possible, as it demonstrated the highest level of homogeneity of all methods explored throughout this chapter. Demonstration of the proposed exact solution of placing random fibers on a square achieves the objective of this chapter.

The extension of Bertrand's paradox framework from the circle to the square yields interesting observations. Many authors concluded Bertrand's question for random chords on a circle has one exact solution, since only one of three proposed methods of random chord placement yields a result invariant to Euclidean transformation. Similarly, only one method explored in this chapter resulted in a homogeneous distribution of fibers on a square that survived the translational invariance test. While a homogeneous result of line density and fragment size can be obtained by combining multiple methods into a mixed solution, the best method of choosing random fibers on a square is the proposed exact solution as presented.

6.5 Chapter Summary

The objective of this chapter to evaluate random uniform distributions of fibers on a square was achieved. A review of Bertrand's paradox guided the establishment of an evaluation framework for varied methods of uniform random fiber placement. Noting the goal of achieving uniform areal line density with invariance of scale, rotation, and translation, only Bertrand's second method of selecting random chord midpoints uniformly along the radius of a circle achieved this goal. For a square, the five initial methods evaluated for random fiber placement resulted in either central or outward tendency. A combined method introduced for modulating the random fiber selection between outward and central tendency methods resulted in uniform line density across the area of the square. Finally, the proposed exact solution of choosing random fibers on a square from a uniform distribution of centerline angles and radial distance to normal fiber line segments demonstrated a homogeneous result. The uniformity of the resulting fiber placement was confirmed by evaluating the distributions of line density and fragment sizes through the square ninths, as well as a regression analysis and correlation factor for the relationship between fragment size and distance from the center of the square. The framework for evaluating random placement of chords on circles and fibers on squares was carried forward into additional regular shapes of triangle, pentagon, and hexagon.

CHAPTER VII

DEVELOPMENT OF A CONVOLUTIONAL NEURAL NETWORK FOR MODELING AIR FILTRATION EFFICIENCY AND AIR FLOW RESISTANCE

In this chapter, a convolutional neural network is developed and optimized using synthetic training data produced from digital twin replication of air filtration media. Air filter digital twins were built to replicate the physical characteristics of actual nonwoven nanofibrous air filter media. Analytical calculations of air filtration efficiency and air flow resistance, based on the single fiber efficiency model, provided the target data, which was provided to the convolutional neural network along with digital grayscale images of the media. The convolutional model architecture included seven convolution layers and two hidden fully connected layers along with width reduction and depth expansion methods. Twelve model parameters were optimized using training and validation data. The model was then employed to predict the air filtration behavior of real-world filter media based on an SEM image. The successful predictions of the convolutional neural network validates the use of synthetic data derived from digital twin media to train a convolutional neural network for real-world applications.

7.1 Introduction

Filtration efficiency and air flow resistance are important factors in the evaluation of air filter materials, as designers seek to maximize efficiency and minimizing flow resistance. The most reliable method for determining an air filter’s actual efficiency and resistance is through physical experimental testing. However experimental testing can be expensive and time consuming, which opens a potential for computational and analytical modeling of air filtration. Furthermore, empirical models often rely heavily on correction factors and fitted variables, thereby potentially reducing a true understanding of the underlying mechanisms in exchange for a model that more closely agrees with specific physical circumstances. Analytical methods, including the single fiber efficiency (SFE) model, are useful for predicting an air filter's efficiency and flow resistance.

The SFE model is dependent on accurate determination of three parameters: 1) the measurement of fiber diameters, 2) the overall thickness of the filter media, and 3) the volumetric solidity or solid volume fraction of the fibers within the filter media. The SFE model is often difficult to apply to actual air filter media because of the challenge in accurately assessing the fiber diameter sizes, the filter thickness, and filter solidity. As an example, the scanning electron microscope (SEM) image of electrospun stabilized polyacrylonitrile air filter media in Figure 7.1 illustrates the difficulty in applying the SFE model to determine the media's filtration efficiency and flow resistance. It is difficult to predict the filter efficiency and air flow resistance analyzing the image, as the assessment of fiber diameters, filter thickness, and filter solidity are a challenge to accurately assess, prone to human error if investigated manually, and are often very time consuming. Creation of a digital twin filter media enables the assessment of parameters required to predict efficiency and flow resistance through the analytical model. This is accomplished implicitly through the generation software, as the physical parameters of the digital replica are easily obtainable as outputs [39]. The purpose of this chapter is to introduce a machine learning technique to aid the assessment of filtration efficiency and flow resistance of nonwoven nanofibrous air filter media from SEM imagery.

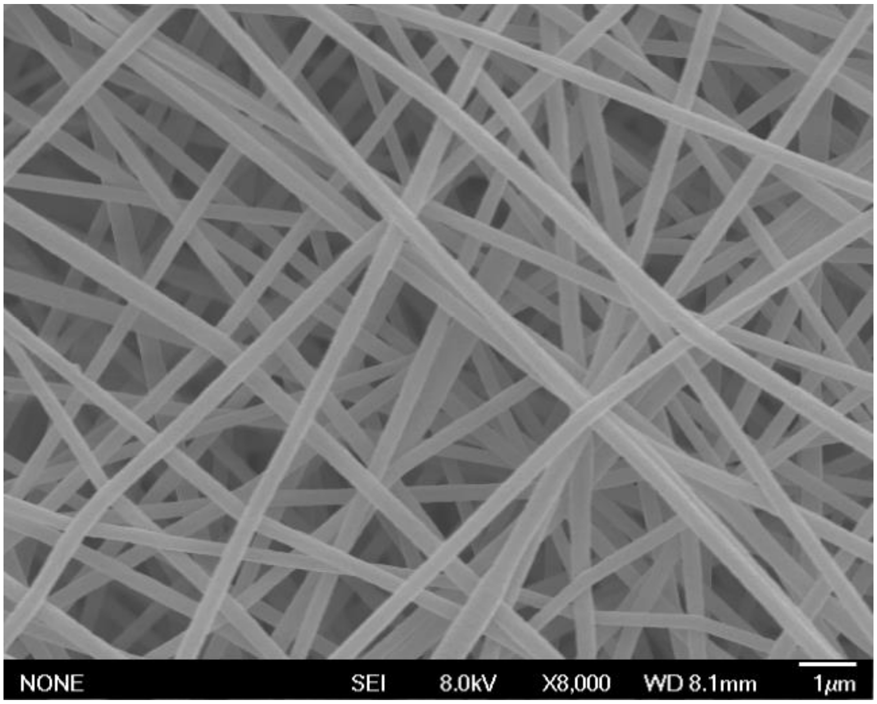

Figure 7.1 SEM image of stabilized polyacrylonitrile air filter media.

7.2 Methodology

The key parameters of nonwoven air filter media can be assessed by creating a digital twin of the filter media using a computer program and geometry creation software [39]. The digital twin geometry can be tuned to mirror the parameters of the SEM image by adjusting the fiber diameter, separation between fibers, and overall thickness. The methodology is illustrated in the flow chart of Figure 7.2.

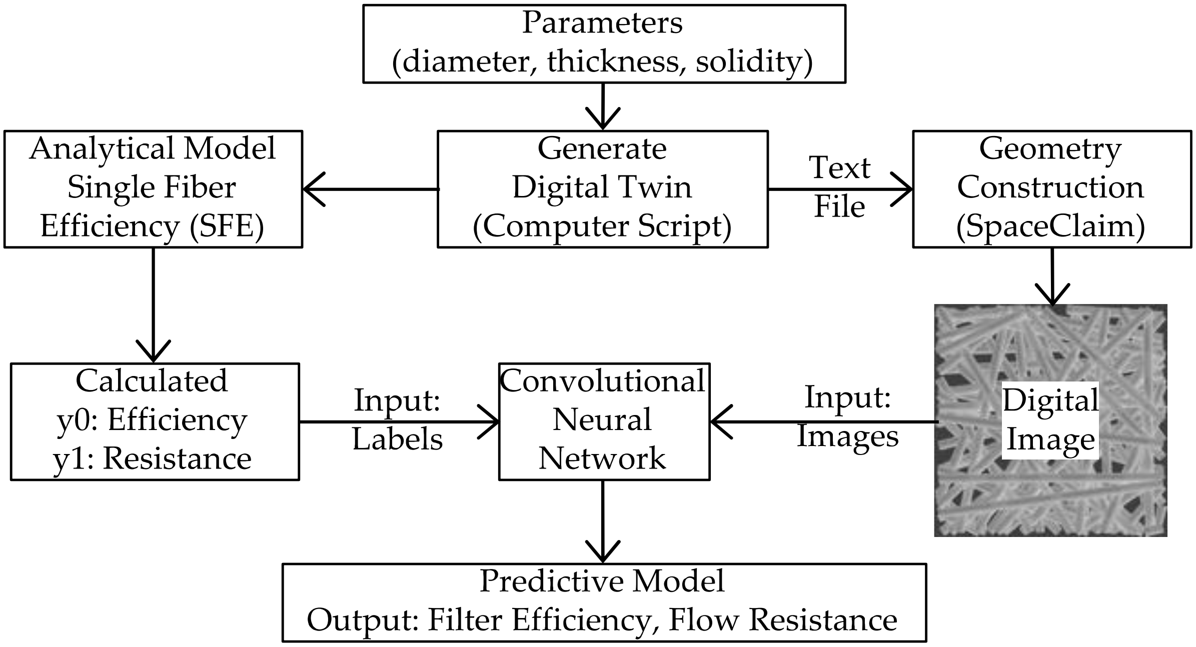

Figure 7.2 Machine learning model process flow chart.

7.2.1 Parameters for Digital Twin Creation

Digital twin geometries resembling the air filter media depicted in Figure 7.1 were constructed using a computer program script that built uniform random distribution of fibers into an air filter media as described in Chapter III [39]. Key parameters for the digital twin included the distribution of fiber diameter sizes, the flexibility of the fibers, spacing between fibers, the density of fibers within the filter media. Using a constant 10 μm × 10 μm dimension, 2100 digital twins were produced using the input parameters described in Table 7.1. For the purposes of this chapter, the term “face coverage” is defined as the ratio of summed cross-sectional area of the fibers normal to the direction of flow compared to the total cross-sectional area of the flow. Face coverage was varied from 1.0 to 3.0 as the design parameter for the 2100 digital twin replicas. Fiber diameters were varied randomly from 0.20 μm to 0.50 μm. Fibers were continually added to the digital twin until the specified face coverage parameter was achieved.

Table 7.1 Design and Input Parameters for Digital Twin Creation

Design and Input Parameters	Symbol	Type	Specified Values
Face coverage (uniform distribution)	FC	Design	1.0 – 3.0
Fiber diameter (uniform distribution)	d_f	Input	0.20 μm – 0.50 μm
Fiber flexibility (fixed)	maxslope	Input	0.15
Spacing between fibers	spacing	Input	1.0

7.2.2 Generation of Digital Twins

The computer program placed fibers into the filter media using a uniform random distribution [39]. Each new fiber rested on previously laid fibers that informed the profile shape of the new fiber. Fibers were continually added to the filter media until the design parameter of face coverage was achieved. The digital twin creation enabled the calculation of filter solidity and thickness, which as previously mentioned are key parameters of the analytical SFE model. The height of the tallest fiber was noted as the overall filter media thickness. The solidity was calculated from the ratio of total fiber volume and volume of the containing enclosure. Table 7.2 lists the results of 2,100 digital twins created for analysis. The computer program produced and exported text files containing endpoints, bending points, and fiber diameters.

Table 7.2 Output Parameters for Digital Twin Creation

Resulting Output Parameters	Symbol	Type	Resulting Values
Solidity, solid volume fraction of fibers	α	Output	5.25% – 13.28%
Thickness of the filter media	t	Output	2.32 μm – 13.53 μm

7.2.3 Geometry Construction (SpaceClaim)

Ansys SpaceClaim was used to create the digital geometry. The scripting feature of Ansys SpaceClaim was used to import the text file data and produce nonwoven fibrous air filter geometry. The geometry was recorded as a snapshot image by SpaceClaim for visual representation of the filter media. The first three images are shown in Figure 7.3 as examples.

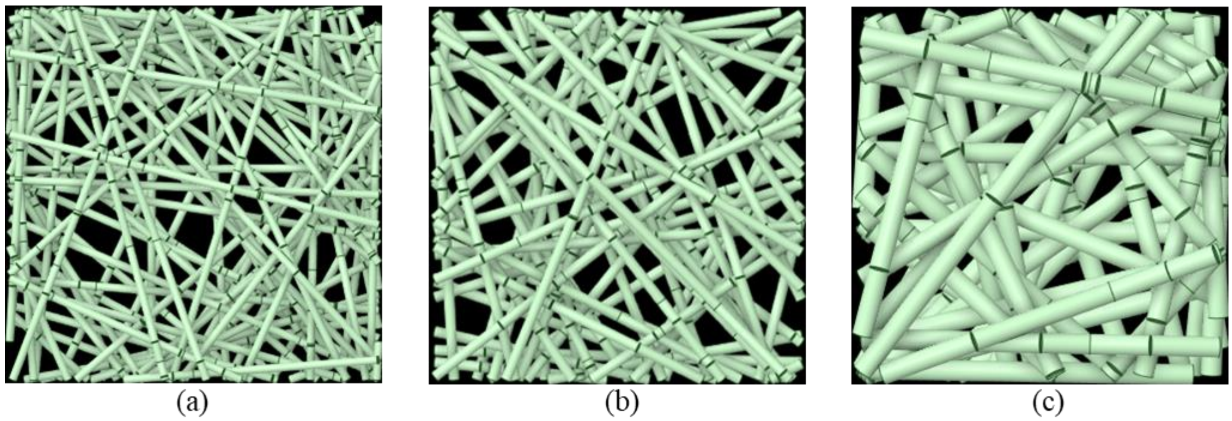

Figure 7.3 Images of first three of 2100 digital twins.

7.2.4 Calculated Filter Efficiency and Air Flow Resistance

The total filter efficiency and air flow resistance were calculated by the computer script using the analytical SFE model shown in Chapter III. Results from the 2,100 digital images are summarized in Table 7.3. As illustrated by the left side of the flowchart in Figure 7.2, the total filter efficiency (E_{F}) and air flow resistance (ΔP) calculated by the SFE model are provided as input target data “y0” and “y1” into the machine learning model.

Table 7.3 Output Parameters and Calculated Analytical Results

Description	Symbol	Type	Results
Total filter efficiency	E_{f}	Calculated	42.0% – 98.1%
Air flow resistance (pressure drop)	ΔP	Calculated	14.0 – 102.4 Pa

A three-dimensional representation of the air filtration efficiency related to the fiber diameter, media thickness, and filter solidity is shown in Figure 7.4. The fiber diameter, media thickness, and filter solidity are the key parameters used in Equations 3.1 through 3.36 to determine the filtration efficiency and flow resistance. Figure 7.4(a) suggests a correlation between the fiber diameter, filter thickness, and resulting filtration efficiency. This figure demonstrates the importance of small diameter fibers, as the most efficient filters had the smallest fiber diameters. Figure 7.4(b) suggests a correlation between filter solidity, fiber diameter, and resulting filtration efficiency, as the most efficient filters had the highest solidity and smallest fiber diameters.

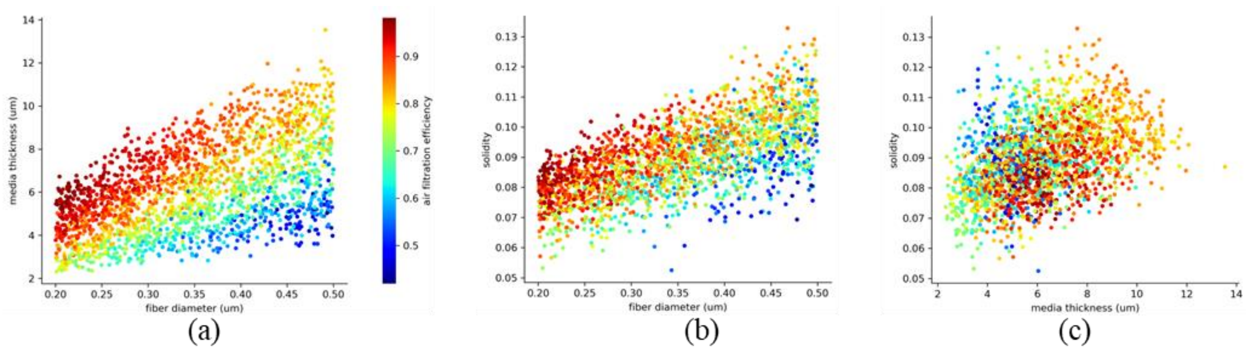

Figure 7.4 Air filtration efficiency related to fiber diameter, filter solidity, and media thickness. (a) Efficiency related to fiber diameter and media thickness. (b) Efficiency related to fiber diameter and solidity. (c) Efficiency related to media thickness and solidity.

Similarly, a three-dimensional representation of the air flow resistance related to the fiber diameter, media thickness, and filter solidity is shown in Figure 7.5. Comparison of Figure 7.4(a) with Figure 7.5(a) suggests a correlation between the filter efficiency and air flow resistance, as the most efficient filters also have the highest pressure drop. Figures 7.5 and 7.6 together demonstrate the difficulty of designing air filter media with high efficiency and low air flow resistance.

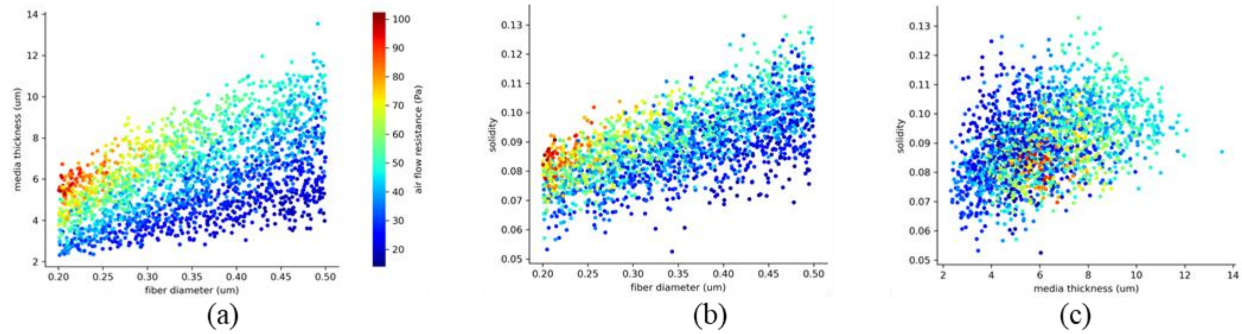

Figure 7.5 Air flow resistance related to fiber diameter, filter solidity, and media thickness. (a) Flow resistance related to fiber diameter and media thickness. (b) Flow resistance related to fiber diameter and solidity. (c) Flow resistance related to media thickness and solidity.

7.2.5 Digital Image Refinement

The digital images of Figure 7.3 were improved to more closely resemble the fibers in the SEM image. In the original SEM image of Figure 7.1, the fibers appear backlit with lighter coloring on the edges and darker coloring along the fiber centerline. SpaceClaim could not match that color scheme. However SpaceClaim could match the color scheme of the inverted SEM image of Figure 7.1, shown in Figure 7.6(a), with darker fiber edges and lighter fiber centerlines. The SEM image was therefore inverted for color matching, with the intent of inverting the resultant SpaceClaim images to match the original SEM image. Figure 7.6(a) shows the inverted SEM image cropped to 10 µm x 10 µm, while Figure 7.6(b) shows the digital twin constructed to the same real size dimensions. Both images are [512, 512] pixel dimensions.

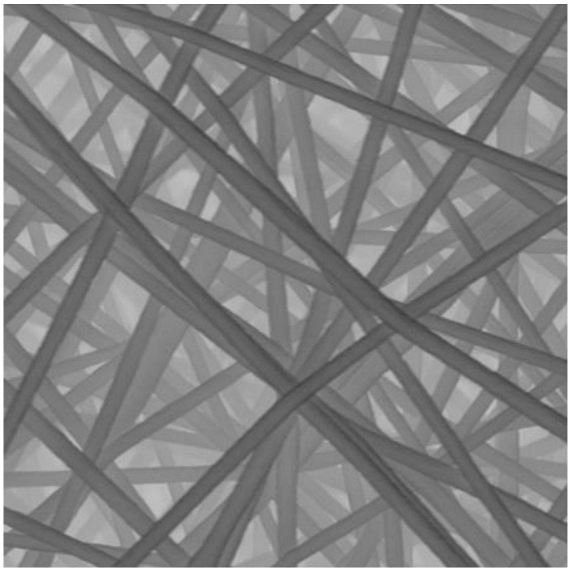

(a)

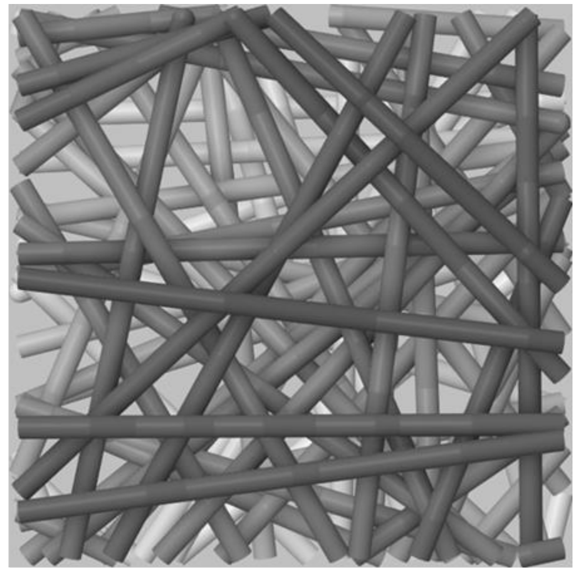

(b)

Figure 7.6 Inverted SEM image and original digital twin. Images are sized at [512, 512] pixels. (a) Inverted 10 μm x 10 μm SEM image. (b) Digital twin of same size.

7.2.5.1 Digital Twin Color Scheme

The digital twin color scheme of Figure 7.6(b) was created to replicate the color patterns seen in the inverted SEM image of Figure 7.6(a). The background color in SpaceClaim was set to “silver” which provided the closest match to the SEM background color. The inverted SEM image provides a sense of depth through lighter colors of fibers that are deeper within the nonwoven mesh. In order to replicate this effect with the digital twin fibers, the color designation of each fiber was varied based on the depth of the fiber in the mesh. The deepest fibers were given a color of (160, 160, 160), while the fibers closest to the surface were given the color (60, 60, 60). This color scheme produced the digital twin images, that when inverted, approximated the colors of the SEM image as shown in Figure 7.7.

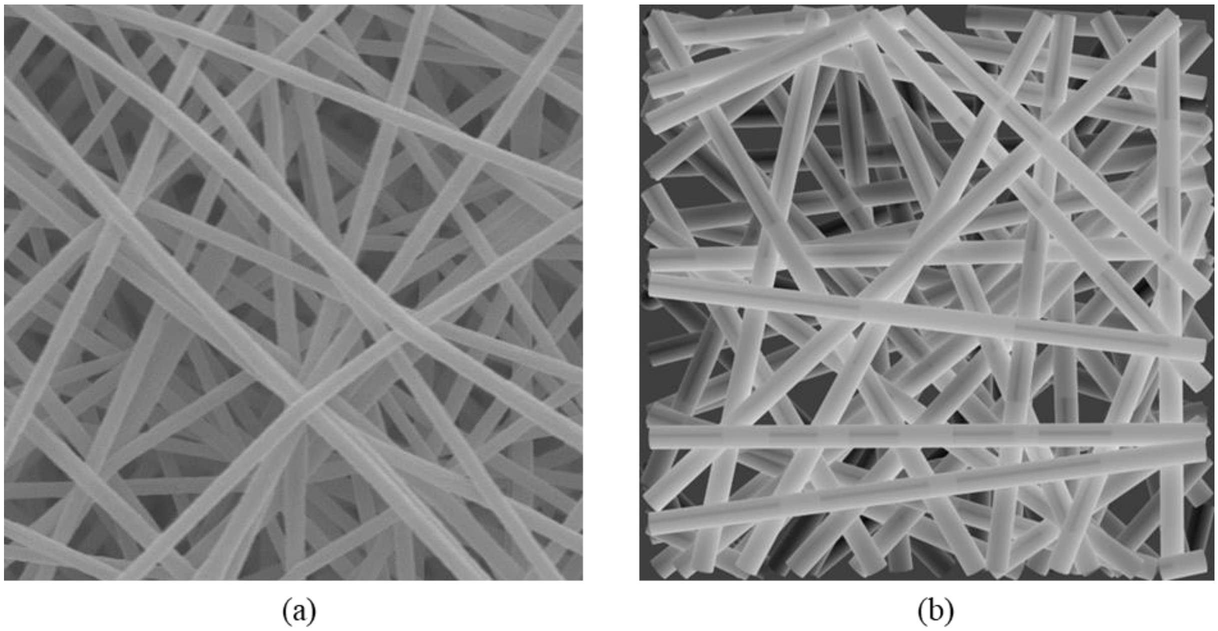

Figure 7.7 Actual SEM image and inverted digital twin. Images are sized at [512, 512] pixels. (a) SEM image. (b) Inverted digital twin image.

7.2.5.2 Digital Image Pixel Dimensions

To save computational effort, all images were resized from dimensions [512, 512] to width and height dimensions of [64, 64] pixels, as shown in Figure 7.8. Larger dimension images may increase the accuracy of the machine learning model however require greater computational effort. The Python Imaging Library (PIL) was useful in adjusting the digital images as required. A total of 2,100 digital twin images similar to Figure 7.8(b) were prepared for input into the machine learning model.

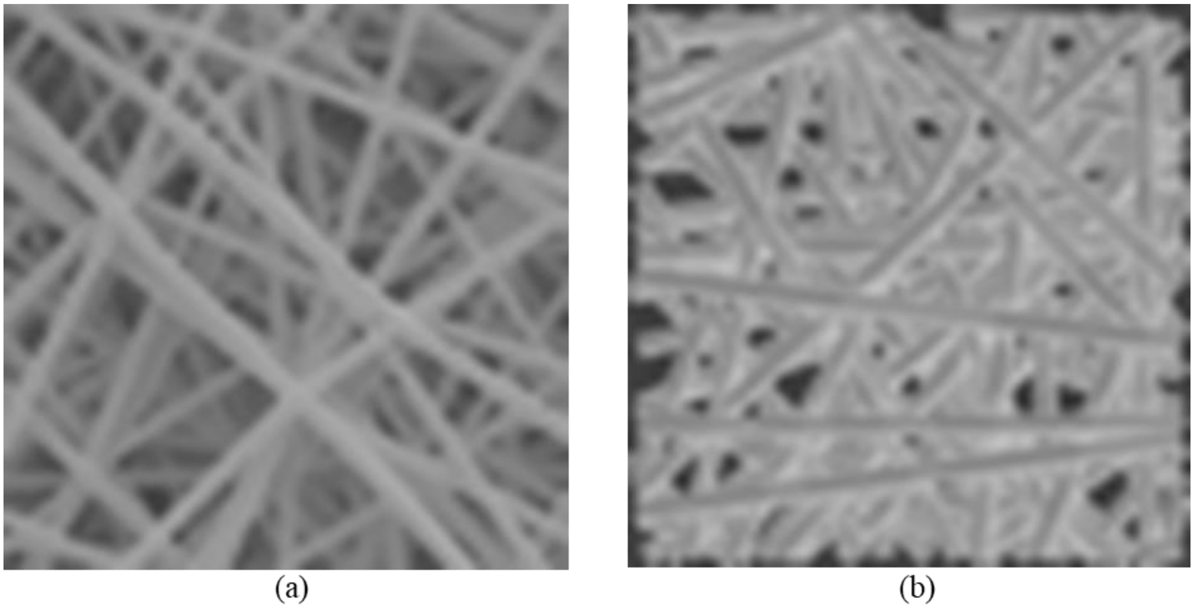

Figure 7.8 Images resized to 64x64. (a) SEM image. (b) Inverted digital twin image.

7.2.6 Manual Prediction by Human Visual Observation

A rough estimation of filtration efficiency and flow resistance can be achieved by visual observation of the SEM image and comparison to the synthetic image of a digital twin. The parameters of the digital twin model can be adjusted until it visually matches the SEM image. For example, the digital twin replica shown in Figures 7.7(b), 7.8(b), and 7.9(b) was created with fiber diameters of 425 nm, filter thickness of 8.55 μm, and filter solidity of 10.4%. This replica reasonably resembles the SEM image of Figures 7.7(a), 7.8(a), and 7.9(a). With an airflow velocity of 2.5 cm/sec at room temperature, the SFE model analytically calculates a total filter efficiency of 84.0% with an air flow resistance of 48.7 Pa for 300 nm particles. This can be taken as a reasonable approximation of the filter performance through manual observation.

7.3 Convolutional Neural Network for Air Filter Media Performance Prediction

While the filter efficiency and flow resistance can be predicted by visual observation, a convolutional neural network (CNN) for regression provides an alternative machine learning prediction. A CNN model was created using Keras Tensorflow following the basic architecture of convolutional layers, feature map dimension reduction, and fully connected layers as shown in Figure 7.9. The digital twin image data was used as the model input, while the analytically calculated air filtration efficiency and air flow resistance became the target data. The basic architecture was created by observing notable CNNs.

7.3.1 Architecture of Notable CNNs

Basic architecture of CNNs consist of four stages: data input, convolution layers, fully connected layers, and data output. The model architecture was constructed through observation of previous well known successful CNN architecture, to include AlexNet, VGG Net, and ResNet. The proposed CNN architecture to evaluate air filtration media for efficiency and flow resistance, inspired by AlexNet, VGG, and ResNet, is shown in Figure 7.9 as the “current plan.”

AlexNet is a notable CNN designed by Alex Krizhevsky, Ilya Sutskever, and Geoffrey Hinton [143]. AlexNet, which was trained on ImageNet data which includes over 15 million images from 22,000 categories, won the 2012 ImageNet Large Scale Visual Recognition Challenge (ILSVRC) in 2012. AlexNet consisted of five convolution layers, some of which are followed by feature dimension reduction by striding and pooling, followed by three fully connected layers and softmax activation into 1,000 categories. AlexNet included dropout layers to prevent overfitting, ReLU activation functions, stochastic gradient descent optimization, and data augmentation techniques that included patch extraction, horizontal and vertical translation and reflection. The first convolution layer of AlexNet included 48 filters with kernel size of [11, 11] and strides of four, reducing the feature map dimensions from [224, 224] to [48, 48]. Subsequent convolution layers consisted of various number of filters of kernel size [3, 3]. AlexNet consisted of 62 million parameters and is shown in Figure 7.9.

The Visual Geometry Group (VGG) Net was developed for image classification and object detection by Karen Simonyan and Andrew Zisserman in 2014 [144]. VGG Net achieved the best results for image classification and localization at ILSVRC in 2014, although the overall winner was GoogLeNet. The CNN consisted of six different configurations from eight to sixteen convolution layers followed by three fully connected layers. Each convolution layer of VGG Net consisted of filter kernel size [3, 3]. Five pooling layers were used on each configuration for feature map dimension reduction. The VGG16 configuration consisted of an input layer, thirteen convolutional layers, five max pooling layers, and three fully connected layers as shown in Figure 7.9. VGG Net used data augmentation, ReLU activation for each convolution layer, and batch gradient descent for optimization. VGG16 consisted of 130 million parameters.

Kaiming He, Xiangyu Zhang, Shaoqing Ren, and Jian Sun from Microsoft Research Asia developed ResNet in 2015 with a record depth at the time of 152 layers [145]. Microsoft ResNet won the ILSVRC 2015 for object detection and localization. A key concept introduced by ResNet is the residual block, in which the original image data is passed along with the results of two convolution layers to the next residual block. ResNet18 is a CNN built with 17 convolutional layers followed by one fully connected layer as shown in Figure 7.9.

Two additional notable CNN networks worth mentioning are the ZF Net and GoogLeNet. ZF Net, constructed by Matthew Zeiler and Rob Fergus, won the ILSVRC 2013 for image classification with an 11.2% error rate [146]. It contained an architecture similar to AlexNet with smaller filter kernel sizes. GoogLeNet was constructed by a team from Google Inc., University of North Carolina, University of Michigan, and Magic Leap Inc. led by Christian Szegedy [147], [148]. GoogLeNet contained a complex arrangement of 22 layers to include convolution, max pooling, average pooling, depth concatenation, normalization, and fully connected layers. GoogLeNet introduced the concept of an inception module, which ran four simultaneous convolutions with varied kernel sizes from [1, 1] to [5, 5], and concatenated the filter outputs for injection into the next inception module. Another notable feature of GoogLeNet was the depth reduction achieved by adding [1, 1] convolutions with fewer filters in each inception module. GoogLeNet won the ILSVRC 2014 overall competition.

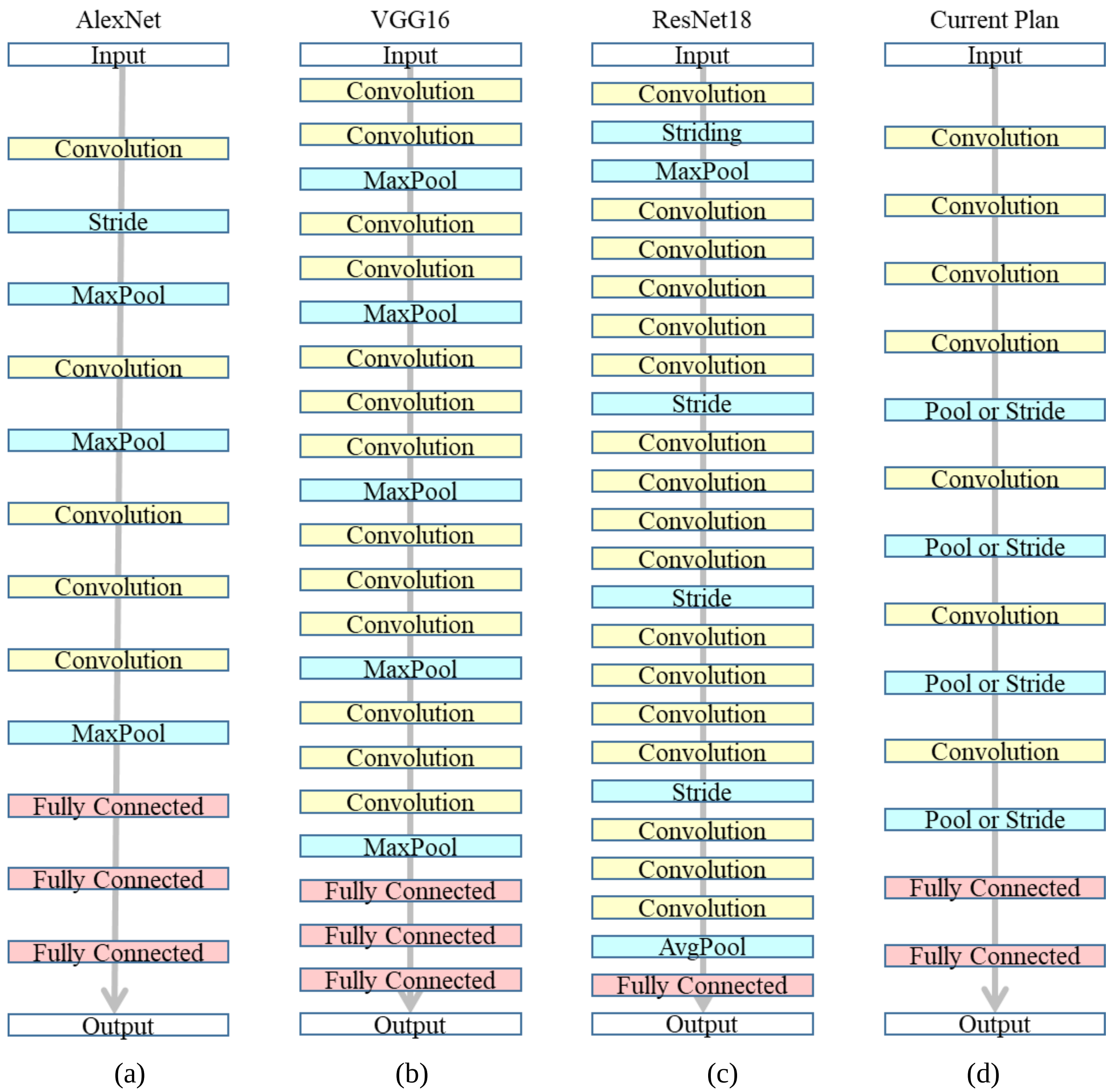

Figure 7.9 Comparison of notable CNN architecture with planned architecture. (a) AlexNet. (b) VGG16. (c) ResNet18. (d) Current Plan.

7.3.2 Data Preparation

7.3.2.1 Image Data

The images were scaled and cropped into a consistent format using PIL. The SEM images were in a two-dimensional grayscale format as [width][intensity], while the digital twin images were in portable network graphic (.png) format, having three channels, [width][height][RGBA]. The third dimension of .png files denotes the intensity of the colors red, green, blue, and the opacity. For compatibility with the SEM image, the digital twin images were converted into grayscale format. The images were loaded into data arrays and converted into grayscale three-dimensional format [width][height][intensity] for compatibility with TensorFlow. A batch dimension was added to the image data array.

7.3.2.2 Analytical Target Data for Filtration Efficiency and Flow Resistance

The analytical air filtration efficiency associated with each digital twin, as calculated with the SFE model, was loaded as the “y0” target data with a range from 0.420 to 0.981. The analytical air flow resistance value for each digital twin was likewise loaded as the “y1” value, having a range from 14.0 to 102.4 Pa.

7.3.2.3 Data Normalization or Standardization

Common practice for a CNN network is to standardize or normalize the input data. Standardizing data consists of shifting the mean to zero by subtracting the mean, then dividing by the standard deviation. Normalizing the data between zero and one is accomplished by subtracting the minimum value then dividing by the range. Normalizing the data from negative one to one is accomplished by subtracting the minimum value, subtracting half of the range, then dividing by half of the range.

The first hyperparameter optimization task was whether or not to normalize or standardize the input data. The model was tested with normalized, standardized, and raw data for 40 epochs. The model performed best with normalized data between zero and one.

7.3.2.4 Data Augmentation

Since the digital twins consisted of randomly oriented fibers representative of air filtration media, data augmentation may be an appropriate method to increase the number of image variants the model sees during training. The air filtration media contained a uniform distribution of fibers invariant to translation and rotation; however the images were not invariant to transformation of scale. As shown in Figures 7.5 and 7.6 above, larger and smaller fiber diameter sizes have an impact on the air filtration efficiency and air flow resistance. A data generator was considered in the CNN to translate and reflect the digital images, while scale adjustments were not allowed because of scale invariance horizontally and vertically.

The second optimization choice was whether to use data augmentation. The model was first run with no data augmentation then re-run with data augmentation for 40 epochs, to include width-shifting by 0.1, height-shifting by 0.1, horizontal flip, and vertical flip of the input images. Data augmentation did not significantly improve the model performance. The CNN was optimized without data augmentation.

7.3.2.5 Data Split

The 2,100 sets of image data with target data labels were split into arrays for training, validation, and testing as shown in Table 7.4. Validation data is intended for use during the model fit training process, while test data is intended to evaluate the model after it is trained. Two hundred digital twins were extracted from the data set for model validation. During model training, the performance of the model was monitored by graphing the loss history of the training data and validation data. One hundred digital twins were extracted from the data set for model testing. Upon completion of training, the minimum and average accuracy was recorded for test data by comparing the expected values to the predicted values.

Table 7.4 Data Arrays for Training, Validation, and Testing

Array Name	Dimensions	Contents	Purpose
x_train	[1800][64][64][1]	Image data	Model Training
x_val	[200][64][64][1]	Image data	Model Validation
x_test	[100][64][64][1]	Image data	Model Evaluation
y_train	[1800][2]	Efficiency and Resistance	Target for Training
y_val	[200][2]	Efficiency and Resistance	Target for Validation
y_test	[100][2]	Efficiency and Resistance	Target for Evaluation

7.3.3 Convolution Layers

The essence of a CNN is the convolutional layers that create feature maps from input images. The number of convolution layers is an important consideration. Based on the relative simplicity of the input image data and inspired by common CNN architecture shown in Figure 7.9, an eleven-layer model was selected with one input layer, seven convolution layers, two fully connected hidden layers, and one binary output layer. For each convolution layer, key parameters to optimize include the number of filters, the kernel size, the mode, and stride size.

7.3.4 Network Width Reduction: Feature Map Dimensions

Common practice, as illustrated by notable CNN architecture, is to increase the network depth while reducing the network width. Striding and pooling are two methods to reduce feature map dimensions. Whether to use, and when to use striding and pooling are important considerations. The first three layers were set to contain no feature map reduction. The third optimization was whether to use max pooling, average pooling, or striding to reduce the feature map dimensions for each of the final four convolution layers.

7.3.4.1 Pooling Layers

Maximum or average pooling layers commonly appear in CNN models to reduce the output dimension. A pooling kernel size [2, 2] reduces the output size from the input size by one half, by either choosing the maximum or average value of the four datapoints. For a [64, 64] dimension input, the first max pooling layer reduces the output to [32, 32], the second layer reduces to [16, 16], and so on.

7.3.4.2 Striding

The stride determines whether the filter kernel will apply at each possible location along the image, or whether it skips. A stride of two will apply the filter kernel to every other location, effectively reducing the image dimensions by one half. In this way, a stride of two is an alternative to pooling for network width reduction.

The model was evaluated for 40 epochs first with max pooling layers, re-evaluated with average pooling, and re-evaluated for convolution stride length of two. While the model performed slightly better with max pooling than with average pooling, the model performed best with convolution strides of two. The model was optimized by removing the pooling layers and achieving feature map dimension reduction using stride length two in the final four convolution layers.

7.3.4.3 Mode

Also known as padding, the mode describes whether and how much the filter kernel extends beyond the image, which makes a difference in the output dimension. A mode of “same” will extend the kernel beyond the image boundary just enough to create an output dimension the same as the input dimension. A mode of “valid” fits the kernel fully onto the image at all locations, thereby creating a feature map dimension slightly smaller than the input dimension. The planned CNN model will use a mode of “same” throughout.

7.3.5 Network Depth Production: Filters

The number of filters produced by each convolution layer reflects the CNN depth. A common convention is to increase the depth throughout the network by increasing the number of filters. The planned CNN architecture consisted of an initial convolution depth of four filters, which doubles in size for each convolution, for a final depth of 256 filters. The specification of filters in this manner was selected, not optimized, to increase the network depth.

7.3.6 Connection Layer

A mechanism is needed to transition the CNN from image analysis to regression. Flattening or global pooling are two methods of connecting the convolution layers to the regression layers. Employing the flatten layer between the final convolution layer and first fully connected layer is a method of connection without losing information. Each remaining set of feature maps is connected to the regression layers.

An alternative to flatten is global pooling, which consolidates remaining feature maps prior to connection to the regression. Global max pooling selects the dominant feature map of each filter set, while global average pooling constructs an average feature map for each remaining filter set. After feature map dimension reduction from an image size of [64, 64] through four striding or pooling operations, the 256 feature maps result in dimensions of [4, 4]. Using a flatten layer, all sixteen sets of 256 feature maps connect to the fully connected layer.

However, in using a global pooling layer instead of the flatten layer, each of the 256 features are consolidated from sixteen to one, so only one set of 256 feature maps is connected to the fully connected layer.

Using global pooling instead of flatten reduces the trainable parameters in the first fully connected layer from 1,048,832 to 65,792, matching the trainable parameters in the second fully connected layer. This significantly reduces the total model parameters by 65% from 1,508,802 to 525,762, resulting in significant reduction of computational effort.

The fourth optimization was whether to use flatten or global pooling for the connection. When tested, the global pooling methods outperformed the flatten method, while global max pooling achieved best performance over 40 epochs. The model was optimized with global max pooling, achieving a significant reduction in computational effort. Feature maps were passed to the fully connected regression layers with dimensions [1, 1, 256].

7.3.7 Fully Connected Regression Layers

The number of fully connected layers performing regression of feature maps into output data is an important consideration. Two hidden fully connected layers were arbitrarily selected, each with 256 nodes to mirror the 256 feature maps of the connecting layer. Figure 7.10 illustrates the CNN network map from input layer through binary regression. A depth of four filters from the first convolutional layer acts upon the input image. The depth is doubled in each subsequent convolution layer for a total of 256 feature maps after the seventh convolution. Modes set to “same” for each convolution layer ensure the output dimensions match the input. Strides set to unity for the first three convolution layers with no pooling maintains constant feature map dimensions equal to the original image dimensions. Width reduction was achieved by reducing feature map dimensions on the final four convolution layers through strides of two.

Starting with a [64, 64, 1] image, network depth production and width reduction resulted in [4, 4, 256] dimensions of the final feature maps. Global max pooling passed the final dimension [1, 1, 256] to the two hidden fully connected regression layers, ending up with a binary linear regression.

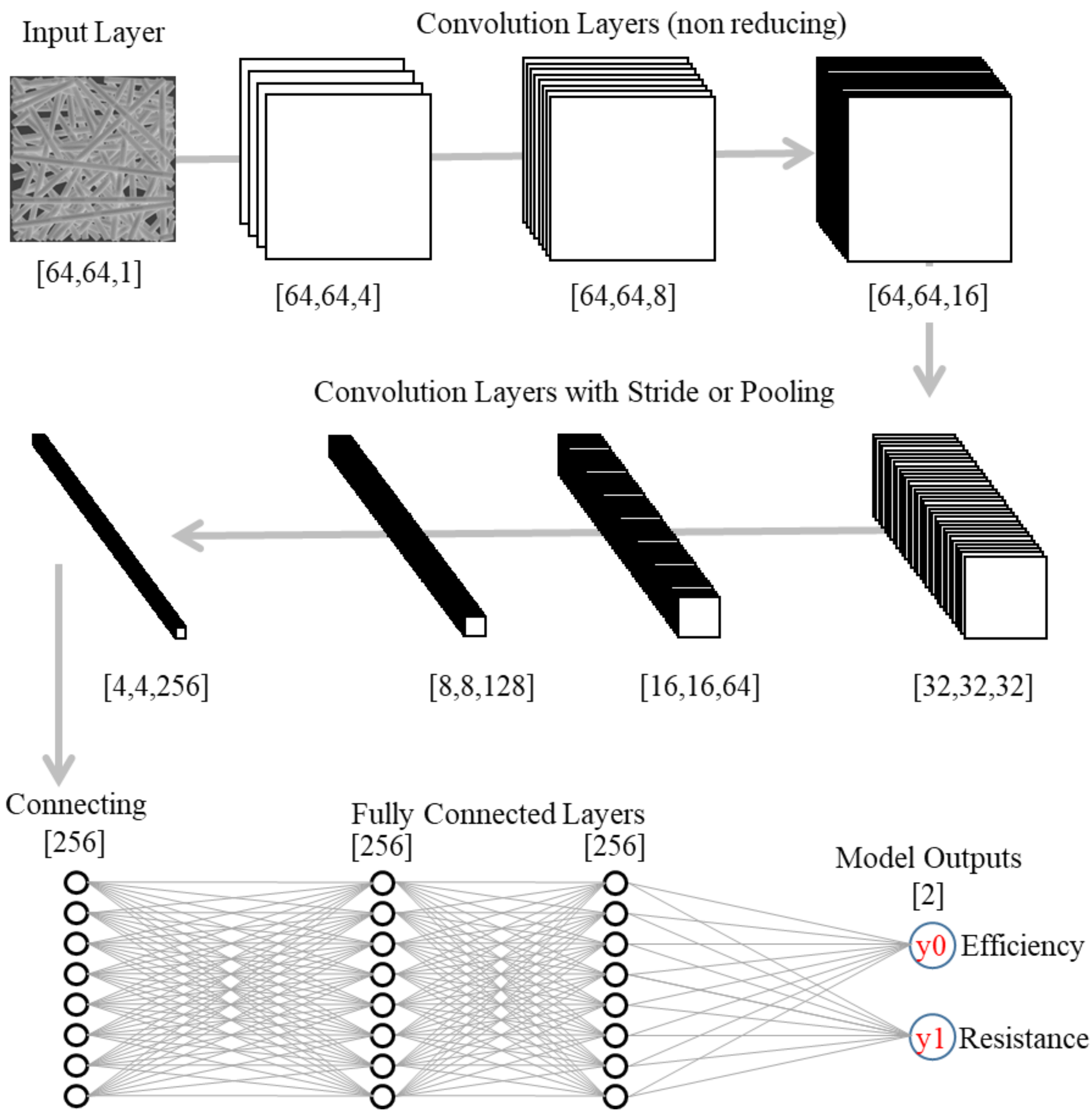

Figure 7.10 Convolutional neural network framework.

7.3.8 Fully Connected Regression Layers

Possible activation functions for the convolution and hidden dense layers include the sigmoid function, the rectified linear unit (ReLU), the exponential linear unit (ELU), the leaky-ReLU, the scaled exponential linear unit (SELU), and the Gaussian error linear unit (GELU). The ReLU was implemented to fix the vanishing gradient problem encountered in early CNN architecture caused by the sigmoid activation function. The ReLU converts any input less than zero to zero, and any input greater than zero is linear output. However, the ReLU activation function may create problems by reducing the update rate for weights and biases if a significant amount of input is negative. The ELU seeks to correct this potential problem by allowing a slightly negative output for negative inputs. The disadvantage of the ELU is additional computational effort is required to calculate the exponential component for the negative term.

The fifth optimization was which activation function to use for each convolution layer and hidden fully connected layer. As shown in Figure 7.11, the best performing activation function was the leaky-ReLU, which was used to optimize the CNN for all but the final layer. The final fully connected layer must have a linear activation function to perform the binary regression.

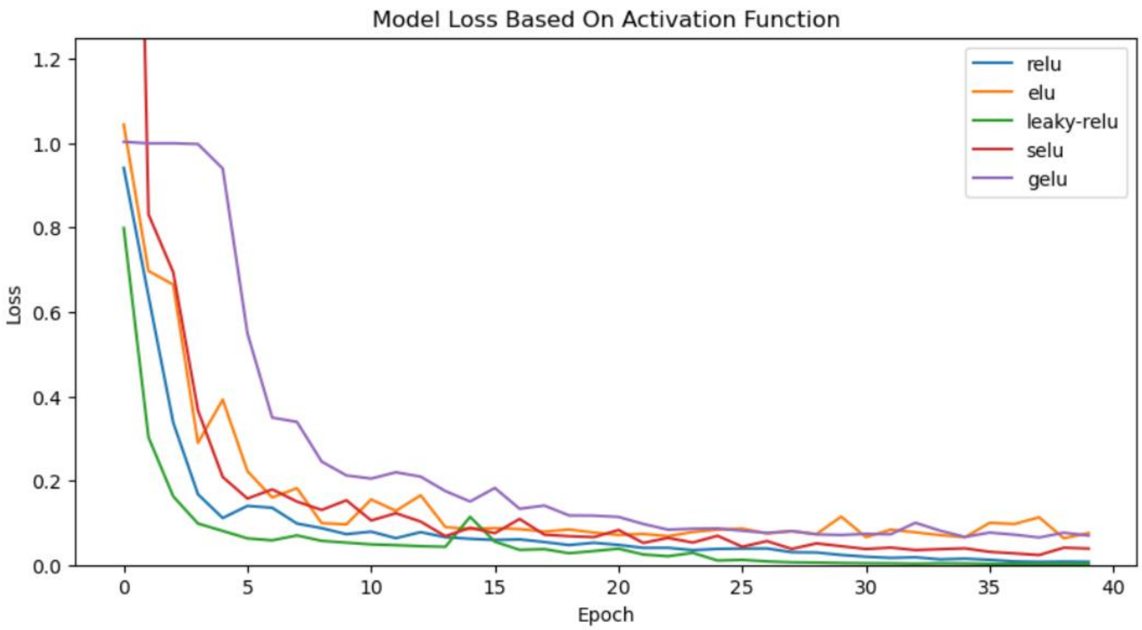

Figure 7.11 Activation function performance over 40 epochs.

7.3.9 Batch Normalization

Batch normalization layers are sometimes used between layers to normalize the output prior to input into subsequent layers. Batch normalization thus maintains the relevance of nodes that produce small numerical output. Whether or not to use batch normalization layers is a choice that was considered for the sixth optimization. The model was run first without batch normalization then re-run with batch normalization for 40 epochs. Adding batch normalization after each convolution layer added 1,016 non-trainable parameters to the model architecture. However, the model performance did not improve with batch normalization, and the CNN was optimized without it.

7.3.10 Kernel Sizing

Smaller kernel sizes such as [3, 3] or [5, 5] are typically used to map small features in an image, while larger kernel sizes such as [7, 7] or [9, 9] help identify larger global features. For kernel sizing, there is no right answer except to try and see which works best. AlexNet started with [11, 11] sized filters, while VGG16 used a consistent [3, 3] kernel size.

The seventh optimization was which kernel size to use for each of the seven convolution layers. The maximum kernel size of the sixth and seventh convolution layer, due to network width reduction, was [16, 16] and [8, 8] respectively. Five convolution kernel sizes were considered for the first six convolution layers: [3, 3], [5, 5], [7, 7], [9, 9], and [11, 11]. Four kernel sizes, [3, 3] through [9, 9], were considered for the seventh convolution layer. This makes 62,500 possible combinations of kernel sizes for the seven layers.

Optuna is a hyperparameter optimization tool that uses a Bayesian optimization algorithm to evaluate options. Optuna starts with a guess, then chooses subsequent guesses based on results of previous trials. Instead of trying all 62,500 combinations, the hyperparameters were tuned with 160 trials using Optuna. The top twenty trials are shown in Table 7.5. The fourth best score was achieved on the fourth trial, while the best score was achieved on the 139th trial.

Table 7.5 Convolution Layer Kernel Size for Twenty Best Trials

Trial	Loss	K1	K2	K3	K4	K5	K6	K7	Parameters
t-139	0.03638	[3, 3]	[3, 3]	[11,11]	[9, 9]	[9, 9]	[3, 3]	[5, 5]	1,248,706
t-22	0.03649	[3, 3]	[7, 7]	[9, 9]	[9, 9]	[7, 7]	[9, 9]	[5, 5]	1,769,154
t-109	0.03747	[3, 3]	[3, 3]	[11,11]	[11,11]	[9, 9]	[11,11]	[5, 5]	2,186,690
t-4	0.03764	[3, 3]	[7, 7]	[11,11]	[5, 5]	[5, 5]	[9, 9]	[5, 5]	1,696,450
t-83	0.03786	[3, 3]	[3, 3]	[5, 5]	[9, 9]	[7, 7]	[9, 9]	[5, 5]	1,760,706
t-84	0.03803	[3, 3]	[3, 3]	[5, 5]	[9, 9]	[7, 7]	[9, 9]	[5, 5]	1,760,706
t-158	0.03809	[3, 3]	[3, 3]	[9, 9]	[9, 9]	[9, 9]	[7, 7]	[5, 5]	1571266
t-89	0.03848	[3, 3]	[3, 3]	[11,11]	[9, 9]	[7, 7]	[11,11]	[5, 5]	2,100,674
t-91	0.03890	[3, 3]	[3, 3]	[11,11]	[9, 9]	[7, 7]	[11,11]	[5, 5]	2,100,674
t-115	0.03895	[3, 3]	[3, 3]	[11,11]	[11,11]	[9, 9]	[11,11]	[5, 5]	2,186,690
t-105	0.03910	[3, 3]	[3, 3]	[11,11]	[9, 9]	[9, 9]	[11,11]	[5, 5]	2,166,210
t-149	0.03953	[3, 3]	[3, 3]	[11,11]	[9, 9]	[9, 9]	[3, 3]	[7, 7]	2,035,138
t-106	0.04025	[3, 3]	[3, 3]	[11,11]	[9, 9]	[9, 9]	[11,11]	[5, 5]	2,166,210
t-104	0.04048	[3, 3]	[3, 3]	[11,11]	[9, 9]	[9, 9]	[11,11]	[5, 5]	2,166,210
t-142	0.04080	[3, 3]	[3, 3]	[11,11]	[9, 9]	[9, 9]	[3, 3]	[5, 5]	1,248,706
t-132	0.04099	[3, 3]	[3, 3]	[11,11]	[11,11]	[9, 9]	[11,11]	[5, 5]	2,186,690
t-141	0.04162	[3, 3]	[3, 3]	[11,11]	[9, 9]	[9, 9]	[11,11]	[5, 5]	2,166,210
t-112	0.04175	[3, 3]	[3, 3]	[11,11]	[11, 11]	[9, 9]	[11,11]	[5, 5]	2,186,690
t-103	0.04238	[3, 3]	[3, 3]	[11,11]	[9, 9]	[9, 9]	[11,11]	[5, 5]	2,166,210
t-114	0.04350	[3, 3]	[3, 3]	[11,11]	[11,11]	[9, 9]	[11,11]	[5, 5]	2,186,690

From the list of top twenty trials, the convolution layer kernel sizes were selected as [3, 3], [3, 3], [11, 11], [11, 11], [9, 9], [11, 11], [5, 5]. Optuna repeated this combination seventeen times in later optimization trials between t109 and t134, suggesting this is a good combination. The top trials indicate smaller filter sizes are important in the first two convolution layers. The top twenty-nine trials started with a [3, 3] size kernel for the first convolution layer, and eighteen of the top twenty trials followed with [3, 3] kernel size in the second convolution layer. Twenty-eight of the top twenty-nine best trials concluded the final convolution layer with filter kernel size [5, 5], suggesting that kernel size was optimum for the final convolution. Larger filter kernel sizes were optimum for middle convolution layers. Nineteen of the top 23 trials had filter kernel size [11, 11] in the third layer, 25 of top 32 trials had [9, 9] in the fourth layer, 27 of 29 top trials had either [7, 7] or [9, 9] in the fifth layer, and 13 of 22 top trials had [11, 11] in the sixth layer. The loss functions are plotted in Figure 7.12 for the ten best trials.

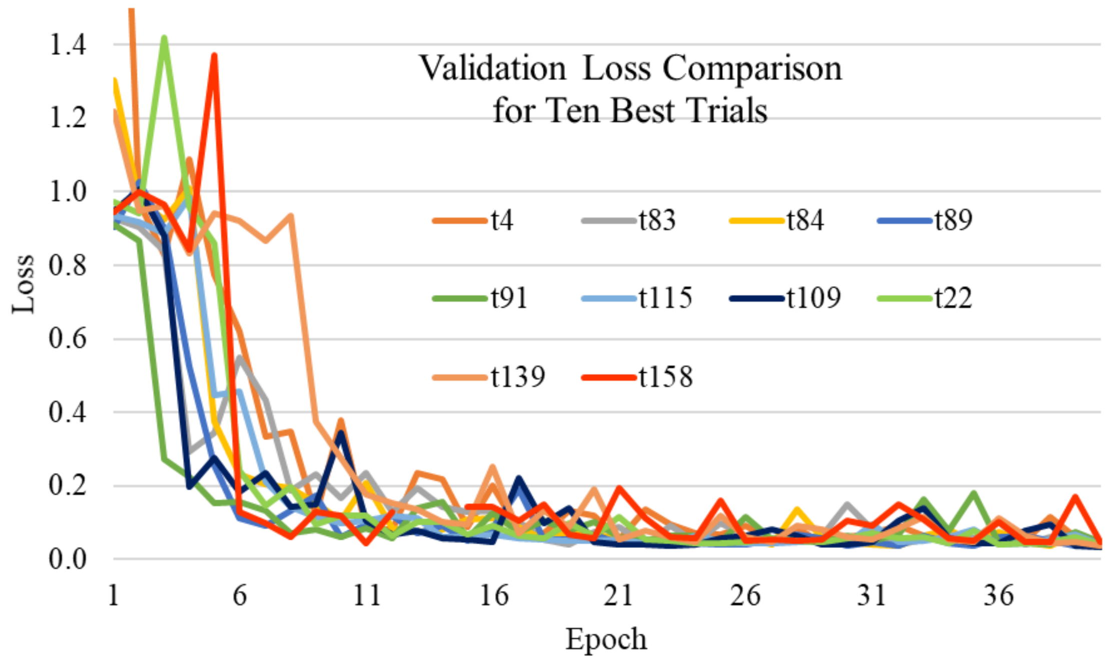

Figure 7.12 Optimization of kernel sizes per convolution layer for top ten Optuna trials.

7.3.11 Total model parameters

The total number of parameters in the model is dependent not only on the number of filters, but also the kernel size and the number of filters in the previous layer. The loss values were plotted against the number of parameters in Figure 7.13 for the 160 trial runs to determine whether a greater number of parameters directly relates to better performance. The twenty top performing models are marked in blue, indicating there is no direct correlation between performance and parameters.

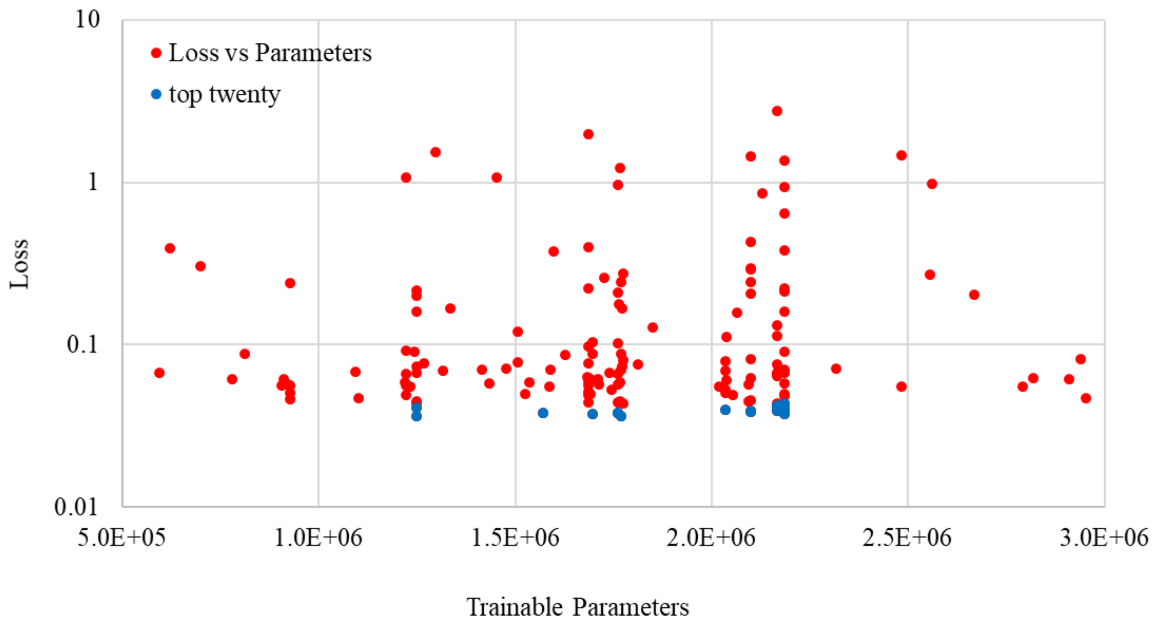

Figure 7.13 Loss plotted against total trainable parameters.

7.3.12 Compiling the Model

7.3.12.1 Optimizer Choices

Two appropriate choices for the model optimizer include adaptive moment estimation (Adam) and stochastic gradient descent (SGD) with learning rate and momentum terms. The eighth optimization was whether to use SGD or Adam for the optimizer. Using the default values for each, the model performed best with the Adam optimizer.

7.3.12.2 Learning Rate Selection

The default learning rate for Adam is 0.001 while the default learning rate for SGD is 0.01. Learning rate scheduling is a technique to initiate the model training with a higher learning rate then reduce the learning rate based on the percentage of completed epochs. What learning rate to use and whether to reduce the learning rate through scheduling are important considerations. The ninth optimization was which learning rate to use with Adam. Using Optuna, learning rates were tested for 30 trials between a low value of 0.0001 and high value of 0.01. The resulting optimum learning rate was 0.001338. The model was run again to compare the default learning rate of 0.001 to the rate 0.001338. The model performed best with the default Adam learning rate of 0.001.

7.3.12.3 Loss Function

For the loss function on a convolutional regression network, two appropriate choices are the mean squared error and the mean absolute error. As the tenth optimization, the model was evaluated with both mean squared error and mean absolute error loss functions. The model performed best and was optimized with the mean squared error function.

7.3.13 Training the Model

7.3.13.1 Batch Size

Common practice is to use batch sizes as powers of two. The eleventh optimization was which batch size to use. The CNN was tested with batch sizes 4, 8, 16, 32, 64, and 128. The model run times were 14, 8, 6, 5, 4, and 4 seconds per epoch respectively, as the larger batch sizes resulted in less computational effort. From the results, batch sizes of 4, 8, 16, and 32 performed slightly better than batch sizes 64 and 128. The model was optimized with batch size 32, which showed good results over 40 epochs.

7.3.13.2 Overfitting Avoidance

The model was initially set to train with 40 epochs. Early stopping is a feature that considers the model performance on validation data and terminates the training at risk of overfitting. Overfitting can be thought of as the model memorizing the input data, which can reduce the performance on validation or testing data. The twelfth optimization was to determine an appropriate number of epochs to fit the model while avoiding overfitting. This is accomplished by monitoring the loss values of the validation set while fitting the model. The Keras callback "early stopping" was employed to monitor the validation loss during training. The model was optimized using the early stopping callback and patience of five iterations.

7.3.14 Hyperparameter Tuning Summary

Table 7.6 summarizes the twelve hyperparameter choices and decisions.

Table 7.6 Hyperparameter Optimization Summary

Parameter	Optimization Choices	Decision
1. Data standardization	Raw, normalize, or standardize	Normalize (0 to 1)
2. Data augmentation	Whether to use data augmentation	No augmentation
3. Width reduction	Pooling or striding	Striding
4. Connection layer	Flatten or global pooling	Global max pooling
5. Activation function	Which activation function	Leaky ReLU
6. Batch normalization	Whether to use batch normalization	No batch normalization
7. Kernel size per layer	[3, 3], [5, 5], [7, 7], [9, 9], or [11, 11]	1:[3, 3], 2:[3, 3], 3:[11,11], 4:[9,9], 5:[9,9], 6:[11,11], 7:[5,5]
8. Optimizer	Choose Adam or SGD	Adam
9. Learning rate	What learning rate to use with Adam	Default 0.001
10. Loss function	Mean squared or mean absolute error	Mean squared error
11. Batch size	Choose 4, 8, 16, 32, 64, or 128	32
12. Overfitting avoidance	How many epochs to avoid overfitting	Early stopping

7.3.15 CNN Model Summary

The final optimized CNN consists of an input layer, seven convolution layers, two hidden fully connected regression layers, and a binary output layer. The optimized CNN model is shown in Table 7.7. The total number of trainable parameters was 2,166,210, with no non-trainable parameters.

Table 7.7 Optimized CNN Regression Model

Input Shape	Layer	Filters	Stride	Kernel	Mode	Output Shape	Parameters
[64, 64, 1]	Input Layer					[64, 64, 1]	0
[64, 64, 1]	Convolution 1	4	1	[3, 3]	same	[64, 64, 4]	40
[64, 64, 4]	Convolution 2	8	1	[3, 3]	same	[64, 64, 8]	296
[64, 64, 8]	Convolution 3	16	1	[11, 11]	same	[64, 64, 16]	15,504
[64, 64, 16]	Convolution 4	32	2	[9, 9]	same	[32, 32, 32]	41,504
[32, 32, 32]	Convolution 5	64	2	[9, 9]	same	[16, 16, 64]	165,952
[16, 16, 34]	Convolution 6	128	2	[11, 11]	same	[8, 8, 128]	991,360
[8, 8, 128]	Convolution 7	256	2	[5, 5]	same	[4, 4, 256]	819,456
[4, 4, 256]	Global Max Pool					[256]	0
[256]	Fully Connected 1					[256]	65,792
[256]	Fully Connected 2					[256]	65,792
[256]	Output Layer					[2]	514

7.4 Results

7.4.1 Image Dimension [64, 64]

Applying the optimized and trained CNN to the SEM image shown in Figures 7.7(a), 7.8(a), and 7.9(a) resulted in a prediction of air filtration efficiency and air flow resistance of the air filter media. Retraining the CNN model and reevaluating the SEM image x times resulted in an average prediction for the filtration efficiency and air flow resistance for the SEM image. The CNN predicted the SEM image had an average air filtration efficiency of 91.1% and produced an air flow resistance of 73.2 Pa.

7.4.2 Retraining and Running the CNN for Additional Image Input Dimensions

One advantage of using global pooling instead of flatten as a connecting layer between convolution layers and fully connected layers is the model is easy to adapt to other initial image dimensions. Since the synthetic training data produced from the digital twin air filter media and the SEM image could support any resolution up to [512, 512], the model was retrained and rerun with higher resolutions. The main difference in the model at higher resolutions is the global max pooling layer applies to larger feature map dimensions. Using resolution [512, 512], the global max pooling layer acts upon feature map dimensions [32, 32, 256] instead of [4, 4, 256]. Essentially the maximum feature map is selected from the pool of 32 instead of the pool of four for each of 256 filters. The higher resolution models still connect to the fully connected layer with dimension [1, 1, 256]. A comparison of image resolutions for the first four sets is shown with Figure 7.14. The [64, 64] image has four times the information of the [32, 32] image, with four times the number of pixels. Similarly, the [128, 128] image has four times the information of the [64, 64] image.

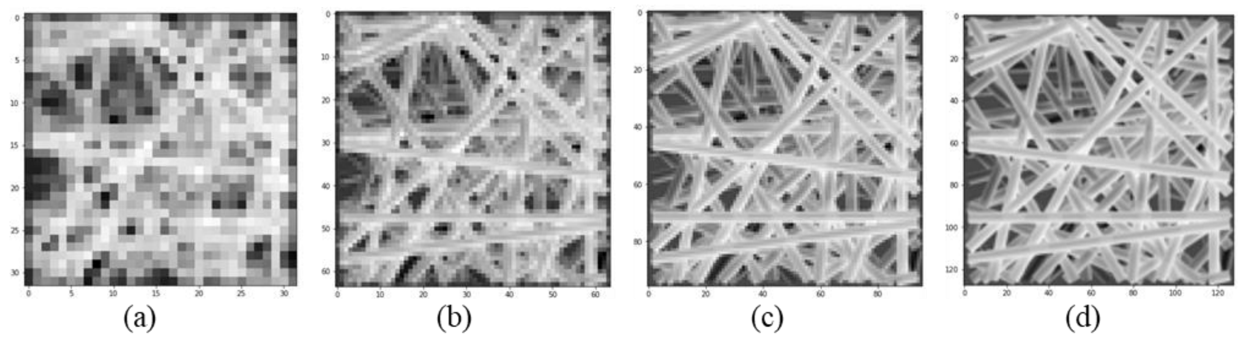

Figure 7.14 Comparison of image resolutions. (a) [32, 32]. (b) [64, 64]. (c) [96, 96]. (d) [128, 128].

Retraining and rerunning the CNN with various input image dimensions ranging from [32, 32] to [512, 512] resulted in air filtration efficiencies and air flow resistance as shown in Figure 7.15 below.

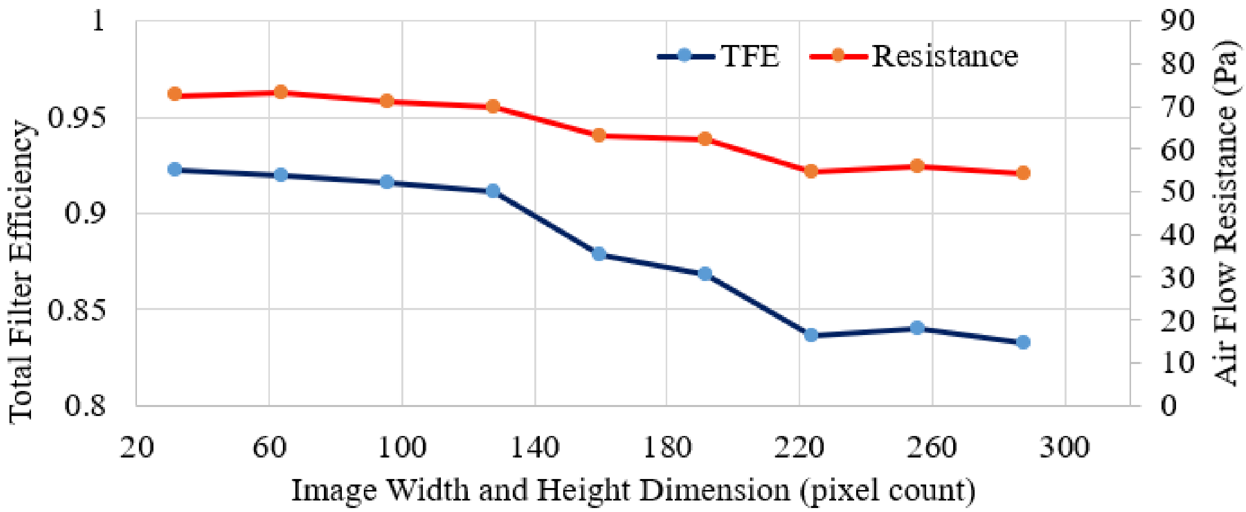

Figure 7.15 Results of the CNN model predictions from [32,32] to [288,288].

The resulting predictions for total filter efficiency and air flow resistance are depicted on Figure 7.16 for the CNN prediction and the manual twin prediction. The training and testing data for the 2,100 digital twins is also shown for comparison.

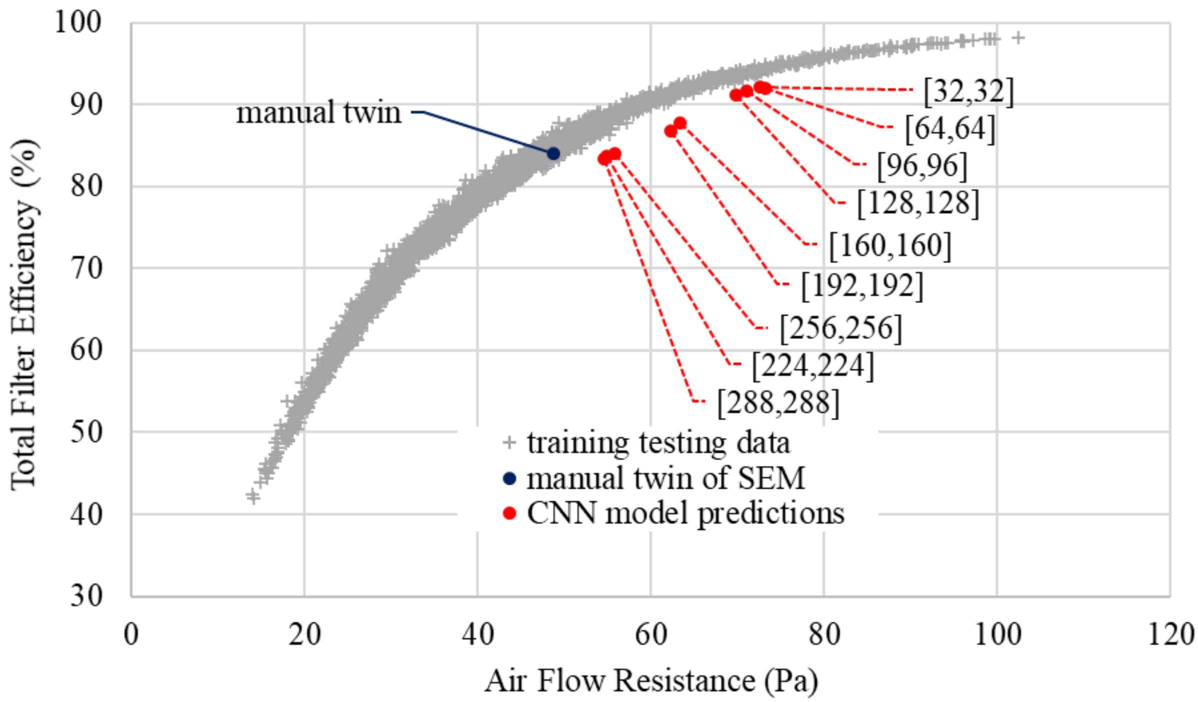

Figure 7.16 Comparison of results from the training data, manual prediction, and CNN predictions for various image dimensions.

7.5 Discussion

7.5.1 Synthetic Training Data

The CNN model presented herein was trained and optimized using synthetic data produced by digital twin replication of actual air filtration media. The model was not exposed to actual air filter media during the optimization and training process. Yet the model successfully predicted values for air filtration efficiency and air flow resistance when exposed to SEM imagery of actual air filtration media. This suggests potential validation of the use of synthetic data to train a CNN intended to predict real world results. However, the model cannot be considered valid unless the actual real world filter efficiency and air flow resistance results are known.

7.5.2 Use of the SFE Model

The SFE model provides a suitable platform for the calculation of the efficiency and pressure drop of air filter media based upon its parameters. However, the limitations of the SFE model must be mentioned. The SFE model at its core is based upon the performance of a lone fiber and is extended to include the effects of neighboring fibers for both particle collection and airflow resistance through the Kuwabara hydrodynamic factor. In its derivation, the Kuwabara factor assumes that the fibers are all parallel and randomly spaced, thus creating a semi-ordered array of fibers. When considering real filtration media, the inherent randomness of the fibers creates tortuous channels through the media. These channels experience increased flow compared to other, less permeable sections of the media, affecting the performance of the media by decreasing the pressure drop and capture efficiency. Since the CNN model presented within this chapter utilizes the SFE model as input target data, it is also implicitly subject to the same limitations. However, there are more elaborate analytical models available to address air filter media inhomogeneity, although naturally they may be expected to be more difficult to implement.

On the subject of media inhomogeneity, it should be noted that the analysis of any air flow characteristics based on an SEM image will be informed only by the theoretical performance of the tiny piece of media seen in the image. The channels created by fiber orientation randomness or areas of the media with biased distribution of diameter sizes will skew the analytical results. With a comparison to real media and SEM images, care must be taken to ensure that the images or number of images gathered is representative of the media as a whole. It must be assumed the macro-performance of the holistic media will differ from the theoretical performance of a single SEM image.

7.5.3 CNN Model Architecture

Based on the relative simplicity of the input data, a simple CNN architecture proved adequate for the task. Since the fibers were placed with a uniform random distribution of position and orientation, the CNN was not tasked to identify different image features at various locations in the image. Although data augmentation was not employed, the translational and rotational invariance of the image enabled the option for augmenting data through rotation, horizontal and vertical shift, and reflection. A simple CNN architecture was inspired by observing the successful performances of AlexNet, VGG Net, and ResNet.

7.5.4 Computer Vision

Analytical predictions of air filtration efficiency and air flow resistance are primarily a result of three parameters: the fiber diameters, the thickness of the air filter media, and the solidity or solid volume fraction taken up by the fibers in the media. These parameters can be visually observed, measured, and estimated for analytical calculations. It is difficult to determine whether the CNN recognized some form of these three parameters or developed new parameters that achieved the same result. The CNN takes as input the raw image data and outputs feature maps by application of convolutional kernels. Observation of the convolutional kernels and feature maps informs our understanding of the convolutional process. Figure 7.17 shows example filters employed by the CNN in various dimensional sizes, while Figure 7.18 shows the original [64, 64] digital twin image and subsequent feature maps created by the seven convolution layers.

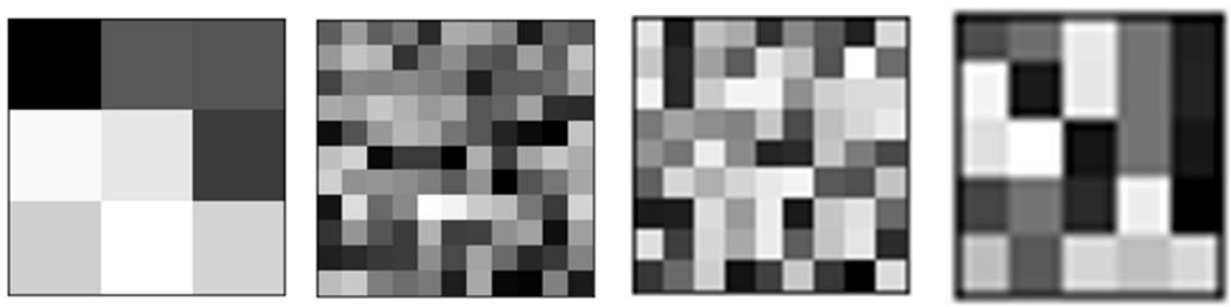

(a) (b) (c) (d)

Figure 7.17 Example filters used by the CNN. (a) [3, 3] filter example in the first and second convolution layers. (b) [11, 11] filter example in the third and sixth convolution layers. (c)[9, 9] filter example in the fourth and fifth convolution layers. (d) [5, 5] filter example in the final convolution layer.

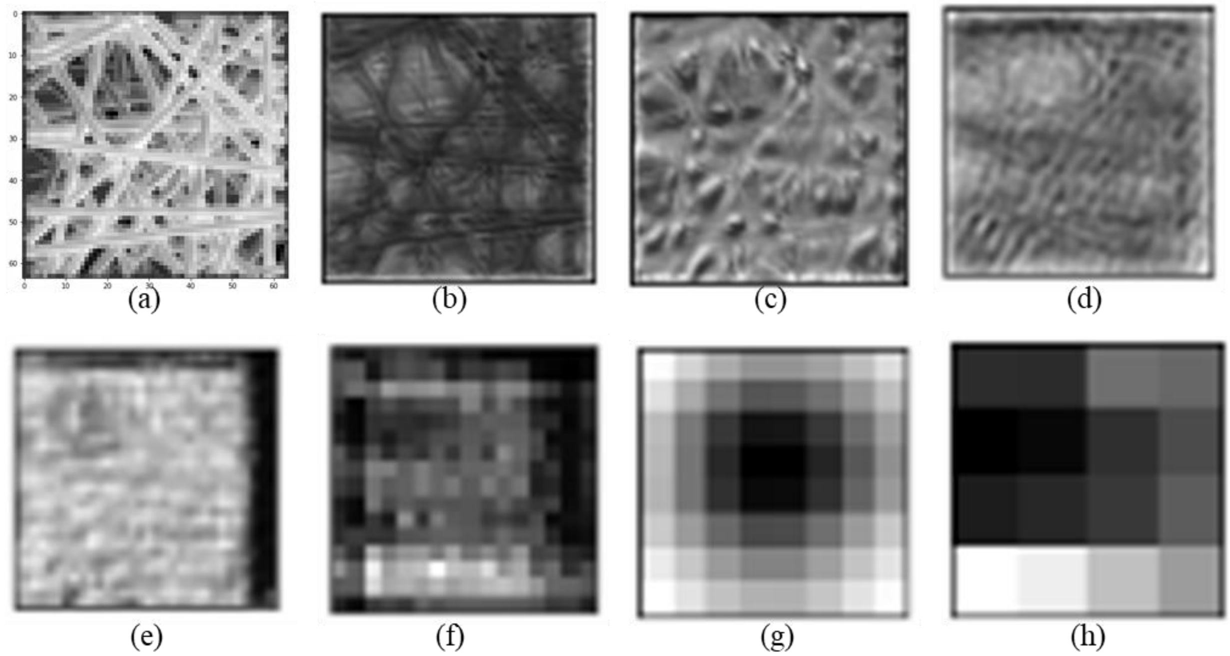

Figure 7.18 Feature map progression. (a) Original image [64, 64]. (b) First convolution [64, 64]. (c) Second convolution [64, 64]. (d) Third convolution [64, 64]. (e) Fourth convolution [32, 32]. (f) Fifth convolution [16, 16]. (g) Sixth convolution [8, 8]. (h) Seventh convolution [4, 4].

7.6 Classification Network for Determination of Fibrous Media

A noted deficiency of the CNN regression network was its agnostic treatment of images. After the network was trained on the digital twin synthetic data, essentially any image that was input into the model produced an output of air filtration efficiency and air flow resistance. While it is possible to carefully check the image prior to exposure to the regression model, another solution is the creation of a classification model that first judges whether the image is fibrous media or something else. Using the same basic architecture of the regression model, a binary classification model was constructed as shown in Table 7.8. The model was constructed with [3, 3] convolution kernels for all seven convolution layers using leaky ReLU activation functions between layers. The final layer used the sigmoid activation function for the binary classification task. The model was compiled with the Adam optimizer, binary crossentropy loss function, and accuracy for metrics.

Table 7.8 CNN Binary Classification Model

Input Shape	Layer	Filters	Stride	Kernel	Mode	Output Shape	Parameters
[64, 64, 1]	Input Layer					[64, 64, 1]	0
[64, 64, 1]	Convolution 1	4	1	[3, 3]	same	[64, 64, 4]	40
[64, 64, 4]	Convolution 2	8	1	[3, 3]	same	[64, 64, 8]	296
[64, 64, 8]	Convolution 3	16	1	[3, 3]	same	[64, 64, 16]	1,168
[64, 64, 16]	Convolution 4	32	2	[3, 3]	same	[32, 32, 32]	4,640
[32, 32, 32]	Convolution 5	64	2	[3, 3]	same	[16, 16, 64]	18,496
[16, 16, 34]	Convolution 6	128	2	[3, 3]	same	[8, 8, 128]	73,856
[8, 8, 128]	Convolution 7	256	2	[3, 3]	same	[4, 4, 256]	295,168
[4, 4, 256]	Global Max Pool					[256]	0
[256]	Fully Connected 1					[256]	65,792
[256]	Fully Connected 2					[256]	65,792
[256]	Output Layer					[2]	257

The model was trained with the same [64, 64] dimension data set of synthetic images from digital twin fibrous media, combined with a [64, 64] dimension data set of random images from the Imagenet64 [143]. An equal number of fibrous and non-fibrous images were shown to the classification model. The image data, loaded into arrays, was normalized between zero and one. The fibrous images were labeled with ones, while the non-fibrous images were labeled with zeros. The first three images from the fibrous images and non-fibrous images are shown in Figures 7.18 and 7.19.

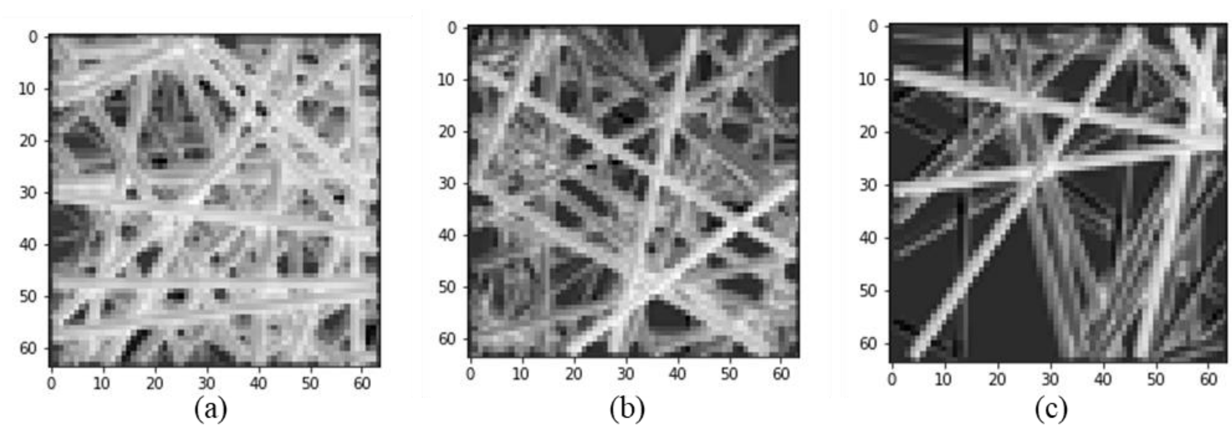

Figure 7.19 Images of fibers, with dimensions [64, 64].

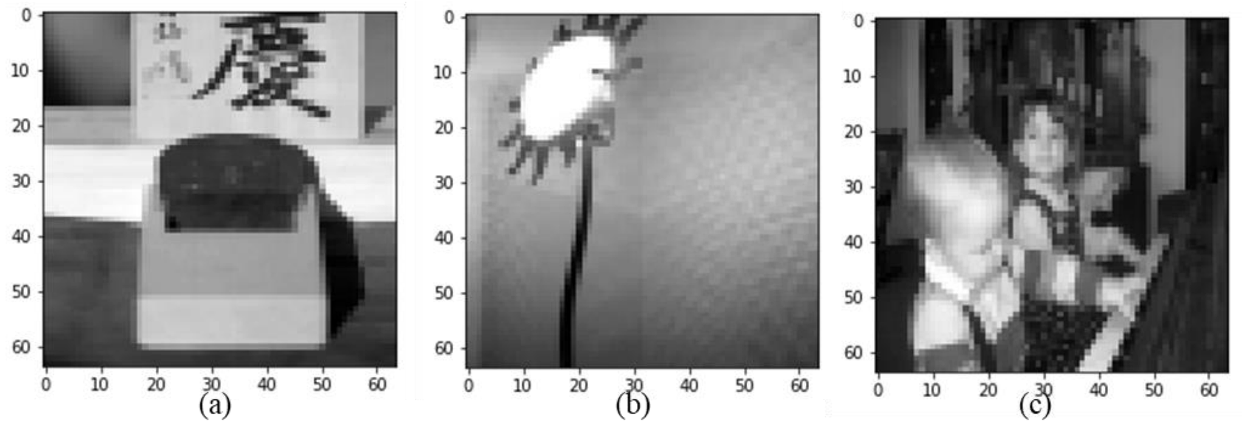

Figure 7.20 Images of non-fibers, with dimensions [64, 64].

Overfitting is a concern with the classifier model. Using the early stopping callback with patience of five epochs, the model would easily recognize synthetic data but would fail to recognize SEM images as fibers. The best results were obtained by training the classifier model with only one epoch.

The resulting network correctly classified challenge images that it had not seen during training as fibrous media or not fibrous media. If the classification network determined an image contained fibrous media, it applied the CNN regression network to determine the air flow resistance and air filtration efficiency. Four examples of correct classification and resulting parameter calculations are shown in Figures 7.21 through 7.24.

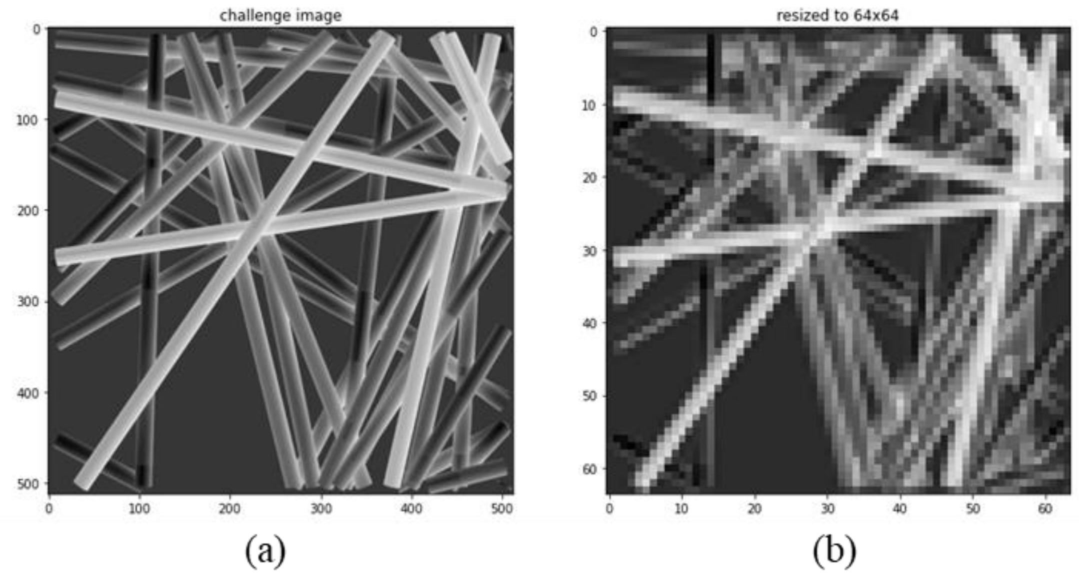

Figure 7.21 The classification network recognized this image of a digital twin as fibrous media and predicted the filtration efficiency as 50% with air flow resistance of 16.8 Pa. (a) Original image. (b) Resized to [64, 64] for evaluation.

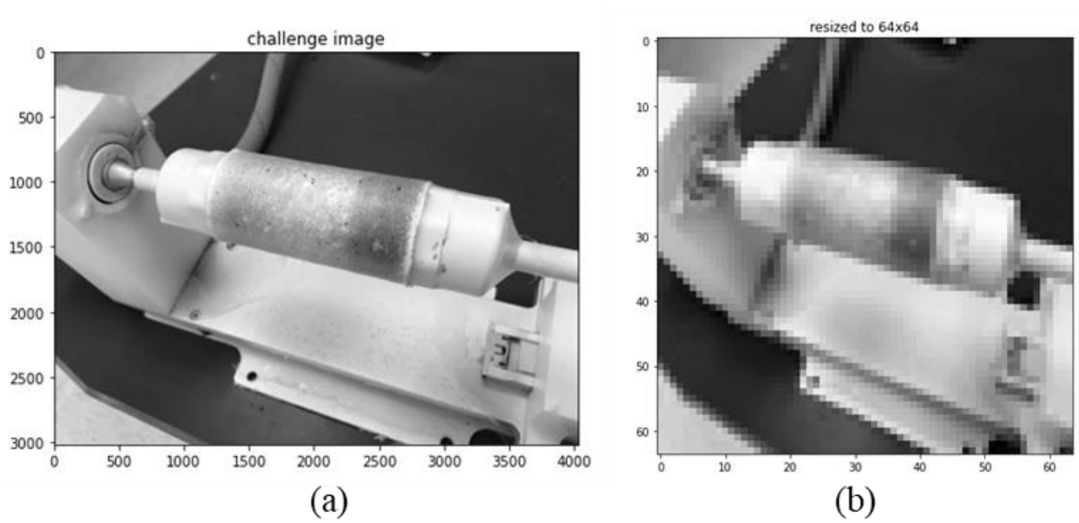

Figure 7.22 The classification network recognized this image was not fibrous media and did not proceed to filtration efficiency and air flow resistance calculations. (a) Original image. (b) Resized to [64, 64] for evaluation.

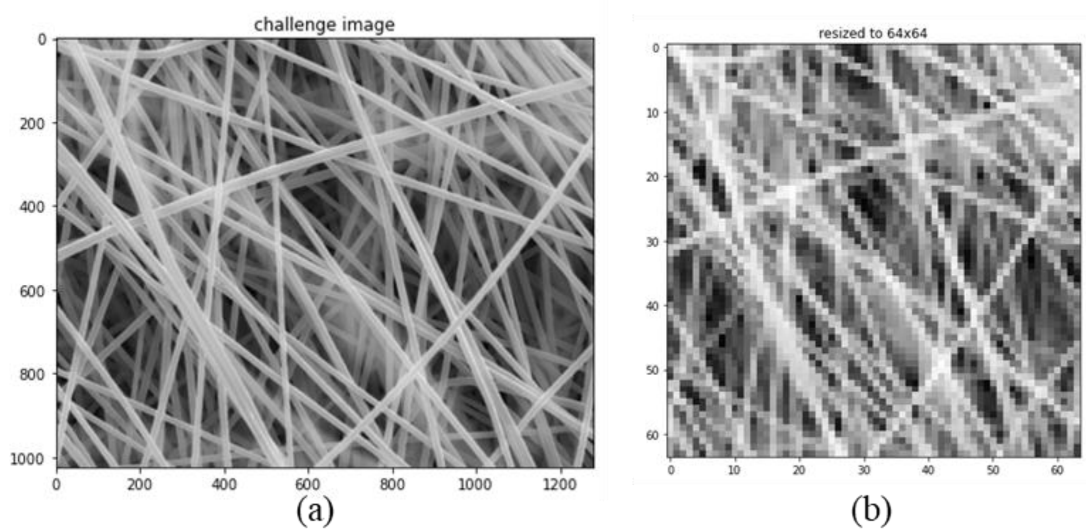

Figure 7.23 The classification network recognized this SEM image was fibrous media and predicted the filtration efficiency as 98.4% with air flow resistance of 99.0 Pa. (a) Original image. (b) Resized to [64, 64] for evaluation.

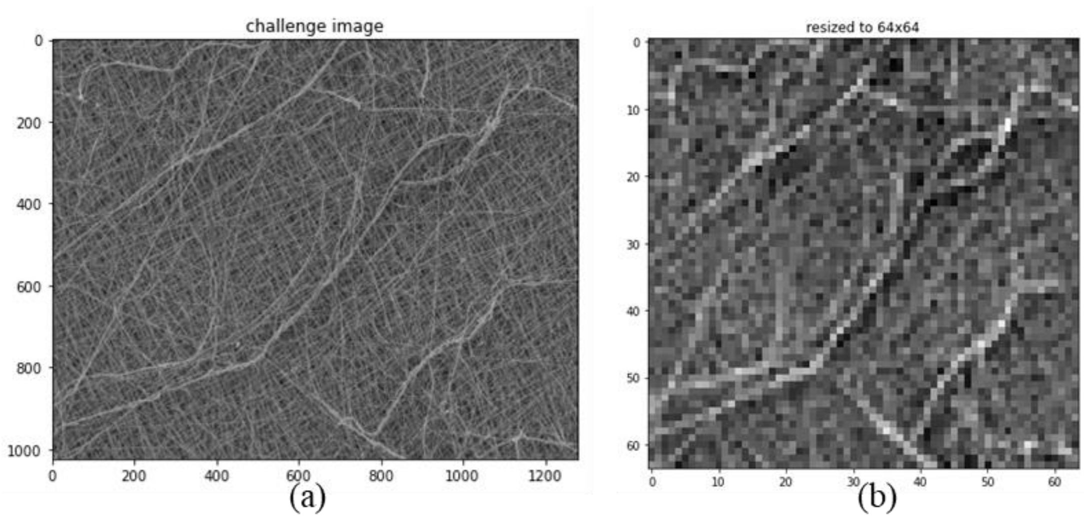

Figure 7.24 The classification network recognized this zoomed-out SEM image was fibrous media and predicted the filtration efficiency as 100% with air flow resistance of 111.5 Pa. (a) Original image. (b) Resized to [64, 64] for evaluation.

7.7 Chapter Summary

Machine learning techniques such as CNNs to predict air filtration efficiency and air flow resistance of filter media are important for the advancement of air filtration technology. The ability to train a convolutional model to evaluate and predict the filtration parameters of a filter media based solely on an SEM image of the media is a significant complement to experimental testing of the media.

CHAPTER VIII

COMPUTATIONAL MODELING OF AIR FILTRATION MEDIA WITH COMPUTATIONAL FLUID DYNAMICS

8.1 Introduction

The development of digital twin air filter geometry enables a holistic approach to air filtration research by integrating computational modeling and machine learning techniques into analytical and experimental research. Digital twin geometry allows a comparison of the flow resistance obtained using the SFE model with that obtained by using the computational model. Ansys Fluent is useful in evaluating the air flow resistance of digital twin geometry. The purpose of this chapter is to illustrate a methodology for the comparison of results obtained from the SFE analytical model and through CFD analysis.

8.2 Methodology

A Linux based high performance computer (HPC) was available to run CFD analysis. The commercial licenses available allowed the preparation of geometry, meshing, and observation of results on local computer workstations, while the computational engines were licensed only for the HPC. This requires the geometry, mesh, and journal files produced on a local workstation must be uploaded to the HPC to run the analysis. The workflow depicted in Figure 8.1 was used to accomplish CFD analysis for digital twin air filter media.

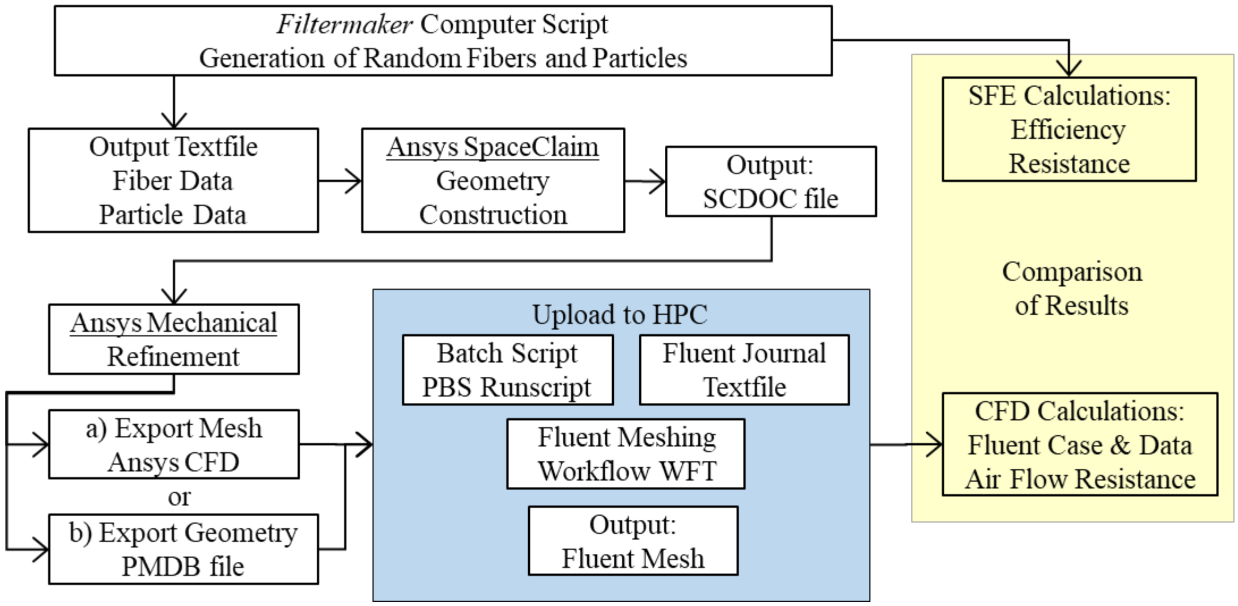

Figure 8.1 Workflow for CFD analysis.

8.3 Hand Verification of SFE Model Results, Filter f1

The first step was to validate the output data from the filtermaker computer script matches the SFE analytical model. Filter f1, shown in Figure 8.2, was chosen for verification.

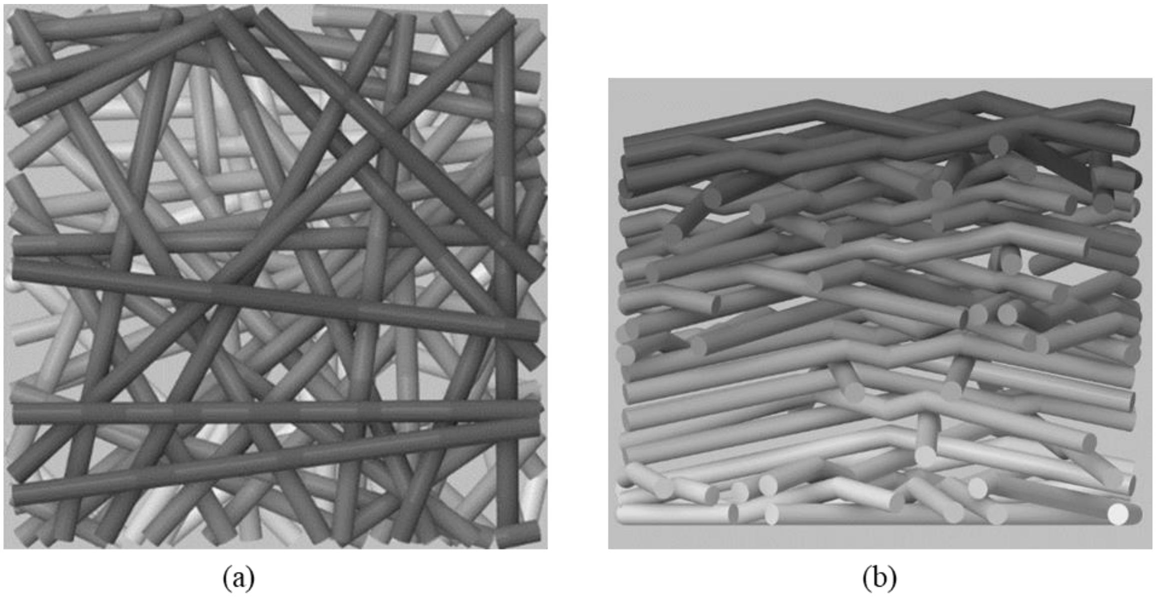

Figure 8.2 Filter f1 was selected for hand validation of the SFE Results. (a) Face view in the direction of air flow. (b) Profile view.

Hand calculations of the data was performed to verify the calculations made by the computerized script. From the text file, digital twin f1 consisted of 75 fibers constructed out of 319 segments, each with a diameter of 0.4257 µm. The summed length of all segments, 624.20 µm, multiplied by the fiber cross sectional area yielded a total fiber volume of 88.85 µm^2. The smallest z-coordinate of all fibers was 0, while the largest z-coordinate of taken at the outer surface of the tallest fiber, was 8.550 µm. This length is taken as the filter thickness. The total volume of the filter, having side lengths of 10 µm, was 855.06 µm^3. The fiber solidity was calculated from the ratio of fiber volume to filter volume as 10.39%. A monodisperse aerosol particle size of 1.0 g/cm^3 density and diameter of 0.3 µm was selected, giving the ratio or particle to fiber diameters as 0.705. Air velocity was set to 2.50 cm/s with temperature of 293 K, density of 1.200 kg/m^3, and viscosity of 1.813 Pa·s. Standard values were assumed for Boltzmann constant, gravitational constant, and the mean free path of air. The Reynold number was calculated using the fiber diameter as 7.05E-4, indicating laminar flow. The Kuwabara hydrodynamic number was calculated from the solidity as 0.483, indicating the prominence of the interception capture mechanism. The Knudsen number was calculated from the mean free path of air and fiber diameter as 0.307, indicating the air flow was in the transient stage between slip flow and free molecule range flow. The interception capture mechanism efficiency was calculated as 0.3304. The Cunningham slip correction factor was calculated from the mean free path of air and particle size as 1.550. The diffusion constant was calculated from the air temperature, viscosity, Boltzmann constant, particle diameter size, and slip correction factor as 1.220E-10 m^2/s. The Peclet number was calculated from the diffusion constant, air velocity, and fiber diameter as 87.2, indicating the rate of advection was significantly greater than the rate of diffusion. The diffusion capture mechanism efficiency was calculated as 0.1017. The interception of diffusing particle capture mechanism was calculated as 0.1513. The particle relaxation time was calculated from the particle mass, air viscosity, and slip correction factor as 4.27E-7 s. The Stokes number was calculated from the air velocity, fiber diameter, and particle relaxation time as 0.0251, indicating a high likelihood of particles remaining on given air flow streamlines, as to be expected with 0.3 µm particles. The inertial impaction capture mechanism was calculated as 0.1073. The summation of particle capture mechanisms resulted in single fiber efficiency of 0.691. Combining the SFE with the filter thickness, solidity, and fiber diameter size resulted in a hand-calculated value of 84%, which matched the value produced by the computer output. Hand calculations for the dominance of capture mechanisms is shown in Table 8.1.

Table 8.1 Hand Calculations for the Prominence of Particle Capture Mechanisms of f1

Capture Mechanism	SFE	SFE (%)	TFE (%)
Interception	0.3304	47.9	58.4
Diffusion	0.1017	14.7	23.7
Interception of Diffusing Particles	0.1513	21.9	33.1
Inertial Impaction	0.1074	15.5	24.8
Combined Capture Mechanisms	0.6908	100.0	84.0

The hand calculations were compared to and matched the computer-generated output data for model f1 shown in Figure 8.2(c). As anticipated, the dominant capture mechanisms for 0.3 µm particles are interception and interception of diffusing particles. However, 0.3 µm particles are not the most penetrating particle size for this filter. As illustrated by Figure 8.3, the most penetrating particle size for filter f1 is 0.17 µm.

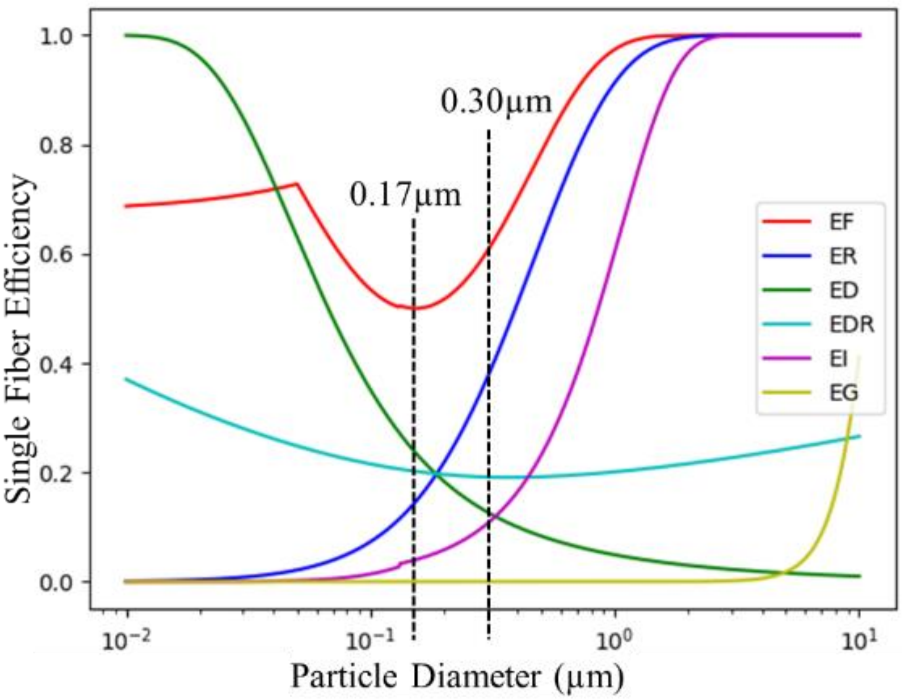

Figure 8.3 Single Fiber Efficiency model particle capture mechanics for f1.

The Davies model was used for analytical air flow resistance calculations. The solidity function was calculated as 2.279, and the total pressure drop was calculated as 48.7 Pa. This validated the output from the computer script.

8.4 CFD Analysis

Eighty digital twin geometries were randomly selected from the set of 2,100 used in the CNN analysis. The geometries were constructed with SpaceClaim, imported into Ansys Mechanical for meshing, and exported as Fluent compatible mesh to the HPC. Fluent journal text files and PBS run scripts were uploaded to the HPC.

8.5 Ansys Fluent Setup

Fluent has two solvers to choose from, a pressure-based solver and a density-based solver. The density-based solver was developed initially for hypersonic flow although it is now capable of laminar flow conditions. The pressure-based solver was selected for CFD analysis of digital twin air filter geometry. The digital twins included velocity inlet, pressure outlet, and four enclosure side walls which were designated as "symmetry" to avoid air flow resistance on the walls. The air temperature, density and viscosity were set to 293 K, 1.2 kg/m^3 and 1.789E-5 kg/(m·s) respectively. The air flow velocity was set to 2.50 cm/s, which produced a mass flow rate of 3.00E-12 kg/s across the inlet and outlet 10 µm x 10 µm cross sectional areas. The operating absolute pressure was designated 101,325 Pa, so the pressure at the inlet could be measured as gauge pressure.

Filter f1 had an initial mesh produced by Ansys Mechanical of 6.0 million tetrahedral cells, with orthogonal quality below 0.01. The mesh was converted by Ansys Fluent into 1.160 million polyhedral cells. The Fluent automatic process was used to improve mesh quality by slight adjustments to node locations for the worst 1% of the cells. This resulted in a minimum orthogonal quality of 0.07, which is still low but acceptable. The model was initialized from the inlet. The solution for f1 converged after five iterations. The node pressure readings were integrated across the inlet and outlet surfaces and recorded. The solution required two minutes and 28 seconds of computational time.

8.6 Results

8.6.1 CFD Results for Filter f1

Results from the CFD analysis of filter f1 showed a pressure drop across the filter of 34.93 Pa, which is approximately 28% lower than the 48.7 Pa anticipated from the SFE model. Figure 8.4 shows the pressure streamlines from the CFD analysis of filter f1.

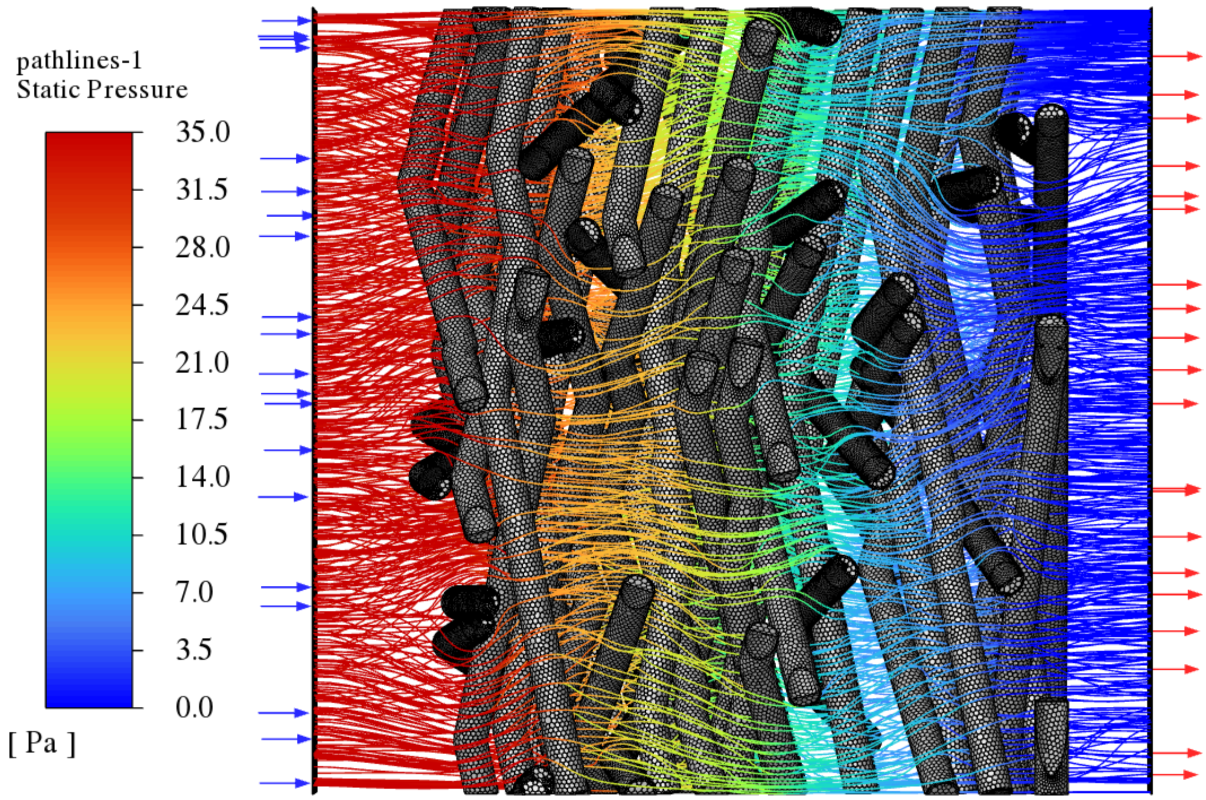

Figure 8.4 Pressure streamlines for filter f1.

8.6.2 CFD Analysis for Eighty Samples

The CFD analysis for each of the 80 digital twins showed air flow resistance well below anticipated analytical calculations from the analytical SFE model. Figure 8.5 compares the calculated air flow resistance from the SFE model on the abscissa and the computational estimation on the ordinate. The linear match-line with slope of unity shows where the datapoints should lie if the analytical model and computational models were congruent. The red dotted linear regression trend line shows a slope of 0.78, indicating the models diverge for higher air flow resistance geometry and converge for lower air flow resistance. However, the high value for the coefficient of determination indicates the analytical and computational models are strongly correlated. This suggests that the analytical and computational models both perceive and consider the same geometry aspects in determination of air flow resistance. Although the analytical model and computational models are not congruent, they are well correlated. The two models demonstrate a high degree of precision.

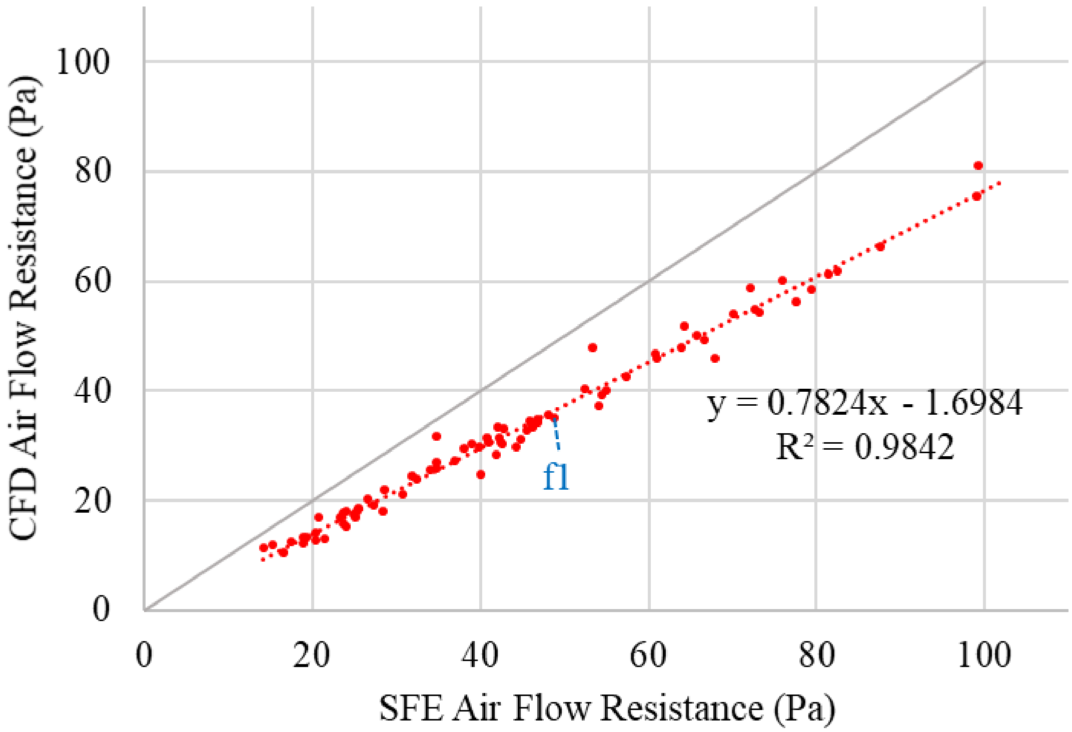

Figure 8.5 Comparison of analytical and computational model results for 80 digital twins.

8.6.3 Sensitivity Analysis

An effort was made to determine whether slight adjustment of the parameters within the analytical model could bring both models into alignment for digital twin f1. The analytical air flow resistance is a function of solidity, air viscosity, air velocity, fiber diameter, and filter thickness. For example, the media thickness in the analytical model was taken as the maximum distance between fibers in a 10 µm x 10 µm area. However, sensitivity analysis showed the thickness of the analytical model would have to be nearly doubled from 8.55 µm to 15.06 µm, which in turn changes the solidity from 10.4% to 5.90%, for the analytical model to match the

CFD model prediction. A more plausible adjustment is decreasing the fiber diameters by only 9.6% from 0.426 μm to 0.385, which in turn changes the solidity from 10.4% to 8.5% and brings the analytical model in line with the predictions made by the CFD model.

8.6.4 Analysis of Geometry Dimensions

The 80 models tested with CFD analysis from the set of 2,100 digital twins have relatively simple geometries with a 10 μm × 10 μm side length dimensions. It was noted that the CFD models with larger side length dimensions show better alignment with the predictions of the analytical SFE model. Figure 8.6 demonstrates three models of increasing side length dimensions, from 10 μm × 10 μm to 40 μm × 40 μm, with air flowing from left to right across the fibers. The red flow within the model near the inlet indicates areas of higher pressure, while the blue flowlines near the outlet indicate lower pressure. Table 8.2 compares the flow resistance calculated using the analytical SFE model and results from the CFD analysis for these three examples as shown in Figure 8.6. The computational results come closer to analytical predictions with increasing complexity of the digital twin.

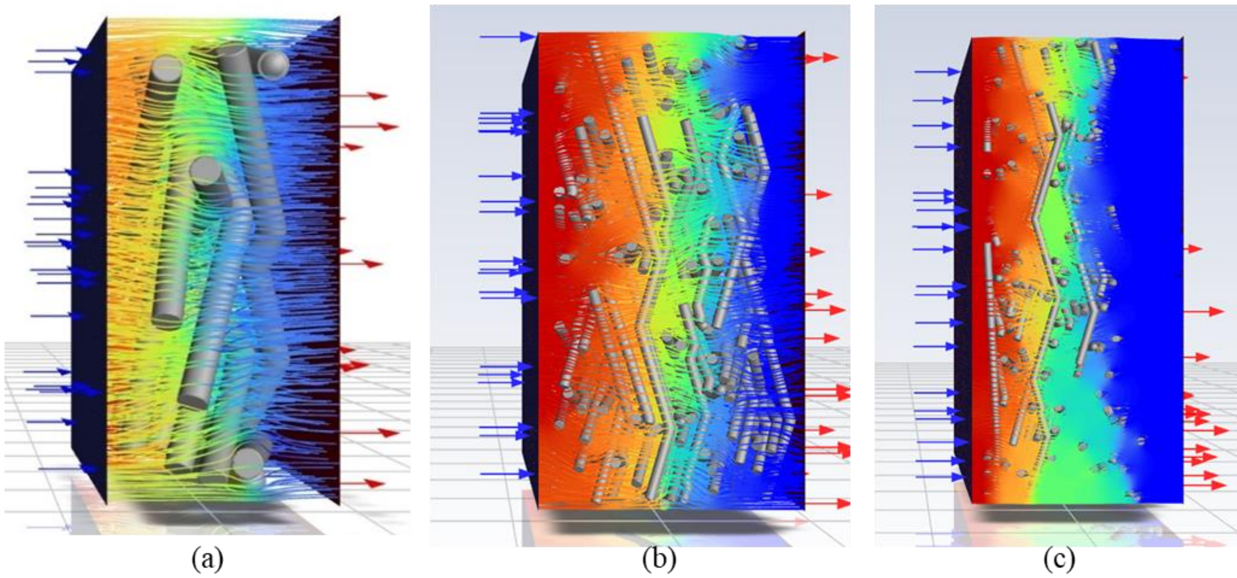

Figure 8.6 CFD analysis for increasing complexity of digital geometry.

Table 8.2 Alignment of SFE and CFD Models with Increasing Complexity

Model Size	Analytical (SFE) (Pa)	Computational (CFD) (Pa)	Alignment (%)
10 µm × 10 µm	16.89	5.30	31.4
A9 30 µm × 30 µm	36.7	20.21	55.1
A10 40 µm × 40 µm	34.2	31.11	91.0

8.6.5 Effects of Particle Loading

Digital twin replication of air filter geometry is also useful for studying the effects of particle loading. In the example below, particles are randomly dropped onto the fiber geometry and considered as attached to the fibers upon contact. This can be done for a specified number of particles or until the solidity of the filter increases to a specified level. Figure 8.7(a) shows a small 10 µm × 10 µm filter segment with 33 clean fibers, each 700 nm diameter, a filter thickness of 7.12 µm, and solidity of 16.4%. To observe the effects of particle loading, random particles were added to the filter until the solidity increased from 16.4% to 18.04%. Dendrites formed on the filter as shown in Figure 8.7(b and c). A total of 5,957 particles attached to the fibers in a uniform distribution of diameter sizes from 0.100 µm to 0.200 µm.

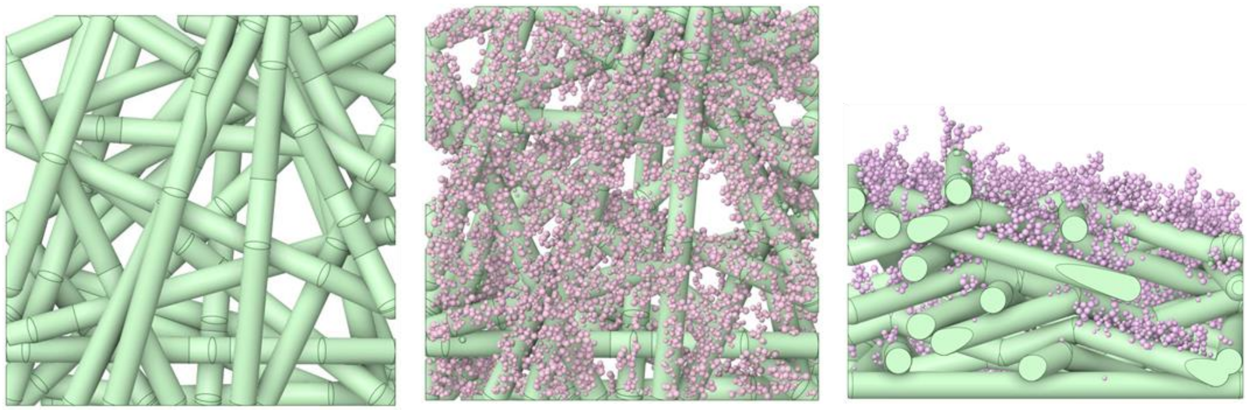

(a) (b) (c)

Figure 8.7 Particle loading analysis of digital twin geometry. (a) Clean digital twin of 10 µm × 10 µm filter. (b) Media loaded with 5,957 particles. (c) Profile view of dendrite formation.

8.6.5.1 SFE Model Analysis of Particle Loading

The SFE analytical model indicated the clean filter media in Figure 8.7(a) obtained a total filter efficiency of 69.2% with a pressure drop of 35.0 Pa. By adjusting the solidity in the analytical SFE model and maintaining constant fiber diameter size and filter media thickness, the analytical SFE model estimated the pressure drop for the particulate-loaded fibers at 43.1 Pa, which is an increase of 23.1% pressure.

8.6.5.2 CFD Model Analysis of Particle Loading

The computational analysis of the digital twin in Ansys Fluent indicated a pressure drop across the clean filter media of 21.1 Pa between the inlet and outlet planes, as shown in Figure 8.8(a). As anticipated, the CFD model estimated a pressure drop well under the pressure drop estimated with the analytical SFE model. The CFD model estimated a pressure drop of 25.8 Pa for the particulate-loaded filter shown in Figure 8.8(b) which is a 22.3% increase from the clean fibers.

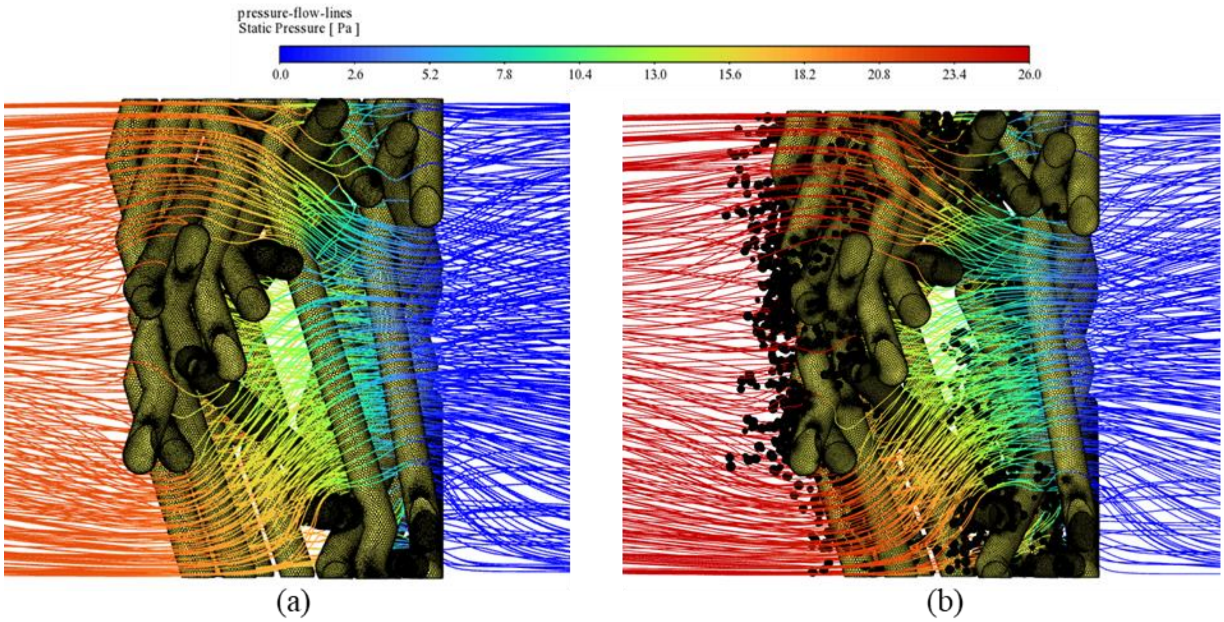

Figure 8.8 CFD Analysis showing pressure flow lines around (a) clean fibers and (b) fibers loaded with 5,957 particles.

The CFD model projection of 22.3% compares well with the SFE model projection of 23.1% for the increase in pressure by loading the clean fibers with 10% additional particulate matter. While the CFD model and SFE model are incongruent, they are consistent with each other and correlate well for estimating the air flow resistance increase from particulate loading of the filter media. The comparison of SFE and CFD predictions for the clean and loaded filter media is shown in Figure 8.9.

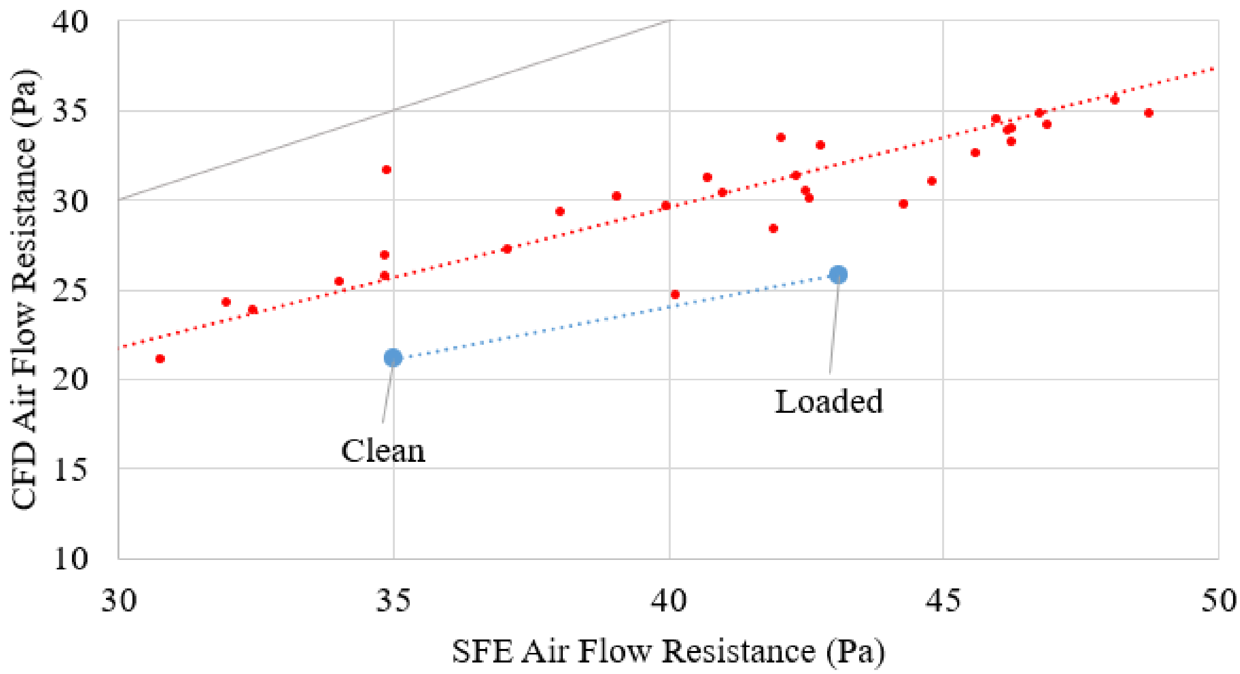

Figure 8.9 Comparison of SFE and CFD predictions of effects of particle loading.

8.6.6 CFD Analysis with a HEPA Digital Twin

A conceptual digital twin air filter medium was created in Chapter V to demonstrate a potential HEPA quality filter design, which included flexible fibers with an average diameter size of 0.500 µm spun into a filter with a thickness of 18.43 µm and solidity of 18.9%. That digital twin achieved an analytical efficiency of 99.97% capture for 0.3 µm particles with an air flow resistance of 241.8 Pa, which is well below the limit of 320 Pa specified by ASME AG-1. However, that conceptual digital twin has no real counterpart. Contemporary HEPA filters made with melt-blown borosilicate glass fiber paper have larger diameter fibers and less solidity.

A digital twin for actual H4 HEPA filter paper was constructed using the parameters shown in Table 8.3, with the side dimensions of 30 µm x 30 µm. Fibers with diameter sizes of 1.40 µm were continually added to the filter media until the air filtration efficiency achieved 99.97%. Various values for fiber flexibility and spacing were tried until the resulting filter thickness and solidity reflected known values reported for H14 filter paper. Using a fiber flexibility of 20% along with a fiber spacing of 1.20 resulted in a digital twin with 388 fibers and 1,766 fiber segments, with total filter thickness of 374.1 μm and filter solidity of 13.7%. These parameters compare favorably with H14 filter paper. The analytical calculation of air flow resistance for this digital twin resulted in a pressure drop of 319.7 Pa across the filter, which is at the maximum limit for nuclear grade HEPA filters. The face view and profile view of the digital twin H14 paper are shown in Figure 8.10.

Table 8.3 HEPA Digital Twin Parameters

Description	Symbol	H14 HEPA[65] (reported)	Digital Twin (SFE)
Fiber diameter	d_f	*	1.4 μm
Fiber flexibility slope	slope	*	20.0%
Total filter efficiency	E_f	99.98%	99.97%
Solidity or solid volume fraction	α	*	13.7%
Thickness of the filter media	t	400.0 μm	374.1 μm
Air flow resistance (at 5.3 cm/s)	ΔP	372 Pa	-
Air flow resistance (at 2.5 cm/s)	ΔP	-	319.7 Pa

* not reported but assumed to match the digital twin

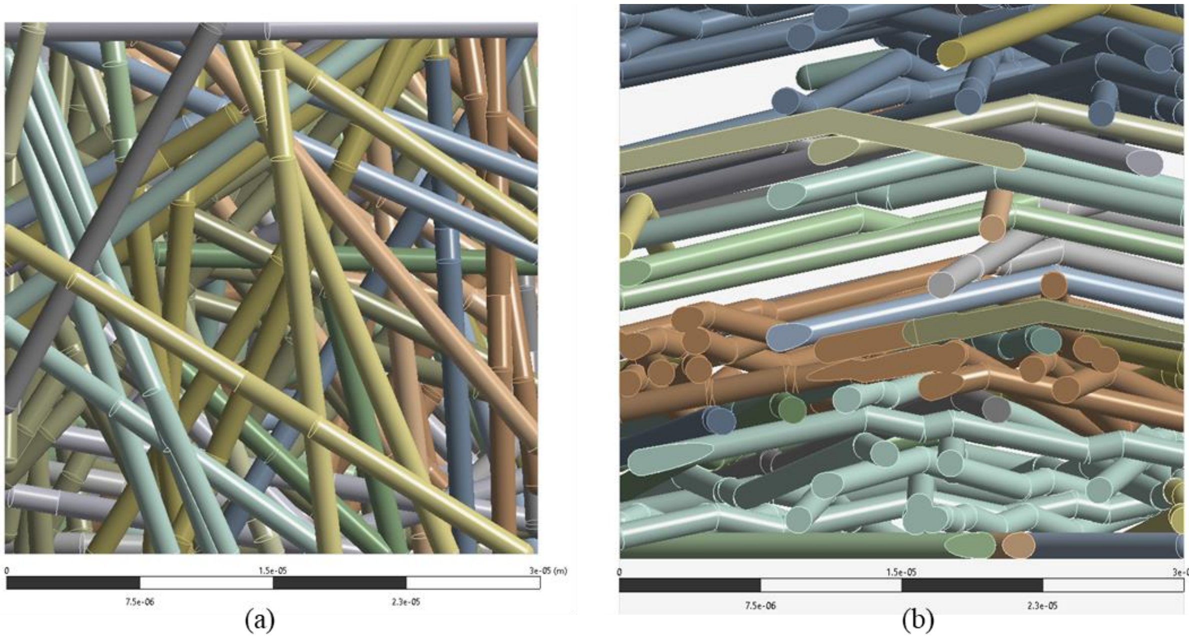

Figure 8.10 (a) Face view of HEPA digital twin. (b) Side view of HEPA digital twin.

Figure 8.11 shows the full-length side view of the digital twin of HEPA filter paper along with the mesh created in Ansys Mechanical, the mesh created in Ansys Fluent, and pressure flow lines from Ansys Fluent. The pressure flow lines shown in Figure 8.11 are for demonstration only. While the CFD solution converged, the poor-quality mesh did not produce a reliable result.

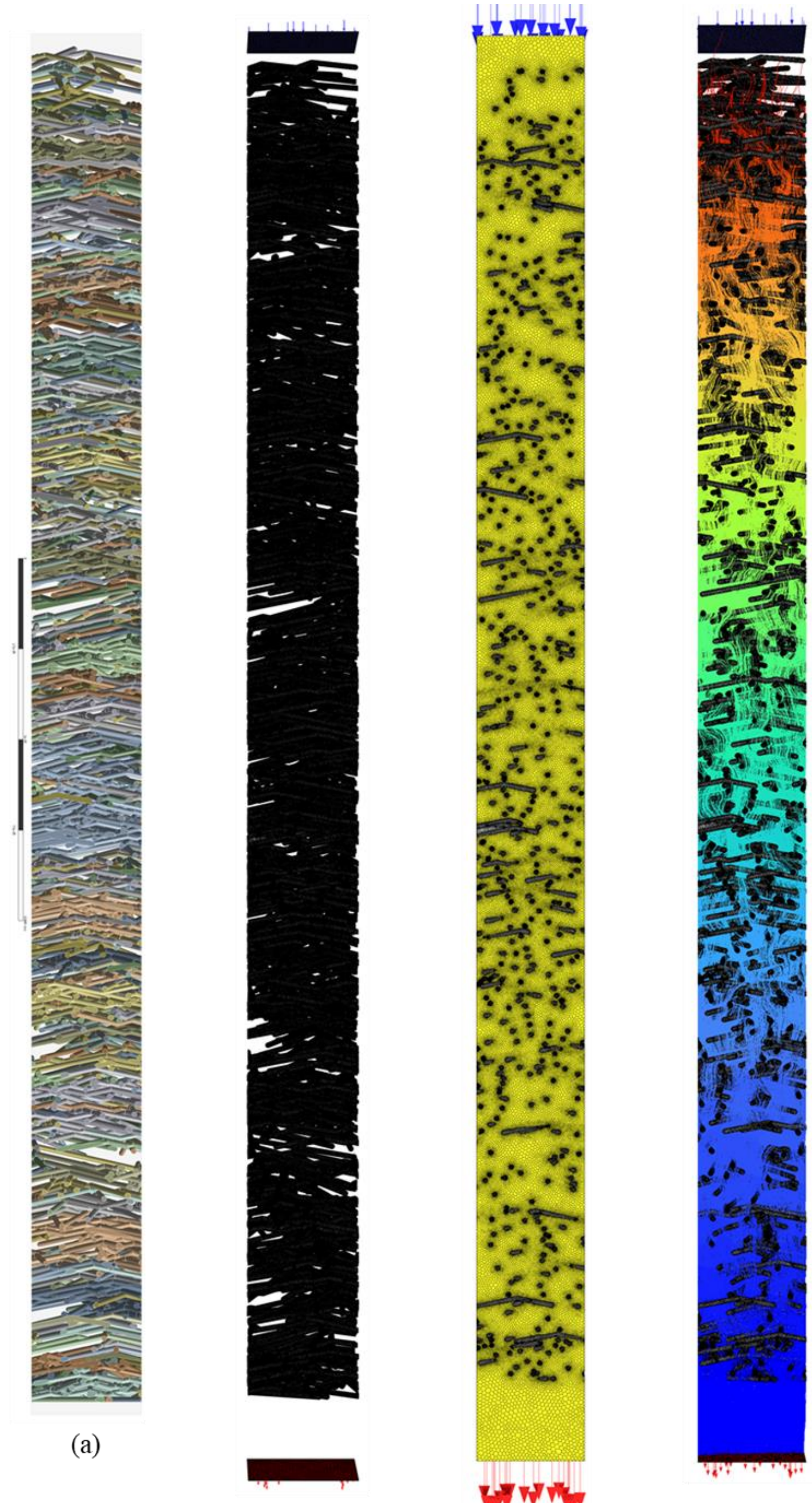

(a) (b) (c) (d)

Figure 8.11 Profile view of HEPA digital twin. (a) Fibers produced by SpaceClaim. (b) As meshed in Ansys Mechanical. (c) As Meshed in Fluent. (d) Pressure flow lines.

The size and complexity of the full geometry led to a highly complex mesh and unsatisfactory results from the CFD analysis. However, slicing the first 50 µm of the geometry enabled production of a satisfactory mesh and reliable CFD results. Figure 8.12 shows the CFD analysis for the first 50 µm slice of the filter.

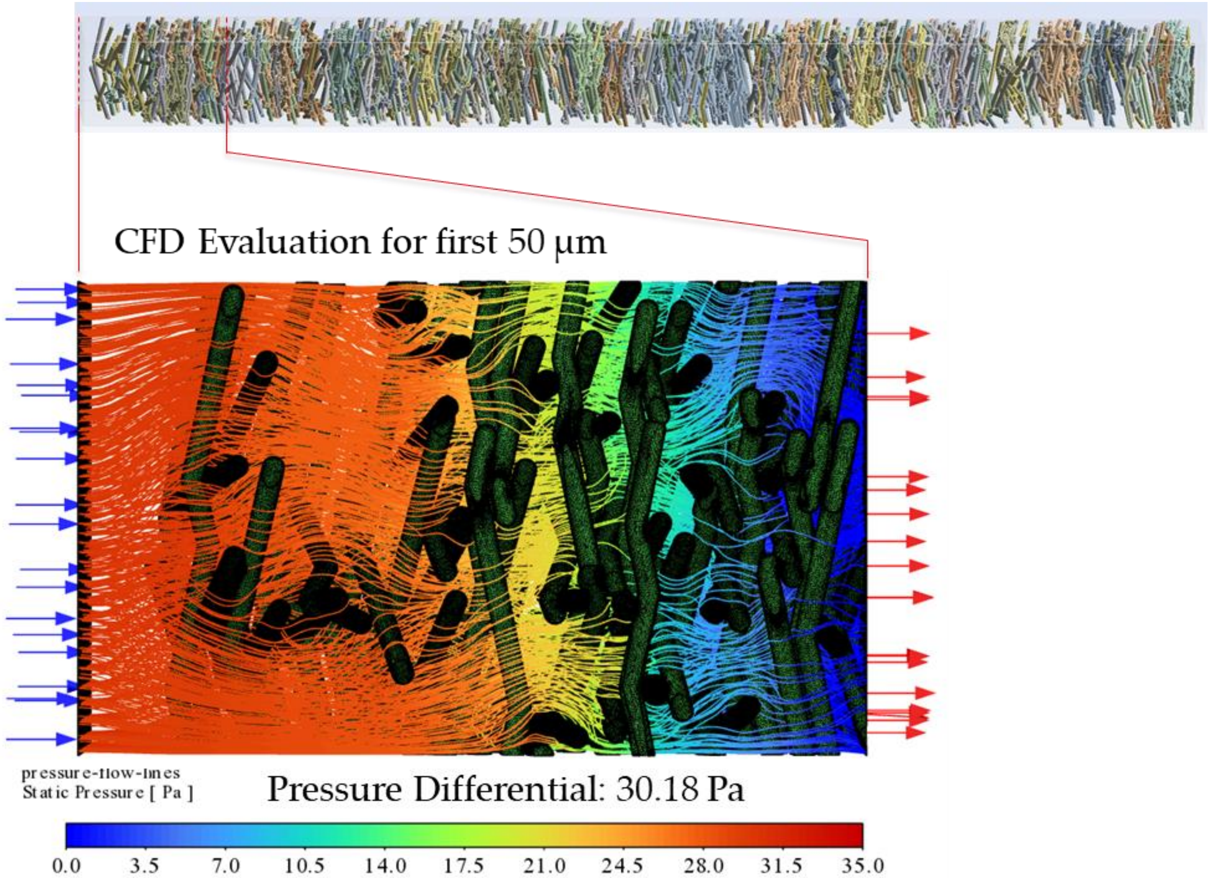

Figure 8.12 CFD evaluation for the first 50 µm of a HEPA filter medium.

The first 50 µm slice of the HEPA medium contained a filter thickness of 46.5 µm and a 3.5 µm gap of air from the inlet to the first fiber. Assuming a homogeneous distribution of fibers throughout the total 374.1 µm thickness of the filter, the upper 50 µm slice contained 12.43% of the total. Successful CFD analysis for this first 50 µm slice showed an air flow resistance of 30.18 Pa. Since the pressure drop across the full length of the filter is additive, this equates to a prediction of 242.8 Pa across the total length of the filter medium. In comparison, the analytical SFE model predicted air flow resistance of 319.7 Pa across the filter medium. In this case, the CFD analysis was 24.1% lower than the analytical model prediction. The analytical and computational predictions for air flow resistance were updated on the graph in Figure 8.13.

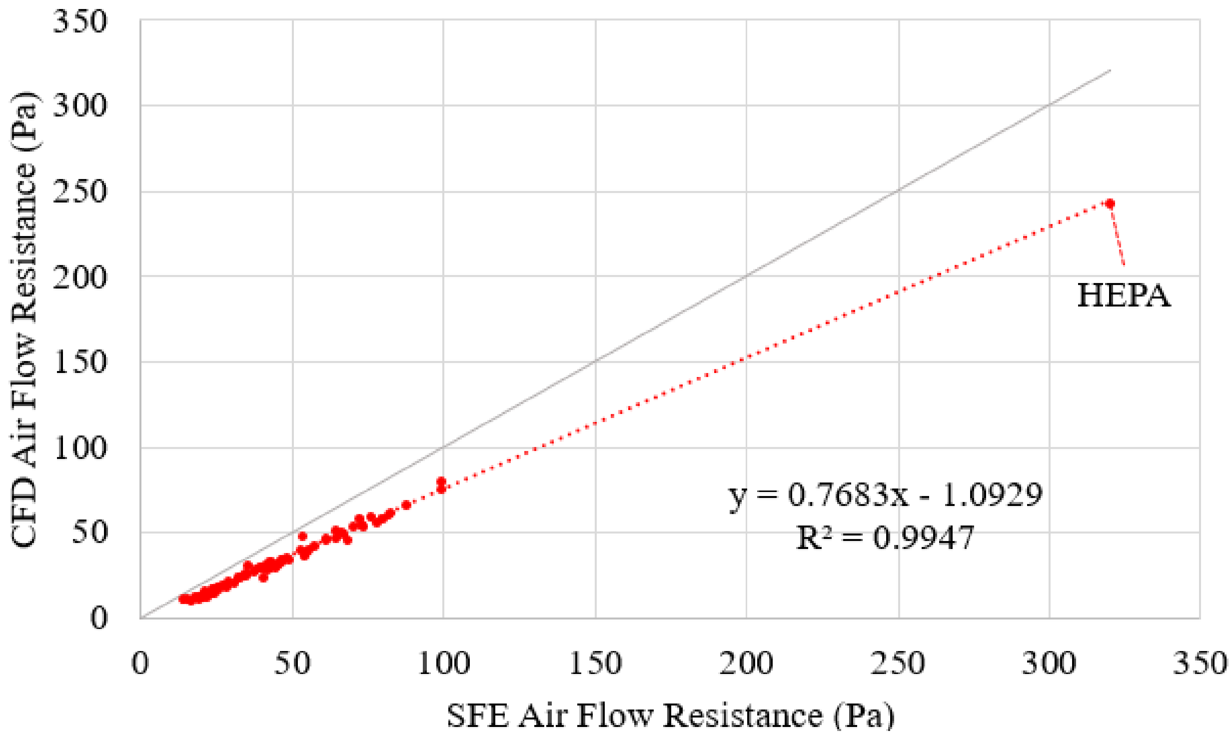

Figure 8.13 Correlation of CFD and SFE models with HEPA digital twin.

This result is consistent with the correlation between analytical SFE and computational CFD models demonstrated earlier in this chapter, and is reflected in Equation 8.1, with CFD representing the computational prediction of air flow resistance and SFE representing the analytical prediction.

$$\mathrm{CFD} = 0.7683(\mathrm{SFE}) - 1.0929 \tag{8.1}$$

Using the HEPA datapoint, the models are correlated with a coefficient of determination of 0.9947. This suggests that the analytical-computational correlation holds true for values as high as 320 Pa, the maximum limit of HEPA filter medium air flow resistance. The analytical and computational results are shown in Table 8.4.

Table 8.4 Analytical and CFD results for H14 HEPA paper.

Description	H14 HEPA (reported)	Digital Twin (SFE)	Computational (CFD)
Air flow resistance (5.3 cm/s)	372 Pa	-	
Air flow resistance (2.5 cm/s)	-	319.7 Pa	242.2 Pa

8.6.7 Challenges Encountered with Ansys Software

Ansys SpaceClaim is a Windows-only platform which is not supported on Linux. Ansys SpaceClaim was selected because of the python scripting capability in the geometry creation workflow allowed the easy import of fiber and particle data from the text files. This created challenges with file types. For example, SpaceClaim geometry output files using SCDOC format are not readable on a Linux machine and had to be converted to Ansys parts manager database (PMDB) format to upload onto the HPC.

The Ansys modules SpaceClaim, Mechanical, and Fluent are not well integrated. The most reasonable workflow involved exporting and importing stand-alone datafiles from one module to another. For example, Ansys Fluent first converts SCDOC files into PMDB format on a Windows machine, however Fluent cannot read SCDOC files on a Linux machine.

The scripting capabilities of each module is separate and distinct, and significantly lacking. Many important features needed in SpaceClaim and Ansys Mechanical required a mouse or trackpad to click a button, as there was no scripting feature. This made it difficult for automating the workflow production of geometry, meshing, and CFD analysis.

8.7 Chapter Summary

This chapter showed the vast potential for analyzing air filter media with CFD modeling at micro and nano scale digital twin geometry. The same digital twin geometries analyzed in machine learning modeling of Chapter VII were analyzed using CFD modeling. This chapter shows a strong correlation between the results of analytical modeling and computational modeling, with a relationship that holds for analysis up through the air flow resistance values associated with HEPA filter media. The development of effective digital twin geometry creates a linkage between experimental, analytical, and computational modeling of air filter media. Additional effort is required to correlate the analytical and computational results of the digital twin geometry with experimental results of real air filter media. Computational, analytical, machine learning, and experimental modeling of air filter media are equally important in building a comprehensive understanding of air filtration.

CHAPTER IX

CONCLUSION AND FUTURE WORK

9.1 Conclusion

The research goal of this dissertation was to advance the science and technology of air filtration for the purpose of improving global health and safety through mitigation of hazardous particulate aerosols. This dissertation advocated for the coordination of four lines of effort into an integrated approach to improve air filtration technology, including experimental modeling, analytical modeling, machine learning modeling, and computational fluid dynamics modeling. Successful coordination of these four lines of effort into one integrated approach will advance the science for the production and application of alternative air filtration materials and methods to improve global air quality. The exploration of mechanical, chemical, and thermal properties of fibers and filter media, the advancement of electrospun nonwoven nanofibrous media, and the production and refinement of effective digital twin air filter media are important enablers within these lines of effort. Successful integration of analytical, computational, machine learning, and experimental modeling enables greater understanding of aerosol science and assists the mitigation of a prominent global problem.

9.2 Future Work

While this dissertation achieved success towards its stated goals, there is significant space for improvement and future work. The future work recommended by this dissertation follows.

9.2.1 Chapter II Alternative High-Performance Fibers for Nonwoven HEPA Filter Media

Recommended future work based on the analysis of mechanical and thermal characteristics of fibers and nonwoven fibrous media is to extend the analysis into binding methods and materials used to create the nonwoven media. The mechanical and thermal analysis of air filtration media must take into account the sizing, chemical bonding, sintering, and any other methods of filter development.

9.2.2 Chapter III Analytical Modeling of Air Filtration

The analytical SFE model shown in Chapter III was developed through many years of effort by notable authors who fully and clearly explained the science of particulate capture mechanisms. However, several variations of the SFE analytical model use empirical correlations and experimental data to achieve desired correlation of analytical and experimental results. A recommended future effort is to simplify the SFE model by observing the relationship between fewer key parameters and the analytical model results. A model with fewer parameters may prove to be nearly as effective and simpler to employ than the full analytical SFE model.

9.2.3 Chapter IV Experimental Production of Electrospun Fibers

9.2.3.1 Carbonization of Electrospun Polyacrylonitrile-Graphene Fibrous Media

The advantage of electrospinning polyacrylonitrile nonwoven media is the ability to carbonize the media. Carbon fibers have mechanical, thermal, and air filtration characteristics that are much different than the precursor polyacrylonitrile fibers. Carbonizing polyacrylonitrile-graphene media requires a furnace capable of inert gas or vacuum that can sustain temperatures in excess of 1,000 °C.

9.2.3.2 VOC Adsorption Testing of Electrospun Filtration Media

The polyacrylonitrile-graphene composite media could be experimentally tested for VOC adsorption capacity. Different amounts of graphene could be added to the polyacrylonitrile-graphene solution to determine the effect of the graphene on VOC adsorption.

9.2.3.3 Production of Polyacrylonitrile with Ceramic, Basalt, Metallic, and Magnetic Additives

While this dissertation focused only on polyacrylonitrile and graphene composite fibers, several other materials should be considered as a composite with polyacrylonitrile. An experimental study could investigate how certain metals, ceramics, or minerals effect air filtration when electrospun into nanofiber composites.

9.2.4 Chapter V Digital Twin Creation

The digital twin creation algorithm in Chapter V can be improved by adapting the model to other geometry creation software such as Abaqus and AutoCAD. Digital scripting capabilities of additional geometry creation software should be explored. While currently the fibers are straight in the x-y plane and only bend in the z-direction, the fiber creation model can be improved by bending the fibers in the x-y plane. Curvature could be added to the fibers, as well as different cross-sectional shapes. Currently all fibers in the model have circular cross sections. The digital twin creation tool can be refined and more advanced into particle loading scenarios.

9.2.5 Chapter VII Convolutional Neural Network

Machine learning is a relatively new set of data analysis tools that is wide open for exploration. The study of SEM images to predict air filtration efficiency and air flow resistance is one of many applications for machine learning. The convolutional network explored in this dissertation could easily be extended into many other newer network architectures to include the diffusion network and generative adversarial networks (GANs).

9.2.6 Chapter VIII Computational Fluid Dynamics

Additional effort is required to resolve the differences encountered within this dissertation of the analytical SFE models and the CFD models. The CFD models consistently estimated lower air flow resistance than the SFE model predictions. Recent advances in high performance computing and data storage increases the prospect of CFD analysis for complex structures. Additional effort is required to refine the CFD modeling presented in this dissertation to provide a consistent and accurate match to the SFE analytical models.

REFERENCES

[1] United Nations Environment Programme (2021), “Actions on Air Quality: A Global Summary of Policies and Programmes to Reduce Air Pollution.,” *Nairobi*, Jul. 02, 2017. http://www.unep.org/resources/assessment/actions-air-quality (accessed Mar. 07, 2022).

[2] United Nations, “General Assembly resolution 70/1. Transforming our world: the 2030 Agenda for Sustainable Development.,” Sep. 25, 2015. https://undocs.org/Home/Mobile?FinalSymbol=A%2FRES%2F70%2F1&Language=E&DeviceType=Desktop&LangRequested=False (accessed Mar. 15, 2022).

[3] United Nations, “General Assembly Resolution 74/212. International Day of Clean Air for Blue Skies,” Jan. 22, 2020. https://documents-dds-ny.un.org/doc/UNDOC/GEN/N19/434/93/PDF/N1943493.pdf?OpenElement (accessed Mar. 15, 2022).

[4] W. Bergman and S. Sawyer, “Development of a High-Efficiency, High-Performance Air Filter Medium,” presented at the 20th DOE/NRC Nuclear Air Cleaning Conference, Boston, MA, Aug. 1988. [Online]. Available: https://www.osti.gov/servlets/purl/6946060.

[5] W. Bergman, G. Larsenl, R. Lopez, K. Wilson, C. Witherell, and M. McGregor, “Further Development of the Cleanable Steel HEPA Filter, Cost/Benefit Analysis, and Comparison with Competing Technologies,” presented at the 24th DOE/NRC Nuclear Air Cleaning and Treatment Conference, Portland, OR, Jul. 1996, p. 37. [Online]. Available: https://www.osti.gov/servlets/purl/325071

[6] M. Mitchell *et al.*, “Ceramic HEPA Filter Program,” presented at the International Society for Nuclear Air Treatment Technologies 32nd Nuclear Air Cleaning Conference, Denver, CO, May 2012. [Online]. Available: https://www.osti.gov/servlets/purl/1043641/

[7] D. J. Adamson, “Experimental Investigation of In Situ Cleanable HEPA Filters,” U.S. Department of Energy, Oct. 1998. [Online]. Available: https://www.osti.gov/servlets/purl/4852

[8] L. Ackland, “The Day They Almost Lost Denver,” *Bull. At. Sci.*, vol. 55, no. 4, pp. 58–65, Jul. 1999, doi: 10.2968/055004016.

[9] U.S. Customs and Border Protection, “Fiber Trade Names & Generic Terms.” https://www.cbp.gov/document/guidance/fiber-trade-names-generic-terms (accessed Apr. 12, 2021).

[10] L. P. Haslett, “Lung Protector,” United States Patent US6529A, Jun. 12, 1849 [Online]. Available: https://patents.google.com/patent/US6529A/en

[11] M. First, “Hepa Filters | Journal of the American Biological Safety Association.” https://www.liebertpub.com/doi/10.1177/109135059800300111 (accessed Mar. 03, 2022).

[12] S. Barnette and G. Smith, *Nuclear Air Cleaning Handbook, Chapter 1, History of the Development of Air Cleaning Technology in the Nuclear Industry*. 2003. Accessed: Jan. 12, 2020. [Online]. Available: https://www.standards.doe.gov/standards-documents/1100/1169-bhdbk-2003-ch1

[13] W. C. Hinds, *Aerosol technology: properties, behavior, and measurement of airborne particles*, 2nd ed. New York: Wiley, 1999.

[14] L. M. Henning *et al.*, “Review on Polymeric, Inorganic, and Composite Materials for Air Filters: From Processing to Properties,” *Adv. Energy Sustain. Res.*, vol. 2, no. 5, p. 2100005, 2021, doi: 10.1002/aesr.202100005.

[15] Q. Wang, “Investigation of Aerosol Filtratoin via Fibrous Filters.” NC State University Libraries, Nov. 06, 2008. Accessed: Oct. 29, 2021. [Online]. Available: https://repository.lib.ncsu.edu/handle/1840.16/5338

[16] G. Kellie, “1 - Introduction to technical nonwovens,” in *Advances in Technical Nonwovens*, G. Kellie, Ed. Woodhead Publishing, 2016, pp. 1–17. doi: 10.1016/B978-0-08-100575-0.00001-2.

[17] C. Luo, S. Stoyanov, E. Stride, E. Pelan, and M. Edirisinghe, “Electrospinning versus fibre production methods: From specifics to technological convergence,” *Chem. Soc. Rev.*, May 2012, doi: 10.1039/c2cs35083a.

[18] Bekaert, “Bekipor® HEPA/ULPA filter media,” *Bekaert*. https://www.bekaert.com/en/products/basic-materials/filtration/bekipor-hepa-ulpa-filter-media (accessed Feb. 16, 2020).

[19] M. J. Denton and P. N. Daniels, *Textile Terms and Definitions*. Manchester, U.K.: Textile Institute, 2002.

[20] I. M. Hutten, *Handbook of Nonwoven Filter Media*. 2015. doi: 10.1016/C2011-0-05753-8.

[21] G. Siqueira, J. Bras, and A. Dufresne, "Cellulosic Bionanocomposites: A Review of Preparation, Properties and Applications," *Polymers*, vol. 2, no. 4, Art. no. 4, Dec. 2010, doi: 10.3390/polym2040728.

[22] Z. Sun *et al.*, "Filtration performance of air filter paper containing kapok fibers against oil aerosols," *Cellulose*, vol. 25, no. 11, pp. 6719–6729, Nov. 2018, doi: 10.1007/s10570-018-1989-7.

[23] S. K. Mandal and B. N. Srimani, "Jute Fiber as a Filter Medium in Microbial Air Filters," *Ann. N. Y. Acad. Sci.*, vol. 506, no. 1, pp. 682–688, 1987, doi: https://doi.org/10.1111/j.1749-6632.1987.tb23867.x.

[24] F. Jianyong and Z. Jianchun, "Preparation and oil/air filtration properties of hemp paper," *J. Ind. Text.*, vol. 45, no. 1, pp. 3–32, Jul. 2015, doi: 10.1177/1528083714521071.

[25] J. P. Manaia, A. T. Manaia, and L. Rodriges, "Industrial Hemp Fibers: An Overview," *Fibers*, vol. 7, no. 12, p. 106, Dec. 2019, doi: 10.3390/fib7120106.

[26] E. Small and D. Marcus, "Hemp: A New Crop with New Uses for North America," p. 43.

[27] R. D. Anandjiwala and L. Boguslavsky, "Development of Needle-punched Nonwoven Fabrics from Flax Fibers for Air Filtration Applications," *Text. Res. J.*, vol. 78, no. 7, pp. 614–624, Jul. 2008, doi: 10.1177/0040517507081837.

[28] S. Jose, S. Rajna, and P. Ghosh, "Ramie Fibre Processing and Value Addition," *Asian J. Text.*, vol. 7, no. 1, pp. 1–9, Dec. 2016, doi: 10.3923/ajt.2017.1.9.

[29] I. D. Lawrence, S. Jayabal, and G. Selvakumar, "Particle Concentrations and Effectiveness of Natural Fibre Air Filter in Split Air Conditioner System," *Int. J. Appl. Eng. Res.*, vol. 10, pp. 4087–4092, Jun. 2015.

[30] P. W. Morgan, "Brief History of Fibers from Synthetic Polymers," *J. Macromol. Sci. Part - Chem.*, vol. 15, no. 6, pp. 1113–1131, Apr. 1981, doi: 10.1080/00222338108066456.

[31] J. Wang, "Assessing sheep's wool as a filtration material for the removal of formaldehyde in the indoor environment," Thesis, 2014. Accessed: Mar. 07, 2022. [Online]. Available: https://repositories.lib.utexas.edu/handle/2152/25838

[32] K. Min, S. Kim, and S. Kim, "Silk protein nanofibers for highly efficient, eco-friendly, optically translucent, and multifunctional air filters," *Sci. Rep.*, vol. 8, no. 1, Art. no. 1, Jun. 2018, doi: 10.1038/s41598-018-27917-w.

[33] S. Yang, Z. Zhu, F. Wei, and X. Yang, "Carbon nanotubes / activated carbon fiber based air filter media for simultaneous removal of particulate matter and ozone," *Build. Environ.*, vol. 125, pp. 60–66, Nov. 2017, doi: 10.1016/j.buildenv.2017.08.040.

[34] P. Li, C. Wang, Y. Zhang, and F. Wei, “Air Filtration in the Free Molecular Flow Regime: A Review of High-Efficiency Particulate Air Filters Based on Carbon Nanotubes,” *Small*, vol. 10, no. 22, pp. 4543–4561, 2014, doi: 10.1002/smll.201401553.

[35] C. Jia *et al.*, “A Foldable All-Ceramic Air Filter Paper with High Efficiency and High-Temperature Resistance,” *Nano Lett.*, vol. 20, no. 7, pp. 4993–5000, Jul. 2020, doi: 10.1021/acs.nanolett.0c01107.

[36] American Society of Mechanical Engineers, “Code on Nuclear Air and Gas Treatment ASME AG-1-2019.” ASME, Jan. 17, 2020.

[37] European Committee for Standardization and European Committee for Electrotechnical Standardization, “Making Standards for Europe.” https://www.cencenelec.eu/ (accessed Mar. 27, 2022).

[38] International Organization for Standardization, *High efficiency filters and filter media for removing particles from air — Part 1: Classification, performance, testing and marking*, vol. ISO 29463-1:2017(en),. Accessed: Mar. 25, 2022. [Online]. Available: https://www.iso.org/obp/ui/#iso:std:iso:29463:-1:ed-2:v1:en

[39] I. P. Beckman, G. Berry, H. Cho, and G. Riveros, “Digital Twin Geometry for Fibrous Air Filtration Media,” *Fibers*, vol. 9, no. 12, Art. no. 12, Dec. 2021, doi: 10.3390/fib9120084.

[40] N. Saifuddin, A. Z. Raziah, and A. R. Junizah, “Carbon Nanotubes: A Review on Structure and Their Interaction with Proteins,” *J. Chem.*, vol. 2013, p. e676815, Sep. 2012, doi: 10.1155/2013/676815.

[41] M. G. Huson, “Properties of wool,” in *Handbook of Properties of Textile and Technical Fibres*, Elsevier, 2018, pp. 59–103. doi: 10.1016/B978-0-08-101272-7.00003-1.

[42] Y. Yan, “2 - Developments in fibers for technical nonwovens,” in *Advances in Technical Nonwovens*, G. Kellie, Ed. Woodhead Publishing, 2016, pp. 19–96. doi: 10.1016/B978-0-08-100575-0.00002-4.

[43] Wikipedia, “Specific Strength.” Accessed: Jan. 06, 2021. [Online]. Available: https://en.wikipedia.org/w/index.php?title=Specific_strength&oldid=995313958

[44] M. De Araújo, “1 - Natural and man-made fibres: Physical and mechanical properties,” in *Fibrous and Composite Materials for Civil Engineering Applications*, R. Fangueiro, Ed. Woodhead Publishing, 2011, pp. 3–28. doi: 10.1533/9780857095583.1.3.

[45] Honeywell, “Honeywell Spectra® Fiber.” https://www.packagingcomposites-honeywell.com/spectra/product-info/spectra-fiber/ (accessed Jan. 06, 2021).

[46] DSM, “Dyneema® UHMWPE Fiber.” https://www.dsm.com/dyneema/en_GB/our-products/dyneema-fiber.html (accessed Jan. 06, 2021).

[47] MatWeb, "Overview of materials for Nylon 6 Fiber." http://www.matweb.com/search/DataSheet.aspx?MatGUID=675b77f996b142f59e4cb60d69d64872 (accessed Jan. 06, 2021).

[48] Dupont, "Kevlar® Aramid Fiber Technical Guide," 2017. https://www.dupont.com/content/dam/dupont/amer/us/en/safety/public/documents/en/Kevlar_Technical_Guide_0319.pdf

[49] Toyobo, "Zylon®(PBO fiber) Technical Information." https://www.toyobo-global.com/seihin/kc/pbo/zylon-p/bussei-p/technical.pdf (accessed Jan. 06, 2021).

[50] MatWeb, "Zoltek^{TM} OX Continuous Tow Oxidized PAN Fiber." http://www.matweb.com/search/DataSheet.aspx?MatGUID=7965dc42c7474350917b4b6086f572d1 (accessed Jan. 06, 2021).

[51] Toray Composite Materials America, "Torayca® Carbon Fiber," *Toray Composite Materials America, Inc.* https://www.toraycma.com/products/carbon-fiber/ (accessed Mar. 15, 2022).

[52] Solvay, "Carbon Fiber - Product catalog," *Solvay*. https://www.solvay.com/en/chemical-categories/our-composite-materials-solutions/carbon-fiber/product-catalog (accessed Jun. 19, 2021).

[53] MatWeb, "Thermal Ceramics Saffil® Bulk Fiber." http://www.matweb.com/search/DataSheet.aspx?MatGUID=92453918bf9c4c039b6eb7350f5faec5

[54] 3M, "Ceramic Fibers and Textiles Technical Reference Guide." https://multimedia.3m.com/mws/media/1327055O/3m-nextel-technical-reference-guide.pdf (accessed Mar. 30, 2022).

[55] Specialty Materials, "SCS Silicon Carbide Fiber." https://www.specmaterials.com/silicon-carbide-fiber-1#:~:text=Specialty%20Materials%27%20SCS%20silicon%20carbide,effective%20for%20high%2Dtemperature%20applications. (accessed Jun. 19, 2021).

[56] Saint-Gobain, "Quartzel Fused Quartz Textiles." https://www.quartz.saint-gobain.com/products/quartzel

[57] AGY, "Specialty Glass Fibers." https://www.agy.com/products/ (accessed Jan. 06, 2021).

[58] F. R. Jones and N. T. Huff, "The structure and properties of glass fibers," in *Handbook of Properties of Textile and Technical Fibres*, Elsevier, 2018, pp. 757–803. doi: 10.1016/B978-0-08-101272-7.00019-5.

[59] Specialty Materials, "Boron Fiber," *Specialty Materials*. https://www.specmaterials.com/boron-fiber-test-page (accessed Mar. 15, 2022).

[60] J. Militký, R. Mishra, and H. Jamshaid, “Basalt fibers,” in *Handbook of Properties of Textile and Technical Fibres*, Elsevier, 2018, pp. 805–840. doi: 10.1016/B978-0-08-101272-7.00020-1.

[61] MatWeb, “Special Metals INCONEL® 601GC® Nickel Superalloy.” https://www.matweb.com/search/DataSheet.aspx?MatGUID=84d2284cc7de4ed788f3e1e04a4df017&ckck=1 (accessed Mar. 15, 2022).

[62] T. Starr, *Carbon and High Performance Fibres Directory and Databook*, Edition 6., 1 online resource (408 pages) vols. Dordrecht: Springer Netherlands, 1995. doi: 10.1007/978-94-011-0695-5.

[63] Guangzhou Clean-Link Filtration Technology Co., “Paint Stop Filter Media/Pre-Filter Media/Carbon Filter Media/Ceiling Filter/Medium Efficiency Pocket Filter/HEPA Filter.” https://clean-link.en.alibaba.com/ (accessed Mar. 27, 2022).

[64] Hebei Amusen Filter Paper Co., “China Filter Paper, Fiberglass Air Filter Paper, Air Filter Paper Supplier.” https://m.made-in-china.com/company-amusenfilterpaper/ (accessed Mar. 27, 2022).

[65] Shandong Renfeng Special Materials Co., “China Filter Paper, Glass Fiber Filter Paper, Microfiber Glass Filter Paper Supplier.” https://m.made-in-china.com/company-sdrenfeng/ (accessed Mar. 27, 2022).

[66] Hebei Fangyu Trade Co., “China Glass Microfiber Filter Media,Wood Pulp Filter Paper,Auto Filter Paper Manufacturer and Supplier.” https://www.filtersmaterial.com/ (accessed Mar. 27, 2022).

[67] CHMLAB Group, “Filtration.” http://www.chmlab.com/en/AboutUs.php (accessed Mar. 27, 2022).

[68] O. Medvedyev and Y. Tsybulya, “Basalt use in hot gas filtration,” *Filtr. Sep.*, vol. 42, no. 1, pp. 34–37, Jan. 2005, doi: 10.1016/S0015-1882(06)70844-8.

[69] J. J. Haslam, “Prototype Ceramic High Efficiency Particulate Air Filter Testing and Filter Media Development for Nuclear Facility Ventilation,” Lawrence Livermore National Lab.(LLNL), Livermore, CA (United States), 2018.

[70] J. J. Haslam and M. A. Mitchell, “Ceramic Filter with Nanofibers,” US 2013/0048579 A1, Feb. 28, 2013

[71] J. P. Kelly, J. J. Haslam, M. A. Mitchell, N. Makeswaran, J. Maguire, and L. Finkenauer, “NSRD-12, Novel Mini-Tubular HEPA Media for Nuclear Facility Ventilation Systems,” United States, Oct. 2018. doi: 10.2172/1497954.

[72] G. M. Manzo, Y. Wu, G. G. Chase, and A. Goux, “Comparison of nonwoven glass and stainless steel microfiber media in aerosol coalescence filtration,” *Sep. Purif. Technol.*, vol. 162, pp. 14–19, Apr. 2016, doi: 10.1016/j.seppur.2016.02.006.

[73] T. P. Liew and J. R. Conder, “Fine mist filtration by wet filters—I. Liquid saturation and flow resistance of fibrous filters,” *J. Aerosol Sci.*, vol. 16, no. 6, pp. 497–509, Jan. 1985, doi: 10.1016/0021-8502(85)90002-3.

[74] J. R. Conder and T. P. Liew, “Fine mist filtration by wet filters-II: Efficiency of fibrous filters,” *J. Aerosol Sci.*, vol. 20, no. 1, pp. 45–57, 1989, doi: 10.1016/0021-8502(89)90030-X.

[75] S. Hwang, J. Roh, and W. M. Park, “Comparison of the relative performance efficiencies of melt-blown and glass fiber filter media for managing fine particles,” *Aerosol Sci. Technol.*, vol. 52, no. 4, pp. 451–458, Apr. 2018, doi: 10.1080/02786826.2017.1423274.

[76] Shanghai Mingguan Purification Materials Co., “H13 High Efficiency Low Air Pressure Drop HEPA Filter Media.” https://www.hepafilterpaper.com/air-filter-media/h13-high-efficiency-low-air-pressure-drop.html (accessed Mar. 28, 2022).

[77] D. P. F. Bonfim, F. G. S. Cruz, V. G. Guerra, and M. L. Aguiar, “Development of Filter Media by Electrospinning for Air Filtration of Nanoparticles from PET Bottles,” *Membranes*, vol. 11, no. 4, p. 293, Apr. 2021, doi: 10.3390/membranes11040293.

[78] F. N. H. Karabulut, G. Höfler, N. Ashok Chand, and G. W. Beckermann, “Electrospun Nanofibre Filtration Media to Protect against Biological or Nonbiological Airborne Particles,” *Polymers*, vol. 13, no. 19, Art. no. 19, Jan. 2021, doi: 10.3390/polym13193257.

[79] M. Zhu *et al.*, “Electrospun Nanofibers Membranes for Effective Air Filtration,” *Macromol. Mater. Eng.*, vol. 302, no. 1, p. 1600353, 2017, doi: 10.1002/mame.201600353.

[80] K. M. Yun, C. J. Hogan, Y. Matsubayashi, M. Kawabe, F. Iskandar, and K. Okuyama, “Nanoparticle filtration by electrospun polymer fibers,” *Chem. Eng. Sci.*, vol. 62, no. 17, pp. 4751–4759, Sep. 2007, doi: 10.1016/j.ces.2007.06.007.

[81] K. W. Lee and B. Y. H. Liu, “Theoretical Study of Aerosol Filtration by Fibrous Filters,” *Aerosol Sci. Technol.*, vol. 1, no. 2, pp. 147–161, Jan. 1982, doi: 10.1080/02786828208958584.

[82] N. Rao and M. Faghri, “Computer Modeling of Aerosol Filtration by Fibrous Filters,” *Aerosol Sci. Technol.*, vol. 8, no. 2, pp. 133–156, Jan. 1988, doi: 10.1080/02786828808959178.

[83] R. C. Brown, *Air filtration : an integrated approach to the theory and applications of fibrous filters*. Oxford; New York: Pergamon Press, 1993.

[84] C. N. Davies, *Air Filtration*. London, New York,: Academic Press, 1973.

[85] S. Kuwabara, “The Forces experienced by Randomly Distributed Parallel Circular Cylinders or Spheres in a Viscous Flow at Small Reynolds Numbers,” *J. Phys. Soc. Jpn.*, vol. 14, no. 4, pp. 527–532, Apr. 1959, doi: 10.1143/JPSJ.14.527.

[86] J. Happel, “Viscous flow relative to arrays of cylinders,” *AIChE J.*, vol. 5, no. 2, pp. 174–177, Jun. 1959, doi: 10.1002/aic.690050211.

[87] G. Kouropoulos, “The Effect of the Reynolds Number of Air Flow to the Particle Collection Efficiency of a Fibrous Filter Medium with Cylindrical Section,” *J. Urban Environ. Eng.*, pp. 3–10, Mar. 2014, doi: 10.4090/juee.2014.v8n1.003010.

[88] F. S. Henry and T. Ariman, “An Evaluation of the Kuwabara Model,” *Part. Sci. Technol.*, vol. 1, no. 1, pp. 1–20, Jan. 1983, doi: 10.1080/02726358308906350.

[89] K. W. Lee and B. Y. H. Liu, “Experimental Study of Aerosol Filtration by Fibrous Filters,” *Aerosol Sci. Technol.*, vol. 1, no. 1, pp. 35–46, Dec. 1981, doi: 10.1080/02786828208958577.

[90] K. W. Lee and B. Y. H. Liu, “On the Minimum Efficiency and the Most Penetrating Particle Size for Fibrous Filters,” *J. Air Pollut. Control Assoc.*, vol. 30, no. 4, pp. 377–381, Apr. 1980, doi: 10.1080/00022470.1980.10464592.

[91] C. N. Davies, “The Separation of Airborne Dust and Particles,” p. 29.

[92] L. Spielman and S. L. Goren, “Model for predicting pressure drop and filtration efficiency in fibrous media,” *Environ. Sci. Technol.*, vol. 2, no. 4, pp. 279–287, Apr. 1968, doi: 10.1021/es60016a003.

[93] G. Berry, I. Beckman, and H. Cho, “A comprehensive review of Particle loading models of fibrous air filters,” *J. Aerosol Sci.*, p. 106078, Sep. 2022, doi: 10.1016/j.jaerosci.2022.106078.

[94] Q. Wang, B. Maze, H. V. Tafreshi, and B. Pourdeyhimi, “A case study of simulating submicron aerosol filtration via lightweight spun-bonded filter media,” *Chem. Eng. Sci.*, vol. 61, no. 15, pp. 4871–4883, Aug. 2006, doi: 10.1016/j.ces.2006.03.039.

[95] A. Mukherjee and M. Agrawal, “A Global Perspective of Fine Particulate Matter Pollution and Its Health Effects,” in *Reviews of Environmental Contamination and Toxicology Volume 244*, P. de Voogt, Ed. Cham: Springer International Publishing, 2018, pp. 5–51. doi: 10.1007/398_2017_3.

[96] U.S. Army, “Army Climate Strategy Draft.” Sep. 28, 2021.

[97] “Climate Change Decreases the Quality of the Air we Breathe,” Centers for Disease Control and Prevention. [Online]. Available: https://www.cdc.gov/climateandhealth/

[98] S. Hartati *et al.*, “Synthesis of Electrospun PAN/TiO2/Ag Nanofibers Membrane As Potential Air Filtration Media with Photocatalytic Activity,” *ACS Omega*, vol. 7, no. 12, pp. 10516–10525, Mar. 2022, doi: 10.1021/acsomega.2c00015.

[99] R. Roche and F. Yalcinkaya, “Electrospun Polyacrylonitrile Nanofibrous Membranes for Point-of-Use Water and Air Cleaning,” *ChemistryOpen*, vol. 8, no. 1, pp. 97–103, 2019, doi: 10.1002/open.201800267.

[100] Y. Song, Y. Wang, L. Xu, and M. Wang, “Fabrication and Characterization of Electrospun Aligned Porous PAN/Graphene Composite Nanofibers,” *Nanomaterials*, vol. 9, no. 12, p. 1782, Dec. 2019, doi: 10.3390/nano9121782.

[101] C. Liu *et al.*, “Transparent air filter for high-efficiency PM2.5 capture,” *Nat. Commun.*, vol. 6, no. 1, Art. no. 1, Feb. 2015, doi: 10.1038/ncomms7205.

[102] K. J. Lee *et al.*, “Activated carbon nanofiber produced from electrospun polyacrylonitrile nanofiber as a highly efficient formaldehyde adsorbent,” *Carbon*, vol. 48, no. 15, pp. 4248–4255, Dec. 2010, doi: 10.1016/j.carbon.2010.07.034.

[103] S. Sundarrajan, K. L. Tan, S. H. Lim, and S. Ramakrishna, “Electrospun Nanofibers for Air Filtration Applications,” *Procedia Eng.*, vol. 75, pp. 159–163, Jan. 2014, doi: 10.1016/j.proeng.2013.11.034.

[104] L. Zhang, A. Aboagye, A. Kelkar, C. Lai, and H. Fong, “A review: carbon nanofibers from electrospun polyacrylonitrile and their applications,” *J. Mater. Sci.*, vol. 49, no. 2, pp. 463–480, Jan. 2014, doi: 10.1007/s10853-013-7705-y.

[105] V. Kumar, Y.-S. Lee, J.-W. Shin, K.-H. Kim, D. Kukkar, and Y. Fai Tsang, “Potential applications of graphene-based nanomaterials as adsorbent for removal of volatile organic compounds,” *Environ. Int.*, vol. 135, p. 105356, Feb. 2020, doi: 10.1016/j.envint.2019.105356.

[106] H. Dai, X. Liu, C. Zhang, K. Ma, and Y. Zhang, “Electrospinning Polyacrylonitrile/Graphene Oxide/Polyimide nanofibrous membranes for High-efficiency PM2.5 filtration,” *Sep. Purif. Technol.*, vol. 276, p. 119243, Dec. 2021, doi: 10.1016/j.seppur.2021.119243.

[107] J. Li, Y. Hu, H. Qiu, G. Yang, S. Zheng, and J. Yang, “Coaxial electrospun fibres with graphene oxide/PAN shells for self-healing waterborne polyurethane coatings,” *Prog. Org. Coat.*, vol. 131, pp. 227–231, Jun. 2019, doi: 10.1016/j.porgcoat.2019.02.033.

[108] C. J. Luo, S. D. Stoyanov, E. Stride, E. Pelan, and M. Edirisinghe, “Electrospinning versus fibre production methods: from specifics to technological convergence,” *Chem. Soc. Rev.*, vol. 41, no. 13, pp. 4708–4735, 2012, doi: 10.1039/C2CS35083A.

[109] Z.-M. Huang, Y.-Z. Zhang, M. Kotaki, and S. Ramakrishna, "A review on polymer nanofibers by electrospinning and their applications in nanocomposites," *Compos. Sci. Technol.*, vol. 63, no. 15, pp. 2223–2253, Nov. 2003, doi: 10.1016/S0266-3538(03)00178-7.

[110] A. Formhals, "Process and Apparatus for Preparing Artificial Threads," U.S. 1975504, Oct. 02, 1934 Accessed: Sep. 24, 2022. [Online]. Available: https://patentimages.storage.googleapis.com/7c/80/a3/67e4165167ebc1/US1975504.pdf

[111] B. S. Gupta and M. Afshari, "Polyacrylonitrile fibers," in *Handbook of Properties of Textile and Technical Fibres*, Elsevier, 2018, pp. 545–593. doi: 10.1016/B978-0-08-101272-7.00015-8.

[112] B. A. Newcomb and H. G. Chae, "The properties of carbon fibers," in *Handbook of Properties of Textile and Technical Fibres*, Elsevier, 2018, pp. 841–871. doi: 10.1016/B978-0-08-101272-7.00021-3.

[113] O. S. Yördem, M. Papila, and Y. Z. Menceloğlu, "Effects of electrospinning parameters on polyacrylonitrile nanofiber diameter: An investigation by response surface methodology," *Mater. Des.*, vol. 29, no. 1, pp. 34–44, Jan. 2008, doi: 10.1016/j.matdes.2006.12.013.

[114] T. Wang and S. Kumar, "Electrospinning of polyacrylonitrile nanofibers," *J. Appl. Polym. Sci.*, vol. 102, no. 2, pp. 1023–1029, 2006, doi: 10.1002/app.24123.

[115] J. Doshi and D. H. Reneker, "Electrospinning process and applications of electrospun fibers," *J. Electrost.*, vol. 35, no. 2, pp. 151–160, Aug. 1995, doi: 10.1016/0304-3886(95)00041-8.

[116] D. H. Reneker and A. L. Yarin, "Electrospinning jets and polymer nanofibers," *Polymer*, vol. 49, no. 10, pp. 2387–2425, May 2008, doi: 10.1016/j.polymer.2008.02.002.

[117] D. H. Reneker and I. Chun, "Nanometre diameter fibres of polymer, produced by electrospinning," *Nanotechnology*, vol. 7, no. 3, pp. 216–223, Sep. 1996, doi: 10.1088/0957-4484/7/3/009.

[118] D. H. Reneker, A. L. Yarin, H. Fong, and S. Koombhongse, "Bending instability of electrically charged liquid jets of polymer solutions in electrospinning," *J. Appl. Phys.*, vol. 87, no. 9, pp. 4531–4547, May 2000, doi: 10.1063/1.373532.

[119] I. Beckman, C. Lozano, E. Freeman, and G. Riveros, "Fiber Selection for Reinforced Additive Manufacturing," *Polymers*, vol. 13, no. 14, p. 2231, Jul. 2021, doi: 10.3390/polym13142231.

[120] M. Wu, Q. Wang, K. Li, Y. Wu, and H. Liu, "Optimization of stabilization conditions for electrospun polyacrylonitrile nanofibers," *Polym. Degrad. Stab.*, vol. 97, no. 8, pp. 1511–1519, Aug. 2012, doi: 10.1016/j.polymdegradstab.2012.05.001.

[121] E. Fitzer, W. Frohs, and M. Heine, “Optimization of stabilization and carbonization treatment of PAN fibres and structural characterization of the resulting carbon fibres,” *Carbon*, vol. 24, no. 4, pp. 387–395, Jan. 1986, doi: 10.1016/0008-6223(86)90257-5.

[122] B. Szepcsik and B. Pukánszky, “The mechanism of thermal stabilization of polyacrylonitrile,” *Thermochim. Acta*, vol. 671, pp. 200–208, Jan. 2019, doi: 10.1016/j.tca.2018.12.004.

[123] A. M. Saleh, H. V. Tafreshi, and B. Pourdeyhimi, “An analytical approach to predict pressure drop and collection efficiency of dust-load pleated filters,” *Sep. Purif. Technol.*, vol. 161, pp. 80–87, Mar. 2016, doi: 10.1016/j.seppur.2016.01.034.

[124] A. M. Saleh, S. A. Hosseini, H. Vahedi Tafreshi, and B. Pourdeyhimi, “3-D microscale simulation of dust-loading in thin flat-sheet filters: A comparison with 1-D macroscale simulations,” *Chem. Eng. Sci.*, vol. 99, pp. 284–291, Aug. 2013, doi: 10.1016/j.ces.2013.06.007.

[125] S. H. Yousefi, C. Tang, H. V. Tafreshi, and B. Pourdeyhimi, “Empirical model to simulate morphology of electrospun polycaprolactone mats,” *J. Appl. Polym. Sci.*, vol. 136, no. 46, p. 48242, 2019, doi: 10.1002/app.48242.

[126] A. Moghadam, S. H. Yousefi, H. V. Tafreshi, and B. Pourdeyhimi, “Characterizing nonwoven materials via realistic microstructural modeling,” *Sep. Purif. Technol.*, vol. 211, pp. 602–609, Mar. 2019, doi: 10.1016/j.seppur.2018.10.018.

[127] A. C. Payatakes and L. Gradoń, “Dendritic deposition of aerosol particles in fibrous media by inertial impaction and interception,” *Chem. Eng. Sci.*, vol. 35, no. 5, pp. 1083–1096, Jan. 1980, doi: 10.1016/0009-2509(80)85097-4.

[128] W. Moelter and H. Fissan, “Structure of a High Efficiency Glass Fiber Filter Medium,” *Aerosol Sci. Technol.*, vol. 27, no. 3, pp. 447–461, Sep. 1997, doi: 10.1080/02786829708965484.

[129] M. Faessel, C. Delisée, F. Bos, and P. Castéra, “3D Modelling of random cellulosic fibrous networks based on X-ray tomography and image analysis,” *Compos. Sci. Technol.*, vol. 65, no. 13, pp. 1931–1940, Oct. 2005, doi: 10.1016/j.compscitech.2004.12.038.

[130] Q. Wang, B. Maze, H. V. Tafreshi, and B. Pourdeyhimi, “Simulating through-plane permeability of fibrous materials with different fiber lengths,” *Model. Simul. Mater. Sci. Eng.*, vol. 15, no. 8, pp. 855–868, Dec. 2007, doi: 10.1088/0965-0393/15/8/003.

[131] B. Maze, H. Vahedi Tafreshi, and B. Pourdeyhimi, “Geometrical modeling of fibrous materials under compression,” *J. Appl. Phys.*, vol. 102, no. 7, p. 073533, Oct. 2007, doi: 10.1063/1.2794476.

[132] B. Maze, H. Vahedi Tafreshi, Q. Wang, and B. Pourdeyhimi, "A simulation of unsteady-state filtration via nanofiber media at reduced operating pressures," *J. Aerosol Sci.*, vol. 38, no. 5, pp. 550–571, May 2007, doi: 10.1016/j.jaerosci.2007.03.008.

[133] S. A. Hosseini and H. V. Tafreshi, "3-D simulation of particle filtration in electrospun nanofibrous filters," *Powder Technol.*, vol. 201, no. 2, pp. 153–160, Jul. 2010, doi: 10.1016/j.powtec.2010.03.020.

[134] S. Fotovati, H. Vahedi Tafreshi, and B. Pourdeyhimi, "Influence of fiber orientation distribution on performance of aerosol filtration media," *Chem. Eng. Sci.*, vol. 65, no. 18, pp. 5285–5293, Sep. 2010, doi: 10.1016/j.ces.2010.06.032.

[135] A. Karakoç, E. Hiltunen, and J. Paltakari, "Geometrical and spatial effects on fiber network connectivity," *Compos. Struct.*, vol. 168, pp. 335–344, May 2017, doi: 10.1016/j.compstruct.2017.02.062.

[136] S. H. Yousefi and H. Vahedi Tafreshi, "Modeling electrospun fibrous structures with embedded spacer particles: Application to aerosol filtration," *Sep. Purif. Technol.*, vol. 235, p. 116184, Mar. 2020, doi: 10.1016/j.seppur.2019.116184.

[137] S. H. Yousefi, D. G. Venkateshan, C. Tang, H. V. Tafreshi, and B. Pourdeyhimi, "Effects of electrospinning conditions on microstructural properties of polystyrene fibrous materials," *J. Appl. Phys.*, vol. 124, no. 23, p. 235307, Dec. 2018, doi: 10.1063/1.5049128.

[138] H. Vahedi Tafreshi, M. S. A Rahman, S. Jaganathan, Q. Wang, and B. Pourdeyhimi, "Analytical expressions for predicting permeability of bimodal fibrous porous media," *Chem. Eng. Sci.*, vol. 64, no. 6, pp. 1154–1159, Mar. 2009, doi: 10.1016/j.ces.2008.11.013.

[139] P.-C. Gervais, N. Bardin-Monnier, and D. Thomas, "Permeability modeling of fibrous media with bimodal fiber size distribution," *Chem. Eng. Sci.*, vol. 73, pp. 239–248, May 2012, doi: 10.1016/j.ces.2012.01.040.

[140] R. Mead-Hunter, A. J. C. King, G. Kasper, and B. J. Mullins, "Computational fluid dynamics (CFD) simulation of liquid aerosol coalescing filters," *J. Aerosol Sci.*, vol. 61, pp. 36–49, Jul. 2013, doi: 10.1016/j.jaerosci.2013.03.009.

[141] M. Grothaus, A. Klar, J. Maringer, P. Stilgenbauer, and R. Wegener, "Application of a three-dimensional fiber lay-down model to non-woven production processes," *J. Math. Ind.*, vol. 4, no. 1, p. 4, Jun. 2014, doi: 10.1186/2190-5983-4-4.

[142] S. Abishek, A. J. C. King, R. Mead-Hunter, V. Golkarfard, W. Heikamp, and B. J. Mullins, "Generation and validation of virtual nonwoven, foam and knitted filter (separator/coalescer) geometries for CFD simulations," *Sep. Purif. Technol.*, vol. 188, pp. 493–507, Nov. 2017, doi: 10.1016/j.seppur.2017.07.052.

[143] A. Krizhevsky, I. Sutskever, and G. E. Hinton, “ImageNet classification with deep convolutional neural networks,” *Commun. ACM*, vol. 60, no. 6, pp. 84–90, May 2017, doi: 10.1145/3065386.

[144] K. Simonyan and A. Zisserman, “Very Deep Convolutional Networks for Large-Scale Image Recognition.” arXiv, Apr. 10, 2015. Accessed: Aug. 22, 2022. [Online]. Available: http://arxiv.org/abs/1409.1556

[145] K. He, X. Zhang, S. Ren, and J. Sun, “Deep Residual Learning for Image Recognition.” arXiv, Dec. 10, 2015. Accessed: Aug. 22, 2022. [Online]. Available: http://arxiv.org/abs/1512.03385

[146] M. D. Zeiler and R. Fergus, “Visualizing and Understanding Convolutional Networks.” arXiv, Nov. 28, 2013. Accessed: Aug. 28, 2022. [Online]. Available: http://arxiv.org/abs/1311.2901

[147] C. Szegedy *et al.*, “Going Deeper with Convolutions.” arXiv, Sep. 16, 2014. Accessed: Aug. 22, 2022. [Online]. Available: http://arxiv.org/abs/1409.4842

[148] C. Szegedy, V. Vanhoucke, S. Ioffe, J. Shlens, and Z. Wojna, “Rethinking the Inception Architecture for Computer Vision.” arXiv, Dec. 11, 2015. Accessed: Aug. 22, 2022. [Online]. Available: http://arxiv.org/abs/1512.00567

[149] MatWeb, “Online Materials Information Resource.” http://www.matweb.com/ (accessed Jun. 19, 2021).

[150] J. W. S. Hearle, “Textile Fibers: A Comparative Overview,” in *Encyclopedia of Materials: Science and Technology*, K. H. J. Buschow, R. W. Cahn, M. C. Flemings, B. Ilschner, E. J. Kramer, S. Mahajan, and P. Veyssière, Eds. Oxford: Elsevier, 2001, pp. 9100–9116. doi: 10.1016/B0-08-043152-6/01643-0.

[151] F. K. Ko and L. Y. Wan, “Engineering properties of spider silk,” in *Handbook of Properties of Textile and Technical Fibres*, Elsevier, 2018, pp. 185–220. doi: 10.1016/B978-0-08-101272-7.00006-7.

[152] Teijin, “Products & Services.” https://www.teijin.com/products/index.html (accessed Mar. 20, 2022).

[153] P. M. Cunniff, M. A. Auerbach, E. Vetter, and D. J. Sikkema, “High Performance ‘M5’ Fiber for Ballistics/Structural Composites,” in *Proceedings of the 23rd Army Science Conference*, Orlando, FL, USA, Dec. 2002, p. 8.

[154] Binani Industries, “Glass Fibre,” *3B The Fiberglass Company*. https://www.3b-fibreglass.com/ (accessed Mar. 20, 2022).

[155] JPS Composite Materials, a Handy and Harman Company, “Technical Reference Handbook.” https://jpscm.com/ wp-content/uploads/2017/10/2017-Data-Book-Small-1.pdf

[156] Texonic, “Fiber Properties Guide.” https://texonic.net/en/tableau/technical/ (accessed Jan. 06, 2021).

APPENDIX A

COMPILED FIBER DATA AND SOURCES FOR LITERATURE REVIEW

Table A.1 Compiled Data for Particular Fibers

Family	Fiber	Density (g/cm^3)	Tensile Strength (GPa)	Tensile Modulus (GPa)	Melting/ Decomposing Temp (˚C)	Moisture Regain (%)	CTE (10^{-6} K^{-1})	Elongation at Break (%)	Diameter (μm)
cellulose	Oak wood fiber [149]	0.74	0.090	2.66	250	15.0	4.9	2.0	13
cellulose	Pine wood fiber [149]	0.35	0.078	468.48	-	-	-	8.2	-
cellulose	American Uppers Cotton [42]	1.52	0.491	7.60	246	8.5	-	7.0	11
cellulose	Flax [44]	1.54	0.831	27.72	-	12.4	-	3.0	5
cellulose	Hemp [44]	1.50	0.705	32.55	-	12.4	-	2.2	-
cellulose	Jute [44]	1.50	0.465	25.80	-	13.8	-	1.8	8
cellulose	Ramie [44]	1.50	0.885	21.90	-	-	-	3.7	-
cellulose	Fortisan, Viscose Rayon [44]	1.50	0.885	24.15	175	16.0	-	6.4	9
cellulose	TriAcetate fiber [150]	1.32	0.172	4.75	230	4.0	-	30.0	15
cellulose	Tenasco Rayon [44]	1.50	0.405	9.00	175	13.0	-	20.0	12
keratin	Wool [41]	1.31	0.185	5.11	222	16.0	9.2	35.0	18
keratin	Silkworm silk [150]	1.34	0.509	9.78	175	10.0	-	23.0	10
keratin	Spider silk [151]	1.31	1.400	-	-	10.0	-	23.0	2
polymer	Toyobo Zylon HM PBO [49]	1.56	5.800	270.00	650	0.6	-6	2.5	1.18
polymer	Nylon 6 [152]	1.13	0.900	3.00	223	4.5	6.5	25.0	14
polymer	Nylon 6.6 [152]	1.13	0.900	5.00	260	6.0	6.5	25.0	14
polymer	Polypropylene (PP) [44]	0.91	0.591	6.46	100	1.0	-	20.0	38
polymer	Polyacrylonitrile (PAN) [152]	1.40	0.300	11.00	327	10.0	-	23.0	-
polymer	Polytetraflouroethylene (PTFE) [20]	2.22	0.392	199.00	-	-	-	25.0	-
polymer	Polybenzimidazole (PBI) [152]	1.43	0.320	5.10	450	15.0	-	27.0	-
polymer	Vectran HT Polyester [149]	1.41	3.200	75.00	-	0.1	-	3.8	-
polymer	P84 Polyimide [62]	1.41	0.540	5.00	-	-	-	30.0	-
polymer	Polyvinyl Alcohol (PVA) [44]	1.30	1.600	22.00	-	-	-	-	-
polymer	Acrylic [150]	1.19	0.321	7.38	235	1.5	-	28.0	12
polymer	Toyobo Tsunooga [49]	0.97	1.400	43.00	145	-	-	6.0	-
polymer	Akzo Nobel M5 PIPD[153]	1.70	3.960	271.00	-	-	-	1.4	-
polymer	Polyester HT [44]	1.39	0.778	18.35	-	-	-	-	-
aramid	Dupont Kevlar 49 [48]	1.44	3.000	112.40	427	3.5	-4.86	2.4	12
aramid	Dupont Kevlar 29 [48]	1.44	3.617	62.00	427	3.5	-	4.0	-
aramid	Dupont Nomex 430 Metaaramid [48]	1.38	0.609	8.30	350	5.1	-	30.5	-
aramid	Teijin Technora [152]	1.39	3.400	74.00	500	1.9	-	4.5	-
aramid	Teijin Twaron [152]	1.45	3.600	120.00	500	5.0	-	4.4	-
aramid	Dupont Kevlar 149 [48]	1.47	3.450	179.00	427	3.5	-	-	-
UHMWPE	DSM Dyneema SK99 [46]	0.97	4.100	155.00	144	0.0	-12	4.0	12
UHMWPE	Honeywell Spectra 1000-75 [45]	0.97	3.680	133.00	147	-	-12	2.9	1.665
carbon	Single Wall Carbon Nanotube [44]	1.40	53.000	5000.00	-	-	-	16.0	-
carbon	Toray T1100G (IM, PAN) [51]	1.79	7.012	324.00	3500	-	-0.5	2.0	5
carbon	Toray M-46J (HM, PAN) [51]	1.84	4.200	436.00	3500	-	-0.9	1.0	5
carbon	Solvay P25 (pitch) [52]	1.95	1.380	159.00	254	-	-0.6	0.5	11
glass	AR1 glass fiber [58]	2.74	3.240	73.00	1290	-	6.5	-	-
glass	A glass High Alkali [58]	2.46	3.100	72.00	1600	-	9	4.8	-
glass	C glass Sodium Borosilicate [58]	2.49	3.400	69.00	800	-	7.1	4.4	3.8
glass	D glass [58]	2.10	2.400	52.00	-	-	2.5	-	-
glass	E glass Alumino Borosilicate [58]	2.53	3.700	76.00	1140	-	5.4	4.8	3
glass	Binani SE1500 ECR [154]	2.62	2.500	81.00	-	-	6.1	-	17
glass	R glass [58]	2.55	4.500	85.00	-	-	4.1	-	-
glass	S glass Owens Corning [62]	2.55	3.450	86.00	-	-	-	-	-
glass	AGY S1 glass [57]	2.52	3.135	90.00	-	-	-	-	-
glass	AGY ZenTron S2 Magn Borosil [149]	2.46	4.890	86.90	816	-	1.6	5.7	7
glass	AGY S3 glass [57]	2.83	3.338	99.00	-	-	-	-	-
quartz	Saint-Gobain Quartzel (SiO2) [56]	2.20	6.000	78.00	1220	-	0.54	7.7	9
quartz	J.P. Stevens Astroquartz II (SiO2) [155]	2.20	6.000	72.00	1120	-	-	-	-
ceramic	Specialty Materials SCS Ultra SiC [55]	3.08	5.900	415.00	1550	-	4.1	0.9	75
ceramic	3M Nextel 610 alumina silica [54]	3.90	2.800	370.00	2000	-	8	-	10
ceramic	Alumina Saffil [149]	3.30	2.000	300.00	2000	-	5.2	-	3
ceramic	Specialty Materials SCS6 SiC [55]	3.08	3.900	380.00	-	-	-	-	-
ceramic	3M Nextel 440 [54]	3.00	1.840	190.00	1800	-	5.3	-	-
ceramic	3M Nextel 720 [54]	3.40	1.940	250.00	-	-	-	-	-
ceramic	3M Nextel 312 Alumina [54]	2.80	1.630	150.00	-	-	-	-	-
mineral	Basalt fiber [156]	2.64	4.137	84.80	1450	3.0	8	3.0	10
mineral	Specialty Materials Boron 4mil [59]	2.61	4.000	428.00	1350	-	4.5	-	102

Family	Fiber	Density (g/cm^3)	Tensile Strength (GPa)	Tensile Modulus (GPa)	Melting/ Decomposing Temp (˚C)	Moisture Regain (%)	CTE (10^{-6} K^{-1})	Elongation at Break (%)	Diameter (μm)
metal	Inconel 601GC Nickel Superalloy [149]	8.11	0.790	206.50	1360	-	13.75	55.0	-
metal	Stainless Steel [43]	8.00	0.505	70.40	1370	-	-	-	-
metal	Brass fiber [43]	8.55	0.580	76.95	1260	-	-	-	-
metal	Copper [43]	8.92	0.220	1516.40	1293	-	-	-	-
metal	Aluminum [44]	2.70	0.620	70.00	-	-	-	-	-

Table A.2 Sources of Data for Fiber Information

Source	Source	Year	Type
Online	Matweb, Wikipedia	2022	All fiber types
Commercial Technical Guides	Dupont Kevlar Aramid Technical Guide	2022	Aramid
	3M Nextel Ceramic Fibers Technical Reference Guide	2021	Nextel
	Dupont Nomex Technical Guide	2021	Nomex
	J.P. Stevens Handbook	2017	Quartz and Glass
	Saint Gobain Quartzel Datasheet	2021	Quartzel
Commercial Datasheets	AGY, Binani, DSM, Dupont, Hexcel, Hiltex, Honeywell, Mitsubishi, Nycon, Solvay, Specialty Materials, Teijin, Texonic, Torray, Toyobo	2021	All fiber types
Handbooks and Data Books	Handbook of Properties of Textile and Technical Fibers	2018	All fiber types
	Handbook of Nonwoven Filter Media	2016	All fiber types
	Advances in Technical Nonwovens	2016	Cellulose
	Ullmann's Encyclopedia of Industrial Chemistry	2012	Ceramic, Glass
	Fibrous Composite Materials for Civil Engineering Applications	2011	All fiber types
	Natureworks Ingeo Technical Bulletin TB180904	2005	Natural
	Handbook of Materials for Product Design	2001	Glass
	Textile Fibers: A Comparative Overview	2001	Natural and Polymer
	Carbon and High Performance Fibres Directory and Databook	1995	All fiber types
	Handbook of Materials for Product Design	2001	Carbon, Ceramic, Glass
	Military Standard 1944, Polymer Matrix Composites	1985	Carbon, Ceramic, Mineral

APPENDIX B

SKEW ANALYSIS FOR FRAGMENT DISTANCE FROM CENTER OF SQUARE

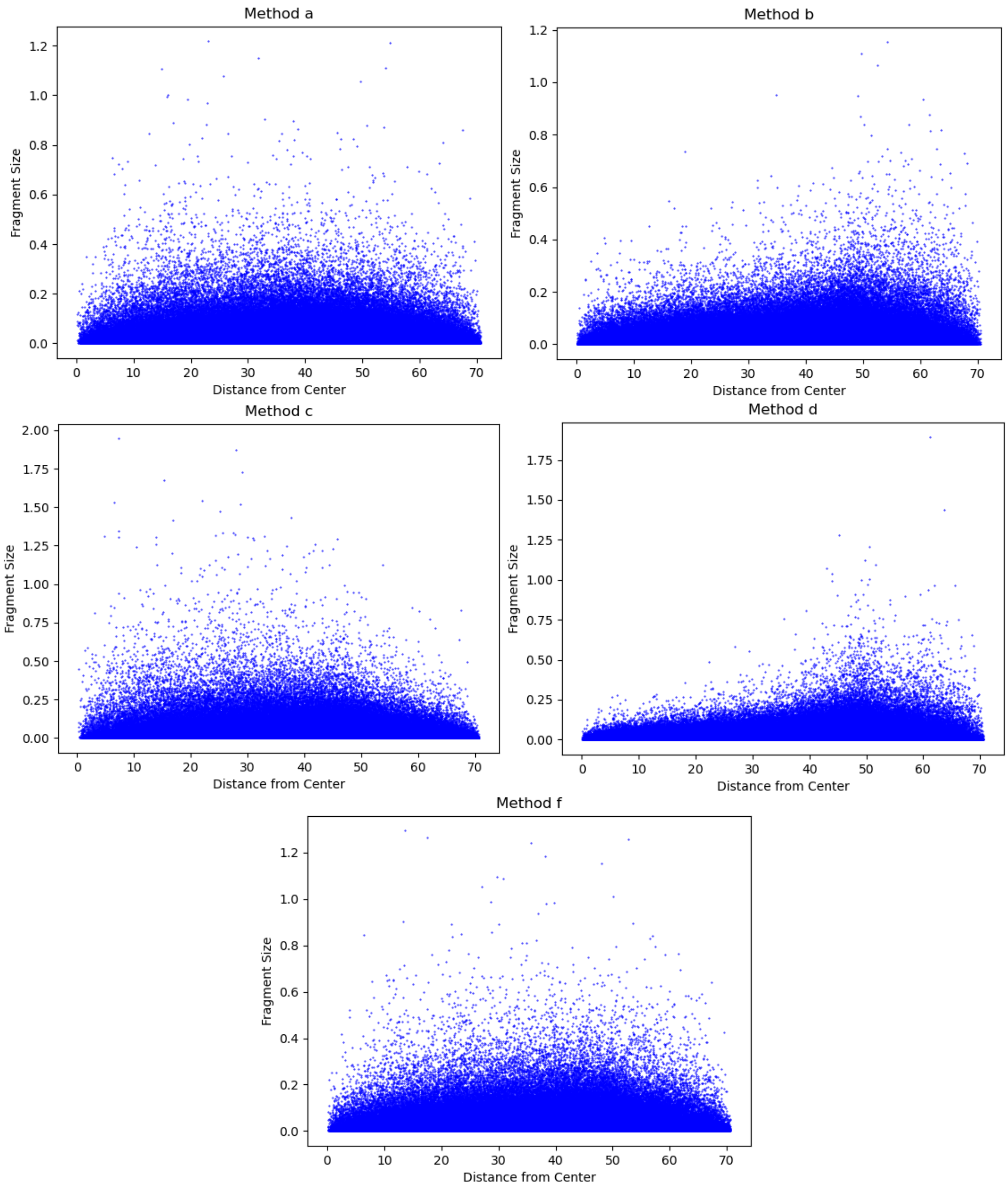

Figure B.1 Skew analysis for fragment centroid distance from center of square.

APPENDIX C

COMPARISON OF SEM IMAGE WITH DIGITAL REPLICAS

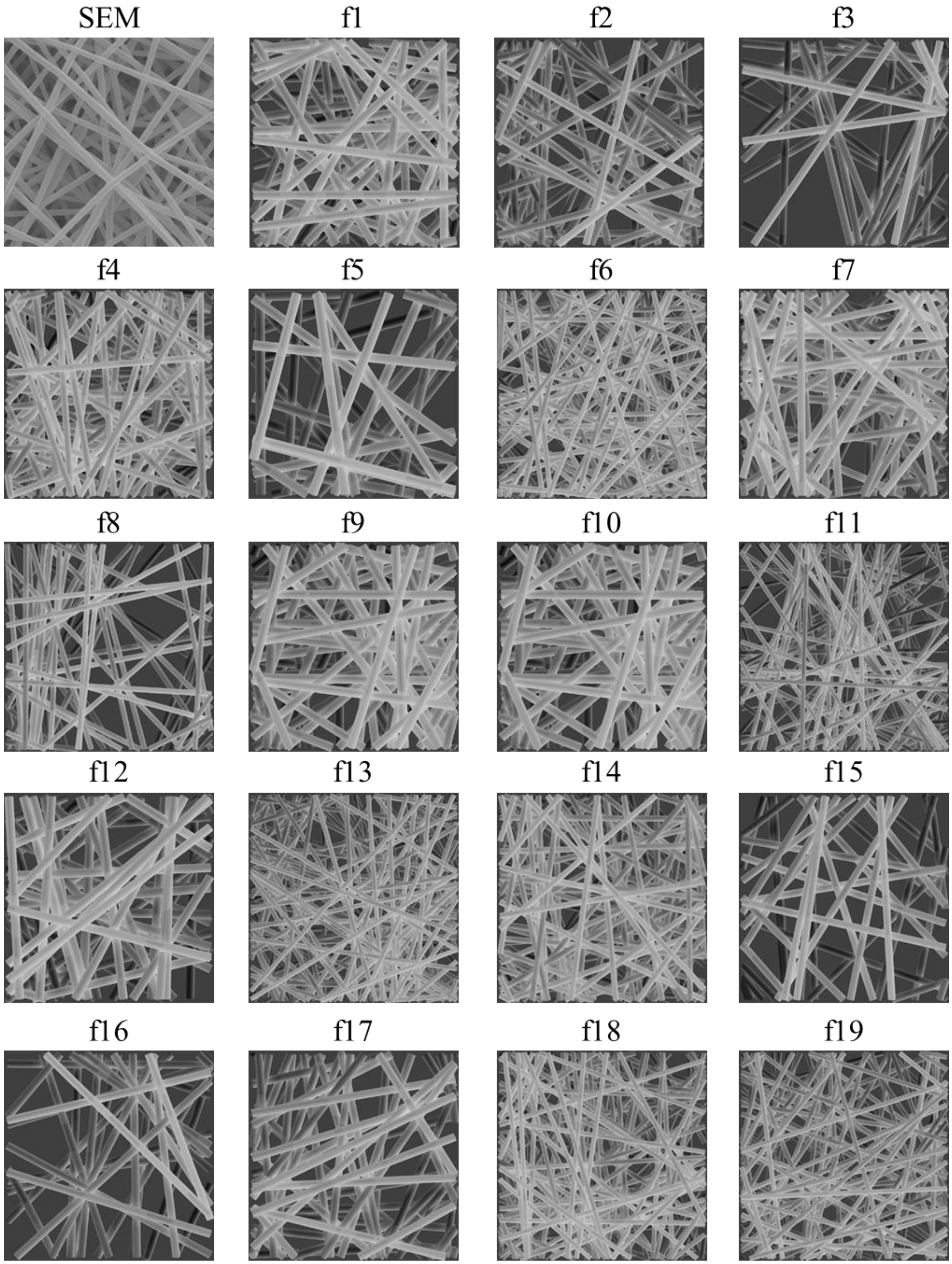

Figure C.1 Comparison of SEM image with digital twin replica air filter media.

REPORT DOCUMENTATION PAGE

1. REPORT DATE
June 2023

2. REPORT TYPE
Final Report

3. DATES COVERED

START DATE	END DATE
FY16	FY22

4. TITLE AND SUBTITLE
Development of Alternative Air Filtration Materials and Methods of Analysis

5a. CONTRACT NUMBER	5b. GRANT NUMBER	5c. PROGRAM ELEMENT
5d. PROJECT NUMBER	**5e. TASK NUMBER**	**5f. WORK UNIT NUMBER**

6. AUTHOR(S)
Ivan Philip Beckman

7. PERFORMING ORGANIZATION NAME(S) AND ADDRESS(ES)
US Army Engineer Research and Development Center (ERDC)
3909 Halls Ferry Road
Vicksburg, MS 39180-6199

8. PERFORMING ORGANIZATION REPORT NUMBER
ERDC MP-23-3

9. SPONSORING/MONITORING AGENCY NAME(S) AND ADDRESS(ES)
Mississippi State University
Department of Mechanical Engineering
75 B. S. Hood Rd
Mississippi State, MS 39762

10. SPONSOR/MONITOR'S ACRONYM(S)
MSU

11. SPONSOR/MONITOR'S REPORT NUMBER(S)

12. DISTRIBUTION/AVAILABILITY STATEMENT
Distribution Statement A. Approved for public release: distribution is unlimited.

13. SUPPLEMENTARY NOTES
This article was originally a dissertation submitted in December 2022 to the faculty of MSU in partial fulfillment of the requirements for the degree of Doctor of Philosophy in Engineering in the Department of Mechanical Engineering. This dissertation was approved by Heejin Cho (major professor), Shanti Bhushan, Like Li, Guillermo A. Riveros, Tonya W. Stone (graduate coordinator), and Jason M. Keith (dean, Bagley College of Engineering).

14. ABSTRACT
Development of high efficiency particulate air (HEPA) filters demonstrate an effort to mitigate dangerous aerosol hazards at the point of production. The nuclear power industry installs HEPA filters as a final line of containment of hazardous particles. An exploration of analytical, experimental, computational, and machine learning models is presented in this dissertation to advance the science of air filtration technology. This dissertation studies, develops, and analyzes alternative air filtration materials and methods of analysis that optimize filtration efficiency and reduce resistance to air flow. Alternative nonwoven filter materials are considered for use in HEPA filtration. A detailed review of natural and synthetic fibers is presented to compare mechanical, thermal, and chemical properties of fibers to desirable characteristics for air filtration media. Digital replication of air filtration media enables coordination among experimental, analytical, machine learning, and computational air filtration models. The value of using synthetic data to train and evaluate computational and machine learning models is demonstrated through prediction of air filtration performance, and comparison to analytical results. This dissertation concludes with discussion on potential opportunities and future work needed in the continued effort to advance clean air technologies for the mitigation of a global health and safety challenge.

15. SUBJECT TERMS
Aerosol technology; Air filtration; Analytical modeling; Bertrand's Paradox; Computational modeling; Convolutional neural network; Digital twin geometry; Electrospinning nanofibers; Experimental modeling; Single fiber efficiency method

16. SECURITY CLASSIFICATION OF:

a. REPORT	b. ABSTRACT	C. THIS PAGE	17. LIMITATION OF ABSTRACT	18. NUMBER OF PAGES
Unclassified	Unclassified	Unclassified	SAR	261

19a. NAME OF RESPONSIBLE PERSON
Dr. Ivan P. Beckman

19b. TELEPHONE NUMBER (include area code)
603-646-4201